CURRENT-VOLTAGE CHARACTERISTICS OF ORGANIC SEMICONDUCTORS: INTERFACIAL CONTROL BETWEEN ORGANIC LAYERS AND ELECTRODES

A Thesis
Presented to
The Academic Faculty

by

Takeshi Kondo

In Partial Fulfillment
of the Requirements for the Degree
Doctor of Philosophy in the
School of Chemistry and Biochemistry

Georgia Institute of Technology
August, 2007

CURRENT-VOLTAGE CHARACTERISTICS OF ORGANIC SEMICONDUCTORS: INTERFACIAL CONTROL BETWEEN ORGANIC LAYERS AND ELECTRODES

Approved by:

Dr. Seth R. Marder, Advisor
School of Chemistry and Biochemistry
Georgia Institute of Technology

Dr. Joseph W. Perry
School of Chemistry and Biochemistry
Georgia Institute of Technology

Dr. Bernard Kippelen, Co-Advisor
School of Electrical and Computer Engineering
Georgia Institute of Technology

Dr. Mohan Srinivasarao
School of Textile and Fiber Engineering
Georgia Institute of Technology

Dr. Jean-Luc Brédas
School of Chemistry and Biochemistry
Georgia Institute of Technology

Date Approved: June 12, 2007

To Chifumi, Ayame, Suzuna, and Lintec Corporation

ACKNOWLEDGEMENTS

I wish to thank Prof. Seth R. Marder for all his guidance and support as my adviser. I am also grateful to Prof. Bernard Kippelen for serving as my co-adviser. Since I worked with them, I have been very fortunate to learn tremendous things from them. Seth's enthusiasm about and dedication to science and education have greatly influenced me. It is always a pleasure to talk with Seth on various aspects of chemistry and life. Bernard's encouragement and scientific advice have always been important to organize my research. I have been fortunate to learn from his creative and logical thinking. I must acknowledge all the current and past members of Prof. Marder's and Prof. Kippelen's research groups for their collaborations and friendships. Also I am thankful for my committee members providing valuable suggestions on my thesis.

Some of the works presented in this thesis were the results of collaborations among different groups. I am grateful to Dr. Qing Zhang in Prof. Marder's group for teaching synthesis techniques. I appreciate some materials provided by Dr. Shijun Zheng and Michal Malicki in Prof. Marder's group, PES and IPES data provided by Prof. Antoine Kahn at Princeton University, and DFT data provided by Prof. Jean-Luc Brédas at Georgia Institute Technology.

I must thank LINTEC Corporation for supporting my family's life and funding for the project related with the work in this thesis.

I have had this important period of time with my family. I am deeply grateful to my wife Chifumi who supports me with love and tender heart, and to my lovely children Ayame and Suzuna who always give me sweetest smiles.

TABLE OF CONTENTS

LIST OF TABLES

LIST OF FIGURES

LIST OF SCHEMES

LIST OF SYMBOLS

I	Current
J	Current density
V	Voltage
q	Magnitude of electronic charge
ϕ_m	Work function of metal
ϕ_{Bn}	Barrier height of metal-semiconductor
χ	Electron affinity of semiconductor
E_C	Bottom of conduction band
E_F	Fermi energy level
E_V	Top of valence band
V_{bi}	Built-in potential
W	Depletion width
V_F	Forward bias
V_R	Reverse bias
A^*	Effective Richardson constant
ε	Permittivity
k	Boltzmann's constant
$\hbar$	Reduced Plank's (= $h/2\pi$)
T	Temperature
m^*	Effective mass
d	Film thickness
ΔE_{ae}	Activation energy of electron

ΔE_{ai}	Activation energy of ions
k_{et}	Charge-transfer rate
t	Intermolecular transfer integral
λ	Reorganization energy
E_t	Transporting energy
T_g	Glass transition temperature
N	Number of charge carriers in the material
e	Elementary charge
v	Velocity
C	Capacitance
R	Resistance
t_t	Transit time
σ	Width of the energetically disorder distribution
Σ	Width of the positional disorder distribution
μ	Mobility
$\mu_{(0)}$	Disorder-free mobility
μ_0	Zero-field mobility
γ	Electric-field coefficient
E	Electric-field
$E_{1/2}$	Redox potential
ΔE_{op}	Optical band-gap

LIST OF ABBREVIATIONS

OLED	Organic light-emitting diode
OFET	Organic field-effect transistor
OPV	Organic photovoltaic cell
MIS	Metal/insulator/semiconductor
LUMO	Lowest occupied molecular orbital
HOMO	Highest occupied molecular orbital
DOS	Density of states
HT	Hole transporting
ET	Electron transporting
NDR	Negative differential resistance
WORM	Write-once-read-many times
WRE	Write-read-erase
TOF	Time-of-flight
PR-TRMC	Pulse-radiolysis time-resolved microwave conductivity
SCLC	Space-charge-limited current
WRE	Write-read-erase
ITO	Indium tin oxide
IP	Ionization potential
EA	Electron affinity
CV	Cyclic voltammetry
HATNA	Hexaazatrinaphthylene
HPLC	High-performance liquid chromatography
NMR	Nuclear Magnetic Resonance

DSC	Differential scanning calorimetry
TGA	Thermal gravity analyzer
XRD	X-ray diffraction
POM	Polarized optical microscopy
DFT	Density functional theory
PES	Photoelectron spectroscopy
IPES	Inverse photoelectron spectroscopy
NP	Nanoparticle
ND	Nanodot
MIM	Metal/insulator/metal
XPS	X-ray photoemission spectroscopy
AFM	Atomic force microscopy
TEM	Transmission electron microscopy
SPR	Surface plasmon resonance
MBA	4-mercaptobenzoic acid
OT	Octane-1-thiol
PVK	Poly(*N*-vinylcarbazole)
WRER	Write-read-erase-reread
PEDOT:PSS	Poly(3,4-ethylenedioxythiophene) doped with polystyrenesulphonic acid
PVP	Poly-4-vinylphenol

SUMMARY

Current-voltage (*I-V*) characteristics of organic molecular glasses and solution processable materials embedded between two electrodes were studied. Particular research emphases were to find molecular glasses or solution processable materials possessing high charge-carrier mobilities by through analyzing *I-V* characteristics, and to design organic memory devices by using interfacial controlled electrode/organic junctions.

Mobility measurements based on *I-V* characteristics in space-charge-limited current regimes with the high injection efficiencies (> 0.3) were in excellent agreement with those determined by other measurement methods. The comparison studies confirm the validity of using analyses of *I-V* characteristics on organic semiconducting thin film to determine their mobilities even when the measured value is limited by the injection efficiency from an electrode into an organic layer; a low injection efficiency will lead to an underestimation of the intrinsic mobility of the material. Hexaazatrinaphthylene derivatives tri-substituted by electron withdrawing groups were synthesized as potential electron transporting molecular glasses, and two isomers and their mixtures were separated from crude products. The presence of two isomers has important implications for film morphology and effective mobility. The statistical isomer mixture of hexaazatrinaphthylene derivatized with pentafluoro-phenylmethyl ester is able to form amorphous film, and electron mobilities with the range of 10^{-2} cm^2/Vs are observed in their *I-V* characteristics. This mobility value is the same order as the highest reported for molecular glasses.

Single-layer organic memory devices consisting of a polymer layer embedded between an Al electrode and ITO modified with Ag nanodots (Ag-NDs) prepared by a solution-based surface assembly were investigated. The systems demonstrated a potential capability as nonvolatile organic memory device with high ON/OFF switching ratios of 10^4. This level of performance could be achieved by modifying the ITO electrodes with some Ag-NDs that act as trapping sites, thereby reducing the current in the OFF state. The electrical characteristics based on thickness dependence and temperature dependence suggest that the currents of the low-resistance state can be attributed to tunneling through low-resistance pathways of metal particles originating from the metal top electrode in the organic layer and that the high-resistance state is controlled by charge trapping by the metal particles including Ag-NDs.

In an alternative approach, complex films of $AgNO_3$: hexaazatrinaphthylene derivatives were studied as the active layers for all-solution processed and air-stable organic memory devices. Rewritable memory effects were observed in the devices comprised of a thin polymer dielectric layer deposited on the bottom electrode, the complex film, and a conducting polymer film as the top electrode. The devices were fabricated by solution processing, with the exception of the bottom electrode. The electrical characteristics which were dependent on factors including different $AgNO_3$ concentrations and different dielectric thicknesses, indicate that the accumulation of Ag^+ ions at the interface of the complex film and the top electrode may contribute to the switching effect.

CHAPTER 1

INTRODUCTION

1.1 Organization of the thesis

This thesis is organized as follow: Chapter 1 provides general background on charge transports of semiconductor and insulator films, organic semiconductor materials, and the state-of-the-art of organic memory devices. Chapter 2 describes why the characterization of charge carrier mobility in organic semiconductors based on applying the disorder formalism to current-voltage (*I-V*) characteristics is a reliable technique and how it compares to other techniques such as time-of flight (TOF) and field-effect transistor (FET). Chapter 3 describes the characterization of hexaazatrinaphthylene (HATNA) derivatives as potential molecular glasses possessing high charge carrier mobilities. The HATNAs tri-substituted by electron withdrawing groups, pentafluoro-phenylmethyl ester and trifluoromethyl, were synthesized and separated as the symmetrical (C_{3h}) 2, 8,14-isomer, the less symmetrical (C_s) 2,8,15-isomer, and their mixtures to compare the material properties of each isomer and the mixture. The charge carrier nobilities of the films of each compound are studied by the *I-V* characteristics based on the SCLC regime as described in Chapter 2. Chapter 4 and Chapter 5 describe the design and characterization of organic memory devices using anomalous *I-V* characteristics on thin films of solution processable organic materials embedded between two electrodes. In Chapter 4, we study effects of Ag-nanodots(NDs) attached on ITO bottom electrode as charge trapping sites on electrical switching properties. To verify the role of Ag-NDs on ITO electrodes, the devices are compared to a device without Ag-NDs

and a device made with Ag-nanoparticles(NPs) randomly distributed throughout the entire thickness of the organic matrix. In Chapter 5, we design and characterize an organic memory device using a complex thin film of silver nitrate and HATNA derivatives (described in Chapter 3) and a conducting polymer electrode as an active component and one of electrodes, respectively, in order to achieve an air-stable, semi-transparent organic memory device. The device fabrication is performed by solution processing such as spin-coating and ink-jet printing. Chapter 6 summarizes the research described in the thesis and suggests future directions that may lead to the improvement of organic memory devices.

1.2 *I-V* characteristics of metal/semiconductor contacts

A *I-V* characteristic showing the relationship between the currents through an electronic device and the applied voltages across its terminals is used as a critical tool to determine basic parameters of a device and to model its behavior in an electrical circuit. In addition, the *I-V* characteristic of an active component embedded between two electrodes can be utilized to estimate material properties such as conductivity, charge carrier mobility, and charge injection efficiency.[1] Electronic devices analyzed by *I-V* characteristics are not restricted to devices based on inorganic materials. In recent years, several types of electronic and optoelectronic devices based on organic and polymeric materials, including organic light-emitting diodes (OLEDs),[2,3] organic field-effect transistors (OFETs),[4] organic photovoltaic cells (OPVs),[5] and organic memory devices,[6,7] have received considerable attention due to their advantages in terms of manufacturing cost, flexibility in terms of fabrication-methods, material variety, and mechanical flexibility. These organic electronic devices have also been studied by using *I-V* characteristics, and theoretical models of their behavior have been developed. To improve the performance of organic electronic devices, understanding the *I-V* characteristics of a given device structure, conduction mechanisms, and influences of the interfaces between organic materials and electrodes on them is indispensable.

I-V characteristics of metal/semiconductor/metal devices are controlled by two basic processes: (a) injection of charge carriers from electrodes into the semiconductor layer; and (b) transport of charge carriers in the bulk of the film. The current is then either injection limited or bulk transport limited due to a mismatch of energy levels between the electrode work function and the corresponding transport levels of the semiconductor and

an intrinsic mobility of the bulk or a charge trapping, respectively. Hence, controlling the conditions and surface states in metal/semiconductor contacts is one of key issues required to understand conduction mechanism and device characteristics. In this section, we review typical cases of metal/inorganic semiconductor contact based on classical semiconductor physics.[8]

1.2.1. Ideal condition and surface states

When a metal makes intimate contact with a semiconductor, the Fermi levels in the two materials must be coincident at thermal equilibrium. Basically, there are the two limiting cases[9] as shown in Figure 1.1. Figure 1.1a shows the electronic energy relations at an ideal contact between a metal and an n-type semiconductor in the absence of surface states. At far left, the metal and semiconductor are not in contact, and the system is not in thermal equilibrium. If a wire is connected between the semiconductor and the metal so that charge will flow from the semiconductor to the metal and thermal equilibrium is established, the Fermi levels on both sides line up. Relative to the Fermi level in the metal, the Fermi level in the semiconductor is lowered by an amount equal to the difference between the two work functions. The work function is the energy difference between the vacuum level and the Fermi level. This quantity is donated by $q\phi_m$ for the metal, and equal to $q(\chi + V_n)$ in the semiconductor, where $q\chi$ is the electron affinity measured from the bottom of the conduction band E_c to the vacuum level, qV_n is the energy difference between E_c and the Fermi level, and q is the magnitude of electronic charge. The potential difference $q\phi_m - q(\chi + V_n)$ is called the contact potential. As the distance δ decreases, an increasing negative charge is built up at the metal surface. An

equal and opposite charge (positive) must exist in the semiconductor. Because of the relatively low carrier concentration, this positive charge is distributed over a barrier region near the semiconductor surface. When δ is small enough to be comparable with interatomic distances, the gap becomes transparent to electrons, and we obtain the limiting case, as shown on the far right in Figure 1.1a. It is clear that the limiting value of the barrier height $q\phi_{Bn}$ is given by

$$q\phi_{Bn} = q(\phi_m - \chi). \qquad \text{Eq. 1.1}$$

The barrier height is simply the difference between the metal work function and the electron affinity of the semiconductor. For an ideal contact between a metal and a p-type semiconductor, the barrier height $q\phi_{Bp}$ is given by

$$q\phi_{Bp} = E_g - q(\phi_m - \chi). \qquad \text{Eq. 1.2}$$

For a given semiconductor and for any metals, the sum of the barrier heights on *n*-type and p-type substrates is thus expected to be equal to the band gap E_g.

The second limiting case is shown in Figure 1.1b, where a large density of surface states is present on the semiconductor surface. At far left, the figure shows equilibrium between the surface states and the bulk of the semiconductor but non-equilibrium between the metal and the semiconductor. In the case, the surface states are occupied to a level E_F. When the metal-semiconductor system is in equilibrium, the Fermi level of the semiconductor relative to that of the metal must fall an amount equal to the contact potential and, as a result, an electric field is produced in the gap δ. If the density of the surface states is sufficiently large to accommodate any additional surface charges resulting from diminishing δ without appreciably altering the occupation level E_F, the space charge in the semiconductor will remain unaffected. As a result, the barrier height

is determined by the property of the semiconductor surface and is independent of the metal work function.

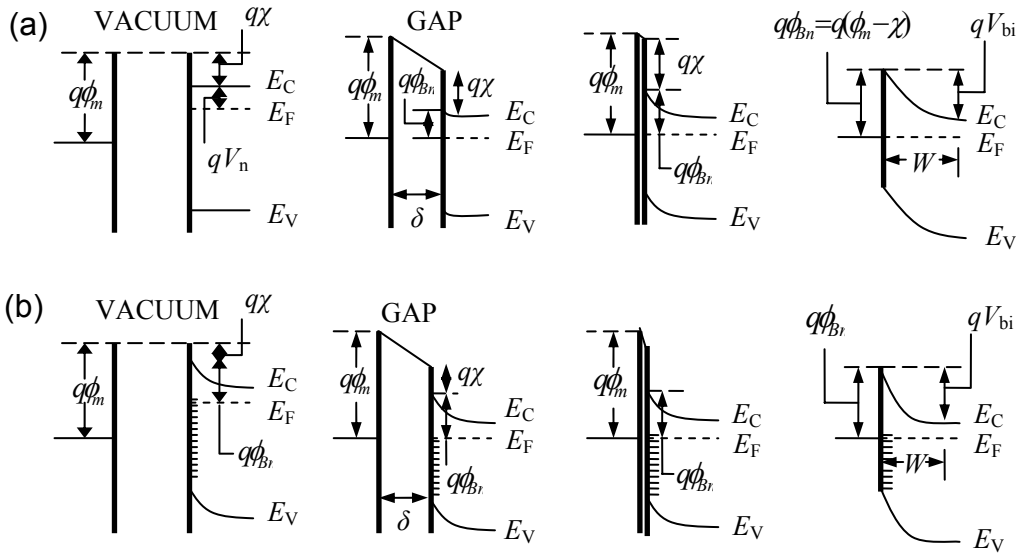

Figure 1.1 Energy-band diagrams of metal-semiconductor contacts. q = magnitude of electronic charge, ϕ_m = work function of metal, ϕ_{Bn} = barrier height of metal-semiconductor, χ = electron affinity of semiconductor, E_C = bottom of conduction band, E_F = Fermi energy level, E_V = top of valence band, $V_n = E_C - E_F$, V_{bi} = built-in potential, and W = depletion width.

1.2.2 Depletion layer

The depletion layer,[13] also called depletion region, as well as junction region or space charge region is an insulating region within a conductive or doped semiconductor layer where the charge carriers have been swept away through recombination. When a metal is brought into intimate contact with semiconductor, the conduction and valence bands of the semiconductor are brought into a definite energy relationship with the Fermi level in the metal as discussed above. Once this relationship is known, it serves as a boundary condition on the solution of the Poisson equation in the semiconductor, which proceeds in exactly the same manner as in p-n junctions.[13] Energy-band diagrams of metal/n-type and metal/p-type semiconductors under different biasing conditions (a) thermal equilibrium, (b) forward bias, and (c) reverse bias are illustrated in Figure 1.2. As a forward bias is applied to the metal/n-type junction (Figure 1.2 b), the Fermi level of the metal is lowered with respect to the Fermi level of the semiconductor. This results in a smaller potential drop across the semiconductor. The balance between diffusion and drift is disturbed and more electrons will diffuse towards the metal than the number drifting into the semiconductor. This leads to a positive current through the junction at a voltage comparable to the built-in potential (V_{bi}). As a reverse bias is applied to the metal/n-type junction (Figure 1.2 c), the Fermi level of the metal is raised with respect to the Fermi level of the semiconductor. The potential across the semiconductor now increases, yielding a larger depletion region and a larger electric field at the interface. The metal-semiconductor junction with positive barrier height has therefore a pronounced rectifying behavior. A large current exists under forward bias, while almost no current

exists under reverse bias. The potential across the semiconductor therefore equals the V_{bi} minus the applied voltage, V (forward bias V_F or reverse bias V_R).

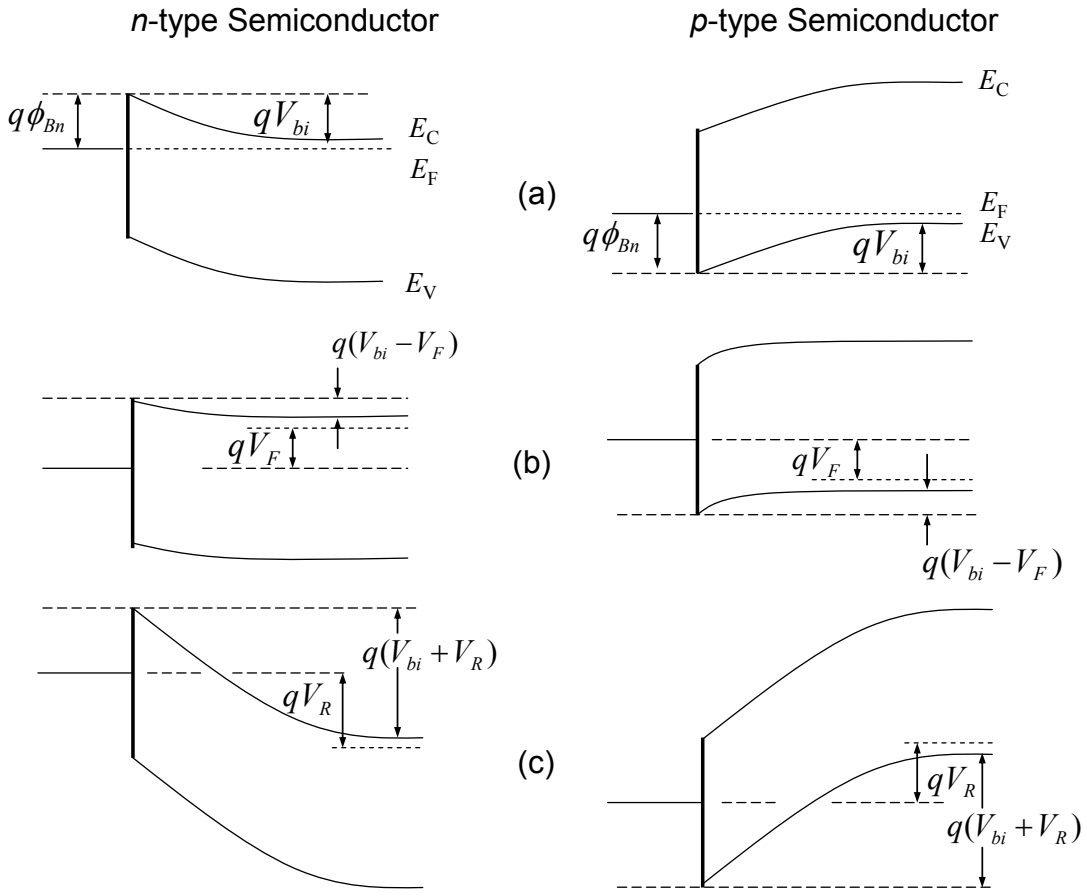

Figure 1.2 Energy-band diagrams of metal/n-type and p-type semiconductors under different biasing conditions: (a) thermal equilibrium; (b) forward bias; and (c) reverse bias.

1.2.3 Current transport processes

Figure 1.3 shows four basic transport processes under forward bias (the inverse processes occur under reverse bias).[11] The four processes are (1) transport of electrons from the semiconductor over the potential barrier into the metal, which is the dominant process for Schottky diodes[10] with moderately doped semiconductors (e.g., Si with doping density of $N_D < 10^{17}$ cm^{-3}) operated at moderate temperatures (e.g., 300 K), (2) quantum-mechanical tunneling of electrons through the barrier (important for heavily doped semiconductors and responsible for most ohmic contacts), (3) recombination in the space-charge region (depletion region) and (4) hole injection from the metal to the semiconductor (equivalent to recombination in the neutral region). In addition, we may have edge leakage current due to a high electric field at the contact periphery or interface current due to traps at the metal/semiconductor interface. The current across a metal/semiconductor junction is mainly due to majority carriers. Three distinctly different mechanisms exist: diffusion of carriers from the semiconductor into the metal, thermionic emission of carriers across the Schottky barrier, and quantum-mechanical tunneling through the barrier. The diffusion theory assumes that the driving force is distributed over the length of the depletion layer. The thermionic emission theory on the other hand postulates that only energetic carriers, those, which have an energy equal to or larger than the conduction band energy at the metal/semiconductor interface, contribute to the current flow. Quantum-mechanical tunneling through the barrier takes into account the wave-nature of the electrons, allowing them to penetrate through thin barriers. In a given junction, a combination of all three mechanisms could exist. However, typically one finds that only one current mechanism dominates.

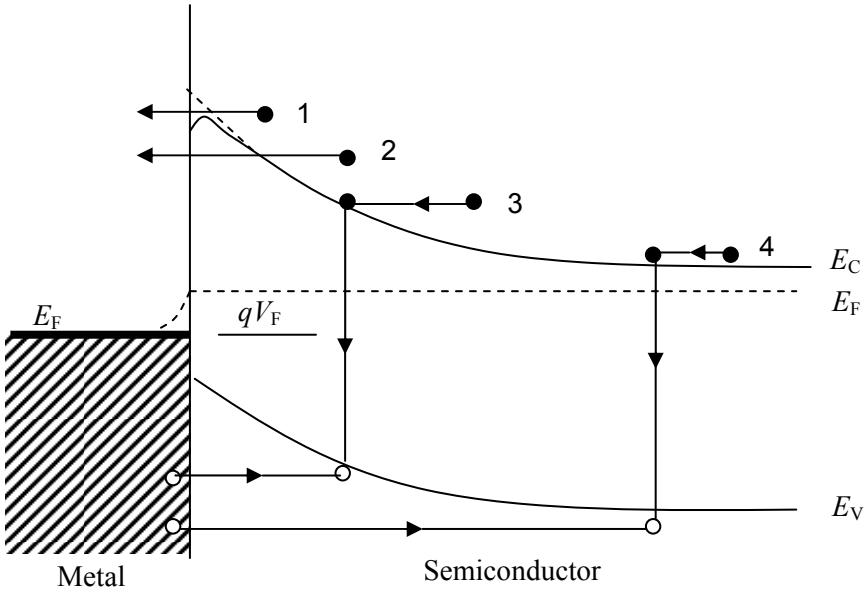

Figure 1.3 Four basic transport processes under forward bias.

1.2.4 Ohmic contact

An ohmic contact[13] is defined as a metal/semiconductor contact that has a negligible contact resistance relative to the bulk or spreading resistance of the semiconductor. A satisfactory ohmic contact should not significantly perturb device performance, and it can supply the required current with a voltage drop that is sufficiently small compared to the drop across the active region of the device. There are two main approaches to make an ohmic contact. One is formation of a low barrier height at the interface of metal/semiconductor, in the case of a low barrier height with lower doping concentrations; the thermionic emission current will dominate the current transport. The other approach, uses a semiconductor with a high level of doping. For contacts with higher-dopings, the tunneling process will dominate, and the contact resistance will depend strongly on doping concentrations. In general it is difficult to make ohmic

contacts on wide-gap semiconductors. A metal does not generally exist with a sufficiently low work function to yield a low barrier. In such cases the general technique for making an ohmic contact involves the establishment of a heavily doped surface layer such as metal/n^+/n or metal/p^+/p contact by various methods[13], such as shallow diffusion, alloy regrowth, in-diffusion of a dopant contained in the contact material, double epitaxy, and ion implantation.

1.3 Charge transport in insulating films

In an ideal metal/insulator/semiconductor (MIS) diode, the conductance of the insulating film is assumed to be zero. Real insulators, however, show carrier conduction when the electric filed or temperature is sufficiently high. For example, in the Si-SiO_2 system, the field for silicon at avalanche breakdown[13] is about 3×10^5 V/cm; the corresponding field in the oxide is then three times larger (the permittivity ratio of ε_{Si} / ε_{SiO_2} = 11.7/3.9), that is, about 10^6 V/cm. At this field the electron and hole conduction in the SiO_2 are negligible even at elevated temperatures. However, mobile ions such as sodium can transport through the oxide and give rise to device instability and a hysteresis effect. For ultra thin SiO_2 or under a very high electric filed, tunneling will occur. In either Si_3N_4 or Al_2O_3 the conductance is generally much higher than in SiO_2.

For organic semiconductors with high purity, the amount of free charge carriers present in the materials is usually negligible and the materials typically show relatively low conductivities. Thus, some organic semiconductors are considered as trap-free dielectric materials, and theories of carrier conductions or injections across

metal/inorganic dielectric interfaces have been applied to metal/organic semiconductor interfaces.[15b,15c]

Table 1.1 summarizes the basic conduction processes in insulators. The Schottky emission process[13] is similar to the process discussed in previous section, where thermionic emissions across the metal/insulator interface or the insulator/semiconductor (in the MIS case) interfaces are responsible for carrier transport. A plot of $\ln(J/T^2)$ versus $1/T$ in which J is current density and T is temperature, yields a straight line with a slope determined by the permittivity ε_i of the insulator. The Poole-Frenkel emission[12] is due to field-enhanced thermal excitation of trapped electrons into the conduction band. For trap states with coulomb potentials, the expression is virtually identical to that of the Schottky emission. The barrier height, however, is the depth of the trap potential wall, and the quantity $\sqrt{q/\pi\varepsilon_i}$ is larger than in the case of Schottky emission by a factor of 2, since the barrier lowering is twice as large due to the immobility of the positive charge. The tunnel emission[13] is caused by field ionization of trapped electrons into the conduction band or by electrons tunneling from the metal Fermi energy into the insulator conduction band. The tunneling emission has the strongest dependence on the applied voltage but is essentially independent of the temperature. Thus, the tunneling emission is usually separated into two processes:[14] (1) direct tunneling (tunneling through a square barrier) at relatively low voltage region and (2) Fowler-Nordheim tunneling (tunneling through a triangular barrier) at relatively high voltage region. The space-charge-limited current[15] results from a carrier injected into the insulator, where no compensating charge is present (see Chapter 2). The current for the unipolar trap-free case is proportional to the square of the applied voltage. At low voltage and high temperature, current is carried by thermally

excited electrons hopping from one isolated state to the next. This mechanism yields an ohmic characteristic exponentially dependent on temperature. The ionic conduction is similar to a diffusion process. Generally, the dc ionic conductivity decreases during the time the electric field is applied, because ions cannot be readily injected into or extracted from the insulator. After an initial current flow, positive and negative space charges will build up near the metal/insulator and the semiconductor/insulator (in the case of MIS), causing a distortion of the potential distribution. When the applied field is removed, large internal fields remain which cause some, but not all, ions to flow back toward their equilibrium position; hysteresis effects result. For a given insulator, each conduction process may dominate in certain temperature and voltage ranges. The processes are also not exactly independent of one another and should be carefully examined.

Table 1.1 Summary of basic conduction processes in insulators

Conduction process	Expression [a]	Temperature dependence	Voltage dependence
Schottky emission[13]	$J = A^* T^2 \exp\left[\frac{-q\left(\phi_B - \sqrt{q(V/d)/4\pi\varepsilon_i}\right)}{kT}\right]$ (Eq. 1.3)	$\ln\left(\frac{J}{T^2}\right) \sim \frac{1}{T}$	$\ln(J) \sim V^{1/2}$
Poole-Frenkel emission[12]	$J \sim \frac{V}{d}\exp\left[\frac{-q\left(\phi_B - \sqrt{q(V/d)/\pi\varepsilon_i}\right)}{kT}\right]$ (Eq. 1.4)	$\ln(J) \sim \frac{1}{T}$	$\ln\left(\frac{J}{V}\right) \sim V^{1/2}$
Direct tunneling[14]	$J \sim V \exp\left[\frac{-2d\sqrt{2m^*\phi_B}}{\hbar}\right]$ (Eq. 1.5)	none	$J \sim V$

Table 1.1 (CONT.)

Fowler-Nordheim tunneling[14]	$J \sim \left(\frac{V}{d}\right)^2 \exp\left[\frac{-4d\sqrt{2m^*}\phi_B^{3/2}}{3q\hbar V}\right]$ (Eq. 1.6)	none	$\ln\left(\frac{J}{V^2}\right) \sim \frac{1}{V}$
Space-charge-limited[15]	$J = \frac{9}{8}\frac{\varepsilon_i \mu V^2}{d^3}$ (Eq. 1.7)	none	$J \sim V^2$
Ohmic conduction[13]	$J \sim \frac{V}{d}\exp\left(\frac{-\Delta E_{ae}}{kT}\right)$ (Eq. 1.8)	$\ln(J) \sim \frac{1}{T}$	$J \sim V$
Ionic conduction[13]	$J \sim \frac{V}{dT}\exp\left(\frac{-\Delta E_{ai}}{kT}\right)$ (Eq. 1.9)	$\ln(JT) \sim \frac{1}{T}$	$J \sim V$

[a] A^* = effective Richardson constant,[13] ϕ_B = barrier height, ε_i = insulator dynamic permittivity, k = Boltzmann's constant, $\hbar$ = Reduced Plank's (= $h/2\pi$), m^* = effective mass, d = insulator thickness, μ = charge carrier mobility, ΔE_{ae} = activation energy of electron, and ΔE_{ai} = activation energy of ions.

1.4 Charge transport in organic semiconductors

As the conduction processes in metal/inorganic film junctions, the charge carriers must overcome the potential barrier at the metal/organic materials interface in order to be injected into an organic semiconductor layer. In the case for small barriers or at high temperatures, a large number of charge carriers will have energies large enough to cross over the interface barrier height which is referred to as donated thermionic emission.[13] But when the temperature decreases or when the potential barrier height presents a large value, the injection can only occur *via* quantum mechanical tunneling through the potential barrier. The charge carriers tunnel from the metal to the empty states at the lowest occupied molecular orbital (LUMO) or the highest occupied molecular orbital (HOMO) level in the organic material. Alternatively, if the organic layer contains a high

concentration of impurities that is able to create new transport sites between the LUMO and HOMO levels of the organic material, the tunneling may occur from the metal to empty localized states in the organic layer by a hopping-type process.[16] It is the smallest barrier at each interface that will dominate the injection.[17]

Particularly in amorphous layers of organic thin films, the density of states (DOS) is quite well represented by a Gaussian-like distribution[18] of localized molecular orbital of individual molecules as shown in Figure 1.4. The charge transport in such amorphous layers is in mainly determined by hopping processes between strongly localized states, which are phonon assisted processes. Therefore, the charge carrier mobilities of amorphous organic materials are usually increased with increasing temperature.[19,20]

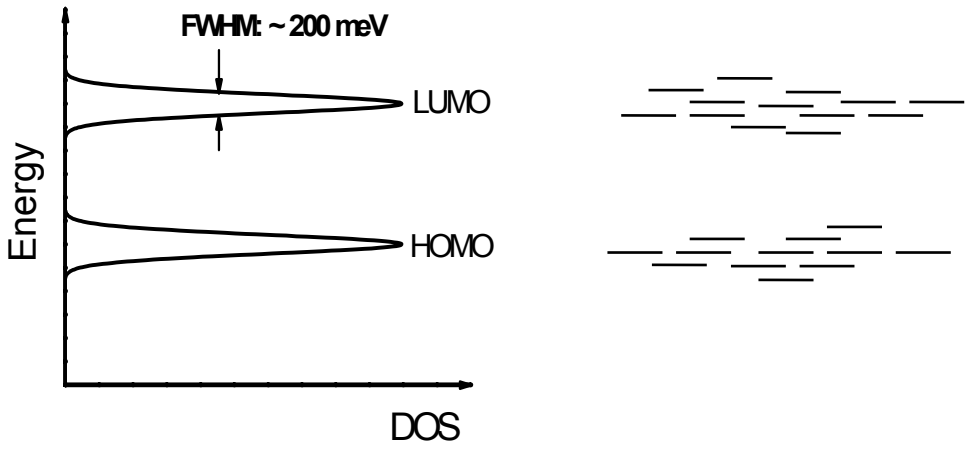

Figure 1.4 Distribution of HOMO and LUMO levels in amorphous organic semiconductors.

In the case of a phonon assisted process, the charge carriers are localized on single molecules and jump from molecule to molecule. The frequency of charge hopping

between two adjacent molecules can be estimated to first approximation on the basis of semiclassical Marcus theory; for such a self-exchange electron-transfer process, it is written as[21]

$$k_{et} = \left(\frac{4\pi^2}{h}\right)\frac{t^2}{\sqrt{4\pi\lambda kT}}\exp\left(\frac{-\lambda}{4kT}\right) \qquad \text{Eq. 1.10}$$

where k_{et} is the charge-transfer rate, t is the intermolecular transfer integral, and λ is the reorganization energy. This equation indicates that the rate of charge hopping depends on two main parameters: the reorganization energy λ and the intermolecular transfer integral t. High transfer rates, and hence high charge mobilities, require small values for the former and large values for the latter. The reorganization energy λ is the sum of two energetic terms: the inner reorganization energy of the molecule (λi) and the reorganization energy of the surrounding medium (λs).[22] On one hand, λi reflects the geometric changes in the molecules when going from the neutral to the ionized state or vice versa; these modifications are significant as a result of the strong electron-vibration coupling characteristic of conjugated materials.[23] λi is the sum of two relaxation energy terms, as shown in Figure1.5b:[24,25] (1) the difference between the energies of the neutral molecule in its equilibrium geometry and in the relaxed geometry characteristic of the ion; (2) the difference between the energies of the radical ion in its equilibrium geometry and in the neutral geometry. On the other hand, λs describes the change in electronic polarization of the surrounding molecules as well as their possible reorientations around the charge carrier; the latter are expected to be significantly limited in the solid state in contrast to the situation in solution.[26] The intermolecular transfer integral is determined by the strength of the electronic coupling between two molecules. The absolute values

can be estimated to a good approximation as half the electronic splitting of the HOMO (LUMO) levels for holes (electrons) in a dimer made of two neutral molecules.[27,28] In order to have a large charge-transfer rate between two molecules and thus a large charge carrier mobility of the material, the reorganization energy should be small and the intermolecular transfer integral should be large. To have a small reorganization energy, the π-electrons of the aromatic molecules should be highly delocalized. To have a large intermolecular transfer integral, the molecules should have a optimized orbital overlap (rotational disorder can have a significant effect on the intermolecular transfer integral) and a small separation distance.

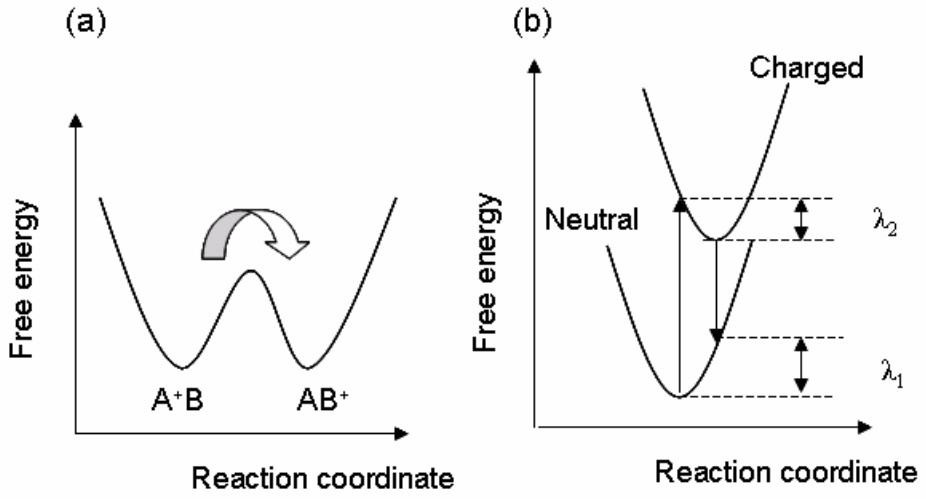

Figure 1.5 Schematic representation of (a) a hole transfer from molecule A to molecule B going through a transition state, as assumed in the semiclassical model, and (b) the two energetic terms λ_1 and λ_2 defining the inner reorganization energy.

1.5 Electronic traps in organic semiconductors

An understanding about properties of electronic traps in organic semiconductors is one of the critical issues for the understanding and controlling the conduction process. In this section, we review the origin of traps in organic semiconductors and the influence of traps on their transport.

Electrical transport is always influenced by the capture of the relevant charge carriers in localized states.[29] Such trapped carriers may be released after a specific retention time or may recombine with carriers having opposite charge. In the case that the release rate is higher than the recombination rate, the localized state is called a trap, while the localized state forms a recombination center in the case of occurring recombination-process dominantly. The state may act as the both recombination-center and trap depending on temperature or ratio of the minority to major carrier concentration. Traps affect strongly the charge transporting properties since trapped charge carriers do not take part in the charge transport. However, their columbic charges will influence the electric field distribution in an organic layer and therewith the transport. And if the release rate of trapped carriers is sufficiently low, there will be significant time necessary to reach thermal equilibrium conditions. The slow release of charge can cause delay and hysteresis effect[31] in alternately operated devices. For all those reasons, it is important form both the perspective of fundamental understanding and technical applications to know the origin of such trap states and to have means to control them.

1.5.1 Hopping band tails

Since trap states are energetically favorable sites, they are located in the energy gap of the semiconductor. In terms of classical semiconductor physics each localized state below the conduction band edge, which is able to capture an electron, is an electron trap and each localized state above the valance band edge, which is able to capture a hole is a hole trap. But in organic semiconductors the width of the bands are very narrow and extended states are rarely observed. The charge transport in such organic layers is mainly determined by hopping processes between strongly localized states. Therefore, it is not obvious how to distinguish between a trap state and a regular transport state. The approach for the issue is given by the transport energy concept introduced by Monro[29] for amorphous inorganic semiconductors and later extended to amorphous organic semiconductors by several authors.[30] This concept is based on a statistical rule, namely, that a carrier in a deep tail state will most probably escape to a state of energy E_t independent on its initial energy in the tail[31] (Figure 1.6a). This makes the energy level E_t a protruding quantity. E_t is called transport energy or escape energy since it describes the level from which a trapped carrier is most probably released to move to a neighboring site. The transport energy has only a statistical meaning, but its role is similar to that of the band edge in inorganic semiconductors. Consequently, each state below the transport energy is a trap state while states above the transport energy are regular transport states, despite all states are localized. However, the transport energy is a function of temperature. Besides the trap states formed by the tail of the regular HOMO/LUMO level distribution there may be existing additional trap states at a discrete energy level or with any arbitrary energy distribution in the gap below the transport energy[31] (Figure 1.6b).

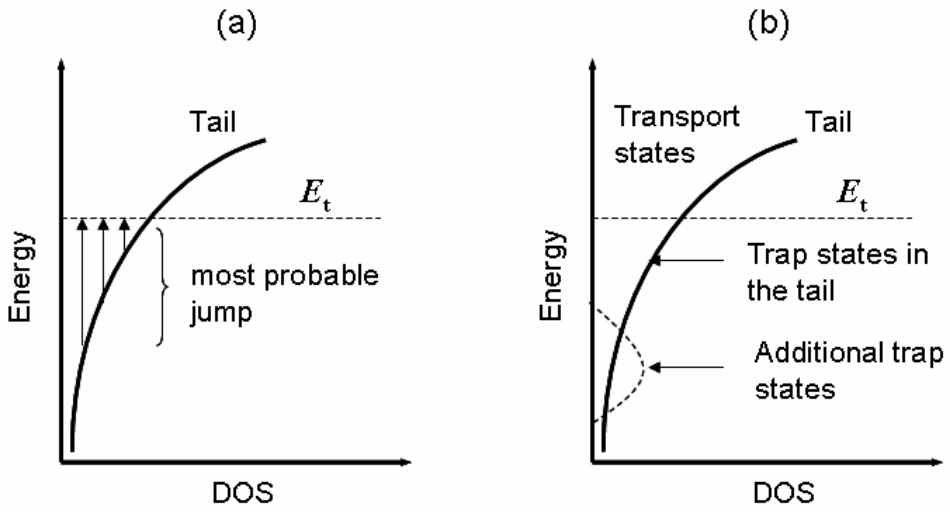

Figure 1.6 (a) Most probable jump of a carrier from a tail state to the transport energy *E*t. (b) Trap states in the tail, additional trap states and regular transport states.

1.5.2 Origin of traps

There are possible sources of trap states in organic semiconductor materials:

(1) Impurities:[32] Since the interactions between molecules in an organic solid are generally weak relative to intramolecular forces, to a first approximation a specific molecule keeps its HOMO/LUMO position independent of the surrounding matrix. If the HOMO or LUMO of an incorporated molecule is positioned in the gap of the host molecules, it will form a trap state.

(2) Structural Defects:[30] Even if there are only molecules of the same species, the HOMO/LUMO levels may vary from molecule to molecule. The exact energy position of the HOMO/LUMO level is not only determined by the chemical structure of the molecule itself but also by the electronic polarization of its surrounding. In case of polymers the effective conjugation length also affects the position of the HOMO/LUMO level. Structural imperfections can lead to a fluctuation of the

surrounding media and in case of polymers to a fluctuation of the conjugation length. As a consequence, in anything but a perfect single crystal, a distribution of HOMO/LUMO levels has to be expected as presented in Figure 1.4. The few states in the tail of this distribution below the transport energy will form the trap states. But structural defects are not necessarily restricted to the formation of tail states alone. If a specific kind of structural defect occurs with enhanced probability, for example, on gain boundaries in polycrystalline layers, structural defects may result in more or less discrete trap states deep in the gap.

(3) Geminate pairs:[32] Due to the low dielectric function of organic solid, Coulomb interactions are strong in these materials. A hole and an electron will experience a significant Coulomb interaction, even if several molecules separate them. Such a pair of Coulomb bond charge carrier is called geminate pair. If the recombination probability between the hole and electron is suppressed by selection rules, a geminate pair forms a Coulomb trap. However, such traps can only occur if both types of charge carriers are present.

(4) Self-trapping:[33] An excess charge carrier residing on an organic molecule leads usually to a molecular deformation, which causes a lowering in energy for the excess charge carrier. Such a carrier together with its produced molecular deformation is a new quasi-particle called polaron. If two charge carriers share the same molecular deformation, a bipolaron is formed. Polarons or bipolarons are not really traps in the original meaning, since they are mobile. However, the mobility of a polaron or bipolaron is at least one or two orders of magnitude lower than the mobility of a free carrier. As long as the lowering in energy is only several tenth of meV the effect can

be neglected compared to other trap states. But in some polymers like polythiophene or polyacetylene the polaron or bipolaron formation caused a lowering in energy of several hundreds of meV.[32] In such cases the charge carrier forms its own trap state on the polymer chain. Such a trapping mechanism is called self-trapping.

1.6 Amorphous molecular materials

In contrast to inorganic materials that consist of covalent or ionic bonds of atoms over the entire solids, organic materials are based on independent molecules and characterized by weak intermolecular interactions.[34] Thus, designs of organic materials can be readily performed on the molecular level. In particular, organic π-electron systems have received attention as potential photo- and electro-active materials.

When these organic materials are used in electronic and optoelectronic devices, they are normally in the form of thin films. Organic thin films are prepared by various techniques including solution printing, spin coating, vacuum vapor deposition, electrochemical deposition, Langmuir-Blodgett and monolayer self-assembly techniques.[34] Both ordered and disordered films can be generated, depending on material properties and techniques of thin film fabrication. Amorphous molecular materials (or molecular glasses) have found successful application for use as electrophotographic photoreceptors[35] for photocopiers and laser printers and OLEDs.[7,36] And they are expected to find further potential applications as OPVs,[37] organic memory devices, photorefractive materials,[38] and resist materials for electron-beam lithography[39] due to the following interesting features. (1) They are characterized by disorder of both intermolecular distance and orientation and by exhibiting isotropic properties, while grain

boundaries of crystalline or liquid crystalline films detorialate their charge transport properties. (2) In contrast to polymeric materials, they have well-defined molecular structures and molecular masses. (3) They can be vitrified by cooling from the melt or by solvent evaporation from the solutions. (4) Uniform, transparent amorphous films on substrates can be prepared by a variety of methods such as spin coating, solvent casting from solution, printing, and vacuum deposition.

One of important requirements for molecular glasses used in optoelectronic device is a morphological stability in thin films. Studies of the relationship between the molecular structure and the glass-forming property such as glass transition temperature (T_g) and stability of the glassy state have been carried out by Shirota and co-workers,[34a] by Wirth,[40] and by Naito and Miura.[41] Shirota has provided several guidelines for the design of morphologically stable molecular glasses. An increase in the number of conformers together with nonplanar molecular structure is the requirement for the formation of amorphous glasses. Introduction of bulky and heavy substituents and enlargement of molecular size are the important factors for attaining the stability of the glassy state. T_g can be increased by the incorporation of a rigid moiety or an intermolecular hydrogen bonding site into nonplanar molecules, by the enlargement of molecular size and by increasing the molecular weight.

1.6.1 Hole transporting molecular glasses

Most of the hole transporting (HT) molecular glasses are built from aromatic amino groups or contain these groups. Aromatic amines possess low ionization potentials (IPs) leading to the readily formable cation radicals (holes). N,N'-diphenyl-N,N’-bis(3-

methylphenyl)-[1,1'-biphenyl]-4,4'-diamine (TPD)[42] and another TPD analogue, N,N'-bis(1-naphthyl)-N,N'-diphenyl-4,4'-diamine (NPB)[43,44] have been widely used as effective HT materials for use in the second layer in OLEDs. The drift mobilities of TPD and NPB have been reported to be 1.0×10^{-3} and 8.8×10^{-4} cm^2/Vs, respectively. These materials are not thermally stable; the T_gs are below 100 °C. Amorphous vapor-deposited films of 1,1-bis(di-4-tolylaminophenyl)cyclohexane (TAPC)[19] show one of the highest hole mobilities of 1.0×10^{-2} cm^2/Vs for disordered organic solids. T_g of TAPC is 78 °C. As in the case of TPD, TAPC glasses are not thermally stable. To overcome the problem of thermal stability, TPD analogues with higher T_gs above 100 °C were developed by introducing dimethylfluorene moieties, and these materials exhibited high mobilities of 1.0×10^{-3} cm^2/Vs.[45] The materials of the tris(diphenylamino)triphenylamine (TDATA) family such as tris[3-methylphenyl(phenyl)-amino]triphenylamine (*m*-MTDATA)[46] have been proven to serve as good hole injection buffer layer in OLEDs due to lower IPs than those of TPD family materials. The these materials of TDATA family exhibited relatively low hole drift mobilities of the order of 10^{-5} cm^2/Vs.[47,48] The materials containing triarylamine group such as N,N-bis(9,9-dimethylfluoren-2-yl)aniline (F_2PA),[49] 4-[bis(9,9-dimethylfluoren-2-yl)amino]biphenyl (F_2BPA),[50] and tris(9,9-dimethylfluoren-2-yl)amine (TFlA)[50] have been developed. F_2PA functions as a good host material for a phosphorescent iridium complex in OLEDs.[49] These materials of the triarylamine family were found to exhibit higher mobilities than those of the materials of the TPD family, exhibiting values greater than 5.0×10^{-3} cm^2/Vs.[34c] Recently, hole drift mobilities of carbazole-based dihydrazones approached 10^{-2} cm^2/Vs at an electric field of 6.4×10^5 V/cm at a room-temperature.[51] More recently, Shirota and co-workers reported

thiophene- and selenophene-containing tris(oligoarylenylamine)s.[52] The mobilities of these materials were found to exceed 1.0×10^{-2} cm^2/Vs at an electric field of 1.0×10^5 V/cm at a room-temperature. These values are of the highest level ever reported for molecular glasses, although field-effect mobilities up to 2.0×10^{-2} cm^2/Vs of ladder 5,7,12,14-tetraazapentacenes thin films were also reported.[53] However, the ability of forming a glass state in thin film of the tetraazapentacenes derivatives have not been proven.

1.6.2 Electron transporting molecular glasses

In contract to numerous reports on hole transporting molecular glasses, much less works on electron transporting (ET) molecular materials have been reported. One of the reasons for this is the problem of electron trapping. Since oxygen, a potential electron trap, is inevitably present, the reduction potentials of ET materials must be lower than that of oxygen. Thus, ET materials, in order to be a good ET, should have large electron affinities.

ET molecular glasses have been first studied as potential components of molecularly doped polymers used in electrophotography. At present the interest in ET molecular glasses used in OLEDs have been increased. The most prevalent ET compound used in OLEDs is tris(8-quinolinato)aluminum (Alq_3), which effectively transports electrons and emits in the green.[42a] Vapor-deposited Alq_3, films consist of two heometric isomers, which may hinder the crystallization of the films and explain its long-term stability in the glassy form.[42a] Kepler et al.[54b] studied the drift mobility of Alq_3 for both carriers, and the effective mobilities of electrons and holes were found to be 1.4×10^{-6}

cm^2/Vs and 2.0×10^{-8} cm^2/Vs, respectively. In a more resent study, it was shown that carefully sublimated Alq_3 leads to non-dispersive transport behavior with a room-temperature electron mobility of 10^{-5} cm^2/Vs.[55]

Oxadiazole, quinoxaline, and phenanthroline derivatives have also been studied for OLEDs. A number of star-shaped oxadiazole derivatives with benzene, triethenylbenzene, triphenylbenzene, and triphenylamine core have been synthesized.[56] Many of them have been reported to form glasses with high T_gs. The electron mobility in 1,3,5-((4-tert-butyl-phenyl)-2-oxadiazolyl)benzene-doped polycarbonate (50 wt.-%) has been measured to be 1.2×10^{-6} cm^2/Vs at 7.0×10^5 V/cm.[56b] A dendrimer of the first generation with 1,3,4-oxadiazole units shows a T_g of 222 °C and the ability of forming amorphous films prepared by spin-coating.[56c] A series of glass-forming star-shaped compounds based on the electron-deficient quinoxaline groups have been synthesized.[57] Glasses of these compounds are morphologically stable and show very high T_gs in the range from 147 °C to 179 °C.[57] The electron mobilities for 1,3,5-tris[(3-phenyl-6-trifluoromethyl)quinoxaline-2-yl]benzene and 1,3,5-tris[{3-(4-tert-butylphenyl)-6-trifluoromethyl}quinoxaline-2-yl]-benzene approach 10^{-4} cm^2/Vs at high electric fields.[57d] Silicon-containing molecular glasses such as 2,5-diarylsiloles[58a,b] and silicon-bridged bithiophenes[58c] have also been reported to exhibit high ET ability and to be suitable for application in OLEDs. For example, a non-dispersive ET with the electron mobility of 2.0×10^{-4} cm^2/Vs was observed from 2,5-bis(6'-(2',2"-bipyridyl))-1,1-dimethyl-3,4-diphenylsilole (PyPySPyPy) thin film.[58b] A high electron mobility exceeding 10^{-4} cm^2/Vs at an electric field of 10^5 V/cm has been observed in vapor-deposited films of 4,7-diphenyl-1,10-phenanthroline (bathophenanthroline).[59] However,

the morphological stability of this film seems to be low.[59b] Also relatively high electron mobilities with the range of 10^{-4} cm^2/Vs have been observed in perylene[60a] and naphthalene[60b] diimides. The morphological stability of perylene diimide is rather low. Amorphous films could be prepared only on substrates maintained at approximately –50 °C. Films prepared on room-temperature substrates were polycrystalline. Recently, electron mobilities approaching 10^{-3} cm^2/Vs have been reported. Ishi-i *et al.*[61a] reported the electron mobility of 8.0×10^{-4} cm^2/Vs at 3.8×10^5 V/cm in an amorphous film of 2,4,6,-tris[4-(1-naphthyl)phenyl]-1,3,5-triazine. Wu *et al.*[62c] reported that nondispersive ambipolar carrier transport with comparably high electron and hole mobilities for amorphous ter(9,9-diarylfluorene)s. High hole and electron mobilities over 10^{-3} cm^2/Vs were achieved with these terfluorenes. In particular, the observed electron mobility may be the highest ever reported for amorphous molecular solids.

Hole and electron mobilities in molecular glasses reviewed in this section are summarized in Table 1.2. Generally mobility values in ET molecular glasses are lower than those in HT molecular glasses.

Table 1.2 Summary of charge carrier mobilities of molecular glasses.

Molecular Structure	T_g [°C]	Mobility / Electric filed at room-temperature [(cm^2/Vs) / (V/cm)]	Carrier	Techniques*	Ref.
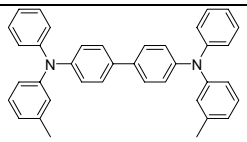 TPD	60	1.0×10^{-3} / 1.5×10^{5}	Hole	TOF	42
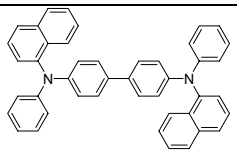 NPB	95	8.8×10^{-3} / 2.3×10^{5}	Hole	TOF	43,44
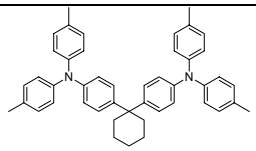 TAPC	78	1.0×10^{-2} / 4.4×10^{5}	Hole	TOF	19
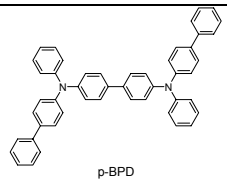 p-BPD	102	1.0×10^{-3} / 1.0×10^{5}	Hole	TOF	45b
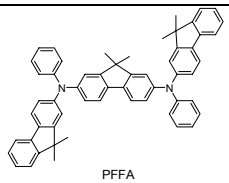 PFFA	135	1.1×10^{-3} / 1.0×10^{5}	Hole	TOF	45c
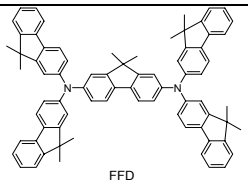 FFD	165	4.1×10^{-3} / 1.0×10^{5}	Hole	TOF	45c
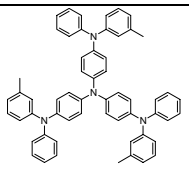 m-MTDATA	75	2.7×10^{-5} / 1.0×10^{5}	Hole	TOF	46

Table 1.2 (CONT.)

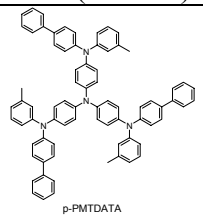 p-PMTDATA	110	3.0×10^{-5} / 1.0×10^{5}	Hole	TOF	47,48
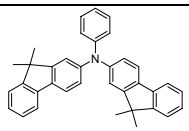 F_2PA	82	6.7×10^{-3} / 1.0×10^{5}	Hole	TOF	34c,49
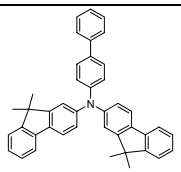 F_2BPA	NA	7.1×10^{-3} / 1.0×10^{5}	Hole	TOF	34c
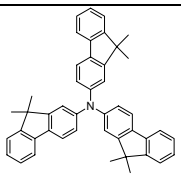 TFIA	NA	8.1×10^{-3} / 1.0×10^{5}	Hole	TOF	34c
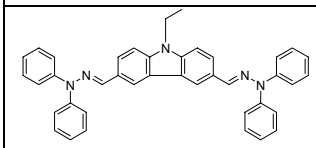	88	1.0×10^{-2} / 6.4×10^{5}	Hole	TOF	51
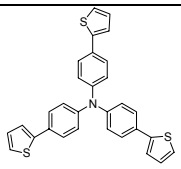 TTPA	70	1.1×10^{-2} / 1.0×10^{5}	Hole	TOF	34c,52
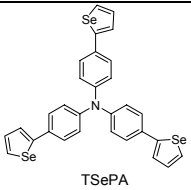 TSePA	80	1.5×10^{-2} / 1.0×10^{5}	Hole	TOF	34c,52

Table 1.2 (CONT.)

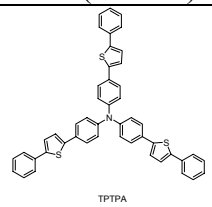 TPTPA	83	1.0×10^{-2} / 1.0×10^{5}	Hole	TOF	34c,52
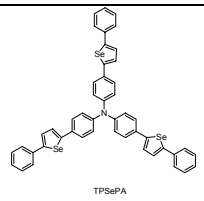 TPSePA	105	1.1×10^{-2} / 1.0×10^{5}	Hole	TOF	34c,52
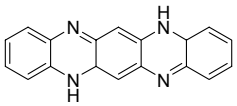	NA	2.0×10^{-2}	Hole	FET	53
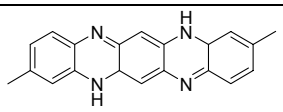	NA	1.0×10^{-2}	Hole	FET	53
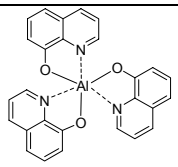 Alq_3	175	1.4×10^{-6} / 4.0×10^{5} 2.0×10^{-8} / 4.0×10^{5}	Electron Hole	TOF	54
		1.0×10^{-5} / 1.2×10^{6}	Electron	TOF	55
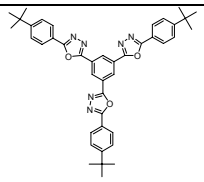	142	1.2×10^{-6} / 7.0×10^{5}	Electron	TOF	56
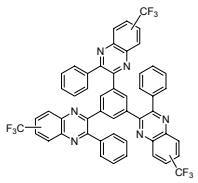	147	9.0×10^{-5} / 9.8×10^{5}	Electron	TOF	57
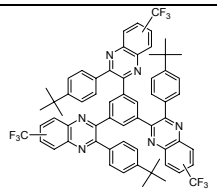	165	8.0×10^{-5} / 9.0×10^{5}	Electron	TOF	57

Table 1.2 (CONT.)

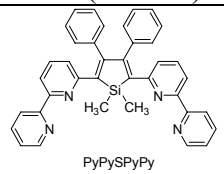 PyPySPyPy	NA	2.0×10^{-4} / 6.4×10^{5}	Electron	TOF	58
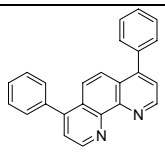	62	4.2×10^{-4} / 3.0×10^{5}	Electron	TOF	59
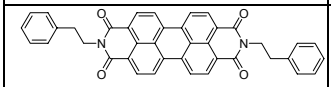	NA	4.8×10^{-4} / 1.7×10^{5}	Electron	TOF	60a
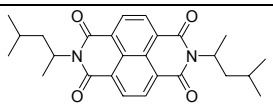	NA	4.0×10^{-4} / 4.0×10^{5}	Electron	TOF	60b
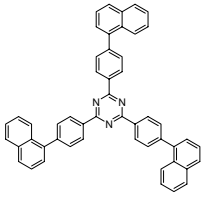	133	8.0×10^{-4} / 3.8×10^{5}	Electron	TOF	61a
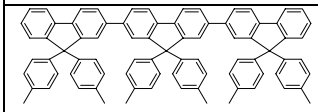	204	1.0×10^{-3} / 6.7×10^{5} 4.0×10^{-4} / 6.7×10^{5}	Electron Hole	TOF	61c

***** Measurements techniques: TOF = time of flight, FET = field-effect transistor. The theories and experimental conditions of TOF and FET are described in Chapter 2.

1.7 State-of-the-art of two-terminal organic memory devices

Another interesting aspect of the effect of traps on conduction processes is that anomalous *I-V* characteristics showing a large hysteresis or current levels switching at a specific voltage are often observed accidentally in thin films of either inorganic and organic insulators or semiconductors embedded between metal electrodes. These electrical switching phenomena have been observed for more than 30 years,[62] and these switching mechanisms have been the subject of many discussions. If these switching effects can be made repeatable and reproducible, the devices can be used for nonvolatile memory devices exhibiting at least two different states of currents at the same applied voltage.

Current solid-state data storage technologies are dominated by dynamic random access memories (DRAM), hard disk drives (HDD), and flash memories. DRAM would permit fast access time; however, it requires continual power in order to maintain data. It is in the class of volatile memory devices. HDD has the largest capacity of data storage but has a long data access time of the order of milliseconds. Flash memory is the most successful nonvolatile memory device with more than 10 years retention time of data, but the fastest writing speed ($> 10^{-6}$ s) is still slower than DRAM (10^{-9} s) by a factor of 1000, and it is more expensive than DRAM and HDD.[7] This technology has experienced a rapid growth in recent years and prices keep dropping rapidly. Nonetheless, the fabrication of flash memories remains relatively expensive due to a complex device architecture based on three or four terminal transistor geometries, which requires advanced semiconductor processing techniques. Thus, there is a clear demand for the next generation nonvolatile memory devices, which can meet or exceed critical

performance of a practical memory device such as long term data retention (at least 10 years), low power consumption (few milliwatts or less), and large number of read-erase cycles (Flash memories are rated for ~10^6 cycles while DRAMs are rated for ~10^{15} cycles).[7]

Recently, numerous scientific reports (*vide infra*) have proposed memory devices based on two-terminal resistive switches as a promising new memory technology. The two-terminal devices can be set to at least two states by applying an appropriate voltage and then read back by measuring current at some lower voltage. The individual bit cells are addressed in a "crosspoint" array.[7] The storage medium is sandwiched between two layers of electrodes running in perpendicular directions, above and below (Figure 1.7). With only two levels of connecting electrodes and an unpatterned active layer, a crosspoint array is conceptually very simple to make, requiring no strict alignment within the array itself. Moreover, the density of memory elements is maximal in where the density only depends on the electrode width and spacing. Thus, it is generally believed that the crosspoint architecture will yield the most economical solid-state memory. Therefore, electrical switching phenomena in organic and polymeric materials possessing solution processability have received considerable attention as active components for a further low-cost nonvolatile memory based on two-terminal devices.[63] Although many electrical switching effects have been observed in not only single-layer organic memory devices but also in OLEDs, OFETs, and OPVs, the literature survey in this section is focused on independent organic memory devices based on two-terminal devices not on multi-device structures combined with other device elements or on three-terminal devices.

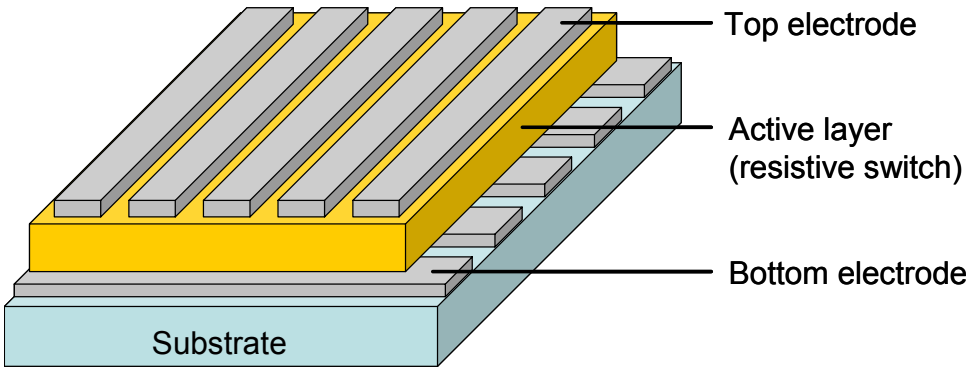

Figure 1.7 Schematic crosspoint memory architecture.

Both small conjugated molecules and polymers were employed as the organic semiconductor materials in organic memory devices. 2-amino-4,5-imidazoledicarbonitrile (AIDCN),[64] Alq_3,[65] pentacene,[66] NPB,[67] and cyanopolyfluorene[68] were used in the device with triple-layer structure, metal/organic/metal/organic/metal. In this type of memory devices, the critical factor generating switching behavior is the presence of a "granular structure" (as defined in reference 65) or "metal-nanocluster" (as defined in refence 64b) of metal embedded into organic layers, which is probably created by an evaporation of an electrode on organic layer with a slow evaporation rate (< 2.0 Å/s). Scott's group referred to the middle embedded Al layer as granular Al while Yang's group used the term of Al nanocluster. In both groups, discontinuous Al grains with nano-size scale into organic layers were observed by the studies based on cross-sectional scanning electron microscopy and atomic force microscopy. In our work, we will refer to these discontinuous metal grains or particles in organic layers as "granular structure." Semiconducting polymers and insulating polymers have been used for these triple-layer devices. Recently, the memory effect utilizing self-assembled inorganic Cu_2O

nanocrystals embedded in polyimide (PI) matrix with the Al/PI/nanocrystal Cu_2O/PI/Al structure was reported.[88] Scott's group studied several polymers having different optical band gaps as an polymer matrix with Au nanoparticles (NPs) distributed throughout the layer, or in only part of it.[67] Most recently, there has been significant interest in the design of organic memory devices with a simple structure, such as a single organic layer embedded between two electrodes, due to their simplicity and potential lower fabrication cost. Single-layer devices using small organic compounds or polymers were demonstrated as well. Small organic compounds include pentacene,[66] NPB,[70] Alq_3,[71] and co-deposited Cu:TCNQ (TCNQ: 7,7,8,8-tetracyanoquinoline).[72] Polymer materials include poly[3-(6-methoxyhexyl)thiophene],[73,74] the copolymer of N-vinylcarbazole and Eu-complexed vinylbenzonate,[75] the copolymer of N-vinylcarbazole and C_{60},[86] Au-NP composites (polystyrene (PS) + Ag-NP + 8-hydroxyquinoline(8HQ)),[76] donor-acceptor composite (PS + [6,6]-phenyl C_{61}-butyric acid methyl ester (PCBM) + tetrathiafulvalene(TTF)),[77] nanocomposite of polyaniline (PANI) nanofibers blended with Au-NP,[78] and Au-NP dispersed polymer semiconductor composites with relatively high energy-gap polymer materials.[67]

Organic memory devices show a bistability or multi-stability, however, the observed *I-V* characteristics are different with different devices or different laboratories. For instance, negative differential resistance (NDR) regime was not observed in Yang's group,[64,76] while it has been observed in some laboratories.[65,67,69,70] Different dependences of film thickness on device performances have also been realized. Adachi's group[72] found that the switching behaviors were almost independent of the organic layer, while Tondelier *et al*.[66] observed a linear dependence of the film thickness on switching

threshold voltage. The origin of these discrepancies remains unknown. Therefore, the switching mechanisms for these devices have been still the subject of debate. Yang's group proposed electric-field-induced polarization of the embedded metal layer for the triple-layer devices[64], and electric-field-induced charge transfer for the Au-NP dispersed polymer systems.[76] The charge transfer mechanism is adopted in the device that use co-deposited Cu:TCNQ[72] or the copolymer of N-vinylcarbazole and Eu-complexed vinylbenzonate.[75] Tondelier *et al*.[66] proposed the formation of nano-filamentary metallic pathways through the organic film that resulted from field-induced percolation of the metal NPs induced in organic layer by diffusion during the middle metal layer and top metal layer for three-layers and single layer structures, respectively. M. Cölle *et al.*[87] also proposed the conduction switching through filament pathways. However, many other groups believe that the switching is related to charge storage (either charge transfer or charge trapping) in the metal NPs. Scott's group[65,67] interpreted NDR of their devices in terms of the Simmons and Verderber (SV) model.[79] They argued that the switching from high to low conductance is due to charge trapping on the metal NPs and the resulting space-charge field inhibits charge injection based on simple band theory. This charge-trapping mechanism was adopted by some other groups as well.[70,80] However, their pristine devices start from a low conduction state that disagrees with the SV model, and the reason has been unclear. And Tang *et al*.[69] disagrees with the SV model in terms of disregarding to potential energy change resulting from the charging process. They proposed that the electrical switching effect in their devices was caused by 2D single-electron tunneling by nanometer-size metal islands, which were formed unexpectedly by nucleation and growth of a metal thin-film where some nuclei were blocked from further

growth by the sealing of electrode outside crevice. Majumdar *et al*.[73,74] proposed that the space charge stored at the polymer layer near the metal/polymer interface controls charge injection and results in hysteresis-type *I-V* characteristics.

As some different devices for special cases, organic memory devices that operate by using ion diffusions,[81,82] redox reactions of metal ions or molecules[90], and field-induced charge transfer[75,77] and conformational change[71,83] of special molecules have also been demonstrated. In the case of using ion diffusion and redox reactions of metal ions or molecules, these devices have a problem of short retention times for the programmed states.

In conclusion of literature survey for organic memory devices, architectures that have been reported to date fall into three major types. Type I is classified by the use of the granular metal structures created by relatively slow evaporations either for the embedded metal in organic layers or top electrode on an organic layer. In this type of devices, some groups found that the device performances were insensitive to the specific materials.[67, 69] Type II is defined by the use of metal NPs or molecules dispersed into the films of polymeric or small molecule compounds as active materials. The gold NPs have been selected favorably, although the memory device using C_{60} dispersed into insulating polymer, poly 4-vinylphenol (PVP) was reported.[84] The polymer materials for this type include semiconductor polymers and insulating polymer blended with small molecule semiconductor compounds. Type III is defined as other types different from the type I and II such as using donor-acceptor systems, ion diffusions of metal ions, redox reactions of molecules, and conformational change of special molecules. Table 1.3 summarizes the organic memory devices in literature.

Table 1.3 Summary of the literature survey for organic memory devices.

Type[a] (# of active layers)	Device structure	Switching effect / Proposed mechanisms[b]	Memory Performances[c]	Ref.
I (3L)	Al/AIDN(50nm)/Al(20nm)/AIDN (50nm)/Al 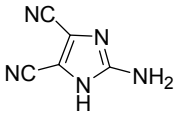 AIDN	Bistable / Electric-field-induced polarization	ON/OFF ratio: ca. 10^3 W(3V)-R(1V)-E(–0.5V), Switching time: ca. 10ns	64
I (3L)	Bottom electrode(50nm)/Alq3(50nm)/embedded metal(5nm)/ Alq3(50nm)/Al(50nm) Bottom electrodes: Al, Cr, Cu, ITO, Au, Ni Embedded metals:Mg, Ag, Al, Cr, Au, CuPc 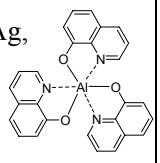 Alq3	Multi-stable, NDR / SV model; charge trapping	ON/OFF ratio: 10–10^6 The materials of bottom electrodes and embedded metals were insensitive to memory performances except for Au embedded layer that was shorted.	65, 67
I (3L)	Al(50nm)/NPB(50nm)/Al(5nm)/ NPB(50nm)/Al(50nm) 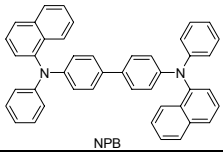 NPB	Multi-stable, NDR / SV model;charge trapping	ON/OFF ratio: ca. 10^3	67
I (3L)	Ag/CPF(100nm)/Ag(17.5nm)/CPF(100nm)/Ag 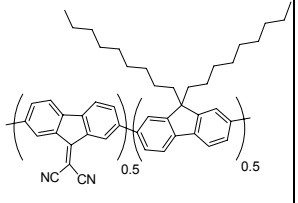 cyanopolyfluorene (CPF)	Bistable/ Not addrested	ON/OFF ratio: ca. 10^8	68
I (3L)	Al/PI(20nm)/Cu_2O nanocrystal/PI(20nm)/Al PI: poylimide	Bistable / Charge trapping	ON/OFF ratio: ca. 100	88

Table 1.3 (CONT.)

I (3L)	Al/Pentacene(50-800nm)/Al(15-20nm)/Pentacene(50-800nm)/Al 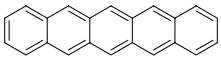 Pentacene	Bistable / Nano-filamentary metallic pathways	ON/OFF ratio: ca. 10^8–10^9 Threshold voltages were observed as an linear dependence of pentacene thickness	66
I (1L)	Al/Pentacene(150-1000nm)/Al	Bistable / Nano-filamentary metallic pathways	ON/OFF ratio: ca. 10^8–10^9 Threshold voltages were observed as an linear dependence of pentacene thickness	66
I (1L)	ITO/NPB(200nm)/Ag (Switching effect was not observed on device using Al electrode instead of Ag)	Multi-stable, NDR (depended upon the negative start voltage) / Charge trapping	ON/OFF ratio: 20 Switching time: 0.15s W(–12V)-R(8V)-E(20V) Achieved 10^6 cycles In air operation	70
I +II (1L)	ITO/fluorescent dye doped NPB(200nm)/Ag Fluorescent dyes: DCJTB, rubrebe, and C545T (each 3% coevaporation with NPB)	Multi-stable, NDR (depended upon the negative start voltage) and the doping dyes / Charge trapping	ON/OFF ratio: up to 10^2 W(–10V)-R(5V)-E(15V) Achieved 10^6 cycles In air operation	85
I (1L)	ITO/DPFA(100nm)/Ag 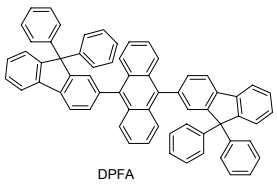 DPFA	Multi-stable, NDR / Charge trapping	In air operation	91
I (1L)	Au or ITO/Alq3/Al, Ag, or Au Au or ITO/NPB/Al, Ag, or Au	Multi-stable, NDR /2D single-electron tunneling	Not addressed	69

Table 1.3 (CONT.)

I (1L)	ITO/P6OMe(50nm)/Al 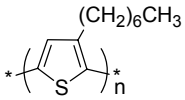 P6OMe	Hysteresis-type / Space charge stored at the interface of polymer/metal	ON/OFF ratio: ~ 10^1 State retain time: > 1hr	73
I (1L)	ITO/Oriented P6OMe(50nm)/Al (Alignment method; rubbed with a velvet cloth fixed on a rotaing cylinder, annealed at 105 °C for 1hr, and then cooled down to room temperature at rate 1 °C /min.)	Hysteresis-type / Space charge stored at the interface polymer/metal	ON/OFF ratio: ~ 10^5 State retain time: > 9hr	74
I (1L)	Al/blue polyspirofluorene (80 nm)/Ba-Al	Multi-stable / Filament conduction	ON/OFF ratio: ~ 10^3 20 cycle test	87
II (1L)	Al/Au-DT+8HQ+PS(50nm)/Al Weight ratio: Au-DT:8HQ:PS=1:1:3 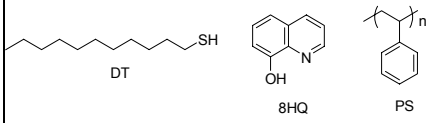 	Bistable / Electric-field-induced charge transfer	ON/OFF ratio: up to 10^5 Switching time: 25 ns W(5V)-R(1V)-E(–2.3V)	76a
II (1L)	Al/Au-2NT+PS(50nm)/Al Weight ratio: Au-2NT:PS=1:3 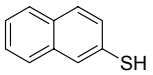 2NT	Write-once-read-many-times (WORM)/ Electric-field-induced charge transfer	ON/OFF ratio: up to 10^3 Write-once-read-many device	76b
II (1L)	Al(80nm)/(PANI-nanofiber+Au-NP+PVA, 70nm)/Al(80nm) Weight ratio: PANI-nanofiber/Au-NP composite:PVA=1:15 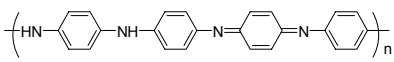 PANI(Emeraldine Base)	Bistable, NDR / Electric-field-induced charge transfer	ON/OFF ratio: up to 10^3 Switching time: 25 ns W(4.8V)-R(1.2V)-E(–6V)	78

Table 1.3 (CONT.)

II (1L)	ITO/Au-NP dispersed polymer composite/Al Au-NP: triphenylphosphine capped Polymer materials: xDHF, xHTPA, xBPF6, and xBP9F (x represents crosslinkable 4-phenylethynyl end group) 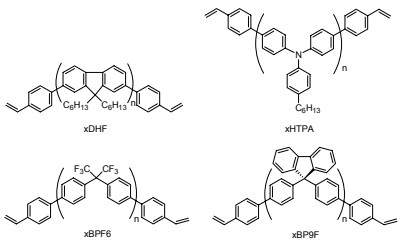 	Multi-stable, NDR / SV model; charge trapping	ON/OFF ratio: ~ 10^2 W(±5V)-R(±1V)-E(±8V)	67
II (1L)	Al/(PVP+C_{60}, 30nm)/Al 5 wt.% C_{60} 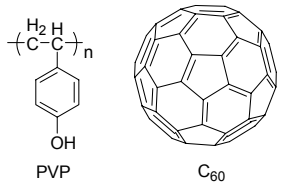 	Hysteresis-type / Not addressed	ON/OFF ratio: up to 10 Switching time: ~ 30 ns W(2.5V)-R(1.5V)-E(–3V) State retain time: > 1hr	84
III (1L)	Anode metal/Alq3(100nm)/Al Anode metals:Al, Au, ITO (Au/Alq3/Au device did not show any switching behavior)	Bistable / Charge induced conformational change	ON/OFF ratio: ~ 10^5	71
III (1L)	ITO(300nm)/Al_2O_3(20nm)/Cu:TCNQ(1:1,50-300nm)/Al(100nm) 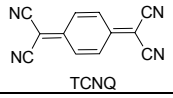 	Bistable / Redox reactions of molecules	ON/OFF ratio: ~ 10^3	72

Table 1.3 (CONT.)

III (1L)	Al/copolymer PKEu(50nm)/ITO 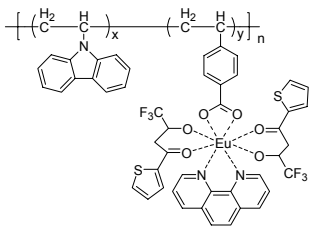 copolymer PKEu: x/y=0.987:0.013	Bistable / Charge transfer (donor-acceptor system)	ON/OFF ratio: up to 10^4 Switching time: 20 μs W(–4V)-R(0–4V)-E(4V) Achieved 10^6 cycles OFF state retain: 3hr	75
III (1L)	Al/copolymer PVK-C_{60}(50nm)/ITO 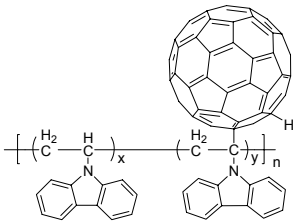 PVK-C_{60} copolymer: x/y=0.99:0.011	Bistable / Charge transfer (donor-acceptor system)	ON/OFF ratio: up to 10^5 Switching time: 20 μs W(–2.8V)-R(–1V)-E(3V)	86
III (1L)	Al/(PS:PCBM:TTF, 50nm)/Al Weight ratio: PS:PCBM:TTF=1:0.66:0.66 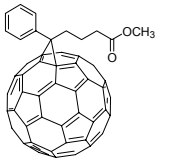 PCBM  TTF	Bistable / Electric-field-induced charge transfer (donor-acceptor system)	ON/OFF ratio: ~ 10^3 Switching time: 100 ns W(5V)-R(1V)-E(–9V)	77
III (1L)	Cu/Buffer layer(4nm)/Organic layer(100nm)/Cu Buffer layer: LiF, Al_2O_3	Bistable / Electric-field-induced ion-concentration change	ON/OFF ratio: ~ 10^5 Switching time: ~ 3 ms W(0.8V)-R(0.1V)-E(–3V)	81
III (1L)	ITO/Organic layer(less than 100nm)/Al Organic materials: 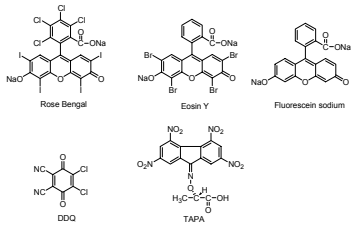 Rose Bengal, Eosin Y, Fluorescein sodium, DDQ, TAPA	Hysteresis- type / Electric-field-induced molecular conformational change	ON/OFF ratio; ~ 10^6 for Rose Bengal, 10^3 for Eosin Y, 10^0 for Fluorescein sodium, 10^4 for DDQ, 10^4 for TAPA	83

Table 1.3 (CONT.)

III (1L)	ITO/PEDOT:PSS/Au Au/PEDOT:PSS/p-i-n Si diode	WORM/ Redox reactions of PEDOT:PSS	ON/OFF ratio: ~ 10^3	89
III (1L)	ITO/DPBT(380nm)/Al ITO/DPBT(380nm)/Hg 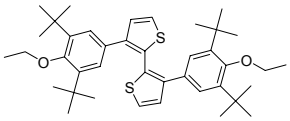 DPBT	Hysteresis-type / Electric-field-induced oxidation of DPBT	ON/OFF ratio: < 10^2 W(–3V)-R(0.5V)-E(2.5V) In air operation	90
III (2L)	ITO/(PEDOT:PSS+$LiCF_3SO_3$+ethylene carbonate)/(P3HT+ ethylene carbonate)/Al	Hysteresis-type / Electric-field-induced ion-concentration change	ON/OFF ratio: < 10^1 W(–6V, 0.1s)-R(–1V, 21ms)-E(4V, 0.5s) Short retention time (<10 min)	82
III (2L)	ITO/(PEDOT:NaCl+ethylene carbonate)/6T-PEO/Al 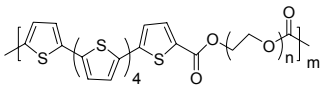 6T-PEO: n~45	Hysteresis-type / Electric-field-induced ion-concentration change	ON/OFF ratio: < 10^1 W(4V)-R(1.5V)-E(–4V) Short retention time (<10s)	92

[a] Type I is defined by the use of granular metal structures created by thermal evaporations either for the embedded metal in organic layers or top electrode on an organic layer. Type II is defined by the use of metal NPs or molecules dispersed into the films of polymeric or small molecule compounds as active materials. Type III is defined as other types different from the type I and II such as using donor-acceptor systems, ion diffusions of metal ions, redox reactions of molecules, and conformational change of special molecules.

[b] NDR= negative differential resistance, SV model= Simmons and Verderber model, and WORM= write-once-read-many times device that is not rewritable.

[c] W-R-E = write-read-erase operation, the values in parentheses represent operational voltages.

1.8 References

1. R. S. Muller, T. I. Kamins, and M. Chan, Device Electronics for Integrated Circuits. (Wiley and Sons, 1986).

2. C. W. Tang and S. A. Van Slyke, Appl. Phys. Lett. 51, 913 (1987).

3. J. H. Burroughs, D. D. C. Bradley, A. R. Brown, R. N. Marks, K. Mackay, R. H. Friend, P. L. Bums, and A. B. Holmes, Nature (London) **347**, 539 (1990).

4. F. Garnier, R. Hajlaoui, A. Yassar, and P. Srivastava, Science **265**, 1684 (1994).

5. N. S. Sariciftci, L. Smilowitz, A. J. Heeger, and F. Wudl, Science **258**, 1474 (1992).

6. L. Ma, J. Liu, S. Pyo, and Y. Yang, Appl. Phys. Lett. **80**, 362 (2002).

7. J. C. Scott, Science **304**, 62 (2004).

8. A. H. Wilson, Proc. R. Soc. Lond. Ser. A, **133**, 458 (1931).

9. H. K. Henisch, Recitifying Semiconductor Contacts (Clarendon, Oxford, 1957).

10. V. L. Rideout, Thin Solid Films **48**, 261 (1978).

11. E. H. Rhoderick, Metal-Semiconductor Contacts (Clarendon, Oxford, 1978).

12. J. Frenkel, Phys. Rev. 54, 647 (1938).

13. (a) S. M. Sze, Physics of Semiconductor Devices, Second Edition (Wiley & Sons, New York, 1981). (b) J. J. Sparkes, Semiconductor Devices, Second edition (CHAPMAN & HALL, London, 1994).

14. W. Wang, T. Lee, and M. A. Reed, Phys. Rev. B **68**, 035416 (2003).

15. (a) N. F. Mott and R. W. Gurney, Electronic Processes in Ionic Crystals, Second Edition (Oxford University Press, Oxford, 1948). (b) M. A. Lampert and P. Mark,

Current Injection in Solids (Academic, New York, 1970). (c) V. I. Arkhipov, P. Heremans, E. V. Emelianova, and G. J. Adriaenssens, Appl. Phys. Lett. **79**, 4154 (2001).

16. M. Koehler and I. A. Hümmelgen, Appl. Phys. Lett. **70**, 3254 (1997).

17. A. J. Champbell, D. D. C. Bradley, and D. G. Lidzey, J. Appl. Phys. **82**, 6326 (1997).

18. H. Bässler, Phys. Status Solidi B **175**, 15 (1993).

19. P. M. Borsenberger, L. Pautmeier, and H. Bässler, J. Chem. Phys. **94**, 5447 (1991).

20. P. M. Borsenberger, E. H. Magin, M. van der Auweraer, and F. C. de Schryver, Phys. Stat. Sol. A **140**, 9 (1993).

21. R. A. Marcus, Rev. Mod. Phys. **65**, 599 (1993).

22. P. F. Barbara, T. J. Meyer, and M. A. Ratner, J. Phys. Chem. **100**, 13148 (1996).

23. J. L. Brédas and G. A. Street, Acc. Chem. Res. **18**, 309 (1985).

24. Y. A. Berlin, G. R. Hutchinson, P. Rempala, M. A. Ratner, J. J. Michl, Phys. Chem. A **107**, 3970 (2003).

25. V. Coropceanu, M. Malagoli, D. A. da Silva Filho, N. E. Gruhn, T. G. Bill, J. L. Brédas, J. Phys. Rev. Lett. **89**, 275503 (2002).

26. V. Lemaur, D. A. da Silva Filho, V. Coropceanu, M. Lehmann, Y. Geerts, J. Piris, M. G. Debije, A. M. van de Craats, K. Senthilkumar, L. D. A. Siebbeles, J. M. Warman, J. L. Brédas, and J. Cornil, J. Am. Chem. Soc. **126**, 3271 (2004).

27. X. Y. Li, X. S. Tang, F. C. He, Chem. Phys. **248**, 137 (1999).

28. J. Cornil, D. Beljonne, J. P. Calbert, J. L. Brédas, Adv. Mater. **13**, 1053 (2001).

29. D. Monro, Phys. Rev. Lett. **54**, 146 (1985).

30. (a) S. D. Baranovskii, T. Faber, F. Hensel, and G. Leising, J. Phys.: Condens. Matter **9**, 2699 (1997). (b) S. D. Baranovskii, H. Cordes, F. Hensel, and G. Leising, Phys. Rev. B **62**, 7934 (2001). (c) V. I. Arkhipov, E. V. Emelianova, G. J. Adriaenssens, and H. Bassler, J. Non-Cryst. Solids **299–302**, 1047 (2001). (d) V. I. Arkhipov, E. V. Emelianova, and G. J. Adriaenssens, Phys. Rev. B **64**, 125125 (2001). (e) R. Schmechel, J. Appl. Phys. **93**, 4653 (2003).

31. R. Schmechel and H. von Seggern, Phys. Stat. Sol. (a) **201**, 1215 (2004).

32. (a) F. Gutman and L. E. Lyons, Organic Semiconductors (Wiley, New York, 1967). (b) N. von Malm, R. Schmechel, and H. von Seggern, J. Appl. Phys. **89**, 5559 (2001).

33. (a) A. J. Heeger, S. Kivelson, J. Schrieffer, and W.-P. Su, Rev. Mod. Phys. **60**, 781 (1988). (b) P. D. Townsend and R. H. Friend, Phys. Rev. B **40**, 3112 (1989).

34. (a) Y. Shirota, J. Mater. Chem. **10**, 1 (2000). (b) P. Strohriegl and J. V. Grazulevicius, Adv. Mater. **14**, 1439 (2002). (c) Y. Shirota, K. Okumoto, H. Ohishi, M. Tanaka, M. Nakao, K. Wayaku, S. Nomura, and H. Kageyama, Proc. SPIE **5937**, 593717 (2005).

35. (a) S.Kutkevicius, A. Stanisauskaite, V. Getautis, and A. Railaite, J. Prakt. Chem. **337**, 315 (1995). J. V. Crazulevicius and P. Strohriegl, Handbook of Advenced Electronic and Photonic Materials and Devices (Ed: H. S. Nalwa), Vol. 10. Academic Press, San Diego, CA. p.233 (2000).

36. (a) S. A. VanSlyke and C. W. Tang, U.S. Patent No. 4539507 (1985). (b) T. Tsutsui, MRS Bull. June, 39 (1997). (c) Y. Shirota, M. Kinoshita, T. Noda, K. Okumoto, and T. Ohara, J. Am. Chem. **122**, 11021 (2000).

37. (a) U. Bach, D. Lupo, P. Comte, J. E. Moser, F. Weissörtel, J. Salbeck, H. Spreitzer, and M. Grätzel, Nature **395**, 583 (1998). (b) M. Kinoshita, N. Fujii, T. Tsuzuki, and Y. Shirota, Synth. Met. **121**, 1571 (2001).

38. C. Hohle, U. Hofmann, S. Scholter, M. Thelakkat, P. Strohriegl, D. Haarer, and S. J. Zilker, J. Mater. Chem. **9**, 2205 (1999).

39. M. Yoshiiwa, H. Kageyama, Y. Shirota, F. Wakaya, K. Gamo, and M. Takai, Appl. Phys. Lett. **69**, 2605 (1996).

40. H. O. Wirth, Angew. Macromol. Chem. **185/186**, 329 (1991).

41. (a) K. Naito and A. Miura, J. Phys. Chem. **97**, 6240 (1993). (b) K. Naito, Chem. Mater. **6**, 2343 (1994).

42. (a) C. H. Chen, J. Shi, and C. W. Tang, Macromol. Symp. **1**, 125 (1999). (b) M. Stolka, J. F. Janus, and D. M. Pai, J. Phys. Chem. **88**, 4707 (1984).

43. Z. Deng, S. T. Lee, D. P. Webb, Y. C. Chan, and W. A. Gambling, Synth. Met. **107**, 107 (1999).

44. (a) C. Adachi, K. Nagai, and N. Tamoto, Appl. Phys. Lett. **66**, 2679 (1995). (b) S. A. Van Slyke, C. H. Chen, and C. W. Tang, Appl. Phys. Lett. **69**, 2160 (1996). (c) C. Giebler, H. Antoniadis, D. D. C. Bradley, and Y. Shirota, J. Appl. Phys. **85**, 608 (1999).

45. (a) K. Okumoto and Y. Shirota, Chem. Lett. 1034 (2000). (b) K. Okumoto, K. Wayaku, T. Noda, H. Kageyama and Y. Shirota, Synth. Met. **111-112**, 473 (200). (c) K. Okumoto and Y. Shirota, Mater. Sci. Eng. B **85**, 135-139 (2001).

46. (a) Y. Shirota, T. Kobata, and N. Noma, Chem. Lett. 1145 (1989). (b) Y. Shirota, Y. Kuwabara, H. Inada, T. Wakimoto, H. Nakada, Y. Yonemoto, S. Kawami, and K. Imai, Appl. Phys. Lett., **65**, 807 (1994).

47. Y. Shirota, K. Okumoto and H. Inada, Synth. Met. **111-112**, 387 (2000).

48. C. Giebeler, H. Antoniadis, D. D. C. Bradley, and Y. Shirota, Appl. Phys. Lett. **72**, 2448 (1998).

49. K. Okumoto and Y. Shirota, Chem. Mater. **15**, 699 (2003).

50. M. Tanaka, H. Kageyama, and Y. Shirota, 84th Annual Meeting of the Chemical Society of Japan, Hyogo, 2004, prepr. no.1, pp.432.

51. J. Ostrauskaite, V. Voska, J. Antulis, V. Gaidelis, V. Jankauskasb and J. V. Grazulevicius, J. Mater. Chem. **12**, 3469 (2002).

52. H. Ohishi, M. Tanaka, H. Kageyama, and Y. Shirota, Chem. Lett. **33**, 1266 (2004).

53. Y. Ma, Y. Sun, Y. Liu, J. Gao, S. Chen, X. Sun, W. Qiu, G. Yu, G. Cui, W. Hu and D. Zhu, J. Mater. Chem. **15**, 4894 (2005).

54. (a) K. Naito, A. Miura, J. Phys. Chem. **97**, 6249 (1993). (b) R. G. Kepler and P. M. Cahil, Appl. Phys. Lett. **66**, 3618 (1995).

55. G. G. Malliaras, Y. Shen, D. H. Dunlap, H. Murata, and Z. H. Kafafi, Appl. Phys. Lett. **79**, 2582 (2001).

56. (a) J. Bettenhausen and P. Strohriegl, Adv. Mater. **8**, 507 (1996). (b) J. Bettenhausen, P. Strohriegl, W. Brütting, H. Tokuhisa, T. Tsutsui, J. Appl. Phys. **82**, 4957 (1997). (c) J. Bettenhausen and P. Strohriegl, Macromol. Rapid Commun. **17**, 623 (1996).

57. (a) C. Hohle, M. Jandke, S. Schloter, N. Koch, R. Resel, D. Haarer, and P. Strohriegl, Synth. Met. **102**, 1535 (1999). (b) M. Jandke, P. Strohriegl, S. Berleb, E. Werner, and W. Brütting, Macromolecules **31**, 6434 (1998). (c) P. Imperia, M. B. Casu, S. Schrader, B. Falk, M. Jandke, and P. Strohriegl, Synth. Met. **121**, 1673 (2001). (d) M. Redecker, D. D. C. Bradley, M. Jandke, and P. Strohriegl, Appl. Phys. Lett. **75**, 109 (1999).

58. (a) M. Uchida, T. Izumizawa, T. Nakano, S. Yamaguchi, K. Tamao, and K. Furukawa, Chem. Mater. **13**, 2680 (2001). (b) H. Murata, G. G. Malliaras, M. Uchida, Y. Shen, and Z. H. Kafafi, Chem. Phys. Lett. **339**, 161 (2001). (c) J. Ohshita, M. Nodano, H. Kai, T. Watanabe, A. Kunai, K. Komaguchi, M. Shiotani, A. Adachi, K. Okita, Y. Harima, K. Yamashita, and M. Ishikawa, Organometallics **18**, 1453 (1999).

59. (a) S. Naka, H. Okada, H. Onnagawa, and T. Tsutsui, Appl. Phys. Lett. **76**, 197 (2000). (b) B. W. D'Andrade, S. R. Forrest, A. B. Chwang, Appl. Phys. Lett. **83**, 3858 (2003).

60. (a) E. H. Magin and P. M. Borsenberger, J. Appl. Phys. 73, 787 (1993). (b) L.-B. Lin, S. A. Jenekhe, P. M. Borsenberger, Proc. SPIE-Int. Soc. Opt. Eng. **3144**, 53 (1997).

61. (a) T. Ishi-i, K. Yaguma, T. Thiemann, M. Yashima, K. Ueno, and S. Mataka, Chem. Lett. **33**, 1244 (2004). (b) K.-T. Wong, Y.-Y. Chien, R.-T. Chen, C.-F. Wang, Y.-T. Lin, H.-H. Chiang, P.-Y. Hsieh, C.-C. Wu, C. H. Chou, Y. O. Su, G.-H. Lee, and S.-M. Peng, J. Am. Chem. Soc. **124**, 11576 (2002). (c) C.-C. Wu, T.-L. Liu, W.-Y. Hung, Y.-T. Lin, K.-T. Wong, R.-T. Chen, Y.-M. Chen, and Y.-Y. Chien, J. Am. Chem. Soc. **125**, 3710 (2003).

62. (a) A. Szymanski, D. C. Larson, and M. M. Labes, Appl. Phys. Lett. **14**, 88 (1969). (b) H. Carchano, R. Lacoste, and Y. Segui, Appl. Phys. Lett. **19**, 414 (1971). (c) J. G. Simmons and R. R. Verderber, Proc. Roy. Soc. A. **301**, 77 (1967).

63. Y. Yang, J. Ouyang, L. Ma, R. J.-H. Tseng, and C.-W. Chu, Adv. Funct. Mater. **16**, 1001 (2006).

64. (a) L. P. Ma, J. Liu, and Y. Yang, Appl. Phys. Lett. **80**, 2997 (2002). (b) L. Ma, S. Pyo, J. Ouyang, Q. Xu, and Y. Yang, Appl. Phys. Lett. **82**, 1419 (2003).

65. L. D. Bozano, B. W. Kean, V. R. Deline, J. R. Salem, and J. C. Scott, Appl. Phys. Lett. **84**, 607 (2004).

66. D. Tondelier, K. Lmimouni, D. Vuillaume, Appl. Phys. Lett. **85**, 5763 (2004).

67. L. D. Bozano, B. W. Kean, M. Beinhoff, K. R. Carter, P. M. Rice, and J. C. Scott, Adv. Funct. Mater. **15**, 1933 (2005).

68. T. Ouisse and O. Stéphan, Org. Electron. **5**, 251 (2004).

69. W. Tang, H. Shi, G. Xu, B. S. Ong, Z. D. Popovic, J. Deng, J. Zhao, and G. Rao, Adv. Mater. **17**, 2307 (2005).

70. J. Chen and D. Ma, Appl. Phys. Lett. **87**, 023505 (2005).

71. A. K. Mahapatro, R. Agrawal, and S. Ghosh, J. Appl. Phys. 96, 3583 (2004).

72. T. Oyamada, H. Tanaka, K. Matsushige, H. Sasabe, and C. Adachi, Appl. Phys. Lett. **83**, 1252 (2003).

73. H. S. Majumdar, A. Bandyopadhyay, A. Bolognesi, and A. J. Pal, J. Appl. Phys. **91**, 2433 (2002).

74. H. S. Majumdar, A. Bolognesi, A. J. Pal, Synth. Met. **140**, 203 (2004).

75. Q. D. Ling, Y. Song, S. J. Ding, C. X. Zhu, D. S. H. Chan, D. L. Kwong, E. T. Kang, and K. G. Neoh, Adv. Mater.**17**, 455 (2005).

76. (a) J. Ouyang, C.-W. Chu, C. Szmanda, L. Ma, and Y. Yang, Nature Mater. **3**, 918 (2004). (b) J. Ouyang, C.-W. Chu, D. Sievers, and Y. Yang, Appl. Phys. Lett. **86**, 123507 (2005).

77. C.-W. Chu and J. Ouyang, J.-H. Tseng, Y. Yang, Adv. Mater. **17**, 1440 (2005).

78. R. J. Tseng, J. Huang, J. Ouyang, R. B. Kaner, and Y. Yang, Nano Lett. 5, 1077 (2005).

79. J. G. Simmons and R. R. Verderber, Proc. Roy. Soc. A. **301**, 77 (1967).

80. S. H. Kang, T. Crisp, I. Kymissis, and V. Bulović, Appl. Phys. Lett. **85**, 4666 (2004).

81. L. Ma, Q. Xu, and Y. Yang, Appl. Phys. Lett. **84**, 4908 (2004).

82. J. H. A. Smits, S. C. J. Meskers, R. A. J. Janssen, A. W. Marsman, and D. M. De Leeuw, Adv. Mater. **17**, 1169 (2005).

83. (a) A. Bandyopadhyay and A. J. Pal, J. Phys. Chem. B **107**, 2531 (2003). (b) A. Bandyopadhyay and A. J. Pal, J. Phys. Chem. B **109**, 6084 (2005).

84. (a) A. Kanwal, S. Paul, and M. Cuhowalla, Mater. Res. Soc. Symp. Proc.**830**, D7.2.1. (2005). (b) S. Paul, A. Kanwal, and M. Cuhowalla, Nanotechnology **17**, 145 (2005).

85. J. Chen and D. Ma, J. Apple. Phys. **100**, 034512 (2006).

86. Q. D. Ling, S. L. Lim, Y. Song, C. X. Zhu, D. S. H. Chan, E. T. Kang, and K. G. Neoh, Langmuir **23**, 312 (2007).

87. M. Cölle, M. Büchel, and D. M. de Leeuw, Org. Electron. **7**, 305 (2006).

88. J. H. Jung, J-H. Kim, T. W. Kim, M. S. Song, Y-H. Kim, and S. Jin, Appl. Phys. Lett., **89**, 122110 (2006).

89. (a) S. Möller, C. Perlov, W. Jackson, C. Taussig, and S. R. Forrest, Nature **426**, 166 (2003). (b) S. Möller ans S. R. Forrest, J. Appl. Phys. **94**, 7811 (2003). (c) S. Smith and S. R. Forrest, Appl. Phys. Lett. **84**, 5019 (2004).

90. M. Caironi, D. Natali, M. Sampietro, C. Bertarelli, A. Bianco, A. Dundulachi, E. Canesi, and G. Zerbi, Appl. Phys. Lett. **89**, 243519 (2006).

91. J. Chen, L. Xu, J. Lin, Y. Geng, L. Wang, and D. Ma, Appl. Phys. Lett. **89**, 83514 (2006).

CHAPTER 2

CHARGE CARRIER MOBILITIES OF ORGANIC SEMICONDUCTORS INVESTIGATED BY *I-V* CHARACTERISTICS AND COMPARED TO DIFFERENT MEASUREMENT METHODS

2.1 Introduction

Charge transport properties in organic semiconductors have been studied using various techniques, including time-of-flight (TOF) measurements,[1-7] pulse-radiolysis time-resolved microwave conductivity (PR-TRMC) technique,[8,9] space-charge-limited current (SCLC) measurements[10-15] and FET measurements.[16-20] TOF measurements have been studied most extensively with organic disordered systems such as polymers and molecularly-doped polymers in where low molecular-weight organic materials are dispersed in binder polymers. It has been shown that charge transport in molecularly dispersed polymer systems is greatly dependent on binder polymers. In fact, hole drift mobilities of molecularly dispersed polymer systems vary by two orders of magnitude depending on the kind of polymer binders.[1-3] It has been suggested that charge-dipole interactions between the charge carrier and the polymer binder are responsible for these phenomena. In order to clarify the intrinsic charge transport properties of small molecules dispersed in polymers, the investigation of charge transport in their amorphous states without any polymer binder is required. Another consideration for TOF measurements is that the measurement using thin films smaller than the light-absorbing length is often difficult to obtain a sufficient transient of photocuurents, thus relatively thick films (the

range of μm) are used favorably. Practical organic electronic devices are usually comprised of less than 1 μm thick films. In many cases, transport properties in thick films may be different from those in thin films [21] due to different morphologies that can result from different film preparation techniques.

OFETs have received considerable attentions recently as driving elements of active matrix displays, and these device geometries have also been used to characterize charge transport properties for organic semiconductor materials.

SCLC measurements, the conventional dc transport measurements in SCLC regimes, are relatively simple experiments analyzing *I-V* characteristics by using a simple diode structure comprised of a single organic film embedded between two electrodes. And a wide range of thickness of the films under study is available, which in many ways resembles the situations in actual devices. The SCLC regime is described by well-known the Mott-Gurney or Child's law [25] (Eq. 2.8), the simple quadratic dependence of current density on biased voltage. In the disordered systems with field-dependence of mobility, this model is no longer valid. The *I–V* characteristics for organic materials following disorder formalism have been evaluated by numerically calculations based on a set of Poisson's equation, and described reasonably monocarrier-type trap free SCLC with disorder formalism which results in field-dependence of mobility.[11]Although the SCLC methods are sensitive the electrical contacts and carrier injection barriers between organic films and electrodes, some comparative studies of charge carrier mobilities obtained by TOF and SCLC measurements for organic amorphous or crystalline films have shown compatible results.[22-24]

PR-TRMC technique for studying charge carrier mobility of discotic liquid crystals developed by Warman and coworkers has been extensively applied to crystalline and liquid crystalline materials.[8,9] However, the mobilities measured by PR-TRMC technique and by TOF are difficult to compare directly. PR-TRMC technique is not sensitive to defects or domain boundaries due to the nanosecond response time for the detection. Within such short time, the charge carrier mobilities can be considered as the effective mobilities within well-organized domains. Also it is not sensitive to the defects and traps due to the low electric field strength (< 100 V/cm) and the ultrahigh frequency (ca. 30 GHz), therefore the random diffusion of the charge carriers is only slightly perturbed and the derived charge carrier mobility represents zero-field, trap-free values of the materials. In addition, PR-TRMC technique can not separate carriers and only determine the sum of the charge carrier mobilities. Therefore, the mobility values measured by PR-TRMC technique are usually higher compared to TOF mobilities in same material. Furthermore, the huge van der Graaff accelerator is not readily available, making PR-TRMC technique mainly limited to the groups at the Delft University of Technology in the Netherlands.

Thus, the work presented in this chapter used the three different mobility measurement techniques, TOF, FET, and SCLC. One of the important differences between the three different methods is the geometry of the sample in which the charge mobility is characterized. In TOF and SCLC, the sample is sandwiched between two electrodes and the conduction of the charges is perpendicular to the substrate plane. By contrast, in a FET the charge mobility is characterized within the plane of the substrate. This geometrical difference is irrelevant when one study the charge transport properties

in an amorphous material but becomes fundamental when the material present some molecular organization such as liquid crystal materials or crystalline materials.

Keeping in mind each advantage/disadvantage and the differences between the three different techniques, the objective for this chapter is to understand why the characterization of charge carrier mobility in organic semiconductors based on applying the disorder formalism to *I-V* characteristics is a reliable technique and how it compares to other techniques such as TOF and FET. The charge transport properties of amorphous organic films embedded between two electrodes have been investigated by analyzing the *I–V* characteristics in the SCLC regimes using an empirical equation representing the disorder formalism or electric-field dependent mobilities. To ensure the effective mobilities and disorder parameters extracted from the SCLC regime are plausible, a comparative study between TOF and SCLC based on the disorder formalism has been carried out by using the same sample of polymer composite doped with a small molecule semiconductor. In the later parts, comparisons between three different mobility measurements: TOF; SCLC; and FET by using two different amorphous materials with different ionization potentials are presented. These studies reveal that the effective mobility values from SCLC are limited by injection efficiency.

2.2 Theories of charge carrier mobility characterization techniques

2.2.1 TOF

The most widely used method to measure drift mobility in organic materials is the TOF technique. As its name already says, the mobility is determined in this experiment by measuring the time charges need to move over a given distance under an applied electric field. The principle of the TOF experiment will be described by following.

A thin film of the materials under study is usually melted between two electrodes. In the case of measuring a hole drift mobility, a transparent electrode is held at a positive potential with respect to the ground, while the other one is grounded through a resistance R which has a much smaller resistance than the sample. This leads to an applied potential V in the material. Hole charges are generated by photo-excitation of the film through irradiation with a short pulse laser (the wavelength of which depends on the absorption band of materials). One of the advantages of using TOF technique is that the hole and electron mobility can be studied separately.

Photo-generated charge carriers will start moving to the negative electrode. The drifting carriers build a current:

$$I = \frac{Ne}{d}\nu, \qquad \text{Eq. 2.1}$$

where N is the number of charge carriers in the material, e is the elementary charge, d is the film thickness, and v is the velocity. According to Ohm's law, this current causes a small perturbation of the applied potential described by

$$\Delta V = R\frac{Ne}{d}\nu. \qquad \text{Eq. 2.2}$$

For current measurements, the condition $CR << t_t$ (C the total capacitance across resistance R) is necessary to prevent the rising time of the signal from being longer than the transit time t_t. The transit time t_t is defined as the time the band of charge carriers needs to travel through the sample.

The theoretical transient current as a function of time is shown in Figure 2.1a. At the excitation of one side of the material, the transient current (j_{ph} = photo-generated current density) increases instantly. In the following time, the photo-generated carriers are traveling through the material, and the current level should stay constant. As soon as the carriers reach the other electrode, the current will decrease rapidly, thus makes a signal. In order to obtain a sufficient transient signal to allow evaluate a transient time, the photo-generated charge carriers have not to be dispersed. Therefore it is important that the duration of the excitation pulse is much shorter than the transient time t_t, and the absorption depth of the excitation is smaller than the thickness of the sample. However, many organic materials under study in TOF experiments with a proper condition could not obtain an ideal transient sharp due to deep traps in materials. Typical signal of an amorphous organic material is shown in Figure 2.1b. This sharp is due to a charge trap or dispersion effect in a material, which means that some charge carriers are hold in different energy levels from a transporting level for a certain time during traveling from one electrode to the other. Such a transient sharp has to be examined in double logarithmic current versus time plot. In this case, the transient time is determined as the intersection between two straight lines with different slopes at short and long times of the transient photocurrent. Finally, the drift mobility μ is obtained from

$$\mu = \frac{d^2}{Vt_t}. \qquad \text{Eq. 2.3}$$

In TOF experiments, relatively thick samples of a few to several micrometers are favorable due to the requirement of a smaller absorption depth of the excitation relative to the film thickness. In addition, determining mobilities for materials having a high charge carrier density is difficult because diffusive charge carriers will affect the drift of photo-generated charge carriers under an electric field.

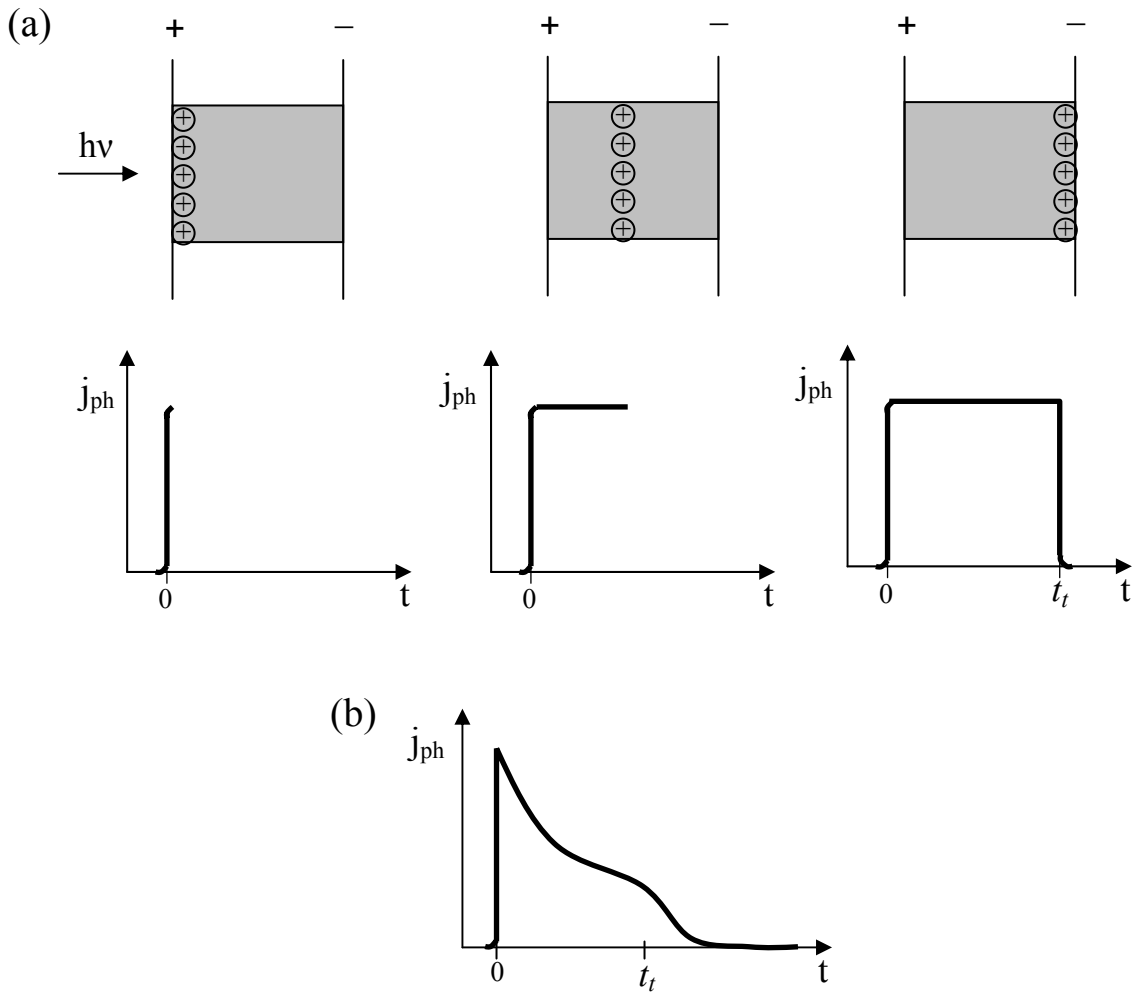

Figure 2.1 (a) Evolution of a theoretical signal in drift hole mobility experiments. (b) Pulse shape in case of deep traps conditions.

2.2.2 Disorder formalism

Drift mobilities of disordered materials have been measured as a function of the applied field $E = V/d$ and as a function of the temperature T to examine the use of the empirical formalism described by Borsenberger and co-workers and Bässler.[1-3] This disorder formalism is based on the assumption that charge transport occurs by hopping through a manifold of localized states with Gaussian distribution of energies, and a superimposed Gaussian distribution of positions. For the hopping sites energies the distribution therefore is the following:

$$g(\varepsilon) = (2\pi\sigma^2)^{-1/2} \exp\left(-\frac{\varepsilon^2}{2\sigma^2}\right), \qquad \text{Eq. 2.4}$$

where the energy ε is measured relative to the center of the distribution and σ is the width of the energetically disorder distribution.

Furthermore it is assumed that hopping between sites i and j can be controlled by jump rates of the form

$$\nu_{ij} = \nu_0 \exp\left(-2\beta a \frac{\Delta R_{ij}}{a}\right) \begin{cases} \exp\left[-\left(\frac{\varepsilon_i - \varepsilon_j}{kT}\right)\right], \varepsilon_i \geq \varepsilon_j \\ 1 \qquad\qquad\qquad\quad , \varepsilon_i \leq \varepsilon_j \end{cases}, \qquad \text{Eq. 2.5}$$

ν_0 is a pre-factor, β is an inverse wave function decay constant, a is the average lattice constant, and ΔR_{ij} is the interstate distance between sites i and j, $\Delta R_{ij} = | R_i - R_j |$. Starting with these assumptions one can describe the mobility as a function of an energetic (diagonal) disorder parameter $\hat{\sigma} = \sigma / kT$ and as a function of the applied electric field E:

$$\mu(\hat{\sigma}, E) = \mu_{(0)} \exp\left[-\left(\frac{2}{3} \hat{\sigma} \right)^2 \right] \exp\left[C\left(\hat{\sigma}^2 - \Sigma^2 \right) E^{1/2} \right], \qquad \text{Eq. 2.6}$$

where $\mu_{(0)}$ is the disorder-free mobility, C is an empirical constant with a value of 2.9×10^{-4} $(\text{cm/V})^{1/2}$, and Σ is the width of the positional disorder distribution. Eq. 2.6 accounts for the fact that $\mu(E)$ resembles the Poole-Frenkel behavior,[1] $\log \mu \propto \gamma E^{1/2}$ relationship, where γ is a electric field coefficient. The equation is only valid for $\Sigma > 1.5$ and between the glass transition temperatures T_g and the critical temperature T_c for the non-dispersive to dispersive transition.

The studies of charge transport in disordered molecular solids that are followed by the above framework of the disorder formalism should observe the following experimental observation: (1) the mobilities are strongly temperature dependent; (2) over an extended range of fields, the mobilities follow the Poole-Frenkel behavior; (3) the slope γ decreases with increasing temperature and can become negative above a certain temperature; (4) TOF signals display well-developed plateau regions, suggestive of what is conventionally termed Gaussian transport; (5) TOF transients feature anomalously broad tails indicative of a dispersion of transit times of nonthermal origin; (6) below a critical temperature, which appears to be related to physical perfection and chemical purity, TOF transients become dispersive; and (7) optical absorption spectra are inhomogeneously broadened which is evidence for the presence of disorders.

2.2.3 SCLC with field-dependent mobility

With ohmic contacts, the current-voltage relationship is often linear at low bias. An ohmic contact is defined as an infinite reservoir of charge that is able to sustain a

steady- state SCLC in a device. The slope of the log-log plot of current (or current density) and voltage at low voltages is then equal to one, and the behavior is described by Ohm's law:[25]

$$J = qN\mu\frac{V}{d}, \qquad \text{Eq. 2.7}$$

where q is the electronic charge, N the charge carrier density, μ the charge carrier mobility, V the applied voltage, and d the thickness of the sample.

At low voltages, the electrical field due to the injected carriers is negligible compared to that due to the applied bias. When the injected carrier density becomes large enough, the field due to the carriers themselves dominates over that of the applied bias and then current becomes space-charge limited. SCLC occurs when the transit time of any excess injected carrier is less than the bulk dielectric relaxation time. Under these circumstances, the trap free SCLC takes the simple form of the Mott-Gurney law, or Child's law:[25]

$$J = \frac{9}{8}\varepsilon_0\varepsilon_r\mu\frac{V^2}{d^3}, \qquad \text{Eq. 2.8}$$

where ε_0 and ε_r are the permittivity of free space and the relative permittivity, respectively. This model is characterized by a strict quadratic dependence of current on voltage. It is not necessary to imply the absence of traps in the materials, but rather that they are all filled.

SCLC in the device can occur if at least one contact is able to inject locally higher carrier densities than the material has in thermal equilibrium without carrier injection.[25] The SCLC model assuming an ohmic contact depends only on the bulk-materials parameters and is independent of field. However, it is well known that the

mobilities in disordered systems such as molecularly doped polymers, molecular glasses, and conjugated polymers can be described by a field dependent behavior observed from TOF measurements. The field dependent behavior[1-3] is described by

$$\mu(E) = \mu_0 \exp(\gamma\sqrt{E}), \qquad \text{Eq. 2.9}$$

where μ_0 denotes the mobility at zero field (units of cm^2/Vs). The field dependence through the coefficient γ in units of $(cm/Vs)^{1/2}$ is comparable to the Poole-Frenkel effect. In this case, the following expression for the dependence of space-charge limited current on voltage can be derived: [26]

$$J = \frac{9}{8}\varepsilon_0\varepsilon_r\mu_0 \exp\left(0.891\gamma\sqrt{\frac{V}{d}}\right)\frac{V^2}{d^3}. \qquad \text{Eq. 2.10}$$

For typical values of the electric-field coefficient γ established by experiments in many organic materials (10^{-2} – 10^{-4} $(cm/Vs)^{1/2}$), the *I-V* characteristic in the SCLC regime is nearly quadratic with exponents slightly larger than 2. In that nearly quadratic regime, a best fit to the data using Eq. 2.10 provides numerical values for μ_0 and γ. With these parameters, the effective mobility is calculated using Eq. 2.9. If the contact is not perfectly ohmic and/or if traps are present, the effective mobility that is derived from this analysis is $\mu_{eff} = \theta\mu$, where θ is a coefficient smaller than unity representing the injection efficiency and/or the presence of traps. Therefore, the effective mobility is an underestimation of the bulk mobility that would exist under trap-free conditions. Likewise, improvements of the ohmic properties of the contact will result in the extraction of larger effective mobility values.

2.2.4 FET

Figure 2.2 shows two common device configurations used in organic FET: (a) top-contact device, with source and drain electrodes deposited onto the organic semiconductor layer; and (b) bottom-contact device, with the organic semiconductor deposited onto prefabricated source and drain electrodes. Charge carrier mobilities of organic semiconductors in FET devices are a critical factor for the devices under operation, and they are determined through the following theory.[25b,27] In the case of evaluating a hole mobility, when the gate electrode is biased negatively with respect to the grounded source electrode, field-effect transistors operate in the accumulation mode and the accumulated charges are holes. At a low drain-source voltage V_{DS}, drain-source current I_{DS} increases linearly with V_{DS} (linear regime) and is approximately described by the following equation:

$$I_{DS} = \frac{WC_i}{L}\mu_{FET}(V_{GS} - V_T - \frac{V_{DS}}{2})V_{DS}, \qquad \text{Eq. 2.11}$$

where L is the channel length, W is the channel width, C_i is the capacitance per unit area of the insulating layer, V_T is the threshold voltage, V_{GS} is the gate-source voltage, and μ_{FET} is the field-effect mobility. The latter can be calculated in the linear regime from the transconductance g_m,

$$g_m = \left(\frac{\partial I_{DS}}{\partial V_{GS}}\right)_{V_{DS}=const} = \frac{WC_i}{L}\mu_{FET}V_{DS}, \qquad \text{Eq. 2.12}$$

by plotting I_{DS} versus V_{GS} at a constant low V_{DS} and equating the value of the slope of the plot to g_m.

For V_{DS} negative with respect to V_{GS}, I_{DS} tends to saturate (saturation regime) owing to the pinch-off of the accumulation layer, and is modeled by the equation:

$$I_{DS} = \frac{WC_i}{2L}\mu_{FET}(V_{GS} - V_T)^2 . \qquad \text{Eq. 2.13}$$

In the saturation regime, μ can be calculated from the slope of the plot of $|I_{DS}|^{1/2}$ versus V_{GS}.

Differences can often be observed in mobility values calculated in the linear region and the saturation region. The linear region mobility can be affected by contact problems, and in such cases there are departures from the linearity of the I_{DS} versus V_{DS} curve which can lead to underestimation of mobility. In the saturation regime, when channel lengths are comparable to the gate insulator thickness or only a few times greater than that thickness, the I_{DS} versus V_{DS} curve do not saturate and exhibit an upward trend at high V_{DS}. In such case, calculating the mobility can lead to erroneously high values.

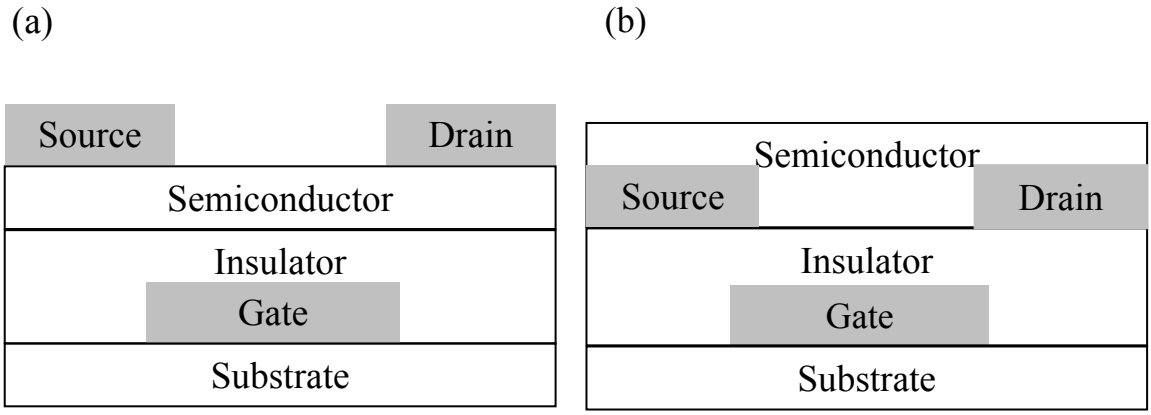

Figure 2.2 OFET device configurations: (a) Top-contact device, with source and drain electrodes evaporated onto the organic semiconducting layer. (b) Bottom-contact device, with the organic semiconducting deposited onto prefabricated source and drain electrodes.

2.3 Comparison of hole mobilities and disorder parameters

In this section, a comparative study between TOF and SCLC measurements for the same sample of polystyrene composite doped with a well-known charge transport material: *N,N'*-diphenyl-*N,N'*-di(3-methylphenyl)-(1,1'-biphenyl)-4,4'-diamine (TPD) is described. The experiments based on electric-field dependence and temperature dependence of mobilities following the Gaussian disorder model were carried out for both of the measurements. Temperature dependence of the TOF measurements for an ITO (Indium tin oxide)/PS: TPD = 1:1 molar ratio (thickness, d=20 μm)/ITO sample is shown Figure 2.3a. Although transient shapes were dispersive, the transit time t_t was determined as the intersection between two straight lines fitted to the two regimes of the photocurrent transients. One of possible reasons for the dispersive transients is the influence of injected charges from the positive electrode due to enhancing injection efficiency by air-plasma treatment to the electrode. According to the literature,[33] the work function of ITO can be increased by air-plasma treatment (from 4.8 eV to 5.1 eV); consequently, a hole-injection barrier from ITO to HOMO level of TPD (5.4 eV)[31] may be reduced. Indeed, the previous TOF experiments in our laboratory (Bernard Kippelen' group) for the same sample geometry as this work without air-plasma treatment observed non-dispersive photocurrent transients.[6] The hole drift mobility was calculated from t_t according to the equation $\mu = d^2 / t_t V$. Hole drift mobility was also measured as a function of the applied field $E = V/d$ and as a function of temperature (Figure 2.4). Experimental data were examined using the empirical formalism with Eq. 2.6. The zero-field mobilities μ_0 were extrapolated from the intercept of a straight line through the field-dependent mobility data at each different temperature. The prefactor $\mu_{(0)}$ and the energetic disorder

width σ were extrapolated from the intercept and the slope of the semi-logarithmic plot of μ_0 versus $1/T^2$ (Figure 2.5a), respectively. Finally, the slope of the field-dependent mobility γ was plotted versus $\hat{\sigma}^2$ (Figure 2.5b), and then the values of C and Σ were determined from the slope and intercept, respectively.

The temperature dependence of the *I–V* characteristics of the same sample as used for TOF experiments is shown Figure 2.3b. As mentioned in the previous section, the μ_0 and γ values at different temperatures could be calculated by numerical fitting with Eq.2.10 in the estimated SCLC regimes. The range of 100 V-200 V was determined as the SCLC regime according to the results of numerical fitting with Eq.2.10 (dashed lines in Figure 2.3b). Thus, the other parameters of the disorder formalism were extrapolated by the same procedure as for the TOF experiments.

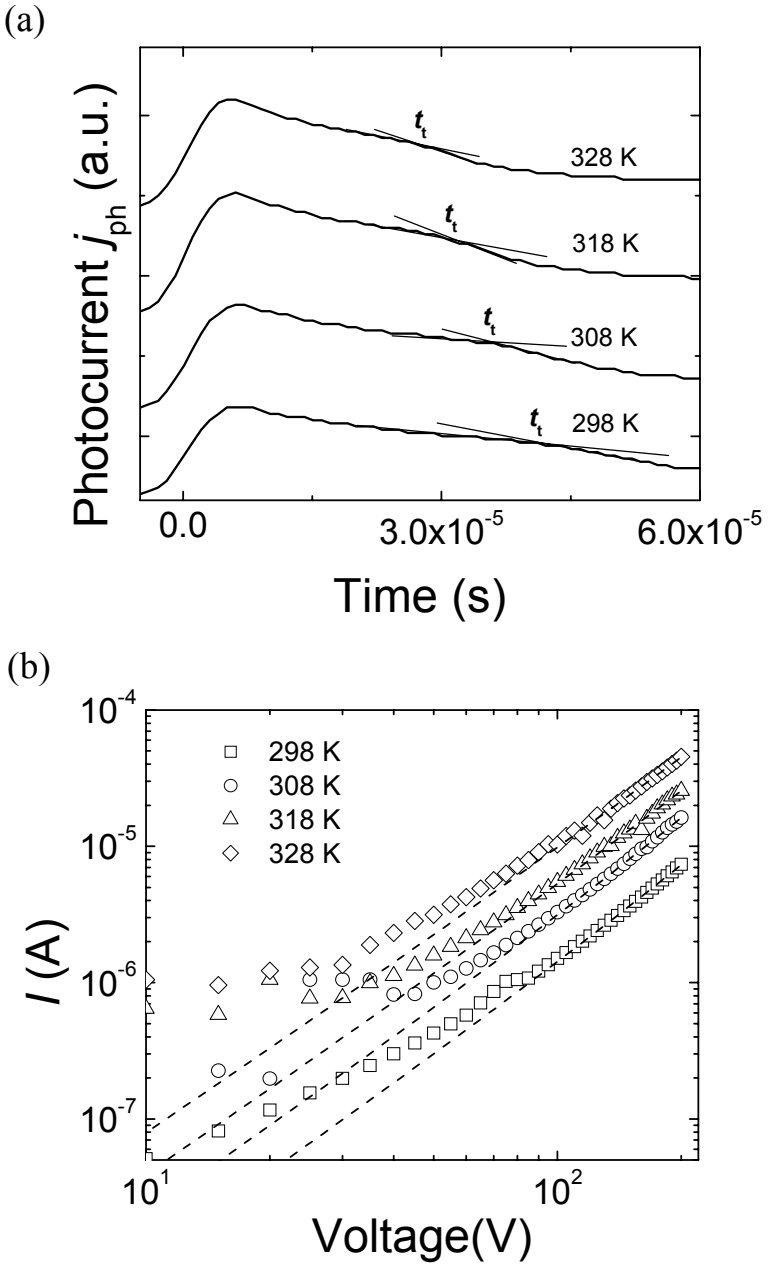

Figure 2.3 (a) Transient photocurrents observed for an ITO/PS: TPD (20 μm)/ITO device at different temperatures. The applied field is 1.75×10^5 V/cm. (b) *I-V* characteristics of the same device in (a) at different temperatures. The dashed lines represent the prediction from the SCLC model characterizing the field-dependent mobility of Eq. 2.10.

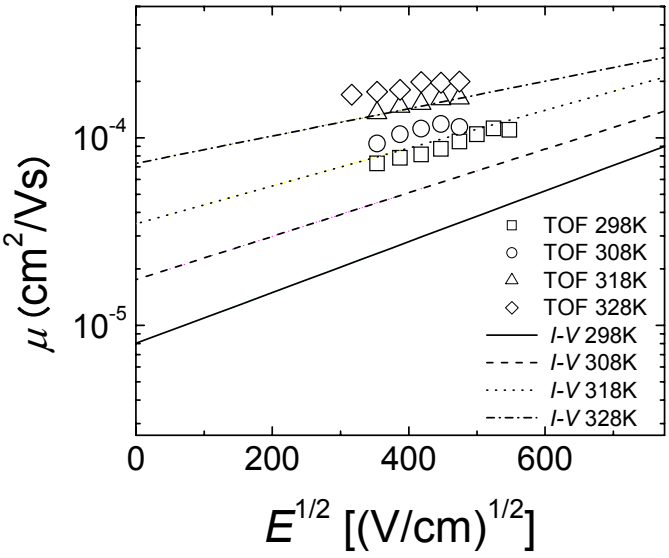

Figure 2.4 Electric-field dependence of the hole mobilities measured for the ITO/PS: TPD = 1:1 molar ratio (d = 20 μm)/ITO device at different temperatures. Symbols represent the TOF experimental data. Lines represent the calculated data obtained from the SCLC experiments.

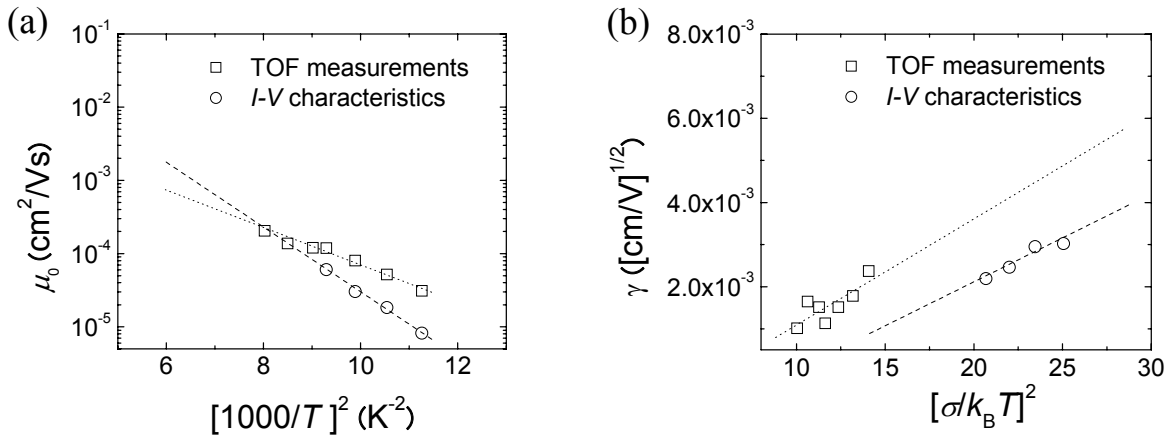

Figure 2.5 (a) Temperature dependence of the zero-field mobility values for the ITO/PS: TPD = 1:1 molar ratio (d = 20 μm)/ITO device measured by two different methods: TOF and SCLC. The lines represent a linear regression according to the disorder formalism. (b) The coefficient of field dependent mobility versus $\hat{\sigma}^2$ ($\hat{\sigma} = \sigma / k_B T$) measured by two different methods. The lines are linear fits according to the disorder formalism (Eq. 2.6).

The resulting mobility values and the parameters of the disorder formalism obtained from TOF and SCLC are summarized in Table 2.1. The mobility values and disorder parameters obtained from TOF and SCLC are compatible with the reported values.[3,6,28] The variation in the parameters σ, Σ, and γ with the two different methods is less than a factor of two. The zero-field mobility and the mobility value at given electric field determined by SCLC show remarkable agreement with TOF, although the values of SCLC are smaller than TOF. For instance, $\mu_0 = 3.1 \times 10^{-5}$ cm^2/Vs and $\mu_0 = 8.2 \times 10^{-6}$ m^2/Vs are obtained by TOF and SCLC experiments at room-temperature, respectively. And hole mobilities of $\mu = 7.3 \times 10^{-5}$ cm^2/Vs and $\mu = 2.1 \times 10^{-5}$ cm^2/Vs are obtained by TOF and SCLC experiments at $V/d = 1.0 \times 10^5$ V/cm and room-temperature, respectively.

Table 2.1 Summary of the mobilities and disorder parameters extrapolated from the TOF and SCLC measurements by using the same ITO/PS:TPD=1:1 molar ratio (d = 20 μm)/ITO sample. The values of μ are at $V/d = 1.0 \times 10^5$ V/cm and room-temperature. The values of μ_0 and γ are at room-temperature.

Samples	Methods	μ (cm^2/Vs)	μ_0 (cm^2/Vs)	γ (cm/V)$^{1/2}$	σ (eV)	C (cm/V)$^{1/2}$	Σ
PS :TPD	TOF	7.3×10^{-5}	3.1×10^{-5}	2.4×10^{-3}	0.096	2.5×10^{-4}	2.39
PS :TPD	SCLC	2.1×10^{-5}	8.2×10^{-6}	3.2×10^{-3}	0.128	2.0×10^{-4}	3.12
PS :TPD[(a)]	TOF				0.090	2.7×10^{-4}	2.57
PS :TPD[(b)]	TOF	1.5×10^{-4}	9.0×10^{-5}	3.2×10^{-3}	0.090	2.7×10^{-4}	2.57

[(a)] Literature values taken from Ref. 3. [(b)] The data of the previous study in our group.[6] The mobility μ values were measured at an average electric field of $V/d = 4.0 \times 10^5$ V/cm and at room-temperature.

To understand the origin of the variation of mobility values calculated from the TOF and the SCLC, we took into account a study of the injection efficiency representing how close an ohmic contact is to ideal between an organic semiconductor film and a metal electrode that was proposed by M. Abkowitz *et al.*[29] The injection efficiency is given by the quotient J_{dc} / J_{TFTOF} where J_{dc} is the steady-state current density measured by *I–V* characteristics, and J_{TFTOF} is the trap-free SCLC calculated by using a mobility value obtained from TOF as a trap-free mobility. According to the TOF experiments, the PS:TPD (1:1) 20 μm device showed $\mu_0 = 3.1 \times 10^{-5}$ cm^2/Vs and $\gamma = 2.4 \times 10^{-3}$ (cm/V)^{½} at room-temperature. The calculated $J_{TFTOF} = 1.2 \times 10^{-4}$ A/cm^2 at $V/d = 1.0 \times 10^5$ V/cm is obtained by using Eq. 2.10. In contrast, the current density J_{dc} of 3.7×10^{-5} A/cm^2 at $V/d = 1.0 \times 10^5$ V/cm was obtained in the SCLC experiment. Thus, the injection efficiency of the PS:TPD (1:1 molar ratio) 20 μm device is determined to be 0.31. This result is shown in Figure 2.6. The injection efficiency of less than 1.0 could be caused by the energy barrier between the work function of ITO (4.5 – 5.1 eV)[30,33] and the ionization potential of TPD (5.4 eV).[31] The height of the energy barrier plays a crucial role in controlling charge injection, and the injection efficiency should increase with a smaller barrier height.[29] Therefore, reducing the barrier height in SCLC measurements should be one of the key factors to obtain a consistent mobility value with TOF measurements. Therefore, we will discuss a comparative study of hole transport in a material having a lower ionization potential than that of TPD by using three different techniques, TOF, SCLC, and FET measurements, in the next section.

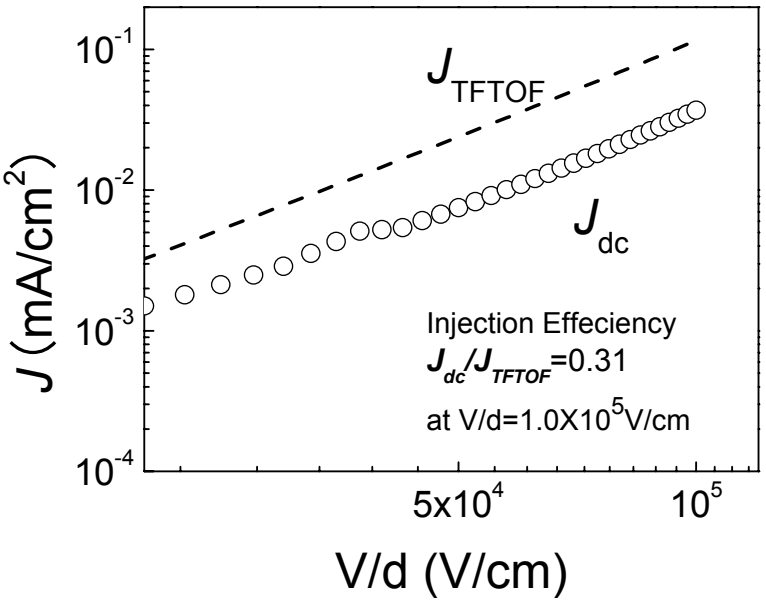

Figure 2.6 Current density J versus electric field V/d of ITO/PS:TPD = 1:1 molar ratio (d = 20 μm)/ITO device at room-temperature. The open circles represent the experimental current density, J_{dc}, in the SCLC experiments. The dashed line represents the trap-free space-charge limiting current, $J_{TFTOF,}$ calculated by Eq. 2.10 with the zero-field mobility and the coefficient of field-dependent mobility obtained from the TOF experiments. The calculated injection efficiency is $J_{dc}/ J_{TFTOF} = 0.31$ at $V/d = 1.0 \times 10^5$ V/cm.

2.4 Three different mobility measurement techniques

2.4.1 Introduction

In this section, comparative studies between three different techniques: TOF; SCLC; and FET by using TPD and a HT material, 2,5-Bis(4-(bis(4-methoxyphenyl)aminostyryl)-3,4-dibutoxythiophene (compound **I**).[32] The estimated ionization potential for compound **I** is lower than that of TPD, which may allow a higher injection efficiency from ITO to HOMO level of the material. The comparison study of the three different techniques by using the two different compounds reveal that SCLC

will be a reliable technique to characterize organic semiconductors if experimental parameter such as injection efficiency is well-controlled to be a sufficiently large. Otherwise, it may lead to underestimation of the intrinsic mobility of the material.

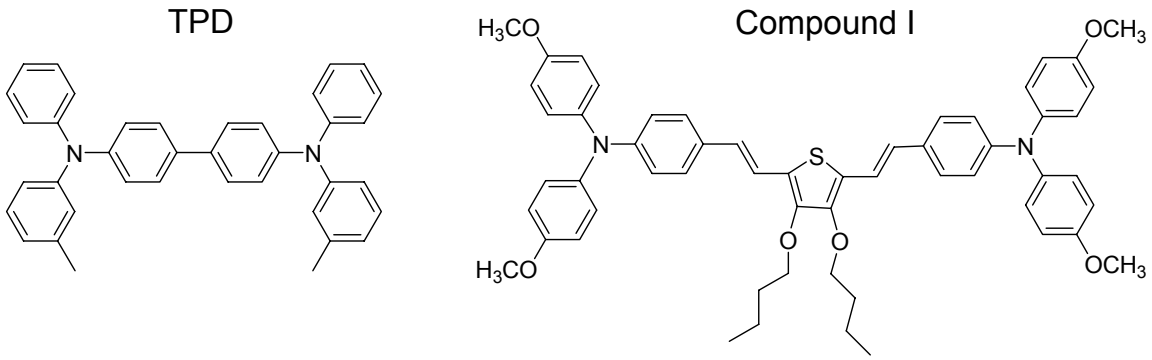

Figure 2.7 Chemical structures of TPD and compound **I**.

2.4.2 TPD

TOF measurements were performed on a sample with a geometry of ITO/TPD (d = 20μm)/ITO. Figure 2.8a shows typical transients of photocurrents with various applied fields at room-temperature. Transient photocurrents were non-dispersive, and the transit time t_t was determined directly from the linear plot of the transient photocurrent versus time. Figure 2.8b shows the linear dependence of the mobility as a function of the applied field with values of several times 10^{-3} cm^2/Vs. These mobility values are consistent with the values published previously in the literature.[6] A zero-field mobility of $\mu_0 = 1.2 \times 10^{-3}$ cm^2/Vs and a coefficient of field-dependent mobility of $\gamma = 1.5 \times 10^{-3}$ $(cm/V)^{1/2}$ were obtained from the intercept and slope of the plot of the field-dependent mobility at room-temperature.

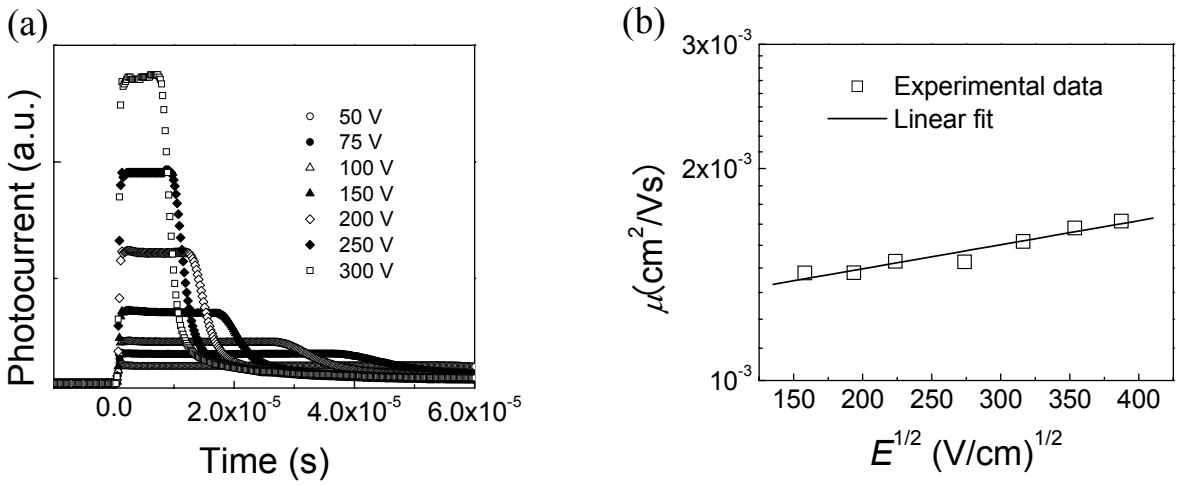

Figure 2.8 (a) Transient photocurrents observed in an ITO/TPD/ITO device for different applied fields. (b) Electric-field dependence of the hole mobilities calculated from the results in (a). Symbols represent the TOF experimental data.

In a bottom contact OFET using a 40 nm thick film of evaporated TPD, mobility values generally increased with channel length and ranged from a minimum of 2.0×10^{-5} cm^2/Vs for a width 1000 μm and length 1 μm device to a maximum value of 1.2×10^{-4} cm^2/Vs for a width 500 μm and length 50 μm device. *I-V* characteristics for the width 500 μm and length 50 μm device are shown in Figure 2.9a for values of V_{DS} up to 60 V and values of V_{GS} up to 60 V in 5 V steps. The non-ohmic behavior at low V_{DS} suggests the presence of contact resistance at the source and drain electrodes. That may explain why this field-effect mobility is one order of magnitude lower than the mobility measured by TOF. Transfer characteristics for this device are shown in Figure 2.9b. The linear fit to the $|I_{DS}|^{½}$ *vs*. V_{GS} data yielded a threshold voltage of approximately –23.3 V and semi-logarithmic plots of I_{DS} *vs*. V_{GS} yielded an on/off current ratio $>10^3$.

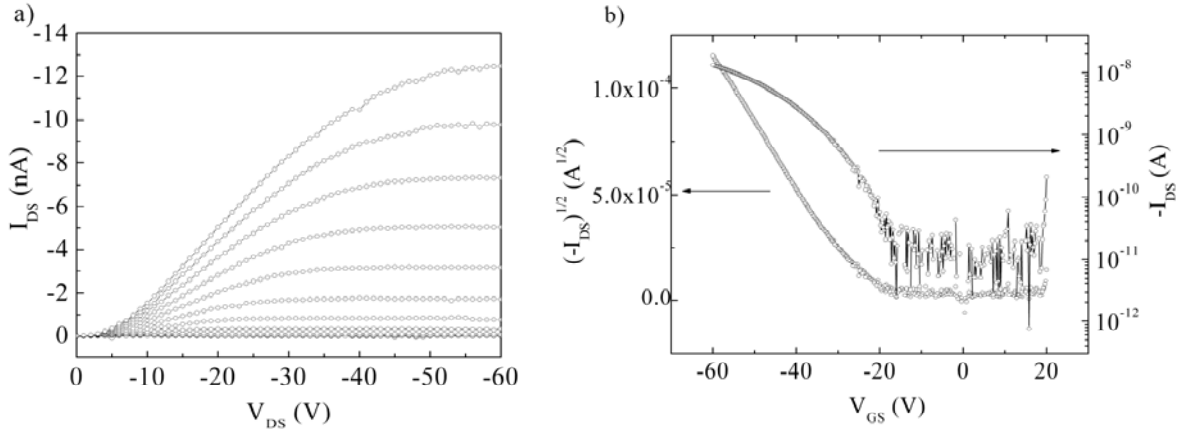

Figure 2.9 Room-temperature transistor characteristics for a bottom contact device with width W = 500 μm, length L = 50 μm, and 40 nm of TPD. (a) Drain current I_{DS} versus drain voltage V_{DS} for a series of gate voltage. (b) $|I_{DS}|^{1/2}$ versus gate voltage V_{GS} (left y axis) at a constant drain voltage $V_{DS} = -40$ V and semi-logarithmic plot of I_{DS} versus V_G (right axis).

Figure 2.10 shows the *I-V* characteristics of a device consisting of a 20 μm thick TPD film sandwiched between ITO and Au electrodes. When ITO is used as the injecting contact, the effective mobility at an average electric filed of $V/d = 7.5 \times 10^4$ V/cm is 7.7×10^{-5} cm^2/Vs. A zero-field mobility of $\mu_0 = 6.6 \times 10^{-5}$ cm^2/Vs and a coefficient of field-dependent mobility of $\gamma = 5.3 \times 10^{-3}$ (cm/V)^{½} were obtained by fitting Eq. 2.10 to the experimental data. When we reversed the bias and used Au as the injecting electrode, we observed that the current density still followed the same dependence on voltages as previously but with values that were much higher. The injection from the Au electrode is more efficient and therefore leads to higher current density. Consequently, the effective mobility extracted from the SCLC regime is calculated to be 1.6×10^{-4} cm^2/Vs at $V/d = 7.5 \times 10^4$ V/cm. A zero-field mobility of $\mu_0 = 1.4 \times 10^{-4}$ cm^2/Vs and a coefficient of field-

dependent mobility of $\gamma = 4.2 \times 10^{-3}$ (cm/V)$^{1/2}$ were obtained from the device with Au as anode.

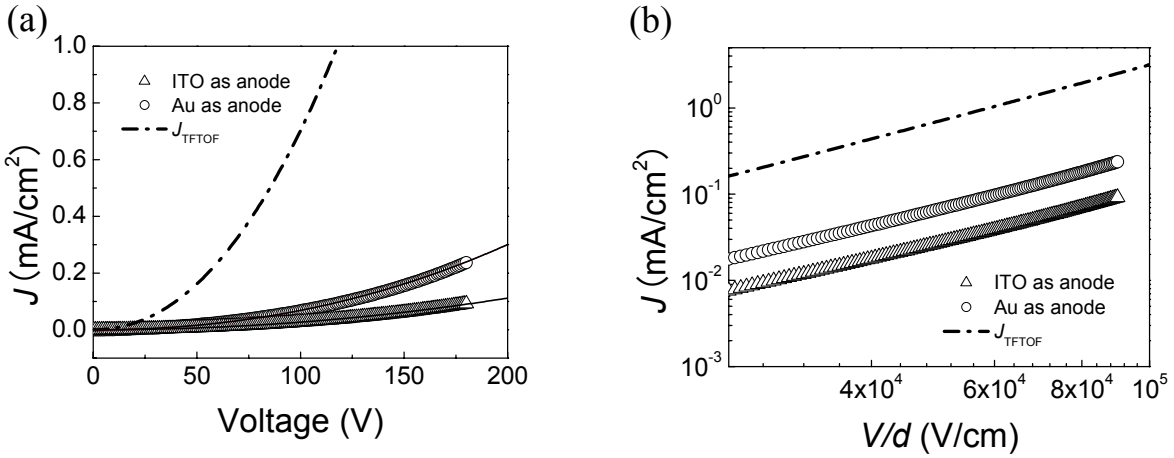

Figure 2.10 (a) *I-V* characteristics for a device of ITO/TPD/Au where ITO and Au are used successively as the anode. (b) Current density-average electric field *V/d* plot of the SCLC regime. The dash-dotted lines represent the trap free space-charge limiting current, $J_{TFTOF,}$ calculated by Eq. 2.10 with the zero-field mobility and the coefficient of field-dependent mobility obtained from the TOF experiments. The injection efficiency from Au (0.092 at $V/d = 7.5 \times 10^4$ V/cm) is higher than that from ITO (0.036 at $V/d = 7.5 \times 10^4$ V/cm) leading to higher current density.

The higher effective mobility in the device with Au as anode may be originating from the higher injection efficiency from the Au electrode (0.092 at $V/d = 7.5 \times 10^4$ V/cm) than that from the ITO electrode (0.036 at $V/d = 7.5 \times 10^4$ V/cm), presumably due to the difference of the work functions between the two electrodes. The differences between the HOMO level of TPD and the work function of ITO and Au are approximately 0.6 eV ($HOMO^{TPD}$ – Work $function^{ITO}$ = 5.4 eV – 4.8 eV) and 0.2 eV ($HOMO^{TPD}$ – Work $function^{Au}$ = 5.4 eV – 5.2 eV), respectively. It is interesting to note that the mobility using the Au anode is comparable to that obtained in an OFET with gold electrodes. Mobilities obtained by the SCLC method are still lower than those obtained

using TOF. As mentioned earlier, SCLC allows for the calculation of an effective mobility, $\mu_{eff} = \theta\mu$, where θ is a coefficient smaller than unity representing in particular the injection efficiency and/or the presence of traps. In our particular experiment, we used the same batch of TPD and condition of device-preparation for TOF and SCLC; therefore, the difference in mobility between the two methods may be attributed to the injection efficiency.

2.4.2 Compound I

As a hole transport material allowing for a small energy barrier between the work function of ITO and HOMO level of the material, compound **I** was chose to compare to the injection efficiency from ITO to TPD. The estimations of ionization potential (IP) and electron affinity (EA) for compound **I** were carried out by electronic spectroscopic and electrochemical experiments. The absorption spectrum of compound **I** in CH_2Cl_2 is shown in Figure 2.11a, and a maximum absorption at 453 nm and an onset of the absorption band at 550 nm are observed. Electrochemical measurements based on cyclic voltammetry (CV) measurements for compound **I** were carried out by using a solution probe molecule, ferrocene ($FeCp_2$), ca. 10^{-4} M in CH_2Cl_2/0.1 M $[^nBu_4N]^+[PF_6]^-$. The CV results reveal two reversible oxidation waves and one irreversible oxidation wave as shown in Figure 2.11b. The first oxidation wave is at 0.0 V (versus $FeCp_2^{+/0}$), which is readily oxidized than TPD (0.26 V versus $FeCp_2^{+/}0$), and the second oxidation potential is at 0.70 V where the potential difference $\Delta E_{1/2}$ between first oxidation potential $E_{1/2}^{+/0}$ and the second oxidation potential $E_{1/2}^{2+/+}$ of 0.70 V is larger than that of TPD ($\Delta E_{1/2}$ = 0.25 V). This indicates that the monocation of dibutoxythiophene-bridged compound **I** is

more stable with respect to disprotonation than that of biphenyl-bridged TPD, presumably due to a greater electronic coupling possible between the two nitrogen centers in the more planner π-system.

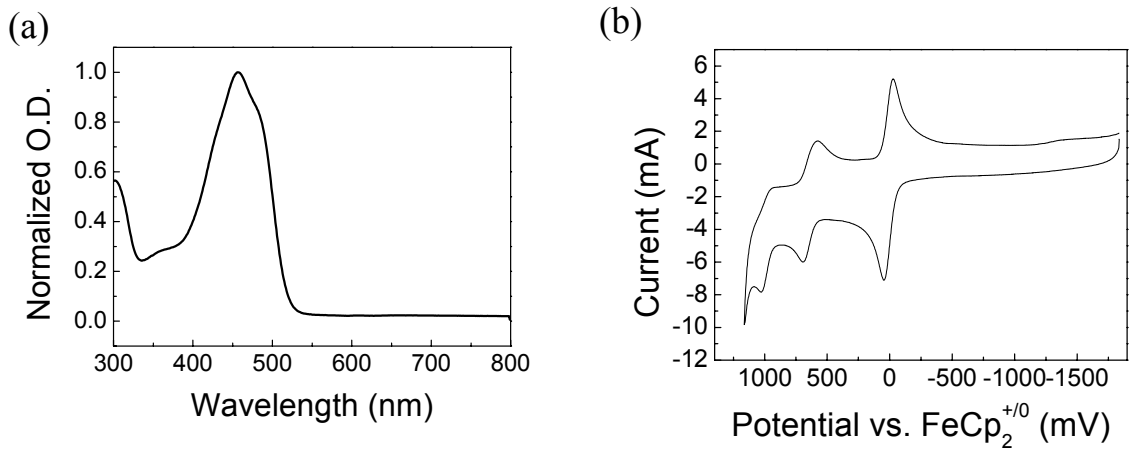

Figure 2.11 (a) Absorption spectrum of compound **I** in CH_2Cl_2 solution. (b) Cyclic voltammograms of compound **I** in 0.1 M Bu_4NPF_6 in CH_2Cl_2 solution with scan rate = 50 mV/s. The potentials are represented as internal potential against the $FeCp_2^{+/0}$ potential.

The IP of compound **I** in solid state can be estimated by comparison of electrochemical data between compound **I** and TPD as a reference material, which has a known IP measured directly from ultraviolet photoelectron spectroscopy (UV-PES).[31] Thus, the solid state IP of compound **I** of ca. 5.1 eV may be obtained from the relation,

$$E_{1/2}^{+/0}(\text{Compound I}) - E_{1/2}^{+/0}(\text{TPD}) = \text{IP}(\text{Compound I}) - \text{IP}(\text{TPD}), \qquad \text{Eq. 2.14}$$

using values of $E_{1/2}^{+/0}$(TPD) = 0.26 V[28] and IP(TPD) = 5.4 eV.[31] The optical band gap ΔE_{op} of 2.2 eV for compound **I** may be estimated by the onset (550 nm) absorption. The LUMO level of compound **I** may be estimated to be ca. 2.9 eV from the $\Delta E_{op.}$ The HOMO level is closer to the work function of ITO than that of TPD. The offset between the LUMO energy level and the work function of ITO will lead to negligible electron

injection from the ITO electrode, hence it is expected that the efficiency of hole injections from ITO to compound **I** will increase. Consequently, a more compatible mobility value should be obtained from the SCLC measurements compared to the case of TPD.

Table 2.2 Electrochemical data and electronic spectroscopic data for compound **I** and TPD.

Material	$E_{1/2}^{+/0}$ [V]	$E_{1/2}^{2+/+}$ [V]	$\Delta E_{1/2}$ [V]	IP [eV]	λ_{max}^{abs} [nm]	ΔE_{op} [eV]
Compound **I**	+0.00	+0.70	0.70	5.1[a]	453	2.2
TPD[b]	+0.26	+0.51	0.25	5.4	354	3.1

[a] The estimated value.
[b]The data of TPD are taken from Ref. 28.

The comparison of the three different techniques by using compound **I** was performed by an analogous way to the experiments for TPD described in the previous section. However, we used different film thicknesses for the compound **I** because the films thinner than 100 μm showed too much dark currents during the TOF experiments. Thus, three different thicknesses were used: a 100 μm thick film sandwiched between two ITO electrodes was used for TOF measurements; a 5 μm thick film sandwiched between two ITO electrodes was used for the SCLC measurements; and a 100 nm thick film prepared by spin-coating was deposited on bottom contact OFET device for field-effect mobility measurements.

A zero-field mobility of $\mu_0 = 8.4 \times 10^{-6}$ cm^2/Vs and a coefficient of field-dependent mobility of $\gamma = 5.1 \times 10^{-3}$ (cm/V)$^{1/2}$ at room-temperature were obtained by the

field-dependence mobilities of the TOF experiments. A drift mobility of $\mu = 8.4 \times 10^{-5}$ cm^2/Vs at $V/d = 2.0 \times 10^5$ V/cm was obtained. Transients of photocurrent as a function of the time at room temperature with various applied voltages for a ITO/compound **I** (100 μm)/ITO are shown in Figure 2.12a. The transient shapes are dispersive probably caused by a high density of injected carrier due to a low IP or a high trap density due to the thick film. In this case, the transient times were determined by the double logarithmic plot of currents versus times.

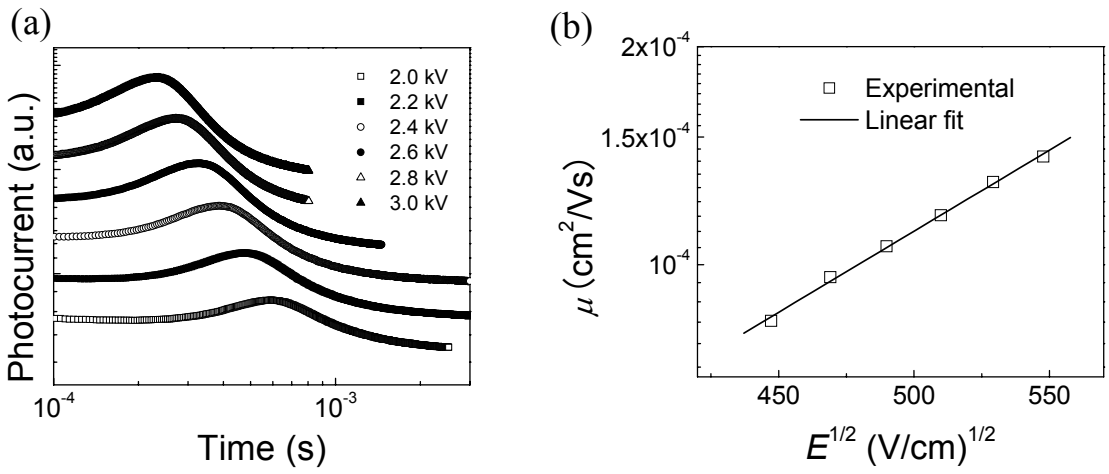

Figure 2.12 (a) Transient photocurrents observed in an ITO/Compound **I**/ITO device for different applied voltages. (b) Electric-field dependence of the hole mobilities calculated from the results in (a). Symbols represent the TOF experimental data.

The field-effect mobility measurements for compound **I** were performed by using a bottom contact device consisting a 100 nm thick film of compound **I**. A typical transistor characteristic at room-temperature is shown in Figure 2.13. The ohmic behavior at low V_{DS} suggests a better contact at the source and drain electrodes comparing to the

case of TPD as shown in Figure 2.9. The linear fit to the $|I_{DS}|^{1/2}$ *vs* V_{GS} data yielded a field-effect mobility of $\mu_{FET} = 2.5 \times 10^{-5}$ cm^2/Vs and a threshold voltage of –4 V. The semi-logarithmic plots of I_{DS} *vs*. V_{GS} yielded an on/off current ratio of 3×10^3. Although the field-effect mobilities vary with different channel lengths as in the case of TPD, these values are compatible with the mobility value obtained from the TOF.

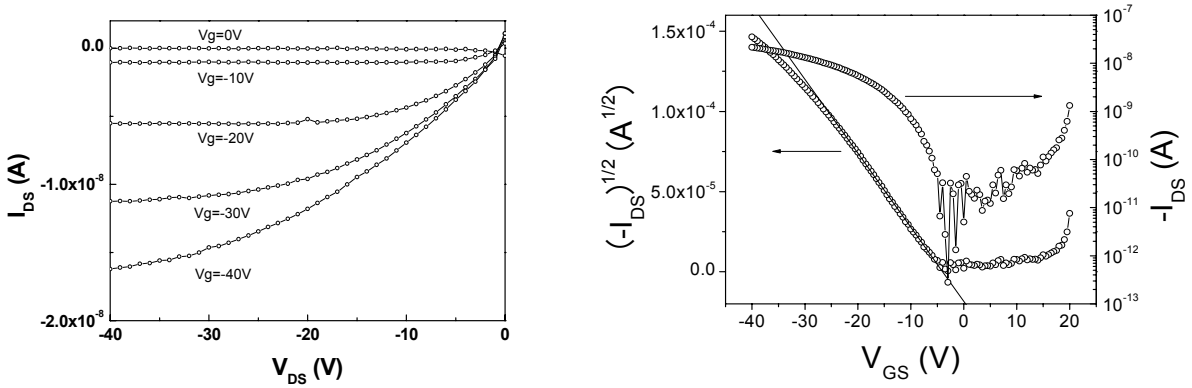

Figure 2.13 Room-temperature transistor characteristics for the compound **I** device. The channel width, length, and film thickness are $W = 1000$ μm, $L = 10$ μm, and around 100 nm respectively. (a) Drain current I_{DS} versus drain voltage V_{DS} for a series of gate voltage. (b) $|I_{DS}|^{1/2}$ versus gate voltage V_{GS} (left y axis) at a constant drain voltage $V_{DS} = -40$ V and semi-logarithmic plot of I_{DS} versus V_G (right axis).

In the SCLC measurements for ITO/compound **I** ($d = 5$ μm)/ITO, a zero-field mobility of $\mu_0 = 8.5 \times 10^{-6}$ cm^2/Vs and a coefficient of field-dependent mobility of $\gamma = 4.7 \times 10^{-3}$ (cm/V)$^{1/2}$ were obtained. And an effective mobility of $\mu_{eff} = 7.0 \times 10^{-5}$ cm^2/Vs at $V/d = 2.0 \times 10^5$ V/cm was extracted. These values are compatible with the values of TOF even though film thicknesses are different between SCLC and TOF. The comparison between J_{TFTOF} and J_{dc} for compound **I** (Figure 2.14) reveals a large injection efficiency of

0.43 at $V/d = 2.0 \times 10^5$ V/cm, and this value is larger than that of TPD. The difference of mobility values between TOF and SCLC measurements is less than a factor of two. Moreover, the mobility values from three different measurements are within the same order. These results indicate that more favorable ohmic contacts are formed between compound **I** and both ITO and Au electrodes due to the smaller ionization potential than that of TPD.

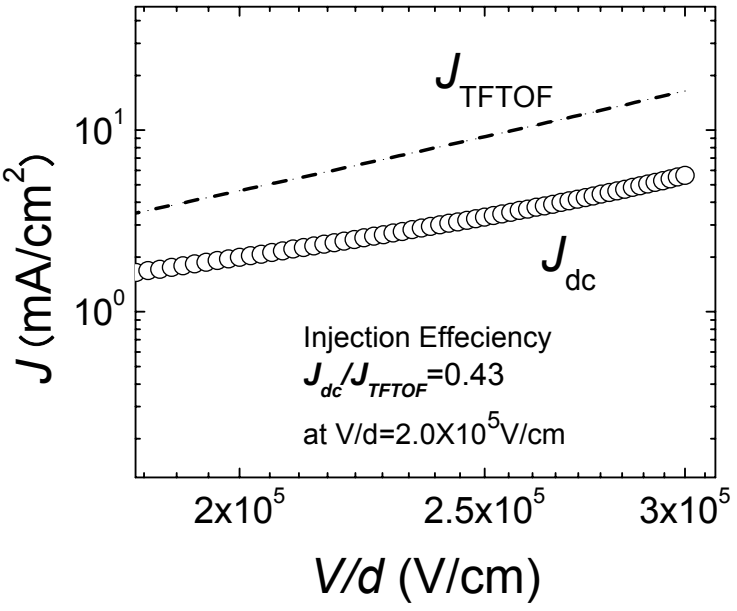

Figure 2.14 Current density J versus average electric field V/d for ITO/Compound **I** (5 μm)/ITO device at room-temperature. The open circles represent the experimental current density, J_{dc}, in the SCLC experiments. The dashed line represents the trap free space-charge limiting current, $J_{TFTOF,}$ calculated by Eq. 2.10 with the zero-field mobility and the coefficient of field-dependent mobility obtained from the TOF experiments. The calculated injection efficiency is $J_{dc}/ J_{TFTOF} = 0.43$ at $V/d = 2.0 \times 10^5$ V/cm.

2.5 Concluding remarks

The mobility measurements for TPD doped in PS by using the empirical equation characterizing the disorder formalism with field-dependence of mobility in the SCLC regime demonstrated the excellent agreement with TOF methods when using the same device between two different methods. Although there is the lower injection efficiency than unity in the SLCL measurement, the effective mobility at room-temperature in SCLC measurements was the same order of magnitude as that in TOF measurements. This result indicates that this method of determining the carrier mobility directly from the *I–V* characteristics is able to yield equivalent information on the mobility of disordered materials.

Mobility measurements by using three different methods: TOF; FET; and SCLC for the well-known HT organic semiconductor, TPD, showed that SCLC method lead to a limited effective mobility depending on the work function of the electrodes. In the device using Au as anode, the effective mobility from SCLC method was comparable within one order of magnitude compared to the mobility from TOF. The HT material (compound **I**) allowing for the higher injection efficiency (0.43) from ITO to HOMO level of the material showed compatible results between three different techniques. These results confirm the validity of using analyses of *I-V* characteristics on organic semiconducting thin film to determine their mobilities even when the measured value is limited by the injection efficiency from an electrode into an organic layer; a low injection efficiency will lead to an underestimation of the intrinsic mobility of the material.

Table 2.3 shows a summary of the evaluated hole-transport properties by using the different materials, experimental techniques, and sample geometries. Usually, TOF

led to the highest mobility value whereas OFET and SCLC mobility values were limited by contact resistance and injection efficiency, respectively.

Table 2.3 Summary of the comparison between three different measurements.

Sample geometry	Method	μ (V/d) [cm^2/Vs]	μ_0 [cm^2/Vs]	γ $[cm/V]^{1/2}$	Injection Efficiency: J_{TFTOF} / J_{dc}
ITO/PS:TPD(1:1),20 μm/ITO	TOF	7.3×10^{-5} (at 1.0×10^5 V/cm)	3.1×10^{-5}	2.4×10^{-3}	
ITO/PS:TPD(1:1), 20 μm/ITO	SCLC	2.1×10^{-5} (at 1.0×10^5 V/cm)	8.2×10^{-6}	3.2×10^{-3}	0.31
ITO/TPD, 20 μm/ITO	TOF	1.5×10^{-3} (at 7.5×10^4 V/cm)	1.2×10^{-3}	1.5×10^{-3}	
ITO(+)/TPD, 20 μm/Au(-)	SCLC	7.7×10^{-5} (at 7.5×10^4 V/cm)	6.6×10^{-5}	5.3×10^{-3}	0.04
ITO(-)/TPD, 20 μm/Au(+)	SCLC	1.6×10^{-4} (at 7.5×10^4 V/cm)	1.4×10^{-4}	4.2×10^{-3}	0.09
Bottom contact: 40 nm of TPD, and Au source/drain	FET				
W = 500 μm, L = 50 μm		1.2×10^{-4}			
W = 1000 μm, L = 1 μm		2.0×10^{-5}			
ITO/Compound **I**, 100 μm/ITO	TOF	8.4×10^{-5} (at 2.0×10^5 V/cm)	8.4×10^{-6}	5.1×10^{-3}	
ITO/Compound **I**, 5 μm/ITO	SCLC	7.0×10^{-5} (at 2.0×10^5 V/cm)	8.5×10^{-6}	4.7×10^{-3}	0.43
Bottom contact: 100 nm of Compound **I**, and Au source/drain	FET				
W = 1000 μm, L = 20 μm		4.4×10^{-5}			
W = 1000 μm, L = 10 μm		2.5×10^{-5}			
W = 1000 μm, L = 5 μm		1.9×10^{-5}			

All data are measured at room-temperature.

2.6 Experimental

The blend of TPD (from Aldrich, sublimated grade) and PS (from Polysciences, Inc., MW. = 125,000 – 250,000) was prepared by dissolving with the weight ratio of 1:1 in dichloromethane. The concentrated solvent was evaporated under reduced pressure by a rotary evaporator. The dry mixture was sandwiched between two electrodes supported on glass substrates and melted at a temperature between 190 ˚C and 220 ˚C, in excess of the melting point of TPD[29], on a heating plate, and then it was cooled to room temperature in air. Analogously, pure TPD and compound **I** were melted between two electrodes at around 190 ˚C – 220 ˚C and 180 ˚C – 200 ˚C respectively for the TOF and SCLC measurements. The capacitances of samples were measured by using an Agilent 16048A TEST LEADS connected to an Agilent 4284A precision LCR meter. For the TOF experiments, a sample was mounted inside a temperature controlled unit (Ransco Industries Model 924-1-6-SR). For the generation of the photocurrent, the sample was exposed to 6 ns pulses from a N_2-laser (337 nm, Laser Science, Inc. VSL-337ND-S) which was externally triggered by a function generator. The bias voltage was applied by a low-noise, high-voltage power supply (Keithley Model 248). The signal was then amplified with a low-noise preamplifier (Stanford Research Systems Model SR560) and monitored on a digital oscilloscope (Agilent infiniium oscilloscope). Resistance was chosen between 10^3 – 10^5 Ω. For SCLC experiments, the measurements of the *I-V* characteristics of all of the devices discussed in this chapter were performed in ambient conditions in the dark. The *I-V* characteristics were measured using a Keithley 2400 Source Meter. In the cases for TOF and SCLC experiments used pre-coated ITO glass substrates, ITO substrates were washed with detergent, de-ionized water, ethanol, and

acetone, and then treated with air-plasma for 5 min. Transistors were fabricated on heavily n-doped silicon substrates (as the gate electrode) with 200 nm of thermally grown silicon dioxide as the gate dielectric (ε_r = 3.9) and Ti/Au (10 nm/100 nm) backside metallization as the external gate contact. Bottom contact geometry Ti/Au (10 nm/100 nm) source and drain electrodes defining channels with widths of 500 μm or 1000 μm and lengths ranging from 1 μm to 50 μm were patterned on the SiO_2 layer using lift-off photolithography.[32] Depositions were performed at room temperature using physical vapor deposition at a pressure of 5×10^{-8} Torr and spin coating in a nitrogen glove-box (O_2, H_2O < 1 ppm) for TPD and compound I, respectively. During testing, electrical connections were made with a micro-probe station contained within a second glove box, and an Agilent E5272A medium power source/monitor unit connected to the probe station was used to perform the electrical measurements. At no point after deposition of the organic layer were the devices exposed to air. UV-Vis absorption spectra were recorded on a Varian Cary 5E UV-Vis-NIR spectrophotometer using photospectroscopic grade solvents. Electrochemical measurements were performed under nitrogen on deoxygenated solutions of tetra-n-butylammonium hexafluorophosphate (0.1 M) in methylene chloride with ferrocene as an internal standard using a computer-controlled BAS 100B electrochemical analyzer, a glassy-carbon working electrode, a platinum-wire auxiliary electrode, and a Ag wire anodized with AgCl as a pseudo-reference electrode. Potentials were referenced to the ferrocenium/ferrocene ($FeCp_2^+/FeCp_2$) couple.

2.7 References

1. P. M. Borsenberger, J. Appl. Phys. **68**, 5188 (1990).

2. P. M. Borsenberger, L. Pautmeier, and H. Bässler, J. Chem. Phys. **94**, 5447 (1991).

3. P. M. Borsenberger, E. H. Magin, M. van der Auweraer, and F. C. de Schryver, Phys. Stat. Sol. A **140**. 9 (1993).

4. H. Kageyama, K. Ohnishi, S. Nomura, and Y. Shirota, Chem. Phys. Lett. **277**, 137 (1997).

5. S. Naka, H. Okada, H. Onnagawa, and T. Tsutsui, Appl. Phys. Lett. **76**, 197 (2000).

6. J.-L. Maldonado, M. Bishop, C. Fuentes-Hernandez, P. Caron, B. Domercq, Y.-D. Zhang, S. Barlow, S. Thayumanavan, M. Malagoli, J.-L. Brédas, S. R. Marder, and B. Kippelen, Chem. Mater. **15**, 994 (2003).

7. R. D. Hreha, C. P. George. A. Haldi, B. Domercq, M. Malagoli, S. Barlow, J-L. Brédas, B. Kippelen, and S. R. Marder, Adv. Funct. Mater. **13**, 967 (2003).

8. (a) P. G. Schouten, J. M. Warman, M. P. de Haas, M. A. Fox, and H.-L. Pan, Nature **353**, 736 (1991). (b) A. M. Van de Craats and J. M. Warman, Adv. Mater. **13**, 130 (2001).

9. K. Ban, K. Nishizawa, K. Ohata, A. M. van de Craats, J. M. Warman, I. Yamamoto, and H. Shirai, J. Mater. Chem. **11**, 321 (2001).

10. P. W .M. Blom, M. J. de Jong, and J. J. M. Vleggaar, Appl. Phys. Lett. **68**, 3308 (1996).

11. P. W. M. Blom, M. J. M. de Jong, and M. G. van Munster, Phys. Rev. B **55**, 656 (1997).

12. A. J. Campbell, D. D. C. Bradley, and D. G. Lidzey, J. Appl. Phys. **82**, 6326 (1997).

13. L. Bozano, S. A. Carter, J. C. Scott, G. G. Malliaras, P. J. Brock, Appl. Phys. Lett. **74**, 1132 (1999).

14. Y. Shen, W. Klein, D. B. Jacobs, J. C. Scott, and G. G. Malliaras, Phys. Rev. Lett. **86**, 3867 (2001).

15. V. D. Mihailetchi, J. K. J. van Duren, P. W. M. Blom, J. C. Hummelen, R. A. J. Janssen, J. M. Kroon, M. T. Rispens, W. J. H. Verhees, and M. M. Wienk, Adv. Funct. Mater. **13**, 43 (2003).

16. S. F. Nelson, Y.-Y. Lin, D. J. Gundlach, and T. N. Jackson, Appl. Phys. Lett. **72**, 1854 (1998).

17. C. D. Dimitrakopoulos and D. J. Mascaro, IBM J. RES. & DEV. **45**, 11 (2001).

18. P. R. L. Malenfant, C. D. Dimitrakopoulos, J. D. Gelorme, L. L. Kosbar, T. O. Graham, A. Curioni, and W. Andreoni, Appl. Phys. Lett. **80**, 2517 (2002).

19. V. Podzorov, S. E. Sysoev, E. Loginova, V. M. Pudalov, and M. E. Gershenson, Appl. Phys. Lett. **83**, 3504 (2003).

20. A. Babel and S. A. Jenekhe, J. Am. Chem. Soc. **125**, 13656 (2003).

21. P. M. Borsenberger, L. Pautmeier, and H. Bässler, Phys. Rev. B **46**, 12145 (1992).

22. D. Poplavskyy and J. Nelson, J. Appl. Phys. **93**, 341 (2003).

23. D. Poplavskyy, J. Nelson, and D. D. C. Bradley, Appl. Phys. Lett. **83**, 707 (2003).

24. R. W. I. de Boer, M. Jochemsen, T. M. Klapwijk, A. F. Morpurgo, J. Niemax, A. K. Tripathi, and J. Pflaum, J. Appl. Phys. **95**, 1196 (2004).

25. (a) M. A. Lampert and P. Mark, Current Injection in Solids (Academic, New York, 1970). (b) S. M. Sze, Physics of Semiconductor Devices, Second Edition (Wiley & Sons, New York, 1981).

26. P. N. Murgatroyd, J. Phys. D: Appl. Phys. **3**, 151-156 (1970).

27. F. Garnier, R. Hajlaoui, A. Yassar, and P. Srivastava, Science **265**, 1684 (1994).

28. M. Stolka, J. F. Yanus, and D. M. Pai J. Phys. Chem. **84**, 4707 (1984).

29. M. Abkowitz, J. S. Facci, and J. Pehm, J. Appl. Phys. **83**, 2670 (1998).

30. D. D. C. Bradley, Synth. Met. **54**, 401 (1993).

31. S. Thayumanavan, S. Barlow, and S. R. Marder, Chem. Mater. **9**, 3231 (1997).

32. J. A. Haddock, B. Domercq, and B. Kippelen, Electronics Letters, **41**, 444 (2005).

33. J. H. Choi, E. S. Lee, S. H. Choi, H. K. Baika, K. M. Song, Y. S. Lim, and S.-M. Lee, J. Vac. Sci. Technol. A**23**, 1479 (2005).

CHAPTER 3

HIGH CHARGE CARRIER MOBILITIES IN TRI-SUBSTITUTED HEXAAZATRINAPHTHYLENE DERIVATIVES

3.1 Introduction

Charge carrier mobilities of organic semiconductors are a key issue for the future development of active materials for low-cost and large-area organic electronics and optoelectronics.[1-3] Recently, high hole or electron filed-effect mobilities of 0.1 – 3 cm^2/Vs in highly ordered organic crystalline thin films on FET devices such as pentacene, perylene diimide derivatives, and C_{60} have been reported.[4-6] Although these values are comparable to that of amorphous silicon, they are still insufficient for practical applications due to poor air-stability and processability. The preparation of a highly ordered thin film based on crystalline materials is useful to control carefully intermolecular distance and relative orientation of the molecules. In such cases, the important advantage of organic materials such as a facile possessing (e.g. wet and wide-area depositions) is less obvious. As one of promising approaches to circumvent of this problem, liquid crystal materials containing a planar π-conjugated core coupled with flexible side chains have been studied. Liquid crystal materials have the attractive prospects of a high solubility in solvents allowing for solution-based fabrication of electronic devices and the capability of molecular self-assembly into columnar discotic liquid crystal mesophases. The intermolecular coupling of such molecules along the columnar stack in mesophases has been recognized as an efficient structure to allow

facile carrier transport along the stack. Mobilities of closed to 1 cm^2/Vs within their mesophases have been reported.[7] However, the device performance using the films of discotic liquid crystals have been restricted presumably due to the presence of defects or grain boundaries in the active area and to the poor contact of the molecules with the electrodes or substrates,[8] while these materials show potentially high mobilities determined by PR-TRMC,[9] TOF,[10] and SCLC[11] techniques. Therefore, an alignment-technique allowing a macroscopic order for the thin films of discotic liquid crystals has been desired to realize the practical use of these materials into organic electronic devices.

In contrast to crystals and liquid crystals which show anisotropic properties, the films of amorphous molecular materials (molecular glasses) may exhibit isotropic properties as well as homogenous properties due to the absence of grain boundaries. It is possible to obtain uniform amorphous films of such molecules by various methods such as solution casting, spin-coating, vapor deposition, as well from the melt. According to some basic guidelines[12a] in which nonplanar molecular structure might interfere with the packing of molecules and impede crystallization, a number of hole transporting (HT) molecular glasses using low molecular-weight organic compounds that readily form stable amorphous glasses above room temperature have been designed and synthesized, and hole mobilities of some molecular glasses have been achieved up to around 10^{-2} cm^2/Vs.[12,13] However, the reports of electron transporting (ET) molecular glasses are, in general rare, and the highest mobility value are one order of magnitude lower than the highest value of HT molecular glasses. One of possible reasons the general observation of lower mobilities in ET materials could be related to electron trapping by oxygen. When oxygen is present in films or their surrounding environments, the reduction potential of

semiconductor materials must be lower than that of oxygen for it not to behave as a trap. Therefore, large electron affinities could be desirable in some cases in order to obtain ET compounds with high electron mobilities. For many organic electronic applications, ET materials with high charge mobilities are indispensable for complementary metal-oxide semiconductor (CMOS) technology such as invertors in where n-type and p-type transistors are used to realize logic functions. In addition, OLEDs based on low molecular-weight organic compounds also require both HT and ET materials with high injection efficiencies and high mobilities to create an efficient p-n junction for carrier recombination. Generally, semiconductor materials for organic electronic devices should meet the following requirements, they should: (1) possess a suitable ionization potential and electron affinity for energy level matching for the injection of charge carriers at the interfaces between the electrode/organic material or organic material/organic material; (2) allow for formation of a uniform film without pinholes; (3) be morphologically stable; (4) be thermally stable; and (5) be electrochemically stable. Hence, new ET molecular glasses have to meet above requirements and have a high electron mobility, as well as the ability of solution processes are desirable for low-cost and large-area organic electronics and optoelectronics devices.

As a potential ET molecular glass with a high electron mobility, tri-substituted hexaazatrinaphthylene (HATNA) derivatives, **3** and **4** (Figure 3-1), consisting in a HATNA core derivatized with pentafluoro-phenylmethyl ester (**3**) and trifluoromethyl (**4**), are chosen based on several considerations. The 5,6,11,12,17,18–HATNA ring has recently been identified as a potential component of ET materials, due to its ease of reduction and its ability, when suitably substituted to self-assemble into columnar

structures with large bandwidths.[13-15] The first reduction potential of HATNA derivatives typically occur the range of –1.0 – –1.4 V *vs.* ferrocenium/ferrocene,[14,16] and these reduction potentials are lower than that of the well known, tris(8-hydroxy-quinoline)-aluminum (Alq_3) for which the first reduction potential is –2.3 V[18b] *vs.* ferrocenium/ferrocene. The HATNA derivative can have large electron affinities. Secondly, the reorganization energy, λ, for intermolecular electron exchange between HATNA and its radical anion is calculated to be 0.1 eV[15d] using density function theory, considerably smaller than that for Alq_3/Alq_3^- (0.26 eV[18a]). The reorganization energy can be defined as the change in free energy required to convert the geometry of the reactant state to the equilibrium geometry of the product state without transfer of the charge.[15e] λ is determined by the structural differences between of the equilibrium configurations of the neutral and ionic states and by the vibrational frequencies of the modes that serve to inconvert these structures.[15f] In the case of the HATNA ring system, the LUMO is delocalized over the relatively large π-conjugated system; addition of an electron to this delocalized LUMO results in only small structural changes and, therefore, a small reorganization energy. This characteristic is a promising feature that is desirable for achieving a low barrier for electron transporting in HATNA ring; the barrier to intermolecular electron-transfer is predicted by Marcus theory to be ca. λ/4.[15d] Third, mobilities as high as 0.9 cm^2/Vs have been reported by using the PR-TRMC technique in the crystalline phases of hexaalkylsulfanyl derivatives.[16] The high mobility values indicate that HATNA parent is promising candidate as a core for ET molecular glasses. However, experimental mobility values of HATNA derivatives have been rare, and interestingly every reported value was determined by PR-TRMC technique. Another

consideration is how to design amorphous molecules with morphologically stable. According to Shirota,[12a] a non-planar molecular structure preventing a easy packing molecules and hence ready crystallization and an increased number of conformers in the molecules are the main preconditions and guideline to design of molecular glasses. However, HATNA ring is planar structure. In the case of using the HATNA core, the selection of substituents should be critical for the design of amorphous molecules. Intermolecular interactions may be reduced by incorporation of bulky substituents. Taking these considerations into account, we focused on compound **3** and **4** substituted by the relatively large group and the small group, respectively. In addition, the previously reported compound **3** was synthesized as an approximately statistical (1:3) mixture of **a** (C_{3h}) to **b** (C_s) isomers (Figure 3.1) in Seth Marder's group. Such the isomer mixture may help to increase the number of conformers and to form a glassy state in the film. However, previous separation of each isomer by using a high-performance liquid chromatography (HPLC) was time consuming and it difficult to obtain sufficient amounts of the material to allow for the characterizations for each isomer and the mixture. Therefore, a separation method yielding relative large quantity was desired.

This chapter describes the characterization for the isomers and the isomer mixtures of both **3** and **4**. The isomers and the isomer mixtures of both **3** and **4** were successfully separated with sufficient quantity by using a recrystallization method and a conventional column chromatography, respectively. The separation of **3** by using a recrystallization is very simple and we were able to separate reasonably large quantities of each isomer. The structure of the isomeric purity of separated isomers for both **3** and **4** were examined by NMR, HPLC, and differential scanning calorimetry (DSC). The

electronic properties of these compounds have been studied by cyclic voltammetry (CV), absorption spectra. These data compared to density functional theory (DET) calculations (by Jean-Luc Brédas's group) and photoelectron spectroscopy (PES) and inverse photoelectron spectroscopy (IPES) measurements of HATNA parent **1** film (by Antoine Kahn's group at Princeton University). The thermal properties and film morphologies of pure isomer and isomer mixtures have been investigated by using DSC, X-ray diffraction (XRD), polarized optical microscopy (POM), and UV-vis absorption spectroscopy. The charge-transport properties of these thin films between two electrodes have been studied by the *I-V* characteristics based on the SCLC technique. Both the morphology and the effective mobility of thin films depend on whether pure isomers or isomer mixtures of them are used. The films of **3** and **4** show high effective mobilities of the order of 10^{-3} – 10^{-2} cm/Vs. These effective mobility values are presumably represented as electron mobilities according to the estimated electron affinity (EA) and ionization potential (IP) values.

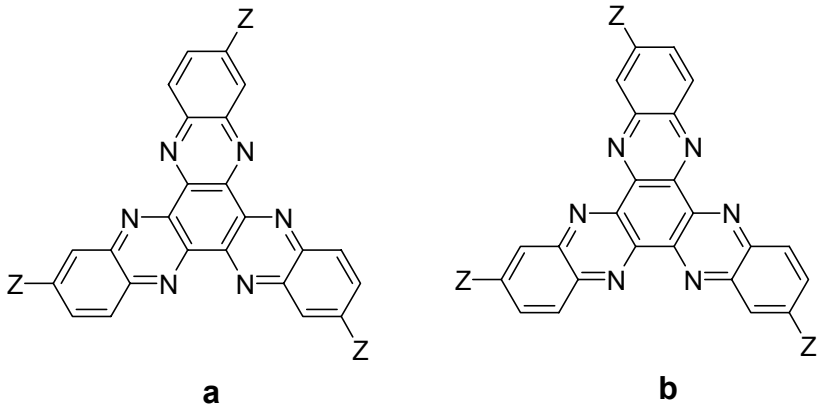

Figure 3.1. Structure of HATNAs. For compound **1**, Z = H; for **2**, Z = CO_2R [R = Et]; for **3**, Z = $CO_2CH_2C_6F_5$; for **4**, Z = CF_3.

3.2 Syntheses and separations

Compound **3** was obtained by esterification of the HATNA tris (acid chloride), with **5** pentafluorophenyl-methanol (Scheme 3.1). The solid that was obtained was dissolved in small amount of $CHCl_3$ and was precipitated with methanol to obtain crude **3** in 46% yield. Compound **4** was synthesized by the following procedure (Scheme 3.2). 2-nitro-4-trifluoromethyl-phenylamine was reduced with tin (II) chloride dihydrate in ethanol to give 4-trifluoromethyl-benzene-1,2-diamine (**6**). The diamine **6** was reacted with hexaketocyclohexane octahydrate to give **4**. Crude **4** was obtained as a yellow solid in 65% yield. It should be noted that introducing the trifluoromethyl group to HATNA ring can lead to drastically improved of solubility in common solvents. For example crude **4** can be dissolved in dichloromethane, chloroform, benzene, toluene, THF and hot methanol within the range of 10^{-2} mol/L.

Scheme 3.1[a] Synthesis of compound **3**.

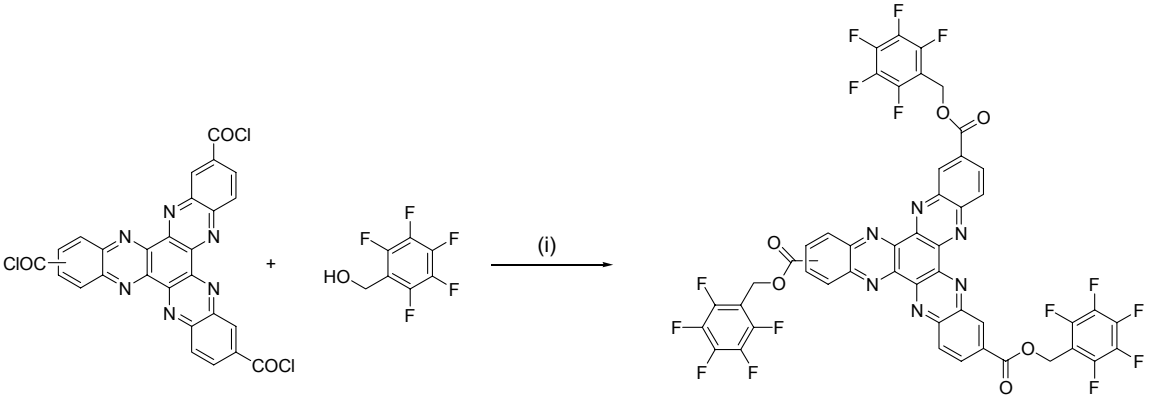

5 **3**

[a] Conditions: (i) THF, pyridine, 50 °C, 72 h.

Scheme 3.2[b] Synthesis of compound **4**.

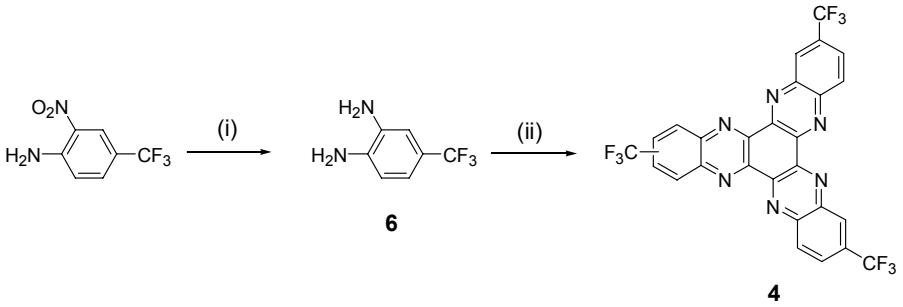

[b] Reagents and conditions: (i) $SnCl_2$, ethanol, 30 min; (ii) hexaketocyclohexane octahydrate, acetic acid,15 h.

Bock and co-workers have previously reported the condensation of hexaketocyclohexane with 3,4-diaminobenzoic acid and esterification of the resulting tri(carboxylic-acid) with a range of alcohols.[14] They reported that these ester species are formed solely as the less symmetrical (C_s) 2,8,15- (**b**) isomer. In contrast, we obtained **3** (and, therefore, presumably also the poorly soluble triacid precursor) as an approximately statistical (1:3) mixture of the **a** (C_{3h}) and **b** isomers. These can be distinguished by HPLC, ^{1}H-NMR, ^{19}F-NMR, and DSC. We found that they can be isolated in large quantities using either recrystallization with CH_2Cl_2 or column chromatography. The 2,8,14-isomer (**3a**, isomer purity > 92 %) can be separated from an isomer mixture by using recrystallization from dichloromethane, in which the 2,8,14-isomer shows a lower solubility than the 2,8,15-isomer. Figure 3.2 shows the HPLC traces of **3a** separated by recrystallization with dichloromethane, and a **3a/b** mixture (ca. 2:1) precipitated from the filtered supernatant solution. ^{19}F-NMR (CDCl3, 376MHz) of **3a**, **3a/b** (ca. 1:3), and **3b** are shown in Figure 3.4. In the 2,8,14-isomer, **3a**, the F_p appeared as triplets because they are coupled to two F_m whilst F_o appeared as a doublet of doublets. In the 2,8,15-isomer,

3b, the F_p appeared as two overlapping triplets of approximate ratio 2:1 corresponding to two different sets of fluorinated aromatic rings.

Crude product **4** was also obtained as an approximately statistical (1:3) mixture of the **a** and **b** isomers; these can be distinguished by HPLC (Figure 3.3), ^{1}H-NMR, and DSC and can be isolated by column chromatography (isomer purity > 90%), using dichloromethane: ethyl acetate (9.5:0.5) as eluent from the crude **4a/b** mixture (ca. 1:3 mixture). The HPLC condition for **4** was different from that of **3**; HPLC grade CH_2Cl_2 and hexane were used for HPLC analysis with 1:9 CH_2Cl_2 / hexane as the initial eluent, with the CH_2Cl_2 content being increased smoothly to 100% between 5 and 15 min. ^{1}H-NMR (Benzene-d_6, 300MHz) of **4a**, **4a/b** (ca. 1:3), and **4b** are shown in Figure 3.5. In the 2,8,14-isomer, **4a**, the H^a appeared as a singlet, and H^b appeared as a doublet coupled to H^c whilst H^c appeared as a doublet of doublets (each H is defined by insets in Figure 3.5). In the 2,8,15-isomer, **4b**, a low-field doublet (appearing at 8.65 – 8.61 ppm) of approximate ratio 2:1 corresponding to the H^a and $H^{a'}$ was successfully observed.

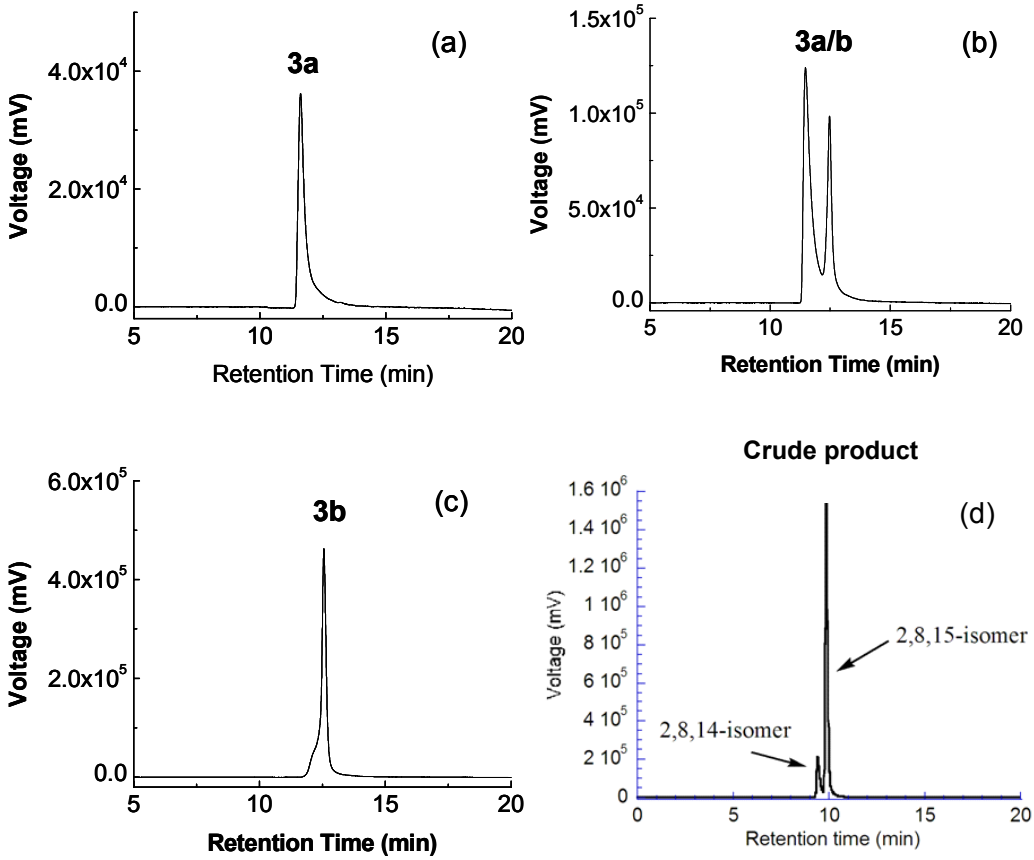

Figure 3.2 HPLC traces of (a) **3a**, (b) **3a/b**, (c) **3b**, and (d) crude product of **3a/b**.

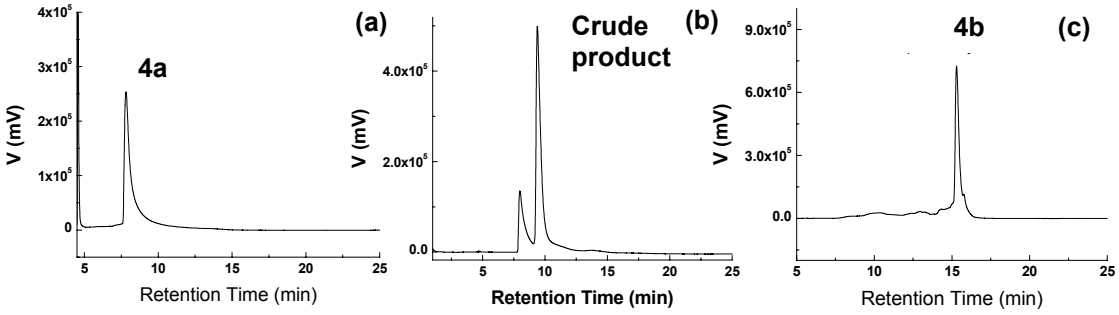

Figure 3.3 HPLC traces of (a) **4a**, (b) crude product of **4a/b**, (c) **4b**.

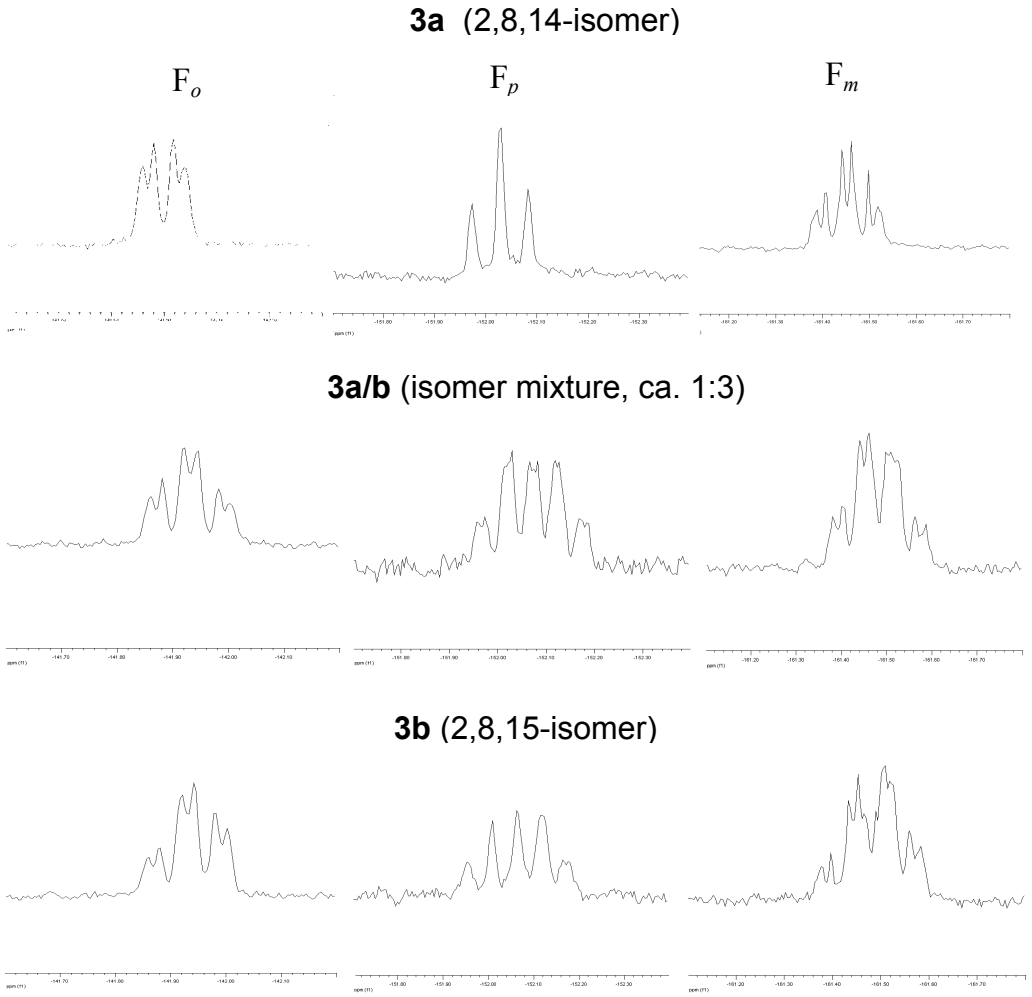

Figure 3.4 ^{19}F-NMR ($CDCl_3$, 376 MHz) of **3a**, **3a/b** (ca. 1:3), and **3b**. The concentration of every sample was 1.8×10^{-3} mol/L in $CDCl_3$.

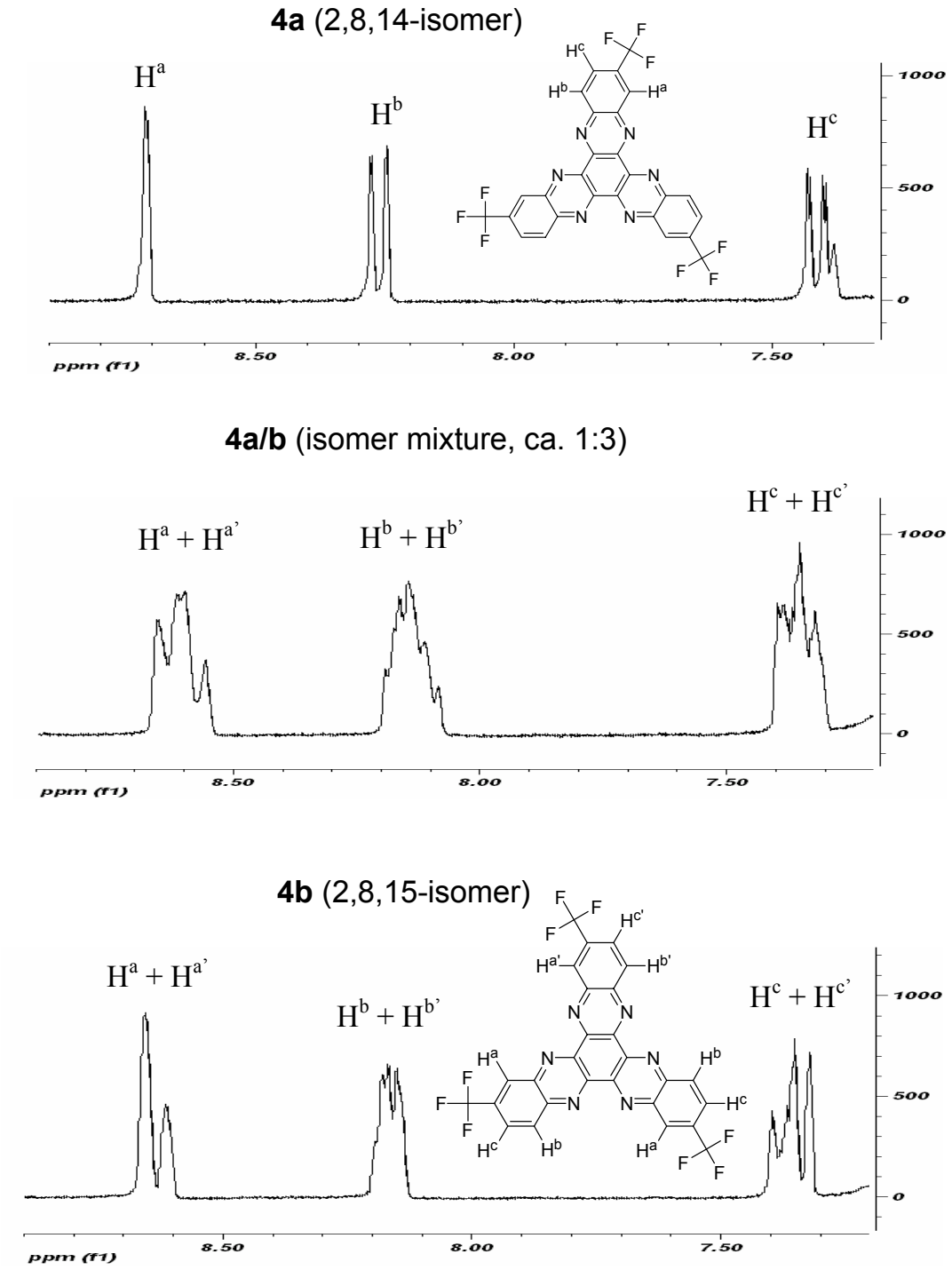

Figure 3.5 ^{1}H-NMR (Benzene-d_6, 300 MHz) of **4a**, **4a/b** (ca. 1:3), and **4b**. The concentrations of **4a**, **4a/b**(ca. 1:3), and **4b** were 3.4×10^{-3} mol/L, 1.0×10^{-2} mol/L, and 1.0×10^{-2} mol/L in benzene-d_6, respectively.

3.3 Estimation of electron affinities and ionization potentials

Films of the parent HATNA, **1**, with thickness ranging from 20-50 Å were deposited on the Au surface at a rate of 1.5 Å/s (assuming a density of 1.5 g/cm^3), and measured PES and IPES (by Antoine Kahn's group at Princeton University). The PES and IPES energy scales were aligned by measuring the position of the Fermi level of a freshly evaporated Au film. The position of the vacuum level at the surface of each film, E_{vac}, was measured using the onset of photoemission[17] to determine IP and EA. According to the results of PES and IPES measurements (Figure 3.6), IP of a film of **1** was determined to be 6.6 ± 0.1 eV using PES and the EA to be –2.8 ± 0.4 eV using IPES. One can, therefore, anticipate that the electron-withdrawing ester groups of **2** and **3** and trifluoromethyl group of **4** will lead to smaller EAs and larger IPs than those of **1**, if one assumes that solid-state aggregation has similar effects on EA and IP for each compound. Indeed, density function theory (DFT) calculations (by Jean-Luc Brédas' group) obtained gas-phase adiabatic EAs of –1.45, –1.97, –2.19, and –2.14 eV for **1**, **2b**, **3b**, and **4b** respectively, and IPs of 7.56, 7.72, 7.78, and 8.10 eV as shown in Table 3.1. The geometries of the molecules were optimized in the neutral, radical-anion, and radical-cation states using DFT. The intramolecular reorganization energies λ for the electron-exchange reaction for **3** and **4** (ca. 0.20 and 0.14 eV, respectively) were larger than that for the parent **1**/**1**$^-$ system (0.10 eV); however, they are still lower than the value estimated in the same way for Alq_3/Alq_3^- (0.26 eV[18a]) or for TPD^+/TPD (0.29 eV[19]), suggesting a low barrier for ET in **3** and **4**. The small difference in the EAs of **2** and **3** is probably due to inductive effects; in both case, the LUMO is restricted to the core and, to a lesser extent, the ester substituents, with negligible coefficient on the R groups.

Electrochemical measurements based on CVs of **1**, **2**, **3**, and **4** were carried out using solution probe molecule, ferrocene ($FeCp_2$), ca. 10^{-4} M in CH_2Cl_2/0.1 M $[^nBu_4N]^+[PF_6]^-$. The CV measurements of these compounds are also potentially complicated by the affects of aggragation[16]; however, we observed reversible reduction peaks (Figure 3.7) at the range of concentration, ca. 0.1 – 0.5 mM. Both isomers were indistinguishable by CV measurements. Table 3.2 summarizes the electrochemical potentials *vs.* $FeCp_2^{+/0}$. The first reduction potentials, $E_{1/2}^{0/-}$, at –1.44, –1.17, –1.12, and –1.12 V for **1**, **2**, **3**, and **4**, respectively. These data were consistent with the trends of EAs from the DFT calculations for isolated molecules and suggesting solid-state EAs of ca. –3.0, –3.1, and –3.1 eV for **2**, **3**, and **4**, respectively. Another way to estimate EAs is that the first reduction potentials of **2**, **3**, and **4** are compared to that of Alq_3, according to:

$$EA(compound) - EA(Alq_3) = E_{1/2}(Alq_3^{0/-}) - E_{1/2}(compound^{0/-}). \quad \text{Eq. 3.1}$$

Taking $E_{1/2}(Alq_3^{0/-}) = -2.30$ V[18b] and $EA(Alq_3) = -2.3$ eV,[18c] values of –3.4, –3.5, and –3.5 eV can be obtained for **2**, **3**, and **4**, respectively. The EA value of –3.4 eV for **2** is consisted with the value obtained by Bock.[14] The EAs of both **3** and **4** are roughly estimated as the range of –3.1 – –3.5 eV, according to the two different estimation methods. Bock et al.[14] has previously estimated IP and EA values of 6.3 eV and –3.4 eV, for alkyl ester (**2**) based on the first oxidation potential ($E_{1/2}^{ester\ +/0}$) and the optical band-gap. However, we were unable to observe oxidation waves below +2.0 V in CH_2Cl_2. Therefore, the estimation of IPs for **3** and **4** is difficult, although optical measurements (optical band-gap, $\Delta E_{op)}$ have been used to deduce the HOMO–LUMO gap. The bulk transport gap of **1** can be estimated to be (EA + IP) = 3.8 eV determined by the PES and IPES measurements. However, it is much larger than the optical band-gap of ΔE_{op} = 2.8 –

2.9 eV estimated from the absorption onset (420 – 430 nm) of **1**, **3**, and **4** in $CHCl_3$ (Figure 3.8). The both isomers were indistinguishable by absorption spectroscopy. In general ΔE_{op} is different from the true band-gap, which is the energy required for forming a free electron-hole pair, due to the Coulombic stabilization energy between the electron-hole pair and the polarization energies of the electron and hole.[20] Therefore, the energy levels of the materials could be more accurately obtained through PES and IPES measurements directly. Thus, the IPs of **3** and **4** will lead to slightly larger IPs than that of **1**, according to the DFT calculations, if one assumes that solid-state aggregation has similar effects on EA and IP for each compound.

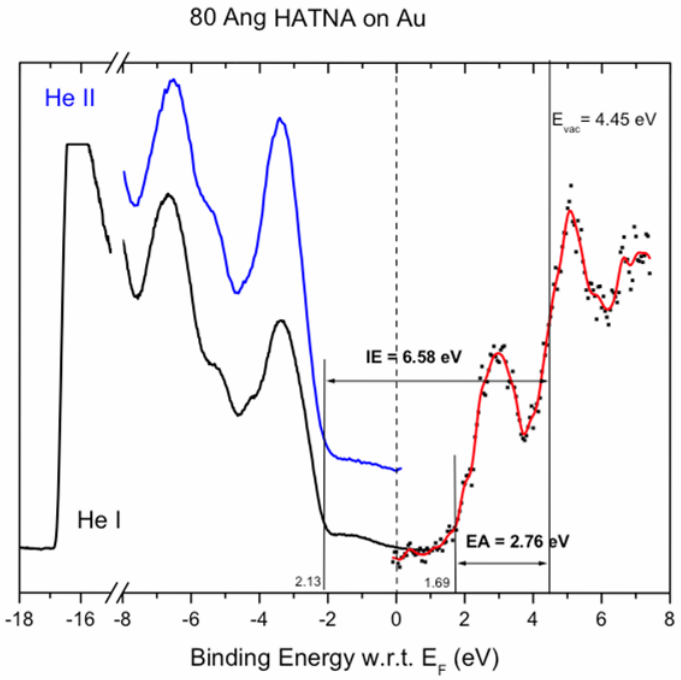

Figure 3.6 PES spectra of a film of **1** on Au using HeI (black) and HeII (blue) radiation, along with IPES spectrum of the same film (red). This data obtained from Prof. Antoine Kahn's group at Princeton University.

Table 3.1 Vertical and adiabatic electron affinities (VEA and AEA, respectively) and vertical and adiabatic ionization potentials (VIP and AIP, respectively), relaxation energies for the neutral [λ_1] and radical-anion/cation [λ_2] potential wells, and the intramolecular reorganization [λ] energy for reduction/oxidation for 1, 2b, and 3b. All energies are in eV.

(eV)	VEA	AEA	VIP	AIP	Radical-anion reorganization			Radical-cation reorganization		
					λ_1	λ_2	λ	λ_1	λ_2	λ
1	–1.40	–1.45	7.63	7.56	0.048	0.047	0.095	0.074	0.063	0.137
2b	–1.89	–1.97	7.82	7.72	0.087	0.083	0.170	0.102	0.096	0.198
3b	–2.09	–2.19	7.83	7.78	0.100	0.097	0.196	0.056	0.052	0.108
4b	–2.07	–2.14	8.19	8.10	0.068	0.071	0.139	0.091	0.091	0.182

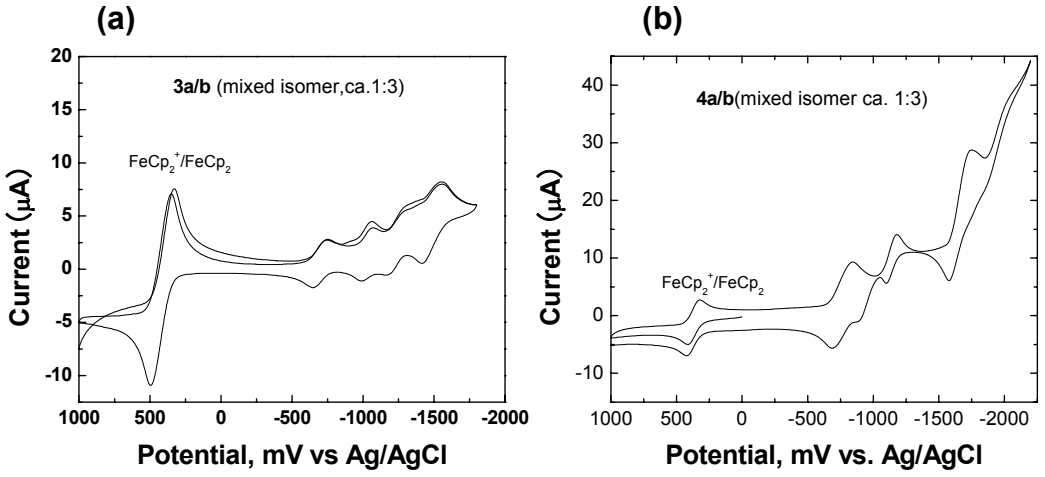

Figure 3.7 Cyclic voltammograms of (a) **3a/b** and (b) **4a/b** in dichloromethane with 0.1 M $[^nBu_4N]^+[PF_6]^-$. The potential scale is relative to a Ag/AgCl pseudo-reference electrode.

Table 3.2 Summary of electrochemical potential (±0.02 V, V vs. ferrocenium/ferrocene) for **1**, **2**, **3,** and **4** in CH_2Cl_2 / 0.1 M $[^nBu_4N]^+[PF_6]^-$.

Compounds	$E_{1/2}^{0/-}$ (V)	$E_{1/2}^{-/2-}$ (V)	$E_{1/2}^{2-/3-}$ (V)	$E_{1/2}^{3-/4-}$ (V)
1	–1.44	–1.79	–1.87	–2.20
2 (R = Et)	–1.17	–1.50	–1.95	
3a	–1.12	–1.46	–1.93	
3a/b (ca. 1:3)	–1.12	–1.45	–1.66	–1.91
3b	–1.10	–1.45	–1.89	
4a	–1.12	–1.48	–2.00	
4a/b (ca. 1:3)	–1.12	–1.48	–2.03	
4b	–1.13	–1.51	–2.03	

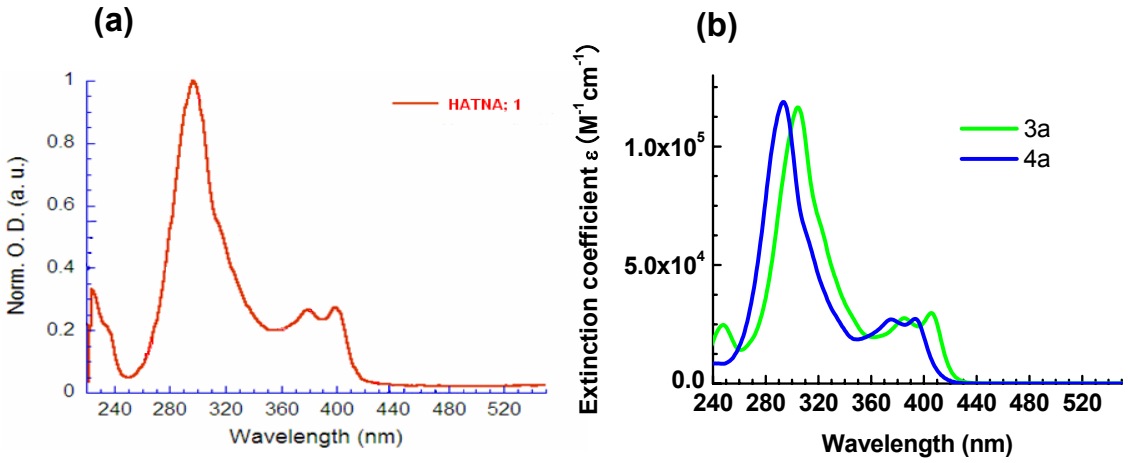

Figure 3.8 Absorption spectra of (a) parent HATNA,**1**, and (b) **3a** and **4a** in $CHCl_3$.

Table 3.3 Electronic absorption data for **1**, **3**, and **4**.

Compounds	λ_{max} / nm (log ε / M^{-1} $1cm^{-1}$)
1[*1]	295, 378, 398
3a[*2]	248(4.39), 304(5.06), 385(4.44), 406(4.47)
4a[*2]	293(5.07), 375(4.43), 3.93(4.44)

[*1] Recorded a saturated solution in $CHCl_3$ due to a low solubility.
[*2] Recorded in 1.0×10^{-5} M in $CHCl_3$.

3.4 Thermal analyses and X-ray diffraction studies

Molecular glasses have been found to show well-defined glass-transition phenomena as well as polymorphism assuming different crystalline forms depending on the history of heat treatments.[12] The formations of glassy state for **3** and **4** were confirmed by DSC, XRD, and POM. Figure 3.9 shows the DSC traces of the second heating for (a) **3a/b** (ca.1:3) and **3b**, and (b) **4a/b** (ca.1:3) and **4b**. The powder samples of **3** and **4** obtained by precipitation from a minimum amount of CH_2Cl_2 and a large amount of methanol were heated above melting points of each compound. When the isotropic liquids were cooled down on standing in air, transparent glasses were spontaneously formed *via* supercooled liquids. When these glass samples were heated again (the second heating at 10 °C/min), glass-transition phenomena, and then exothermic peaks due to crystallization to form another crystal were observed. For example, the second heating of **3a/b** (ca.1:3) showed a glass-transition at 117 °C, and then an exothermic peak due to crystallization to form crystal X_1 at 147 °C. Thereafter, an exothermic peak due to solid-solid phase transition from the crystal X_1 to crystal X_2 was observed at around 188 °C,

followed by the melting of the crystal X_2 at 252 °C. The same DSC traces were reproduced repeatedly. Such the phenomena of polymorphism observed for many molecular glasses suggest the existence of different conformers, which is responsible for the ready formation of the glassy state.[12a] Therefore, it is suggested that the incorporation of the mixture of **a** to **b** isomers increases the number of conformers or the mode of packing of molecules, preventing crystallization, and facilitating glass formation. Indeed, the melting points, T_m, of the isomer mixtures of **3** and **4** were lower than those of the pure isomers in the order **a/b** < **b** < **a**. In contrast, the same glass-transition temperatures, T_gs, were observed between **a/b** and **b** at 117 °C and 138 °C for **3** and **4**, respectively. It can be rationized by the understanding of T_g as the temperature at which molecular motions of particularly substituted groups are starting, which are caused by intramolecular bond rotations, resulting in a change in the center of the gravity of molecules. Thus, the T_gs of **a** and **b** should be identical. To apply molecular glasses for electronic and optoelectronic devices, high T_g materials are required for thermal stability. The T_gs of **3** and **4** are relatively high compared to well-known amorphous compounds such as TPD (ca. 60 °C at scan rate 5 °C/min[34]). Therefore, they may be promising amorphous materials for electronic and optoelectronic devises. The T_g and other transition temperatures of the pure isomer **a** for both **3** and **4** could not be determined due to the onset of decomposition at the melting points used in the first heating process. The onset of decomposition temperatures of 320 °C and 355 °C for **3a** and **4a** were observed in thermal gravity analyzer (TGA) traces, which are almost same temperature of T_m for each of the compounds (Figure 3.10). Table 3.4 summarizes T_g, crystallization temperature, T_c, and T_m of **3** and **4**.

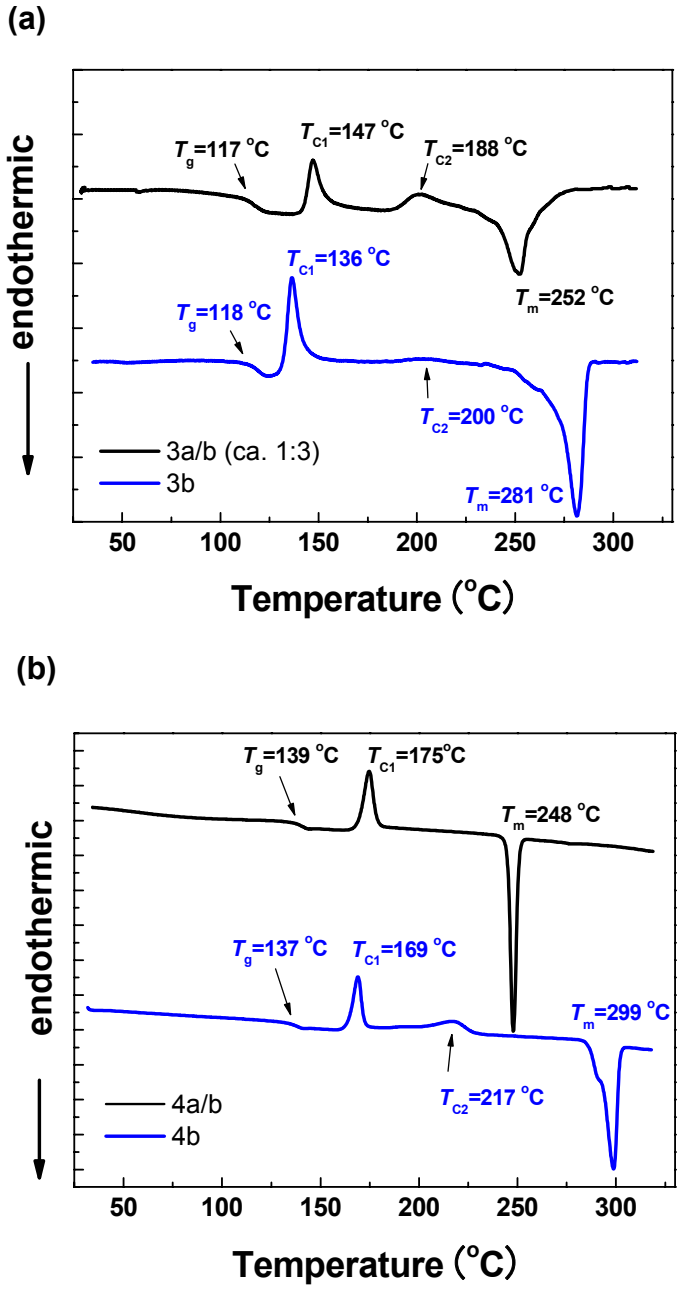

Figure 3.9 DSC traces of the second heating for (a) **3a/b** (ca.1:3, solid line) and **3b** (dashed line), (b) **4a/b** (ca.1:3, solid line) and **4b** (dashed line). All measurements were carried out with heating rate of 10 °C/min

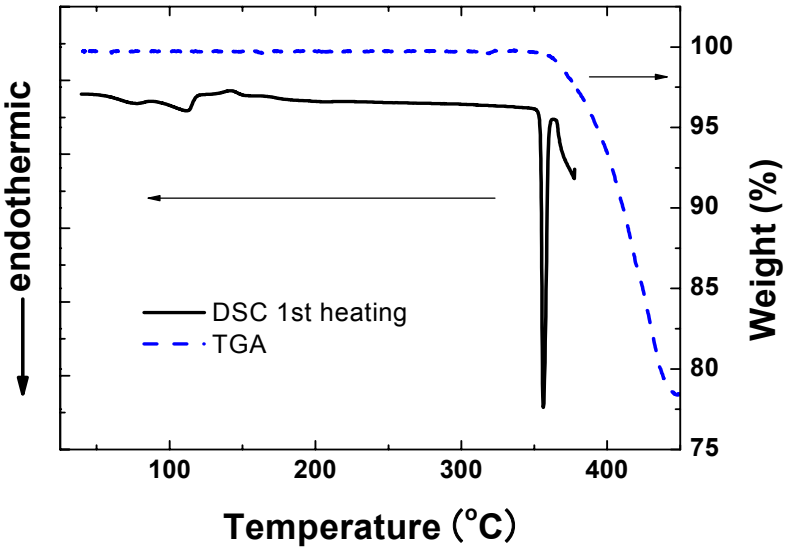

Figure 3.10 DSC trace of the first heating (black solid line) and TGA trace (blue dashed line) for **4a**.

Table 3.4 Glass-transition temperatures (T_g), crystallization temperatures (T_c), and melting points (T_m) of the compounds **3** and **4**.

Compound	T_g (°C)	T_{c1} (°C)	T_{c2} (°C)	T_m (°C)
3a	---[a]	---[a]	---[a]	320[b]
3a/b (ca.1:3)	117	147	188	252
3b	118	136	200	281
4a	---[a]	---[a]	---[a]	356[b]
4a/b (ca.1:3)	139	175		248
4b	137	169	217	299

[a] The second heating could not carry out due to a decomposition during the first heating.
[b] Estimated from the first heating.

The thin films of the isomer mixture **a/b** and the pure isomer **b** for both **3** and **4** were prepared by cooling from the isotropic liquids between two ITO-coated glass slides with calibrated glass spacers. Figure 3.11 shows the XRD data and the POM images of the **3a/b** (ca.1:3) and **3b** thin films prepared by a fast cooling rate (ca. 100°C/min). It should be noticed that this cooling rate consists with the cooling rate between the first and second heating in DSC measurements. In the **3a/b** (ca.1:3) film, no diffraction peaks in the X-ray pattern and no textures under POM are observed. Theses results indicate that the **3a/b** (ca.1:3) film should be amorphous. In addition, the film showed no evidence of crystallization after storage at room temperature for 18 months. In the **3b** film, weak diffraction peaks in the X-ray pattern and a distinct texture under POM are observed. The **3b** film probably has a polycrystalline phase coexisting isotropic and crystalline phases due to the difficulty of maintaining a supercooled liquid-state. The similar results as **3a/b** (ca.1:3) and **3b** are observed in the films of **4a/b** (ca.1:3) and **4b** (Figure 3.12). However, few bright spots presumably due to a crystalline texture are observed in the **4a/b** (ca.1:3) film as shown in the POM image, although the X-ray pattern shows the absent of diffraction peaks. According to the DSC data and the POM observation, the isomer mixture, **4a/b** (ca.1:3), does not readily form an isotropic film presumably due to the higher T_g and the less polymorphism (the absent T_{c2}) compared to **3a/b** (ca.1:3).

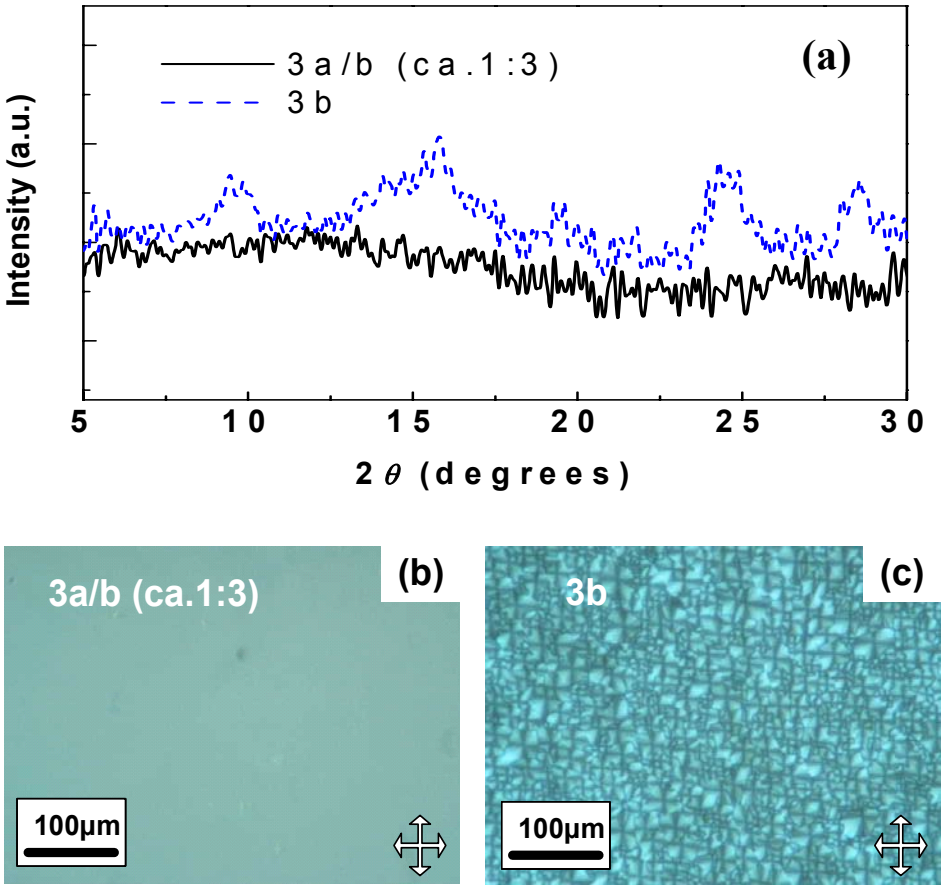

Figure 3.11 (a) X-ray diffraction at room temperature of the rapidly cooled (ca. 100 °C/min) films of **3a/b** (ca.1:3) and **3b** on glass (background due to glass subtracted and data smoothed). Panels (b) and (c) are cross-polarized optical microscopy images of the same samples.

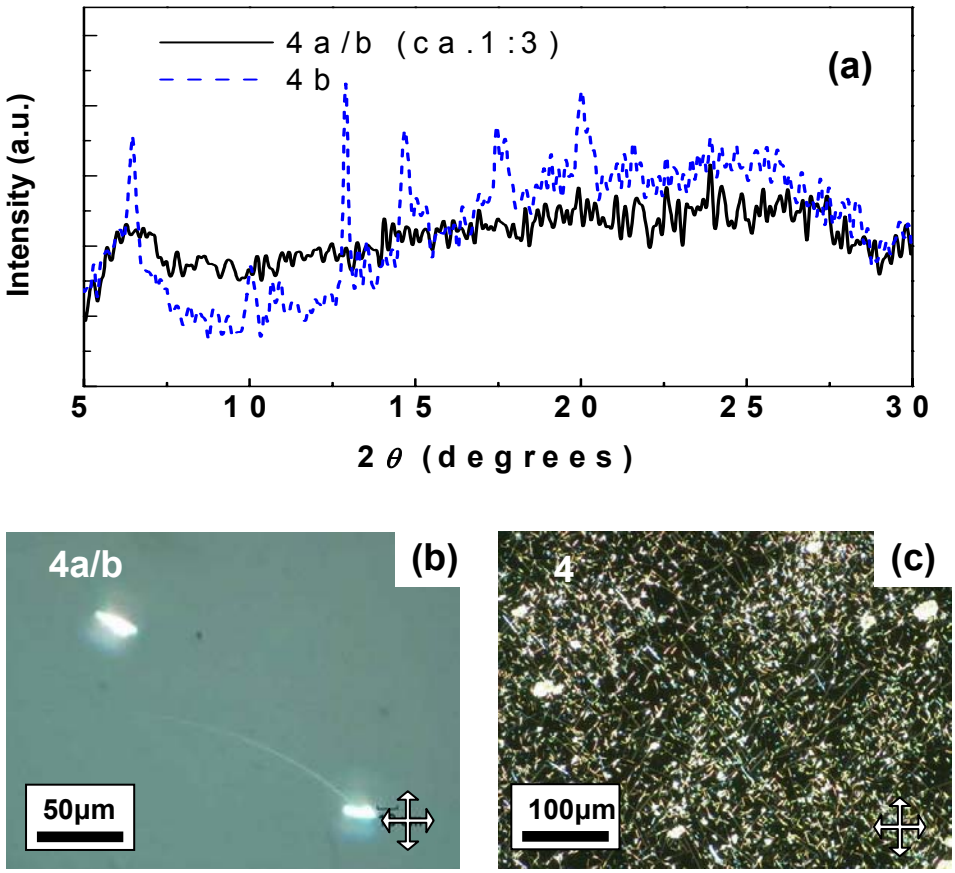

Figure 3.12 (a) X-ray diffraction at room temperature of the rapidly cooled (ca. 100 °C/min) films of **4a/b** (ca.1:3) and **4b** on glass (background due to glass subtracted and data smoothed). Panels (b) and (c) are cross-polarized optical microscopy images of the same samples.

3.5 Influence of cooling rate on film morphologies of pure isomer b

The influence of the cooling rates from isotropic liquids on film morphologies of **3b** and **4b** were investigated. In contrast to the rapidly cooled film of **3b**, the formation of well-ordered spherulites nucleated randomly over the whole sample is observed in the slow cooled (ca. 10 °C/min) film (Figure 3.13b). Spherulites are an ubiquitous form of crystal aggregate characterized by radial growth leading to spherical symmetry that can be observe in a wide range of different materials.[21] However, reports of spherulite formation of discotic systems have been rare especially for discotic materials possessing high melting points over 250°C.[22] The spherulites of **3b** revealed high anisotropy under the cross-polarizers expressed by a "Maltese cross" [21a] pattern, where the isogyres followed the extinction of the analyzer/polarizer direction. The POM image indicates that the film may be a coherent long-range order. The analysis using a first order retardation plate (λ = 530 nm) of the POM image of the **3b** spherulites shows the blue color distribution parallel to the fast axis of the retardation plate and the yellow color distribution parallel to the slow axis of the retardation plate (Figure 3.13c). It probably indicates that the spherulites are optically negative, which the refractive index parallel to the radial direction is smaller than that perpendicular to it. Consequently, the discotic columns would be oriented in the spherulite growth (radial) direction with an edge-on arrangement of the molecules. In addition, the X-ray pattern of the spherulites (Figure 3.13a) shows stronger diffraction peaks at low angles (2θ = 3.3°, 5.3°, 9.7°, and 15.8°) than those of the film prepared by the rapid cooling (ca. 100 °C/min). However, the intensities of diffraction peaks at high angles (2θ = 24.6° and 28.6°) are almost same between the two films. Although it is necessary a further detail analysis to understand this

result, it may support that the molecular orientation is dominantly edge-on arrangement in the spherulitic texture.

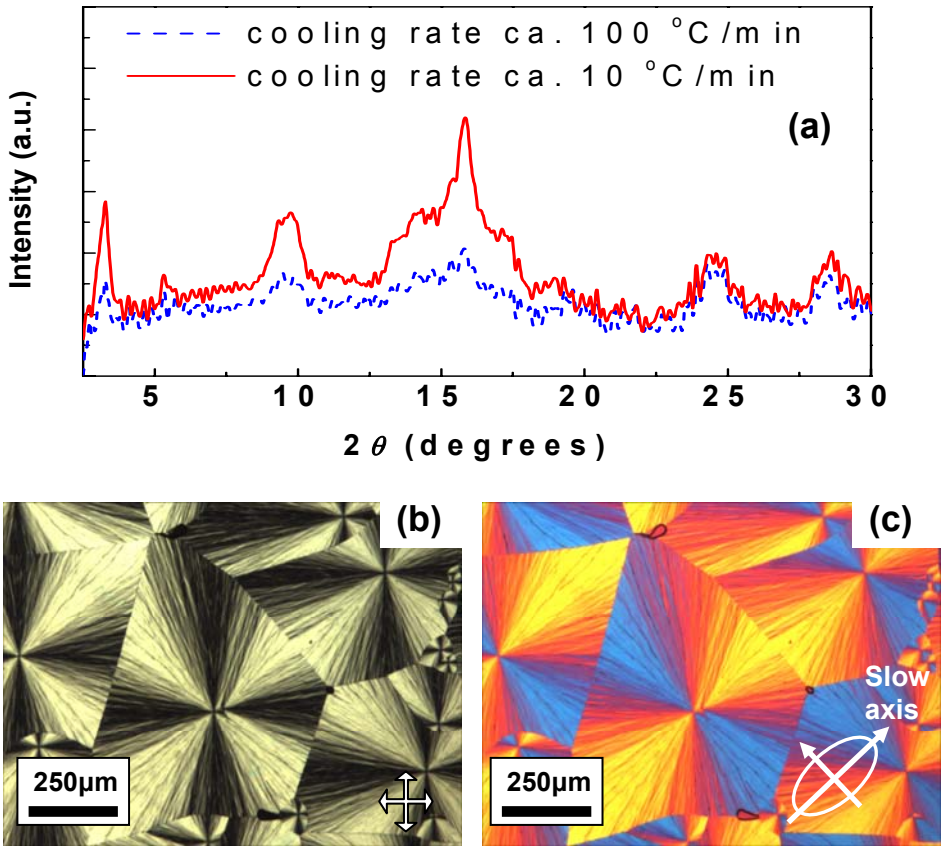

Figure 3.13 (a) X-ray diffraction at room temperature of the rapidly cooled (ca. 100 °C/min, blue dash line, same sample in Figure 3-11) and slow cooled (ca. 10 °C/min, red solid line) films of **3b** on glass (background due to glass subtracted and data smoothed). Panel (b) is cross-polarized optical microscopy images of the slow cooled film. Panel (c) is the same sample (b) using a retardation plate (530 nm).The inset arrows represent the slow and fast axis of retardation plate.

The investigation of the kinetically growth spherulites with different cooling rates from the isotropic liquids reveals that the sizes of spherulites are increased with slower cooling rates. The many crystal nucleuses randomly located in the films are observed in

the samples of relatively fast cooling rates (Figure 3.14a and b). The slower cooling rates can form large spherulites with specific arrangement from crystal nucleus. In the film prepared by the slowest cooling rate of 1.0 °C/min, large spherulites having the diameter exceeding few micrometers were obtained (Figure 3.14d).

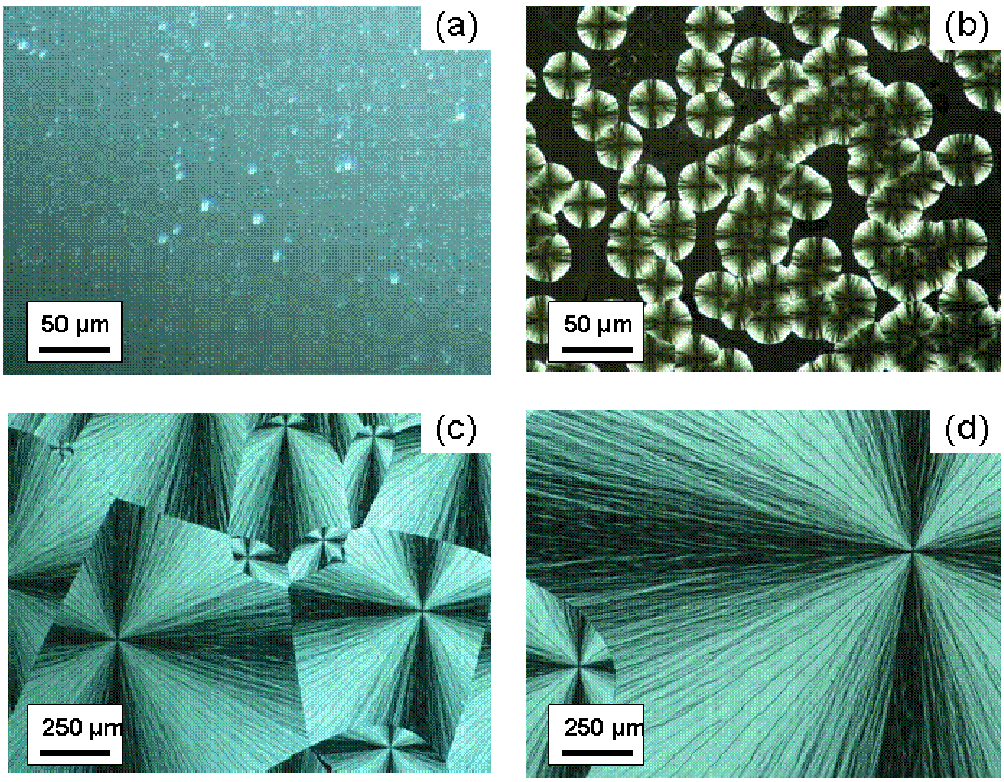

Figure 3.14 Cross-polarized optical microscopy images of **3b** films, (a) solidification from isotropic liquid with 100 °C/min cooling rate; (b) with 60 °C/min cooling rate; (c) with 10 °C/min cooling rate; (d) with 1.0 °C/min cooling rate. All samples were allowed to solidify between two glass slides or ITO glasses.

The interesting self-organization behavior of **3b** with the directional crystal growth, suggested the use of crystallizations with temperature-gradient such as zone-crystallization technique [21b, 22b] to obtain macroscopically ordered structures for possible application in electronic devices. Indeed, the investigation of edge part of texture

indicated that there was relatively unidirectional crystal growth in where would be expected long-range uniaxially ordered column growth (Figure 3.15) presumably due to a temperature-gradient between the edge and center of the sample. Such high ordered self-organization behavior over long-range and columns is a promising candidate as an organic semiconductor material for the FETs due to the edge-on arrangement of the molecules. It is possible to control the direction of charge transporting and the channel direction between source-drain electrodes.

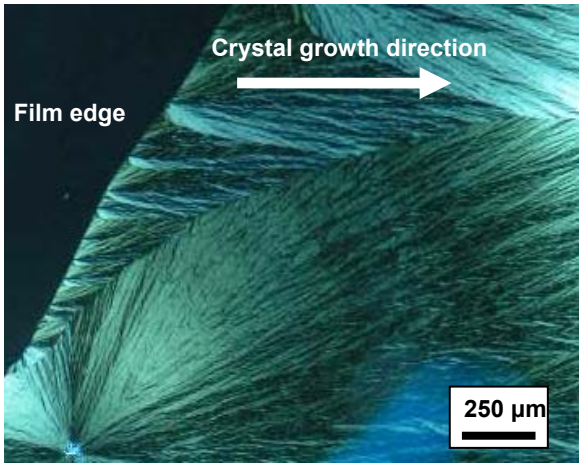

Figure 3.15 Cross-polarized optical microscopy images of **3b** films cooled from the isotropic liquid with the rate of 10 °C/min.

In contrast to **3b**, when **4b** was cooled slowly; i.e. cooling rate of 10 °C/min from the isotropic liquid, fan-shaped (Figure 3.16c) and strand-shaped (Figure 3.16d) textures were observed, which depend on film thickness. Usually fan-shaped textures were observed in thick films (ca. 5µm), and the strand-shaped textures were observed in thin films (ca. 800nm). Interestingly, the strand-shaped textures with the length of few hundreds micrometers and the width of few tens micrometers, show a strong optical anisotropy and a blue color distribution parallel to the slow axis of the retardation plate

(Figure 3.16d). Presumably, it suggests that the strand-shaped textures are optically positive in where the refractive index along to the long axis of textures is higher than that perpendicular to it. Consequently, the discotic columns would be oriented perpendicular to the long axis of textures with an edge-on arrangement of the molecules.

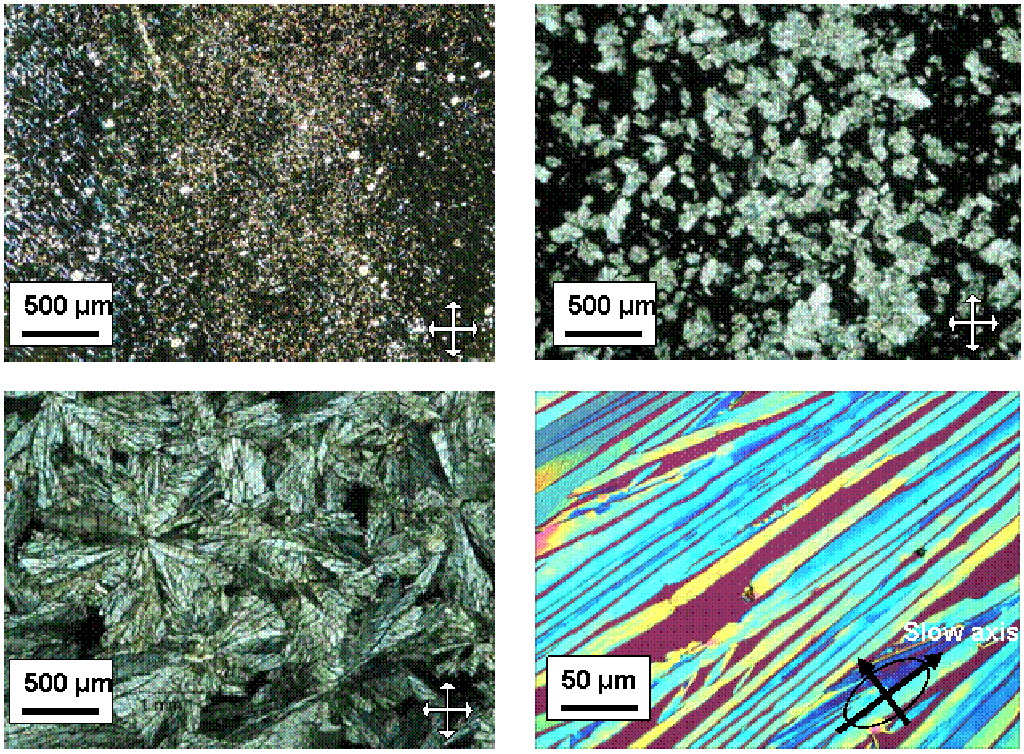

Figure 3.16 Cross-polarized optical microscopy images of 5 µm films for **4b**, (a) solidification from isotropic liquid with 95 °C/min cooling rate; (b) with 55 °C/min cooling rate; (c) with 10 °C/min cooling rate; (d) same condition as (c) except for the film thickness (ca. 800 nm). All samples were allowed to solidify between two glass slides or ITO glasses.

3.6 Charge transport properties

The charge transport properties of compound **3** and **4** have been studied by using the *I–V* characteristics as described in Chapter 2, which utilizing the empirical expression (Eq. 2.10[26] in Chapter 2) of the space-charge limited current density taking account into Poole-Frankel type field dependence of the mobility.[23,24]

Figure 3.17 shows the *I-V* characteristics at room temperature for the device geometry of ITO(+)/**3a/b** (ca.1:3), 5μm/ITO(–). One can observe the initial linear dependence of the current density with a slope 1.18, characteristic of an ohmic conduction[25], followed by a slightly larger than quadratic dependence of the current density of the power 2.28 characteristic of the SCLC regime at higher applied voltage. A zero-field mobility of $\mu_0 = 0.011$ cm^2/Vs and a coefficient of field-dependence of $\gamma = 1.8 \times 10^{-3}$ (cm/V)$^{1/2}$ were extracted. An effective mobility of 0.032 cm^2/Vs at $V/d = 4.0 \times 10^3$ V/cm was obtained. This effective mobility is same order as the highest reported for amorphous molecular materials.[12,28] It is interesting to point out that the calculated values of $\gamma \sim 10^{-3}$ (cm/V)$^{1/2}$ are comparable to that of typical doped amorphous films such as triphenyldiamine (TPD) doped into polystyrene,[24] and the effective mobility of the **3a/b** (ca.1:3) film is one order of magnitude higher than that of pure TPD (10^{-3} cm^2/Vs at $E = 10^5$ V/cm at room-temperature).[27]

The energy levels, LUMO (3.1 – 3.5 eV) and HOMO (≥ 6.6 eV), of compounds **3** and **4** were estimated by the solid-state EAs of **1** or Alq_3 and their first reduction potential based on electrochemical experiments. The work function of Ag (4.2 eV) is closer to the LUMO level of these materials than ITO (in this work ITO electrodes were not treated by air-plasma treatment. The work function of ITO was estimated as 4.5 – 4.8 eV), thus

electron injection from Ag into the LUMO of **3** is expected to be more efficient than from ITO. Therefore, a larger effective mobility would be derived from the device with Ag as the cathode than from the device with ITO as the cathode. However, no significant deference of *J-V* curves between the **3a/b** (ca. 1:3) devices using Ag and ITO cathodes was observed (Table 3.4). According to the literature,[34] exposure to oxygen can induce a shift in a band alignment at metal/organic interfaces. For example, for a porphyrin/Ag interface, this shift in the effective work function of the metal is 0.7 eV further from vacuum.[34a] We suspect that the experimental conditions, in which the devices were exposed ambient conditions and heated at ca. 280 °C for few minutes to melt compounds, may affect the effective work function of Ag electrode. Therefore, we used ITO electrodes as both anode and cathode for further experiments. Even though using ITO cathode, the energy barrier for hole injection from the anode (ITO, 4.5 – 4.8 eV) into the HOMO (≥ 6.6 eV) level of these materials is significantly higher than that for electron injection. Hence, the majority of the charge carriers injected into and transported through **3** and **4** films are predicted to be electrons. If the effective mobility of **3a/b** film is assumed as an electron mobility, the value of 10^{-2} cm^2/Vs will be the highest value in ET amorphous molecular materials.[12,28]

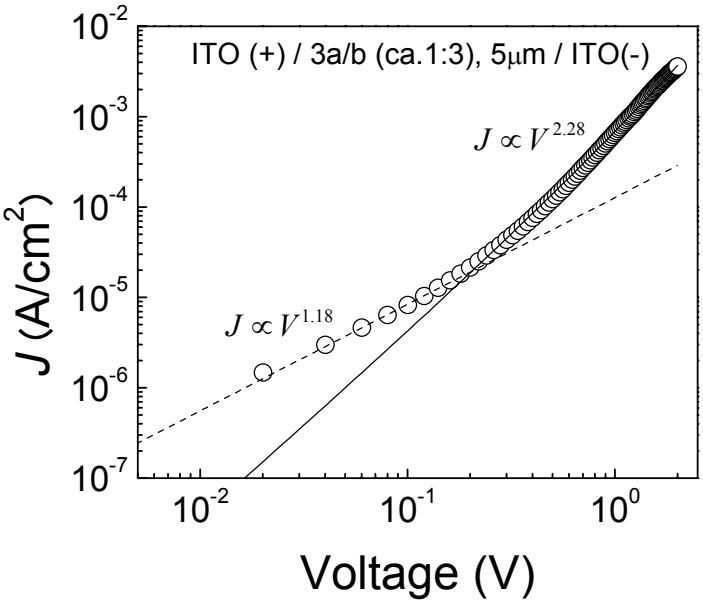

Figure 3.17 Typical *I-V* characteristics of ITO(+)/**3a/b** (ca.1:3) (5 μm)/ITO(–) device at room temperature. The solid line and dashed line represent the predictions from the SCLC model characterizing the field-dependent mobility in Eq. 2.10 and from ohmic conduction, respectively.

The dependence of *I-V* characteristics on film-morphology of **3b** was investigated. Figure 3.18 shows the comparison of the *J-V* curves between the rapid cooled film (ca. 100 °C/min) and the relatively slow cooled film (10 °C/min). As mentioned before, the crystalline texture and the spherulite (diameter: few hundreds micrometer) texture were observed in the rapid cooled film and the slow cooled film, respectively, as shown in the panels of Figure 3.11c and Figure 3.13b. The current densities at whole voltage range of the device with rapid cooled film are two orders of magnitude higher than those of the device with slow cooled film. The zero-field mobilities of $\mu_0 = 0.045$ cm^2/Vs and $\mu_0 = 0.001$ cm^2/Vs, and the coefficients of field-dependence of $\gamma = 2.4 \times 10^{-3}$ (cm/V)$^{1/2}$ and $\gamma =$

5.6×10^{-3} $(cm/V)^{1/2}$ were extracted from the rapid and slow cooled films, respectively. The effective mobilities of 0.050 and 0.0014 cm^2/Vs at the average field of V/d = 0.5 $\times 10^4$ V/cm were obtained from the device with rapid cooled film and slow cooled film, respectively. The one of possible reasons for the poor transport properties in the slow cooled film (spherulite textures) is the different molecular orientation. The molecular orientation of **3b** in spherulites is presumably along the crystal growth or radial direction with an edge-on arrangement of the molecules. Thus, this molecular orientation should be less favorer to the charge transporting in the direction between ITO electrodes, which is normal to in the crystal growth direction. On the other hand, the rapid cooled film is assumed as a polycrystalline or a film aggregated by small spherulites. In such as film, the molecular orientation should be more random. Another possibility is mere the issue of film quality. Many cracks along the grain boundaries were observed in the spherulites.

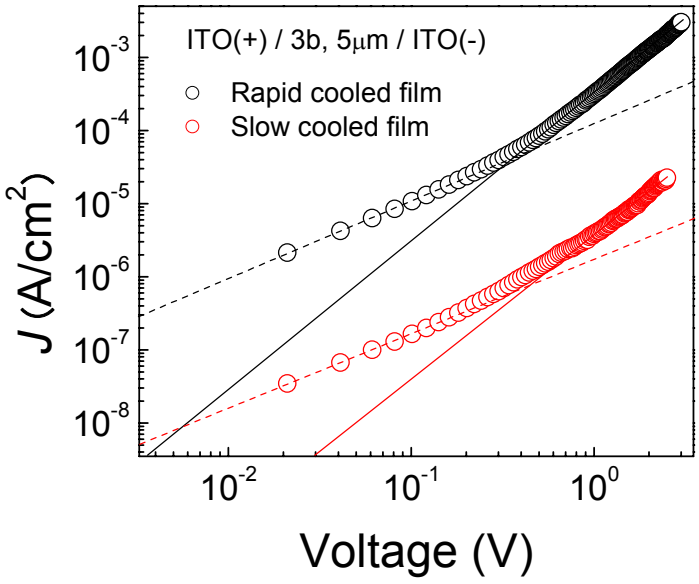

Figure 3.18 Typical *I-V* characteristics of the rapid cooled film (ca. 100 °C/min, black open-circle) and the slow cooled film (ca. 10 °C/min, red open-circle) of **3b** with the device geometry of ITO(+)/**3b** (5 μm)/ITO(–) at room temperature. The solid lines and dashed lines represent the prediction from a SCLC model charactering the field-dependent mobility of Eq. 2.10 and from an ohmic conduction, respectively.

Figure 3.19 shows the comparison of the *I-V* characteristics between **4a/b** (ca.1:3) and **4b** films prepared by rapid cooling rate (ca. 100 °C/min). The *J-V* curves of both devices were similar; the zero-field mobilities of $\mu_0 = 2.0 \times 10^{-3}$ cm^2/Vs and $\mu_0 = 53.6 \times 10^{-3}$ cm^2/Vs, the coefficients of field-dependence of $\gamma = 11.2 \times 10^{-3}$ (cm/V)$^{1/2}$ and $\gamma = 9.7 \times 10^{-3}$ (cm/V)$^{1/2}$, and the effective charge mobilities of 4.0×10^{-3} (at an average field of $V/d = 0.4 \times 10^4$ V/cm) and 7.6×10^{-3} cm^2/Vs (at an average field of $V/d = 0.6 \times 10^4$ V/cm) were obtained from the device with **4a/b** (ca.1:3) and **4b**, respectively. *I-V* characteristics of the slow cooled film of **4b** were also carried out; however, they could not obtain sufficient SCLC regime due to a poor contact caused by delaminating from ITO electrodes. The effective mobilities of the **4** films were one order of magnitude lower

than films of **3** films (depending on cooling rates). Although the reason is obscure, we predict that the lower mobilities of **4** is caused by a poor film quality wherein cracks occurring around the crystalline domains present as shown in Figure 3.12. Another interesting point is that larger effective mobilities were observed on the rapid cooled films of the isomer **b** instead of the isomer mixture **a/b** for both **3** and **4**. Although, due to the different techniques employed, the mobilities for **3** and **4** can not be directly compared to the high mobilities reported HATNAs in ref 16, it is interesting to note that in both cases the highest mobilities were observed on films showing at least some crystallinity.

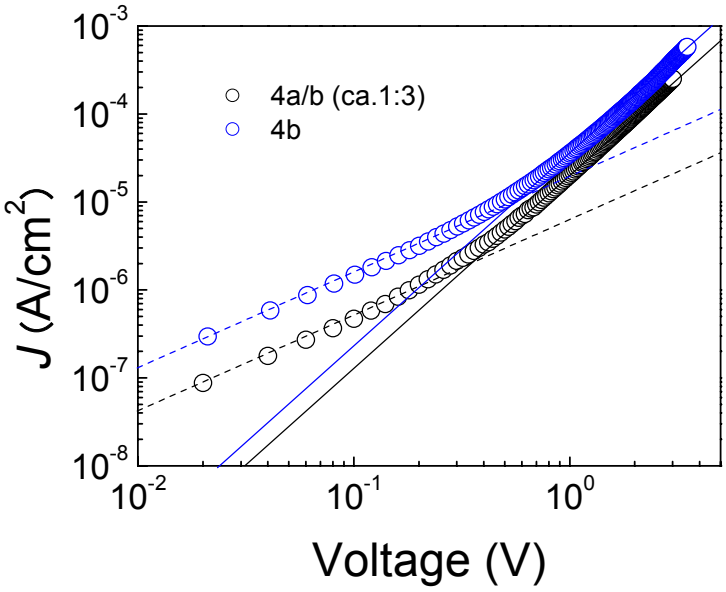

Figure 3.19 Typical *I-V* characteristics of ITO(+)/**4a/b** (ca. 1:3) (5 μm)/ITO(–) devices (black open-circles) and ITO(+)/**4b** (5 μm)/ITO(–) devices (blue open-circles), at room temperature. The both films were obtained by the rapid cooling (ca. 100 °C/min) from the isotropic liquid of each compound. The solid lines and dashed lines represent the prediction from a SCLC model charactering the field-dependent mobility of Eq. 2.10 and from an ohmic conduction, respectively.

The pure isomer **a**s of both **3** and **4** are not available for the film preparation method using the cooled film from isotropic liquid of materials due to the decomposition and the strong tendency to crystallize and to delaminate from electrodes. Table 3.5 summarizes the carrier mobility characteristics for the compound **3** and **4**.

Table 3.5 Summary of the carrier mobility characteristics at room temperature for films of **3** and **4**.

Materials	Expected film morphology	cathode	Thickness, d (μm)	μ_0 (cm^2/Vs)	γ $(cm/V)^{1/2}$	$(V/d)_{max}$ (V/cm)	μ_{eff} (cm^2/Vs) at $(V/d)_{max}$
3a/b[(1)] (ca. 1:3)	amorphous	ITO	5	0.012	1.7×10^{-3}	3.1×10^4	0.017
3a/b[(2)] (ca. 1:3)	amorphous	Ag	5	0.017	1.1×10^{-3}	2.8×10^4	0.021
3a/b[(3)] (ca. 1:3)	amorphous	ITO	5	0.010	1.2×10^{-3}	0.4×10^4	0.032
3b[(2)]	crystalline	ITO	20	0.056	2.5×10^{-3}	0.7×10^4	0.071
3b[(3)]	crystalline	ITO	5	0.045	2.4×10^{-3}	0.6×10^4	0.054
3b[(3)]	spherulite	ITO	5	0.001	5.6×10^{-3}	0.5×10^4	0.001
3a[(3)]	crystalline	ITO	5	----	----	----	----
4a/b[(1)] (ca. 1:3)	crystalline	ITO	5	0.001	4.7×10^{-3}	0.5×10^4	0.003
4a/b[(2)] (ca. 1:3)	crystalline	ITO	5	0.002	11.2×10^{-3}	0.4×10^4	0.004
4b[(2)]	crystalline	ITO	5	0.004	9.7×10^{-3}	0.6×10^4	0.008
4a[(2)]	crystalline	ITO	5	----	----	----	----

[(1)] the product from first reaction batch
[(2)] the product from second reaction batch
[(3)] the product from third reaction batch

3.7 Concluding remarks

HATNA derivatives substituted by three electron withdrawing pentafluoro-phenylmethyl ester (**3**) and trifluoromethyl (**4**) were synthesized and separated as the symmetrical (C_{3h}) 2, 8,14-isomer **a**, the less symmetrical (C_s) 2,8,15-isomer **b**, and their mixtures (**a**:**b** = ca. 1:3). The presence of two isomers can have important implications for film morphology and effective mobility. The statistical isomer mixture could form an amorphous film, particularly the films of isomer mixture, **3a/b** (ca. 1:3), obtained by the rapid cooling (ca. 100 °C/min) from the isotropic liquid showed the excellent storage stability for 18 months at room temperature. The cooled film of **4a/b** (ca. 1:3) under the same conditions as **3a/b** (ca. 1:3) showed a stronger tendency to crystallize than those of **3a/b** (ca. 1:3). The amorphous films of the isomer mixture, **3a/b** (ca. 1:3), showed an effective mobility with the range of 10^{-2} cm^2/Vs that is same as the order of the highest reported for molecular glasses. The films of **4a/b** (ca. 1:3) showed the effective mobility with the range of 10^{-3} cm^2/Vs. In contrast, films of the pure isomers, 2,8,14-isommer, **a**, and 2,8,15-isomer, **b**, showed strong tendencies to crystallize; the **b** films of both **3** and **4** can exhibit widely differing morphologies and carrier mobilities depending critically on the processing conditions. Under the same condition for the film preparation, the pure isomer **b** of both **3** and **4** showed the higher effective mobilities than those of the isomer mixtures. These results suggest that these materials may be promising active components of electronic and optoelectronic devices, due to the potential to control morphologies and mobilities by changing the isomer ratio.

3.8 Experimental

General: The tris (acid chloride) **5** (shown in scheme 1) and the tris (ethylester) **2** (R = Et) were synthesized according to a literature procedure.[14] All chemicals were purchased from Aldrich and used as received. The ^{1}H, ^{13}C, and ^{19}F NMR spectra were taken on Varian 300 MHz or Bruker 500 MHz spectrometer using tetramethylsilane (TMS; $\delta = 0$ ppm) as an internal standard for standard ^{1}H and ^{13}C NMR, and using trifluoromethylbenzene as an external standard for ^{19}F NMR. MALDI mass spectra were obtained on an Applied Biosystems 4700 Proteomics Analyzer. Flash column chromatography was performed on silica gel (32-63 μm, 60 Å, Sorbent Technologies). Elemental analyses were carried out by Atlantic Microlads using a LECO 932 CHNF elemental analyzer. UV-Vis absorption spectra were recorded on a Varian Cary 5E UV-Vis-NIR spectrophotometer using photospectroscopic grade solvents. Extinction coefficients were measured with concentration in the range of 10^{-5} M. Electrochemical measurements were performed under nitrogen on deoxygenated solutions of tetra-n-butylammonium hexafluorophosphate (0.1 M) in methylene chloride with ferrocene as an internal standard using a computer-controlled BAS 100B electrochemical analyzer, a glassy-carbon working electrode, a platinum-wire auxiliary electrode, and a Ag wire anodized with AgCl as a pseudo-reference electrode. Potentials were referenced to the ferrocenium/ferrocene ($FeCp_2^+/FeCp_2$) couple. The PES and IPES measurements were performed by Prof. Antoine Kahn group at Princeton University. The measurements were carried out in a multi-chamber ultra-high vacuum system comprising a growth chamber with organic evaporation stations and quartz-crystal flux monitor connected to a surface analysis chamber equipped with PES and IPES. The four materials were loaded in

separate PBN crucibles in the growth chamber. The substrates were Si wafers covered with a 50 Å Ti layer (for adhesion) and a 1200 Å Au layer. Prior to insertion in vacuum, the substrates were degreased by boiling in trichloroethylene, and rinsed in acetone and methanol. Films of **1** with thickness ranging from 20-50 Å were deposited on the Au surface at a rate of 1.5 Å/s (assuming a density of 1.5 g/cm^3) and transferred to the analysis chamber. PES was performed using the standard He I (21.22 eV) and He II (40.8 eV) photon lines from a He discharge lamp, and a cylindrical mirror analyzer, giving an experimental resolution of 150 meV. IPES was carried out in the isochromat mode using a fixed-photon-energy detector centered at 9.2 eV[29] and a Kimbal Physics electron gun, giving a combined resolution of 500 meV. The IPES electron-beam current density was limited to 1 μA/cm^2 to minimize degradation of the organic material. In all cases, PES was carried out first on the fresh film, and repeated after the IPES measurement to assess electron-beam-induced degradation. The PES and IPES energy scales were aligned by measuring the position of the Fermi level of a freshly evaporated Au film. The position of the vacuum level at the surface of each film, E_{vac}, was measured using the onset of photoemission to determine IP and EA. In accord with the *ad-hoc* procedure widely accepted in the literature,[30] the experimental values of adiabatic IP and EA are taken as the energy difference between E_{vac} and the *leading edge* of the HOMO and LUMO feature, respectively. The DFT calculations were performed by Jean-Luc Brédas group at Georgia Institute of Technology. The calculations were carried out using the B3LYP functional, where Becke's three-parameter hybrid exchange functional is combined with the Lee-Yang-Parr correlation functional,[31] with a 6-31G** split valence plus polarization basis set. All DFT calculation were performed with Gaussian98(revision A.

11).[32] DSC traces were taken on a SHIMADZU DSC-60 instrument at 10 °C/min. XRD data was collected on a Scintag X1 diffractometer with a Cu Kα source (λ = 1.5406 Å) in a continuous scan mode with a step size of 0.02 degree. POM images were obtained using an Olympus BX51 microscope equipped with an Olympus U-TU1 X digital camera and an Instec ST200 temperature controller. SCLC measurements were performed by measuring the steady-state current-voltage chrematistics with a Keithley 2400 source meter on samples prepared by cooling from the isotropic liquid of the materials between two glass-supported electrodes and the thickness of the sample was controlled by calibrated glass spacers. In the case using pre-coated ITO glass substrates, ITO substrates were washed with detergent, de-ionized water, ethanol, and acetone. The capacitance of the devices were measured using an Agilent 16048A test leads connected to a Agilent 4284A precision LCR meter and found between 100 pF and 375 pF depending on the area and thickness. The device fabrications and characteristics were carried out in ambient conditions.

5,6,11,12,17,18-Hexaaza-trinaphthylene-2,8,14-tricarboxylic acid tri (pentafluoro-phenylmethyl ester) and 5,6,11,12,17,18-Hexaaza-trinaphthylene-2,8,15-tricarboxylic acid tri (pentafluoro-phenylmethyl ester), 3. The tris (acid chloride), **5**, (2.0 g, 3.5 mmol) was suspended in 15 mL of THF and pentafluorophenyl-methanol (15.0 g, 75.7 mmol) was added. Pyridine (15.0 mL) was slowly added to the reaction mixture, which was stirred at 50 °C for 72 h. Solvent was evaporated under reduced pressure. The resulting solid was purified using a short column of silica gel and dichloromethane as eluent. The solvent was evaporated and the resulting solid was

further purified by column chromatography using dichloromethane: ethyl acetate (9:1) as eluent, followed by solvent evaporation. The obtained solid was dissolved in 30 mL of $CHCl_3$ and was precipitated with 60 mL of MeOH to yield 1.78 g of crude **3a/b** mixture (yield 46 %, ca. 1:3 mixture). The ratio of isomer mixtures were estimated by HPLC analysis. Three recrystallizations from dichloromethane allowed for isolation of the pure 2,8,14- isomer, **3a**, as a yellow solid, 0.7 g, 39 % yield (from crude product). The supernatant from the first recrystallization was evaporated, and resultant solid was dissolved in the minimum amount of chloroform and was precipitated with 300 mL of MeOH to yield the yellow solid that was shown to be 2,8,14-isomer : 2,8,15-isomer (ca. 2:1) **3a/b** mixture. To obtain the pure 2,8,15- isomer, **3b**, careful column chromatography was performed on the crude product (2.38 g, yield 35%, ca. 1:3 mixture) of another reaction batch using dichloromethane / ethyl acetate (9:1) as eluent. After solvent evaporation, the compound was dissolved in 10 mL of $CHCl_3$ and was then reprecipitated in 300 ml MeOH yielding a solid (1.19 g, 50% yield from crude product).

[3a/b ca. 1:3]. ^{1}H NMR (300 MHz, 1.8×10^{-3} mol / L, $CDCl_3$) δ 9.42-9.41 (m, 3H), 8.78 & 8.76 (two br singlets, 3 H), 8.65 (quartet, J = 2 Hz, 2H), 8.63 (quartet, J = 1.5 Hz, 1H), 5.59 & 5.58 (two br singlets, 6H). ^{19}F NMR (376 MHz, 1.8×10^{-3} mol / L, $CDCl_3$) δ (−141.72)–(−141.92) (m, 6F), (−151.82)–(−152.12) (m, 3F), (−161.22)–(−161.50) (m, 6F). ^{19}F NMR Chemical shifts are relative to trifluoromethylbenzene which was used as an external standard. MALDI-TOF MS: *m/z* 1057 ($M+H^+$). Anal. calcd. for $C_{48}H_{15}F_{15}N_6O_6$: C, 54.56, H, 1.43, N, 7.95. Found: C, 54.28, H, 1.43, N, 7.95.

[3a]. ^{1}H NMR (300 MHz, 1.8×10^{-3} mol / L, $CDCl_3$) δ 9.39 (two quasi-doublets, J = 1.5 Hz, 3H), 8.73 & 8.76 (two br singlets, 3H), 8.60 (dd, J = 9.0, 1.80 Hz, 3H), 5.61-5.63 (two br singlets, 6H). ^{13}C NMR (125 MHz, $CDCl_3$) δ 164.35, 146.89 (m), 145.17, 144.87 (m), 144.54, 144.37, 144.35, 143.99, 143.80, 143.09 (m), 142.67, 142.62, 141.15 (m), 138.69 (m), 136.71 (m), 136.57, 133.55, 133.51, 132.68, 132.64, 132.52, 131.61, 131.49, 131.11, 130.89, 109.15, 108.94, 54.65 ppm. ^{19}F NMR (376 MHz, 1.8×10^{-3} mol / L, $CDCl_3$) δ −141.80 (dd, J_1 = 21.4 Hz, J_2 = 6 Hz, 6F), −151.94 (t, J = 21.4 Hz, 3F), −161.36 (sextet, J = 9.0 Hz, 6F). ^{19}F NMR Chemical shifts are relative to trifluoromethylbenzene, which was used as an external standard. MALDI-TOF MS : *m/z* 1058, ($M+2H^+$). Anal. calcd. for $C_{48}H_{15}F_{15}N_6O_6$: C, 54.56, H, 1.43, N, 7.95. Found: C, 54.16, H, 1.32, N, 7.98.

[3b]. ^{1}H NMR (300 MHz, 1.8×10^{-3} mol / L, $CDCl_3$) δ 9.22 (two quasi-doublets, J = 1.5 Hz, 3H), 8.60 & 8.59 (two br singlets, 3H), 8.53-8.48 (m, 3H), 5.59 & 5.58 (two br singlets, 6H). ^{13}C NMR (125 MHz, $CDCl_3$) δ 164.32, 146.88 (m), 145.17, 144.87 (m), 144.54, 144.37, 144.35, 143.99, 143.80, 143.09 (m), 142.67, 142.62, 141.15 (m), 138.69 (m), 136.71 (m), 136.57, 133.55, 133.51, 132.68, 132.64, 132.52, 131.71, 131.59, 131.02, 130.96, 109.09, 108.96, 54.68 ppm. ^{19}F NMR (376 MHz, 1.8×10^{-3} mol / L, $CDCl_3$) δ (−141.70)–(−141.92) (m, 6F), −151.96 (quartet, J = 19.6 Hz, 3F), (−161.20)–(−161.52) (m, 6F). ^{19}F NMR Chemical shifts are relative to trifluoromethylbenzene which was used as an external standard. MALDI-TOF MS (M+H): *m/z* 1057 ($M+H^+$). Anal. calcd. for $C_{48}H_{15}F_{15}N_6O_6$: C, 54.56, H, 1.43, N, 7.95. Found: C, 54.16, H, 1.32, N, 7.98.

4-Trifluoromethyl-benzene-1,2-diamine, 6. This synthesis was performed by Dr. Qing Zhang in Seth Marder's group. 2-Nitro-4-trifluoromethyl-phenylamine (25.00 g, 121.30 mmol) and Tin(II) chloride dihydrate (136.83 g, 606.40 mmol) in ethanol (350 mL) were heated to reflux under nitrogen atmosphere for 30 min. After the mixture cooled down to room temperature, it was poured onto ice. The pH of the solution was made slightly basic by addition of 5% of sodium hydroxide solution. The solution was extracted with ethyl acetate. The combined organic layer was dried over magnesium sulfate and the solvent was removed under reduced pressure to give a solid (19.00 g, 89%). ^{1}H NMR (300 MHz, benzene-d_6) δ 6.91 (dd, J = 7.9, 1.9, Hz, 1H), 6.51 (d, J = 1.9 Hz, 1H), 6.03 (d, J = 7.9 Hz, 1H), 2.59 (brs, 2H), 2.35 (brs, 2H).

5,6,11,12,17,18-Hexaaza-trinaphthylene 2,8,14-tris-trifluoromethyl, and 5,6,11,12,17,18-Hexaaza-trinaphthylene 2,8,15-tris-trifluoromethyl, 4. A mixture of hexaketocyclohexane octahydrate (2.27g, 7.27mmol) and **6** (3.84g, 21.81mmol) was added to a degassed acetic acid (250 mL). The mixture was refluxed for 15 hrs under nitrogen. After the mixture cooled down to room temperature, solvent was removed under reduced pressure. The solid was purified by flash chromatography on silica gel eluting with dichloromethane to give a yellow solid. The resultant solid was dissolved in 30 mL of $CHCl_3$ and was precipitated with 60mL of MeOH to yield 2.81 g of crude **4a/b** mixture (yield 65 %, ca. 1:3 mixture). The ratio of isomer mixtures was estimated by HPLC analysis. To separate isomers, careful column chromatography was performed on the crude product using dichloromethane / ethyl acetate (9.5:0.5) as eluent. After solvent evaporation, the solids were dissolved in a minimum amount of $CHCl_3$, and they were

reprecipitated in 300 ml MeOH to yield a solid (0.1 g, 3.6 % yield from crude product) from early fraction as the isomer **a**, and to yield a solid (0.5 g, 17.8 % yield from crude product) from the late fraction as the isomer **b**.

[4a/b ca. 1:3]. ^{1}H NMR(300 MHz, 1.0 × 10^{-2} mol / L, benzene-d_6) δ 8.60 (quasi-dd, J = 12.3, 4.20 Hz, 3H, H^{a}, $H^{a'}$), 8.19-8.08 (m, 3H, H^{b}, $H^{b'}$), 7.40-7.25 (m, 3H, H^{c}, $H^{c'}$); ^{1}H NMR(300 MHz, 4.0 × 10^{-2} mol / L, $CDCl_3$) δ 8.98 (quasi-doublet, J = 0.90 Hz, 3H), 8.78 (d, J = 9.0 Hz, 3H), 8.19 (tt, J = 9.0, 1.80 Hz, 3H); ^{13}C NMR (75 MHz, CD_2Cl_2): 144.64, 144.31, 144.06, 142.47, 134.78, 134.34, 133.89, 133.45, 131.96, 131.87, 128.65, 128.25, 125.03, 121.41. ^{19}F NMR (376 MHz, 4.0 × 10^{-2} mol / L, $CDCl_3$): δ –79.83. HRMS EI: m/z calcd for $C_{27}H_9F_9N_6$ 588.0745, Found 588.0734. Anal. Calcd. For $C_{27}H_9F_9N_6$: C, 55.11; H, 1.54; N, 14.28. Found: C, 55.05; H, 1.34; N, 14.29.

[4a]. ^{1}H NMR (300 MHz, 3.4 × 10^{-3} mol / L, benzene-d_6) δ 8.71 (s, 3H, H^{a}), 8.26 (d, J = 8.7 Hz, 3H, H^{b}), 7.41 (dd, J = 9.0, 2.10 Hz, 3H, H^{c}); ^{1}H NMR(300 MHz, 3.4 × 10^{-3} mol / L, $CDCl_3$) δ 8.99 (s, 3H), 8.77 (two quasi-doublets, J = 9.0, 0.60 Hz, 3H), 8.22 (dd, J = 8.7, 1.80 Hz, 3H); ^{13}C NMR (75 MHz, CD_2Cl_2): 144.66, 144.33, 144.08, 142.49, 134.79, 134.35, 133.91, 133.47, 131.98, 131.89, 128.67, 128.26, 125.04, 121.43. ^{19}F NMR (376 MHz, 3.4 × 10^{-3} mol / L, $CDCl_3$): δ –79.82. HRMS EI: m/z calcd for $C_{27}H_9F_9N_6$ 588.0745, Found 588.0734. Anal. Calcd. For $C_{27}H_9F_9N_6$: C, 55.11; H, 1.54; N, 14.28. Found: C, 54.85; H, 1.40; N, 14.14.

[4b]. ^{1}H NMR(300 MHz, 1.0 × 10^{-2} mol / L, benzene-d_6) δ 8.63 (d, J = 12.3 Hz, 3H, H^{a}, $H^{a'}$), 8.20-8.13 (m, 3H, H^{b}, $H^{b'}$), 7.40-7.31 (m, 3H, H^{c}, $H^{c'}$); ^{1}H NMR(300 MHz, 1.0 ×

10^{-2} mol / L, CD_3Cl) δ 8.97 (s, 3H), 8.74 (d, J = 9.0 Hz, 3H), 8.20 (d, J = 9.0 Hz, 3H); ^{13}C NMR (75 MHz, CD_2Cl_2): 144.46 144.13, 144.03, 142.43, 134.92, 134.50, 134.08, 133.64, 131.90, 131.74, 128.68, 128.28, 125.10, 121.52. ^{19}F NMR (376 MHz, 1.0×10^{-2} mol / L, $CDCl_3$): δ –79.83. HRMS EI: m/z calcd for $C_{27}H_9F_9N_6$ 588.0745, Found 588.0734. Anal. Calcd. For $C_{27}H_9F_9N_6$: C, 55.11; H, 1.54; N, 14.28. Found: C, 54.92; H, 1.49; N, 14.09.

3.9 References

1. C. W. Tang, S. A. Van Slyke, Appl. Phys. Lett. **51**, 913 (1987). (b) J. H. Burroughes, D. D. C. Bradley, A. R. Brown, R. N. Marks, K. Mackey, R. H. Friend, P. L. Burns, A. B. Holmes, Nature **347**,539 (1990). (c) B. Geffroy, P. le Roy, C. Prat, Polym. Int. **55**, 572 (2006).

2. (a) G. Horowitz, Adv. Mater. **10**, 365 (1998). (b) C. D. Dimitrakopoulos, P. R. L. Malenfant, Adv. Mater. **14**, 99 (2002). (c) G. Wang, Y. Luo, P. H. Beton, Appl. Phys. Lett. **83**, 3108 (2003).

3. (a) P. Peumans, S. R. Forrest, Appl. Phys. Lett. **79**, 126 (2001). (b) C. Waldauf, P. Schilinsky, J. Hauch, C. J. Brabec, Thin Solid Films **503**, 451 (2004). (c) S. Yoo, B. Domercq, B. Kippelen, Appl. Phys. Lett. **85**, 5427 (2004).

4. S. F. Nelson, Y.-Y. Lin, D. J. Gundlach, T. N. Jackson, Appl. Phys. Lett. **72**, 1854 (1998).

5. P. R. L. Malenfant, C. D. Dimitrakopoulos, J. D. Gelorme, L. L. Kosbar, T. O. Graham, A. Curiooni, W. Andreoni, Appl. Phys. Lett. **80**, 2517 (2002).

6. (a) A. Tapponnier, I. Biaggio, P. Günter, Appl. Phys. Lett. **86**, 112114 (2005). (b) J. A. Haddock, B. Domercq, B. Kippelen, B. Electronics Letters **41**, 444 (2005).

7. (a) H. Eichhorn, J. Prophyrins Phthalocyanines **4**, 88 (2000). (b) K. Ohta, K. Hatsusaka, M. Sugibayashi, M. Ariyoshi, K. Ban, F. Maeda, R. Naito, K. Nishizawa, A. M. van de Craats, J. M. Warman, Mol. Cryst. Liq. Cryst. **397**, 25 (2003). (c) J.

M. Warman, M. P. de Haas, G. Dicker, F. C. Grozema, J. Piris, M. G. Debije, Chem. Mater. **16**, 4600 (2004).

8. W. Pisula, A. Menon, M. Stepputat, I. Lieberwirth, U. Kolb, A. Tracz, H. Sirringhaus, T. Pakula, K. Müllen, Adv. Mater. **17**, 648 (2005).

9. (a) A. M. van de Craats, J. M. Warman, A. Fechtenkötter, J. D. Brand, M. A. Harbison, K. Müllen, Adv. Mater. **11**, 1469 (1999). (b) K. Ban, K. Nishizawa, K. Ohta, A. M. van de Craats, J. M. Warman, I. Yamamoto, H. Shirai, J. Mater. Chem. 11, 321 (2001).

10. (a) D. Adam, P. Suhuhmacher, J. Simmerer, L. Häussling, K. Siemensmeyer, K. H. Etzbach, H. Ringsdorf, D. Haarer, Nature **371**, 141 (1994). (b) Y. D. Zhang, K. G. Jespersen, M. Kempe, J. A. Kornfield, S. Barlow, B. Kippelen, S. R. Marder, Langmuir **19**, 6534 (2003).

11. Z. An, J. Yu, S. C. Jones, S. Barlow, S. Yoo, B. Domercq, P. Prins, L. D. A. Siebbeles, B. Kippelen, S. R. Marder, Adv. Mater. **17**, 2580 (2005).

12. (a) Y. Shirota, J. Mater. Chem. **10**, 1 (2000). (b) Y. Shirota, T. Kobata, and N. Noma, Chem. Lett. **20**, 1731 (1991). (c) A. Higuchi, H. Inada, H. Nakano, and Y. Shirota, Adv. Mater. **3**, 549 (1991). (d) Y. Kuwabara, H. Ogawa, H. Inada, N. Noma, and Y. Shirota, Adv. Mater. **6**, 677 (1994). (e)H. O. Wirth, Angew. Makromol. Chem. **185/186,** 329 (1991). (f) K. Naito, Chem Mater. **6**, 2343 (1994). (g)A, Cravino, S. Roquest, O. Alévêque, P. Leriche, P. Frère, and J. Roncali, Chem. Mater. **18**, 2584 (2006).

13. S. Skujins and G. A. Webb, Tetrahedron **25,** 3935 (1969).

14. H. Bock, A. Babeau, I. Seguy, P. Jolinet, and P. Destruel, ChemPhysChem, 532 (2002).

15. (a) C. W. Ong, S.-C. Liao, T. H. Chang, and H.-F. Hsu, Tetrahedron Lett. **44**, 1477 (2003). (b) C. W. Ong, S.-C. Liao, T. H. Chang, and H.-F. Hsu, J. Org. Chem. **69**, 3181 (2004). (c) X. Crispin, J. Cornil, R. Friedlein, K. K. Okudaira, V. Lemaur, A. Crispin, G. Kestemont, M. Lehmann, M. Fahlman, R. Lazzaroni, Y. Geerts, G. Wendin, N. Ueno, J.-L. Brédas, and W. R. Salaneck, J. Am. Chem. Soc. **126**, 11889 (2004). (d)V. Lemaur, D. A. da Silva Filho, V. Coropceanu, M. Lehmann, Y. Geerts, J. Piris, M. G. Debije, A. M. van de Craats, K. Senthilkumar, L. D. A Siebbeles, J. M. Warman, J.-L Brédas, and J. Cornil, J. Am. Chem. Soc. **126**, 3271 (2004). (e) R. A. Marcus, Rev. Mod. Phys. **65**, 599 (1993). (f) V. Coropceanu, M.

Malagoli, D. A. da Silva Filho, N. E. Gruhn, T.G. Bill, and J. L. Brédas, Phys. Rev. Lett. **89**, 275503-1 (2002).

16. M. Lehmann, G. Kestemont, R. Gómez Aspe, C. Buess-Herman, C.; M. H. J. Koch, M. G. Debije, J. Piris, M. P. de Haas, J. M. Warman, M. D. Watson, V. Lemaur, J. Cornil, Y. H. Geerts, R. Gearba, And D. A. Ivanov, Chem. Eur. J. **11**, 3349 (2005).

17. D. Cahen, A. Kahn, Adv. Mater. **15**, 271 (2003).

18. (a) B. C. Lin, C. P. Cheng, Z.-Q. You, and C.-P. Hsu, J. Am. Chem. Soc. **127**, 66 (2005). (b) J. D. Anderson, E. M. McDonald, P. A. Lee, M. L. Anderson, E. L. Ritchie, H. K. Hall, T. Hopkins, E. A. Mash, J. Wang, A. Padias, S. Thayumanavan, S. Barlow, S. R. Marder, G. E. Jabbour, S. Shaheen, B. Kippelen, N. Peyghambarian, R. M. Wightman, and N. R. Armstrong, J. Am. Chem. Soc. **120**, 9646 (1998). (c) D. Cahen and A. Kahn, Adv. Mater. **15**, 271 (2003).

19. M. Malagoli, J.-L. Brédas, Chem. Phys. Lett. **327**, 13 (2000).

20. J. D. Wright, Molecular Crystals, (Cambridge University Press, Cambridge 1987).

21. (a) A. Keller, J. Polym. Sci. **17**, 291 (1955). (b) A. J. Lovinger, C. C. Gryte, Macromolecules **9**, 247 (1975). (c) J. K. Hobbs, D. R. Binger, A. Keller, P. J. Barham, J. Polym. Sci. **38**, 1575 (2000). (d) J. L. Hutter, J. Bechhoefer, J. Crystal Growth **217**, 332 (2000).

22. (a) M. L. Bushey, A. Hwang, P. W. Stephens, C. Nuckolls, J. Am. Chem. Soc. **123**, 8157 (2001). (b) W. Pisula, M. Kastler, D. Wasserfallen, T. Pakula, K. Müllen, J. Am. Chem. Soc. **126**, 126, 8074 (2004).

23. M. A. Lampert, P. Mark, Current Injection in Solids, (Academic Press, NY 1970), p. 18.

24. P. M. Borsenberger, E. H. Magin, M. van der Auweraer, and F. C. de Schryver, Phys. Stat. Sol. A **140**, 9 (1993).

25. N. F. Mott, D. Gurney, Electronic Processes in Ionic Crystals, (Oxford University Press: New York, 1940), p. 172.

26. P. N. Murgatroyd, J. Phys. D: Appl. Phys. **3**, 151 (1970).

27. M. Stolka, J. F. Janus, D. M. Pai, J. Phys. Chem. **88**, 4707 (1984).

28. C. Wu, T.-L. Liu, W.-Y. Hung, Y.-T. Lin, K.-T. Wang, R.-T. Chen, Y.-M. Chen, and Y.-Y. Chien, J. Am. Chem. Soc. **125**, 3710 (2003).

29. C. I. Wu, Y. Hirose, H. Sirringhaus, A. Kahn, Chem. Phys. Lett. **272**, 43 (1997).

30. (a) C. Shen. A. Kahn, and I. G. Hill, Conjugated polymer and molecular interfaces: science and technology for photonic and optoelectronic application. (b) W. R. Salaneck, K. Seki, A. Kahn, J. J. Pireaux, Marcel Dekker, Incoroporated: New York, 351 (2002).

31. (a) A. D. Becke, Phys. Rev. A **38**, 3098 (1988). (b) A. D. Becke, J. Chem. Phys. **98**, 5648 (1993). (c) C. Lee, W. Yang, and R. G. Parr, Phys. Rev. B **37**, 785 (1988).

32. M. J. Frisch, G. W. Trucks, H. B. Schlegel, G. E. Scuseria, M. A. Robb, J. R. Cheeseman, J. J. A. Montgomery, T. Vreven, K. N. Kudin, J. C. Burant, J. M. Millam, S. S. Iyengar, J. Tomasi, V. Barone, B. Mennucci, M. Cossi, G. Scalmani, N. Rega, G. A. Petersson, H. Nakatsuji, M. Hada, M. Ehara, K. Toyota, R. Fukuda, J. Hasegawa, M. Ishida, T. Nakajima, Y. Honda, O. Kitao, H. Nakai, M. Klene, X. Li, J. E. Knox, H. P. Hratchian, J. B. Cross, V. Bakken, C. Adamo, J. Jaramillo, R. Gomperts, R. E. Stratmann, O. Yazyev, A. J. Austin, R. Cammi, C. Pomelli, J. W. Ochterski, P. Y. Ayala, K. Morokuma, G. A. Voth, P. Salvador, J. J. Dannenberg, V. G. Zakrzewski, S. Dapprich, A. D. Daniels, M. C. Strain, O. Farkas, D. K. Malick, A. D. Rabuck, K. Raghavachari, J. B. Foresman, J. V. Ortiz, Q. Cui, A. Baboul, S. Clifford, J. Cioslowski, B. B. Stefanov, G. Liu, A. Liashenko, P. Piskorz, I. Komaromi, R. L. Martin, D. J. Fox, T. Keith, M. A. Al-Laham, C. Y. Peng, A. Nanayakkara, M. Challacombe, P. M. W. Gill, B. Johnson, W. Chen, M. Wong, C. Gonzalez, and J. A. Pople, Gaussian03, Revision B.05, Gaussian, Incorporated: Wallingford, CT, (2004).

33. K. Suzuki, T. Kanemura, K. Nakata, K. Nakamura, Japanese Patent JP 10069108 (1998).

34. (a) S. Norioka, H. Ishii, D. Yoshimura, M. Sei, Y. Ouchi, K. Seki, S. Hasagawa, T. Miyazaki, Y. Harima, and K. Yamashita, Appl. Phys. Lett. **67**, 1899 (1995). (b) M. S. Whitea, D. C. Olson, S. E. Shaheen, N. Kopidakis, and D. S. Ginley, Appl. Phys. Lett. **89**, 143517 (2006).

CHAPTER 4

SILVER NANODOTS ATTACHED ON ITO SURFACE AS A TRAP LAYER IN ORGANIC MEMORY DEVICES

4.1 Introduction

In recent years several types of electronic and optoelectronic devices based on organic and polymeric materials have been explored, including OLEDs,[1,2] OFETs,[3] and OPVs.[4] Moreover, another important electronic device, nonvolatile memory devices based on organic and polymeric materials have received considerable attention due to their advantages in terms of low-cost, facility of fabrication, material variety, and mechanical flexibility. These memory devices exhibit at least two different states of currents at the same applied voltage. These effects are represented by anomalous *I-V* characteristics showing a large hysteresis or a threshold voltage switching current levels. Although anomalous *I-V* characteristics have been observed for more than 30 years,[5,6] since the discovery of high performance and reliable organic memory devices based on a three layer organic/metal/organic structure embedded between two electrodes,[7–9] many groups have demonstrated switching phenomena in different types of organic and polymeric materials with different device structures.[10–18] The physical origin of the switching mechanism for these devices is still a subject of discussion. Recently, there has been significant interest in the design of organic memory devices with a simple structure, such as a single organic layer embedded between two electrodes, due to their simplicity and potential lower fabrication cost.[19–30] One major type of single-layer organic memory device is made of polymeric materials, which are comprised of donor-acceptor systems

[19,20] and polymer composites blended with metal nanoparticles (NPs),[21,22] fullerenes,[23,24] or dyes.[25] In the devices using a polymer composite with metal NPs, Au-NPs have been selected as a critical material to generate an electrically switching behavior, but other metal NPs have received scarce attention. Recently, Wang et al.[31] reported the memory effect with long retention time (exceeding 8 hours) of monolayer-isolated Ag nanodots (NDs) embedded within Al_2O_3 gate dielectric in a metal-insulator-silicon (MIS) structure. They formed Ag-NDs through the annealing process of an evaporated 10 nm Ag-film and argued that it can be applied to charge storage applications such as floating-gate memory devices. Another major type of single-layer organic memory device is simply made of an organic film prepared by either a small molecule or a polymer[26–30] as in a metal-insulator-metal (MIM) electroformed device[32], where the critical factor to generate a memory effect is the inclusion of metal particles or atoms in the insulator layer during the evaporation of the top electrode. However, in these devices, ON/OFF ratios are usually low, particularly for devices using indium tin oxide (ITO) as one of the electrodes. Chen and Ma reported a single-layer memory device based on an ITO/organic molecules/Ag structure with a maximum ON/OFF ratio of 20, and after introducing doping fluorescent dyes in the organic layer, they obtained an ON/OFF ratio up to 100.[28,29] Scott *et al*.[22] observed ON/OFF ratios in the range of $10^2 – 10^6$ in a three layer device when using metal electrodes such as Al and Cr. However, when using an ITO electrode, the ON/OFF ratios dropped to 100. ITO is an important and widely used transparent electrode for organic optoelectronic devices. Moreover, various ITO pre-coated glass or flexible plastic substrates are commercially available. Thus, rewritable memory devices using ITO as an electrode with large ON/OFF ratios, long storage state retention time are highly desirable.

Such devices could for instance be used as current controlling elements and integrated with other organic electronic devices on ITO such as organic light-emitting diodes and organic field-effect transistors.[38]

This chapter describes the electrical switching characteristics of a single-layer organic memory device with enhanced ON/OFF ratios that were obtained by introducing Ag-NDs between the organic layer and the ITO surface. The performance of such a device is compared to that of a control device without Ag-NDs and to that of a device made with Ag-NPs dispersed in the organic matrix. The active layers of the devices were fabricated by solution processing: the Ag-NDs attached on ITO surface was prepared by a solution based self-assembly of Ag-NPs; and both organic and Ag-NPs composite films were deposited by spin coating. The surface characterizations by absorption spectra, contact angle measurements, X-ray photoemission spectroscopy (XPS), and atomic force microscopy (AFM) provide the evidence of forming Ag-NDs on ITO surfaces and the effect of a bridging reagent. A drastic improvement of electrical switching properties has been observed in the device comprised of poly(*N*-vinylcarbazole) (PVK) film embedded between an Al electrode and ITO modified with Ag-NDs. This device shows promise as a nonvolatile organic memory device according to the results of write-read-erase-reread cycles, stress tests, and retention times of programmed states. Temperature dependence of the electrical characteristics suggests that the current of the low-resistance state can be attributed to Schottky charge tunneling through low-resistance pathways of Al particles in the polymer layer and that the high-resistance state can be controlled by charge trapping by the Ag-NDs. In order to obtain further understanding for the origin of the

switching behavior, the different materials of top-electrodes and the different organic materials with different energy band-gaps are investigated.

4.2 Ag-NDs attached to an ITO surface

4.2.1 Preparation of Ag-NDs to an ITO surface

Ag-NPs attached to surfaces have been recognized as potential approaches for improving optical and electrical surface properties such as surface-enhanced Raman scattering (SERS),[33] localized surface plasmon resonance (SPR)[34], and electrocatalytic effects.[35] The approaches for attaching Ag-NPs to substrate surfaces have been employed by not only dry processes but also solution processes using bridging reagents, such as 3-mercaptopropyltrimethoxysilane for glass substrate and 3-mercaptopropionic acid for gold electrode.[33,36,37]

The Ag-NDs attached to ITO surfaces were prepared by solution-based surface assembly using a solution of Ag-NPs capped with octane-1-thiol (OT) and 4-mercaptobenzoic acid (MBA) modified ITO substrates. The Ag-NPs were prepared according to literature procedure based on a two-phase reaction method,[39] which yields a narrow size distribution (1.3-8.5 nm in diameter) and a mean diameter of 5.4 nm (The synthesis and characterizations were performed by Michal Malicki in Seth Marder's group). Ag-NPs were characterized by transmission electron microscopy (TEM), and the mean diameter was determined by measuring 900 particles. The image TEM and size histogram of Ag-NPs are shown in Figure 4.1. MBA was used as a bridging reagent between Ag-NPs and ITO surfaces. The Ag-NDs modified ITO surfaces were prepared by the following procedure. A AgNPs solution of 0.1 wt. % in toluene was sonicated for

1 hour to dissolve, and then the solution was filtered through a PTFE filter (0.45 μm mesh size). Cleaned ITO glass substrates were immersed in a MBA solution (0.01 M) in CH_2Cl_2 / ethanol (7/3 with volume ratio) for 3 hours. After removing the ITO substrates from the MBA solution, the MBA modified ITO substrates were continually immersed in the filtered Ag-NPs solution (0.1 wt % in toluene) for 15 hours, and then removed from the solution and washed by sonicating in ethanol for 20 min. To examine the effect of MBA, cleaned ITO substrates were also treated with Ag-NPs solution without immersing in the MBA solution. Finally, the Ag-NPs modified ITO substrates were transferred to a N_2 atmosphere and annealed at 300 °C for 30 min to decompose remaining organic species and to create Ag-NDs. In experiments of absorption spectra, the Ag-NPs deposited on back side ITO substrates (glass surfaces) were completely wiped off with a silver-etching solution ($K_2S_2O_3$:$K_3Fe(CN)_6$:$K_4Fe(CN)_6 \cdot 3H_2O$=1:0.1:0.01 molar ratio). Figure 4.2 shows the procedure of solution-based surface assembly for the Ag-NDs on ITO surface.

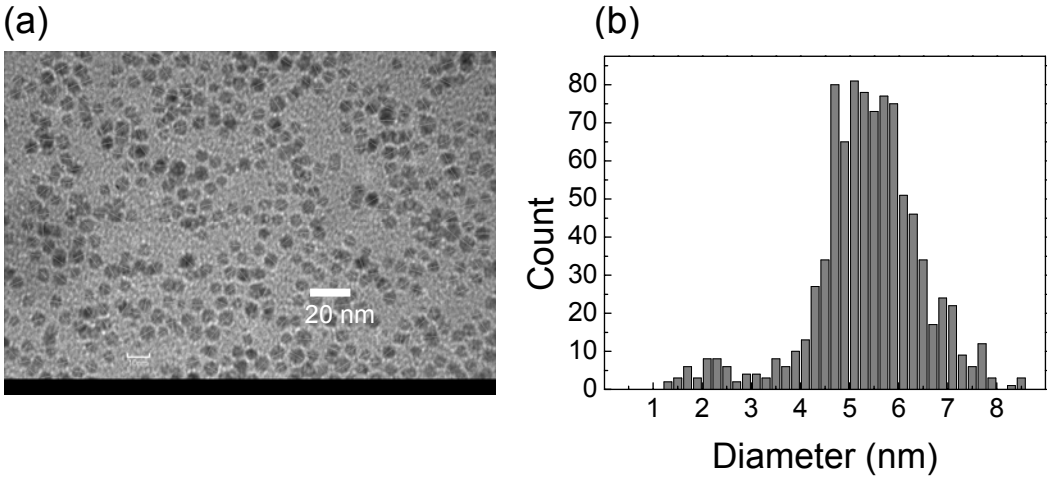

Figure 4.1 (a) Transmission electron microscopy and (b) size histogram of Ag-NPs.

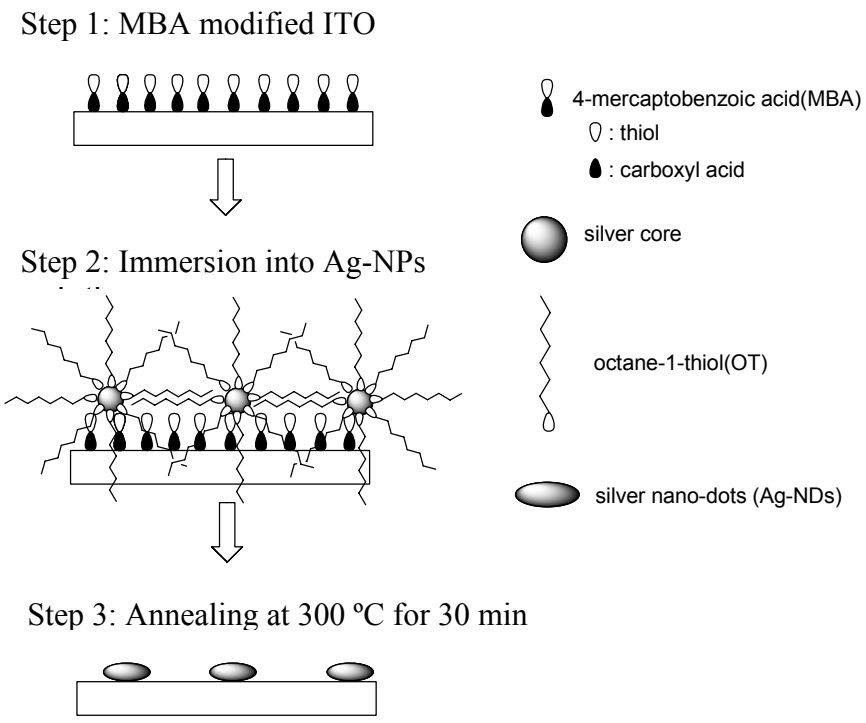

Figure 4.2 Assembly strategy for the Ag-NDs attached to an ITO surface.

4.2.2 Characterizations of Ag-NDs on ITO surface

The Ag-NDs attached on ITO substrates were characterized by XPS, absorption spectra, AFM, and contact angle measurements. Figure 4.3 shows XPS survey spectra for seven different surfaces: (1) air-plasma treatment for 5 min of cleaned ITO; (2) treated Ag-NPs on (1); (3) washed (2) (sonicated in EtOH for 20 min); (4) annealed (3) at 300 °C for 30 min in N_2 atmosphere; (5) treated MBA on (1); (6) washed (sonicated in EtOH for 20 min) after treating Ag-NPs on (5); and (7) annealed (6) at 300 °C for 30 min in N_2 atmosphere. These spectra confirm the presence of the desire elements in these samples and allow us to calculate their atomic composition, although the sulfur signals have been very weak due to inelastic scattering of the S (2p) electrons.[46] The calculations of atomic compositions used standard XPS cross sections, and Table 4.1 shows the atomic

compositions derived from the survey spectra in Figure 4.3. Every Ag-NPs treated ITO shows Ag $3d_{5/2}$ and Ag $3d_{3/2}$ peaks at 368.7 eV and 374.6 eV, respectively. These high-resolution scans are well-fitted with one component of Gaussian peak shape (Figure 4.4). However, Ag-atomic compositions show a strong dependence on the treatment procedure. The surfaces using the MBA modified ITO substrates obtain Ag-atomic compositions of 12 % and 9 % for before and after annealing, respectively. In contrast, the surfaces using cleaned ITO substrates obtain compositions of 6 % and 3 %. These results indicate that MBA can act as a bridging reagent to enhance the interaction between the Ag-NPs and the ITO surface. The reason for the decrease in Ag-atomic compositions after annealing is not clear, but we predict that some portions of Ag-NPs adsorbed the ITO surface are decomposed by annealing process, and these species may be easily evaporated by a low-pressure condition of the XPS experiment ($< 10^{-8}$ Pa). The annealing process will decompose also organic species. In fact, C and S compositions are decreased, and O compositions are increased after annealing as shown in Table 4.1. Figure 4.5 shows the high-resolution scans at O 1s region of the surfaces before and after annealing ((6) and (7)). In the surface post-annealed, the peak of O 1s is larger than that of before annealing, and the ratio of the higher-binding energy component at 532.3 eV (the peak b) is increased compared to the low-binding energy peak (the peak a). The peak b may be assigned as hydroxide and/or oxy-hydroxide that are attributed to oxygen of a surface layers but not lattice oxygen.[47] This result indicates that the annealing process can decompose some organic species on the ITO surface such as capping (OT) and bridging (MBA) reagents of Ag-NPs, consequently the ratio of surface hydroxide would be increased.

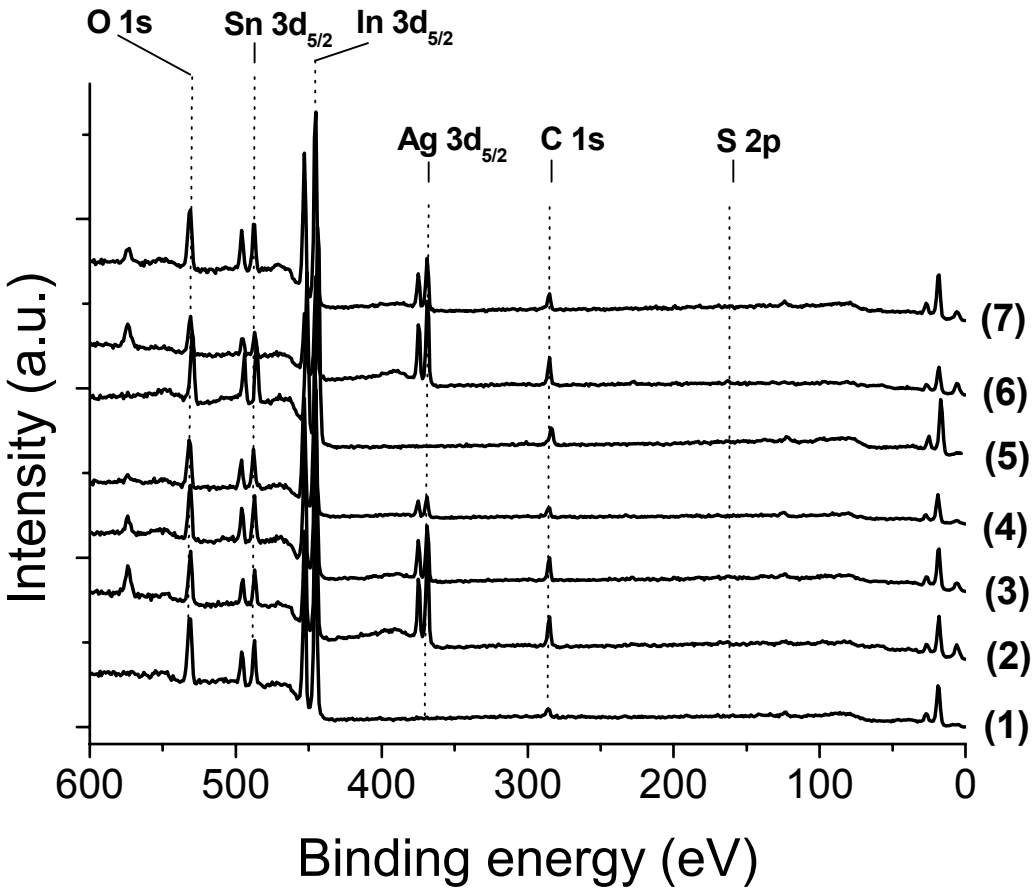

Figure 4.3 XPS general surveys for seven different samples. (1) air-plasma treated ITO, (2) treated Ag-NPs on (1); (3) washed (2) (sonicated in EtOH for 20 min), (4) annealed (3) at 300 °C for 30 min in N_2 atmosphere, (5) treated MBA to (1), (6) washed (sonicated in EtOH for 20 min) after treating Ag-NPs on (5), and (7) annealed (6) at 300 °C for 30 min in N_2 atmosphere.

Table 4.1 Atomic compositions derived from the survey spectra in Figure 4.3.

	Observed compositions (%)					
Samples	C	S	O	Ag	In	Sn
(1) air-plasma treated ITO	15		54		26	5
(2) treated Ag-NPs using (1) without any rinsing after treatment	40	2	29	11	15	3
(3) washed* (2)	30	1	36	6	22	5
(4) annealed (3) at 300 °C for 30 min in N_2 atmosphere	19		47	3	25	6
(5) treated MBA to (1)	27	2	42		24	5
(6) washed* after Ag-NPs treated to (5)	42	2	28	12	13	3
(7) annealed (6) at 300 °C for 30 min in N_2 atmosphere	22		41	9	23	5

* The condition for washing after Ag-NPs treatment is sonication in EtOH for 20 min.

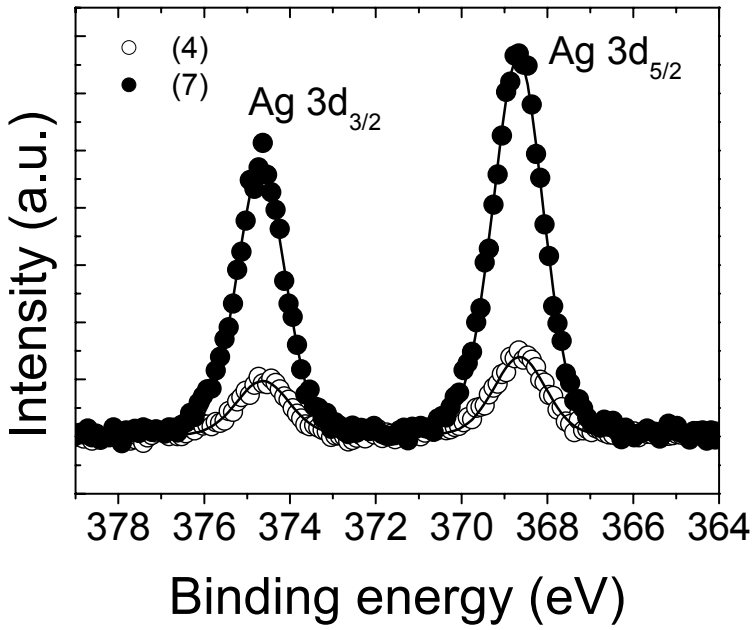

Figure 4.4 High-resolution XPS scans at Ag 3d regime of (4) annealed Ag-NPs treated ITO without MBA and (7) annealed Ag-NDs treated MBA modified ITO.

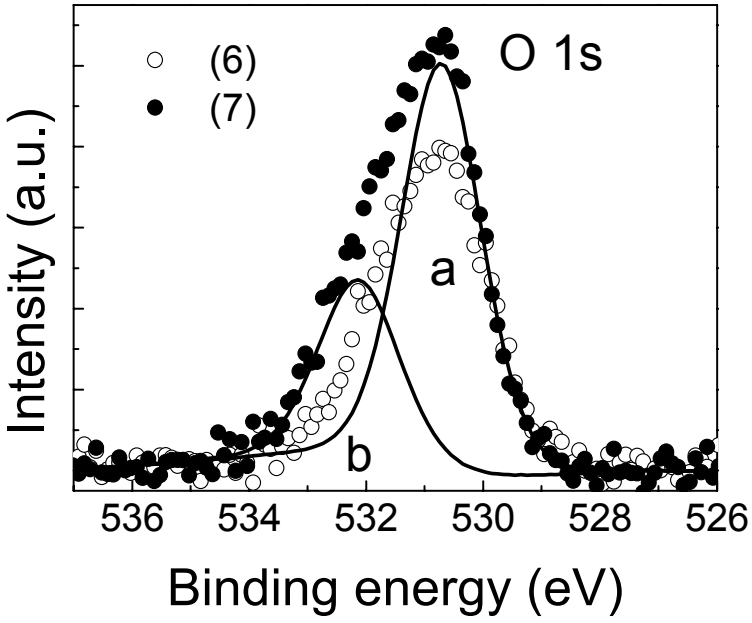

Figure 4.5 High-resolution XPS scans at O 1s regime comparing between before and after annealing of the Ag-NPs treated MBA modified ITO.

The absorption spectra of (1) air-plasma treated ITO, (6) washed after treating Ag-NPs on the MBA modified ITO, (7) annealed (6), and a filtered Ag-NPs solution in toluene are shown in Figure 4.6. In both samples, broad absorption bands at 400 – 600 nm with peaks at 480 – 506 nm presumably due to surface plasmon resonance (SPR) effects are observed. In contrast, a SPR with a peak at 430 nm is observed in the Ag-NPs solution in toluene. In the annealed substrate, the peak is slightly red sifted (from λ_{max} = 480 nm to 506 nm), and the maximum absorption increases compared to the substrate before annealing. The result may indicate that the morphology or the particle size of the Ag-NPs on the ITO surface is changed by the annealing at 300 °C for 30 min. The morphology-change was confirmed by the AFM studies. Figure 4.7 shows the AFM images of (1) air-plasma treated ITO surface, (4) annealed Ag-NPs treated ITO without MBA modification, (6) washed after treating Ag-NPs on the MBA modified ITO, and (7) annealed (6). Although nano-size grains are observed in the air-plasma treated ITO surface, randomly distributed grains and dots with extraordinary large-size are exhibited in the 2 μm × 2 μm images of both (4) and (6). After annealing Ag-NPs treated ITO with the MBA modification, the large dots are more clearly observed and distributed randomly in the entire image and isolated from each other as shown in (7). The diameter and height of the large dots are approximately in the range of 10 – 100 nm and 5 – 50 nm, respectively. The image of these dots is similar to Ag-NDs created by a evaporated Ag-film of 10 nm thickness after annealing at 400 °C for 1 hour.[31] The larger size compared to the original Ag-NPs (the average diameter is 5.4 nm) is presumably caused by an aggregation effect in toluene and a self-assembling effect in the annealing process.[31]

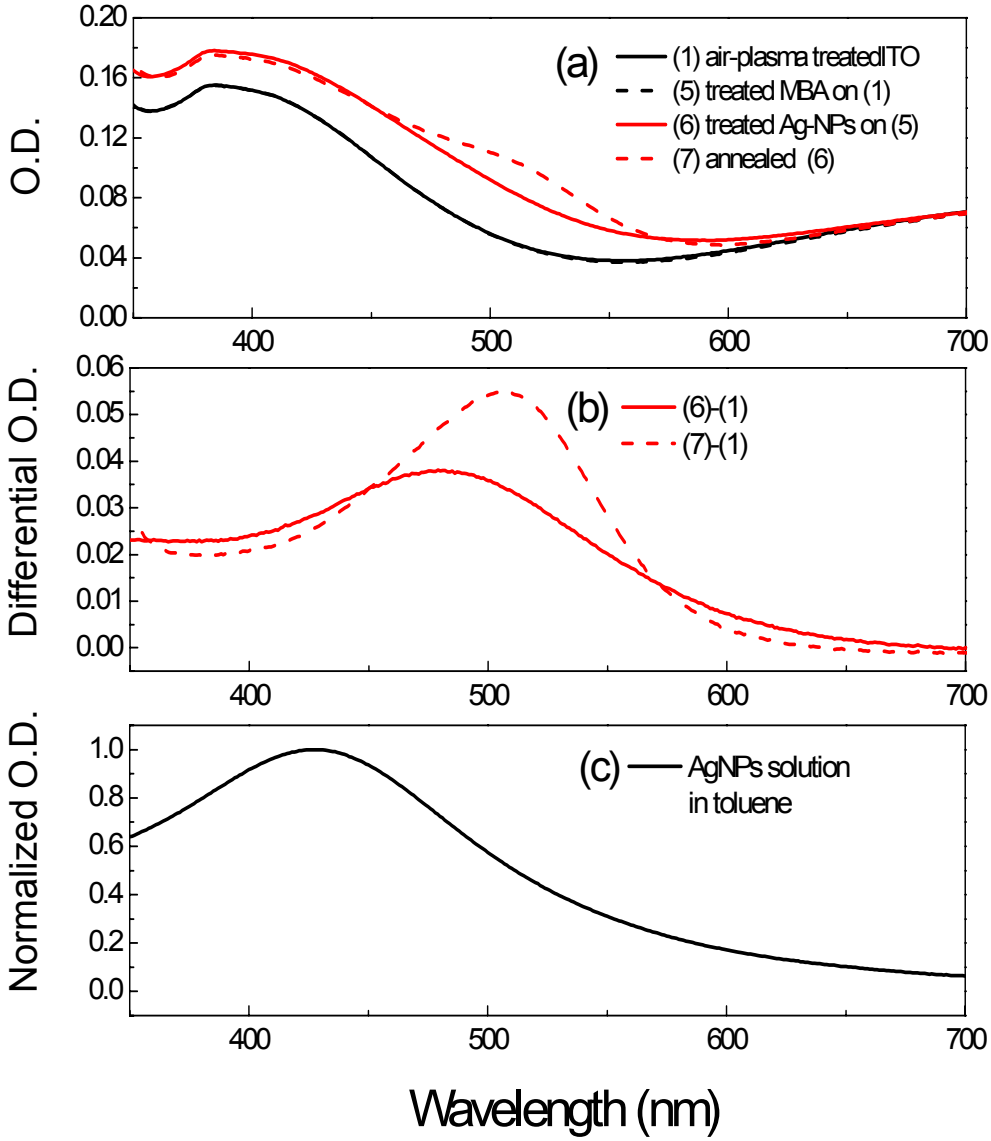

Figure 4.6 (a) Absorption spectra of (1) air-plasma treated ITO, (5) treated MBA, (6) washed Ag-NPs treated (5), and (7) annealed (6). (b) Differential absorption spectra between (6) – (1) and (7) – (1). (c) Absorption spectra of the Ag-NPs solution in toluene.

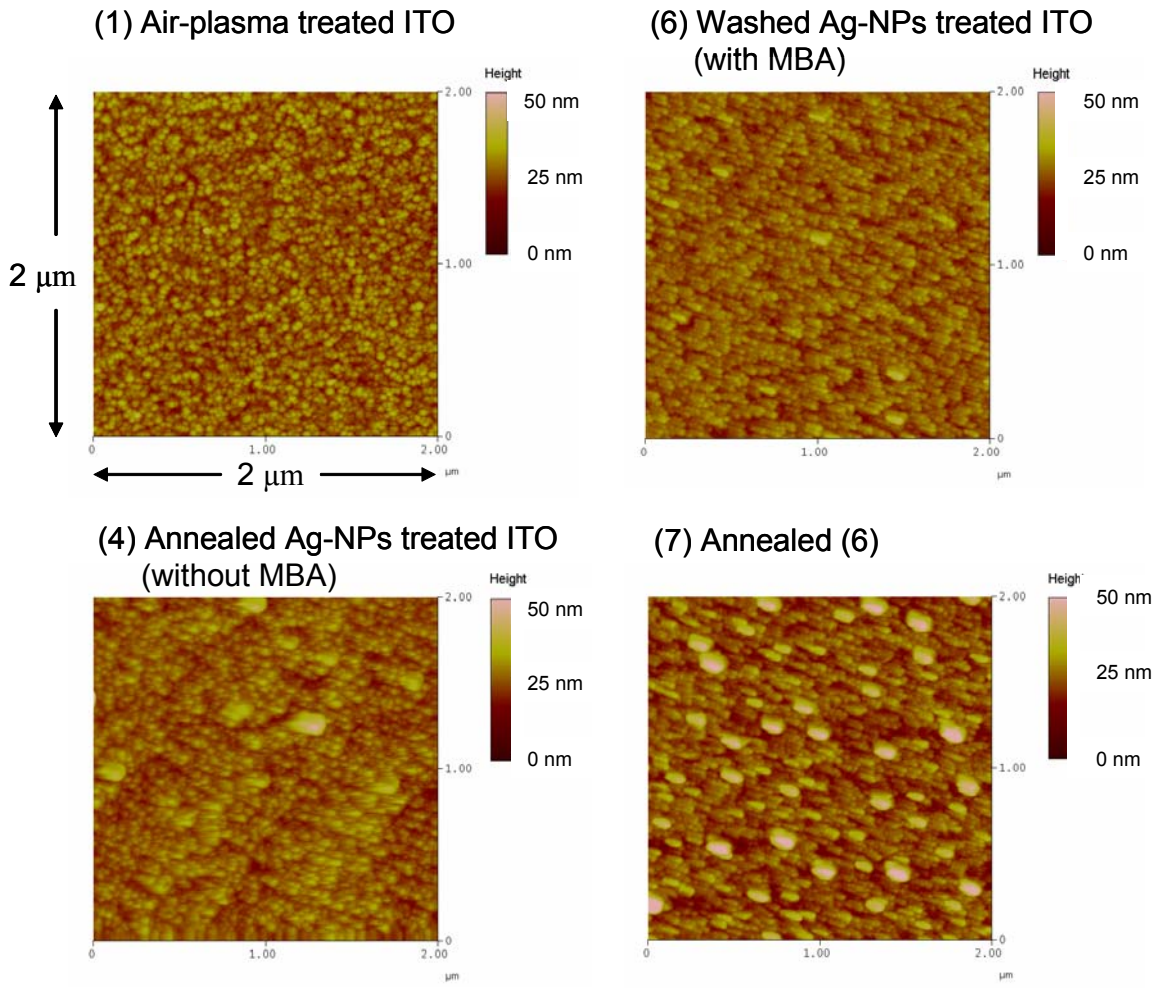

Figure 4.7 AFM image of (1) air-plasma treated ITO, (4) annealed Ag-NPs treated ITO surface without MBA, (6) washed Ag-NPs treated ITO surface using a MBA modified ITO, and (7) annealed (6).

The annealing temperature of 300 °C in this experiment was chosen according to the result of TGA measurement for the Ag-NPs as shown in Figure 4.8. A weight loss of ca. 21 % is observed during heating from room-temperature to 500 °C at a heating rate of 15 °C/min. The weight loss is almost saturated above 290 °C. After measuring TGA, the color and appearance of the Ag-NPs changed from black powders to Ag flakes. The TGA

results support the possible decomposition of organic species and a resulting morphology change due to the annealing process.

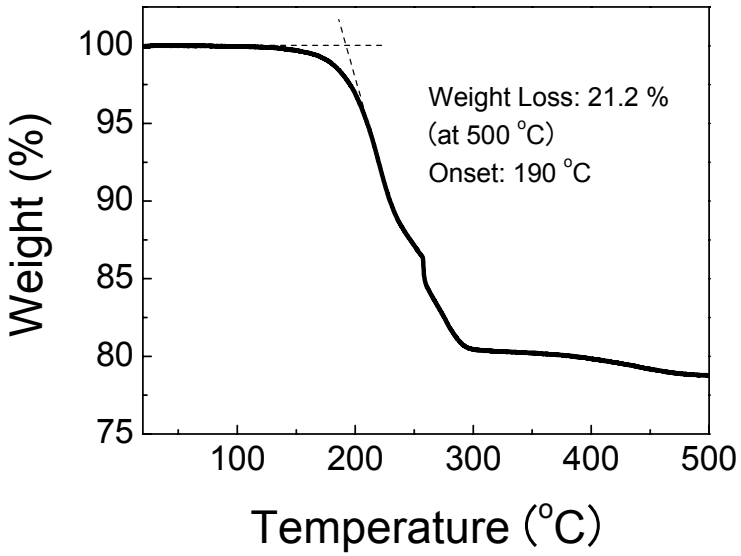

Figure 4.8 TGA result of the Ag-NPs.

The results of contact angle measurements (Table 4.2) also indicate that the change in surface properties through the annealing process. The average contact angle of water droplets on the Ag-NPs treated ITO surface without annealing shows a high contact angle of 107 ° indicating a hydrophobic nature presumably due to the organic capping agent (OT) of Ag-NPs. In contrast, the annealed surface shows a hydrophilic nature in where the average contact angle is less than 15 °. This value of contact angle is similar to that of a cleaned bulk silver surface. These results indicate that some organic species may decompose caused by the annealing process, and it induces a change in wetability of the surface. The comparison of the contact angles between before and after annealing by

using the cleaned ITO, which shows a slight increase in the contact angle after annealing, confirms that the change in the contact angle after annealing of the Ag-NPs treated ITO is attributed to a change in surface properties of Ag-NPs instead of ITO.

Table 4.2 Summary of the contact angles for the five different samples.

Samples	*Average contact angle (°)	*Standard deviation	Droplet images
(1) air-plasma treated ITO	< 15	----	
(1') annealed (1)	30	2.9	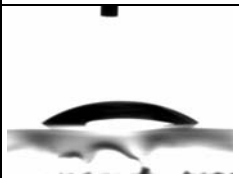
(5) treated MBA to (1)	59	1.9	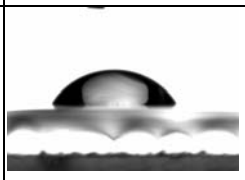
(6) treated Ag-NPs to (5)	107	3.3	
(7) annealed (6)	< 15	----	

* The average contact angles and standard deviations are calculated from five-times measurements using same sample.

4.3 Nonvolatile organic memory device using the Ag-NDs attached on ITO surfaces

4.3.1 Device structures and fabrications

In this section, PVK, a well-known charge transporting material, was used as the solution processed organic layer for three different types of devices as shown in Figure 4.9. Devices of type **I** were comprised of a PVK layer embedded between two electrodes (ITO/PVK/Al). Devices of type **II** had of a similar structure but Ag-NDs were added on the surface of the ITO substrate (ITO/Ag-NDs/PVK/Al). In devices of type **III,** Ag-NPs (10 wt. %) were dispersed in the PVK layer and embedded between a bare ITO electrode and Al (ITO/PVK+Ag-NPs/Al). A solution of PVK (MW = 135600, Scientific Polymer Product Inc., 20 mg / mL in toluene) was spun on the cleaned ITO and the Ag-NDs modified ITO substrates for device **I** and **II**, respectively, to obtain a PVK layer with a thickness in the range of 50 – 320 nm by changing spin-coating speeds. A 10 wt % Ag-NPs dispersed PVK solution of chloroform (Ag-NPs/PVK/chloroform = 2 mg/20 mg/1 mL) was spun on cleaned ITO substrates to fabricate device **III**. The spin-coating of PVK and its Ag-NPs composite were carried out in a N_2 filled glove box. The substrates with deposited active layers were transferred into a vacuum deposition system (Spectros, Kurt J. Lesker) connected to the glove box. A ~ 150 nm thick film of Al (or Ag) was evaporated starting at a rate of 0.1 nm/s and increasing to 0.3 nm/s over the duration of the evaporation at a base pressure of ~ 10^{-7} Torr to form the top electrode. Each substrate has five devices with an average area of 10 mm^2. In the device using PEDOT:PSS electrode, a high conductive grade of PEDOT:PSS solution(Baytron F-HC, H.C. Starck Inc.) was spun on organic film and dried at 150 ºC for 1 hour to form a top electrode. The average thickness of ca. 230 nm was obtained by spin coating at 1000 r.p.m. for 90 s

using the original solution of Baytron F-HC. The sheet resistivities of both PEDOT:PSS films were measured by a four point probe, and the range of 1.2 – 3.0 k Ω/□ was obtained. The active areas of the devices using spin coated PEDOT:PSS electrodes were isolated by a sharp blade, and each active area was around 0.05 cm^2. *I-V* characteristics and the write-read-erase-reread cycles were performed using a Keithley 2400 source meter controlled by a computer. All electrical measurements were performed in the glovebox.

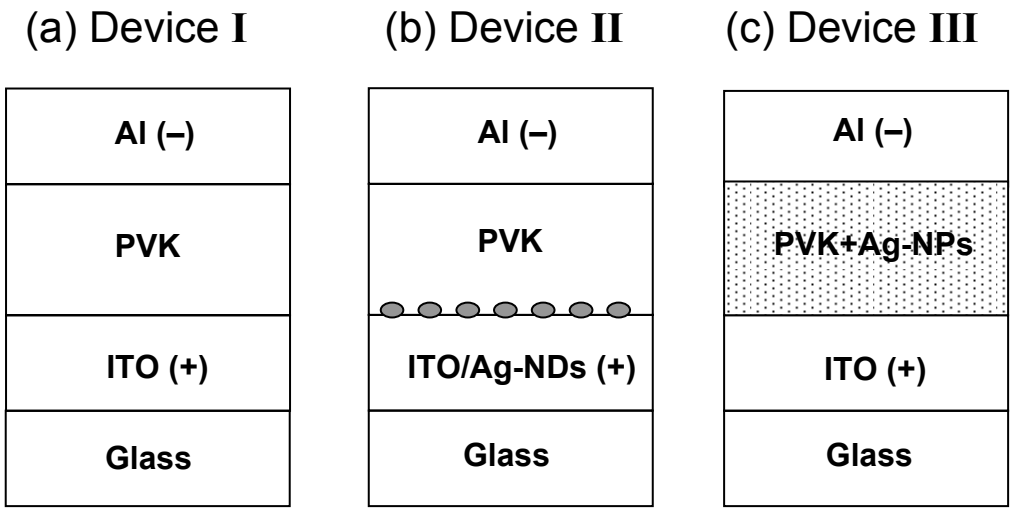

Figure 4.9 Schematic device structures of (a) device **I** with ITO/PVK/Al, (b) device **II** with ITO/Ag-NDs/PVK/Al, and (c) device **III** with ITO/PVK+Ag-NPs/Al.

4.3.2 Electrical switching behavior

Figure 4.10 shows, on semilogarithmic scales, typical *I-V* characteristics for (a) device **I**, (b) device **II**, and (c) device **III** with a 150 nm thick organic layer. All devices exhibit analogous operational characteristics. The typical switching effects of each device obtained by sweeping the voltage from zero to a high voltage and resetting to zero, and then quickly starting voltage-sweep from zero towards a high voltage again. Pristine

devices start in a low-resistance (high current density) state which we refer to as the ON state. When the voltage is increased, the current exhibits a local maximum current at a maximum voltage V_{max} (2.5 – 4.5 V). Beyond this value, the *J-V* curve shows a regime of negative differential resistance (NDR) until a local minimum in current is reached at a voltage V_{min} (5.5 – 6.5 V). After reaching a highest voltage (in this case: 8 V) that is defined as a reset voltage V_{reset}, the voltage is abruptly reset to zero, the devices are now in a high-resistance state in contrast to pristine devices, which we refer to as the OFF state. When the voltage is swept towards V_{reset} again, the current level abruptly switches back to the ON state at a threshold voltage V_{th} of ~ 2.0 – 2.5 V. Beyond this value of the voltage, the current follows the same curves as that of pristine devices operating in the ON state. If the voltage is swept slowly from V_{reset} towards zero, the devices remain in the ON state. If the voltage is rapidly reset to zero when the voltage is in the NDR regime, that is when $V_{reset} < V_{min,}$ the current in the OFF state will start at a higher value, resulting in a lower current ratio between the ON and OFF states. Therefore, to have the largest ON/OFF ratio, V_{reset} should be larger than V_{min}. Hence, these devices can be used as reversible logic bistable memory devices with ON and OFF states characterized by two different resistances with a read-ON and a read-OFF voltage (0 – V_{th}), an OFF to ON states switching voltage ($V_{th} - V_{max}$), and an ON to OFF states switching voltage ($V_{reset} > V_{min}$). These operational characteristics have also been observed when applying the reverse bias, as the *J-V* characteristics are nearly symmetric.

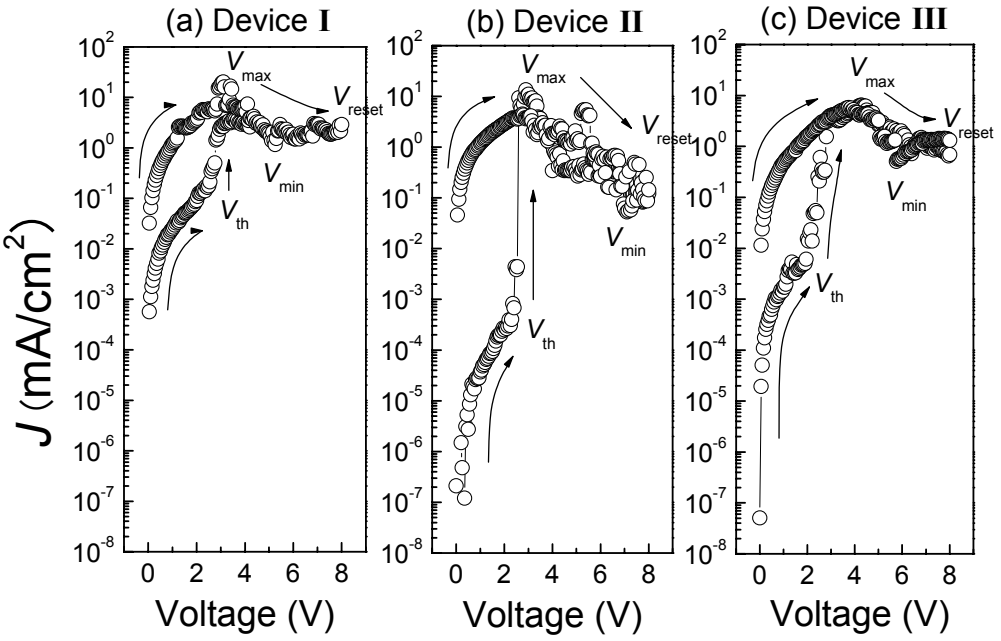

Figure 4.10 Typical *I-V* characteristics, on semilogarithmic scales, for (a) device **I** with the structure ITO/PVK (150 nm)/Al, (b) device **II** with the structure ITO/Ag-NDs/PVK (150 nm)/Al, and (c) device **III** with the structure ITO/PVK+Ag-NPs (150 nm)/Al. In these figures, ITO and Al electrodes are used as the anode and cathode, respectively.

The typical ON/OFF ratios observed in the *I-V* characteristics sweep for a read-out voltage of 1.0 V are 20, 10^4, and 10^2 for devices **I**, **II**, and **III**, respectively. Interestingly, the current level in the ON state in the V_{max} region (5.5 – 13.5 mA/cm^2) is almost insensitive to the device structure, while that of the OFF state is drastically changed by introducing Ag-NDs or Ag-NPs. These results suggest that the Ag-NDs or Ag-NPs play an important role in enhancing the ON/OFF ratio, especially by reducing the current level in the OFF state. Devices with an Ag-NDs interlayer between ITO and PVK are much more efficient than those with homogenously dispersed Ag-NPs in the PVK layer. Devices using the ITO modified by Ag-NDs showed an excellent repeatability for the switching effect when the voltage-sweep was continuously cycled

between zero and V_{reset} (8.0V) for 10 times. In contrast, the device using the PVK composite blended with Ag-NPs showed a gradual degradation of the switching effect for a number of voltage-sweep cycles.

The effects of the thickness of the PVK layers in the electrical characteristics of type **II** devices are shown in Figure 4.11 and reveal that the current level in the ON state (until V_{max} is reached) is almost independent on the thickness within the range of 50 – 150 nm, while the current level in the OFF state decreases with increasing thickness. In the device with a 320 nm-thick PVK layer, no switching effect is observed as the current level appears to stay in the OFF state and never switches to a low-resistance state. This observation is similar to that made by Tondelier *et al.*[26] in a Al/Pentacene/Al device in which electrical conductivity was attributed to a filamentary conduction process. However, they observed a linear-dependence of the film thickness on V_{th} and no NDR regime. In contrast, the devices in the present study show a more complex variation of V_{th} and NDR on film thickness.

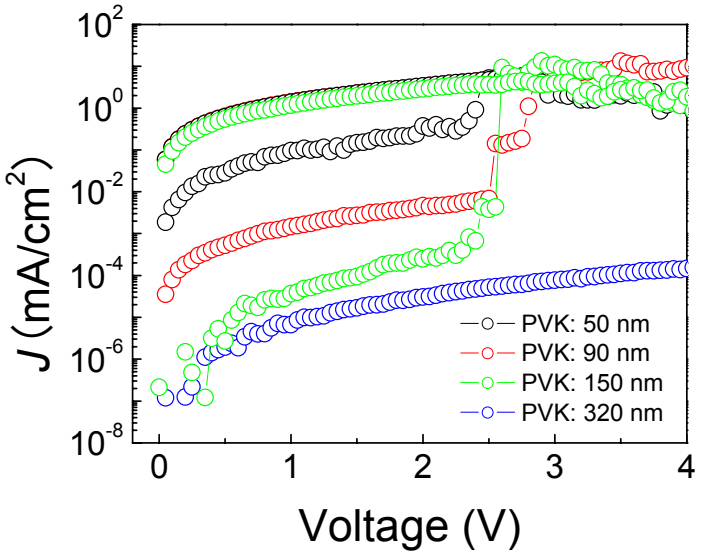

Figure 4.11 *I-V* characteristics of the device **II** with different PVK film thicknesses.

Further information about transport mechanisms can be obtained from temperature-dependence measurements. Figure 4.12a shows the current measured at 0.1 V as a function of temperature for device **II** in both the ON and OFF states with a 150 nm-thick layer of PVK. The OFF state can be fitted by a thermally activated transport model with an activation energy of about 0.4 eV, while the current in the ON state is almost temperature-independent within the temperature range of 0 – 50 °C. The *J*-*V* curves for device **II** in both the ON and OFF states between zero and 1.5 V (until V_{th}) at room temperature are shown in Figure 4.12b. The current in the ON state shows an almost linear-dependence on applied voltage, and this and the small temperature-dependent indicate that the ON state is dominated by transporting mechmisms with a small activation energy such as direct tunneling or Fowler-Nordheim tunneling.[21,48] These two tunneling mechanisms can be distinguished due to their distinct voltage dependences (Direct tunneling: $J \sim V$, Fowler-Nordheim tunneling: $\ln(J/V^2) \sim 1/V$). Analysis of $\ln(J/V^2)$ versus $1/V$ showed no significant voltage dependence, indicating no obvious Fowler-Nordheim transport behavior in this bias range (0 – 1.5 V). Thus, our observations in the ON state in this bias range and the temperature range are compatible with direct tunneling conduction. In contrast, the slightly higher than quadratic relation between the current and voltage in the high field regime (above $V/d = 3.0 \times 10^4$ V/cm, d = PVK thickness) is observed in the OFF state at room temperature. This suggests that the transporting mechanism is governed by SCLC model.[40,41] According to this model, an effective mobility of 1.0×10^{-9} cm^2/Vs at a maximum field of 6.6×10^4 V/cm is deduced by assuming that the relative permittivity of PVK is 3.0 and the mobile charges are predominantly holes. This value is two orders of magnitude lower than the average

reported values in the range of 10^{-8} – 10^{-6} cm^2/Vs based on the time-fight and SCLC measurements.[42] The low effective mobility is probably due to a large trap density or a poor charge injection efficiency caused by the Ag-NDs on the ITO surface.

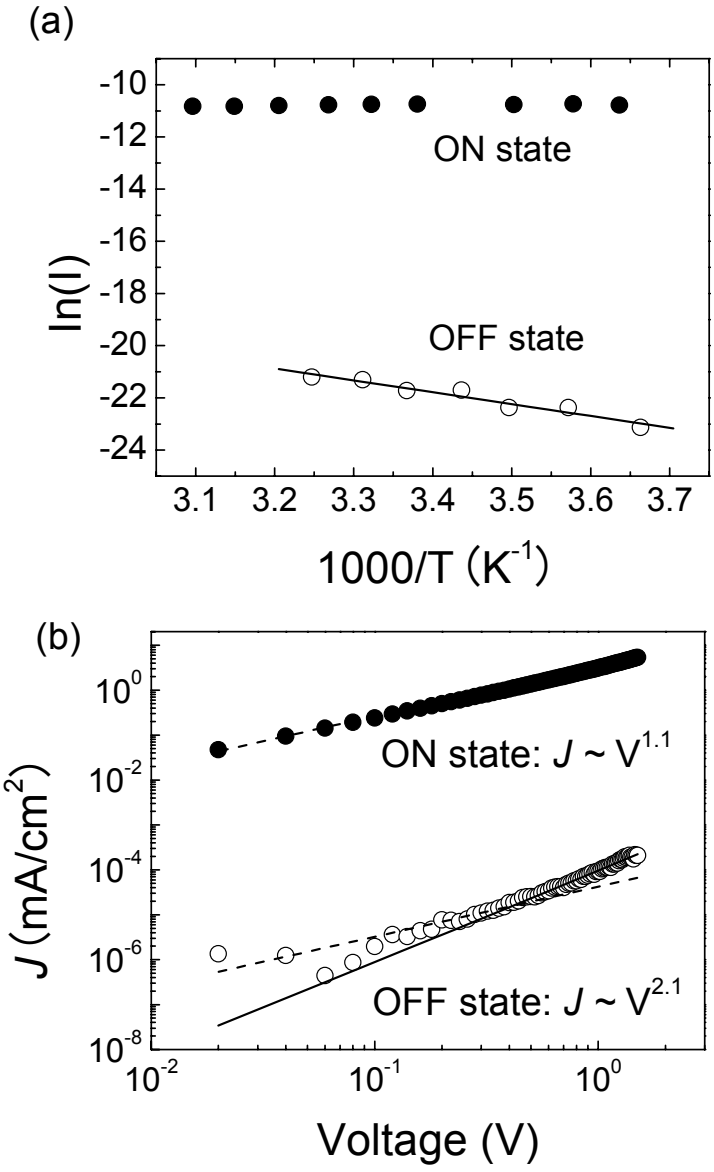

Figure 4.12 (a) Arrhenius plots of the ON and OFF states current at 0.1 V for device **II** with the structure ITO(+)/PVK (150 nm)/Al(–). In the OFF state, the activation energy is calculated as 0.4 eV from linear fitting (the solid line). (b) The *I-V* characteristics in the voltage range of 0 – 1.5V for the ON and OFF states of the same device as in (a) at room temperature. The dashed lines represent linear relations between *J* and *V*. The solid line represents the prediction from a SCLC model characterizing the field-dependent mobility (Eq. 2.10). The extracted effective mobility is μ_{eff}= 1.0×10^{-9} cm^2/Vs at 6.6×10^4 V/cm.

Figure 4.13a shows the write-read-erase-reread cycles for device **II** with 150 nm of PVK. The duration of each sequential voltage-pulse was about 3.0 s, and currents were measured for 5 points within each voltage level. The current responses as a function of time were plotted with the absolute value of currents. In this case, the write, read, erase, and reread (WRER) voltages are set to the OFF to ON states switching voltage, the read-ON voltage, the ON to OFF states switching voltage, and the read-OFF voltage, respectively. For the sake of convenience in this work we will refer to the ON to OFF states voltage as the erase voltage with the understanding that it does not erase the ON state completely. We investigated different values and polarities of the WRER pulse voltages since the *I-V* characteristic is nearly symmetric. Larger ON/OFF ratios were observed when the pulse voltages were set to W (3.5 V)-R (1.0 V)-E (–8.0 V)-R (1.0 V). Therefore, we used these pulse voltages for further experiments. The good stability of operation measured over 10^3 cycles without any clear degradation confirms the reliability and rewritability of devices **II.** In continuous cycling experiments devices **I** did also exhibit good rewritability but with smaller ON/OFF ratios of only 10. In contrast, devices **III** showed poor switching properties (30% failure in 100 cycles).

The retention times and stress tests of both the ON and OFF states are important for practical applications of nonvolatile electronic memory devices. Devices reported in this work have retained a programmed state for at least 3 days without any applied voltage. The stress test of device **II** for both the ON and OFF states is shown in Figure 6. The ON and OFF states were programmed by applying 3.5 V and –8.0V, respectively, for a pulse duration of 500 ms. The currents in both states were stable for at least 12 hours under a constant voltage of 1.0 V.

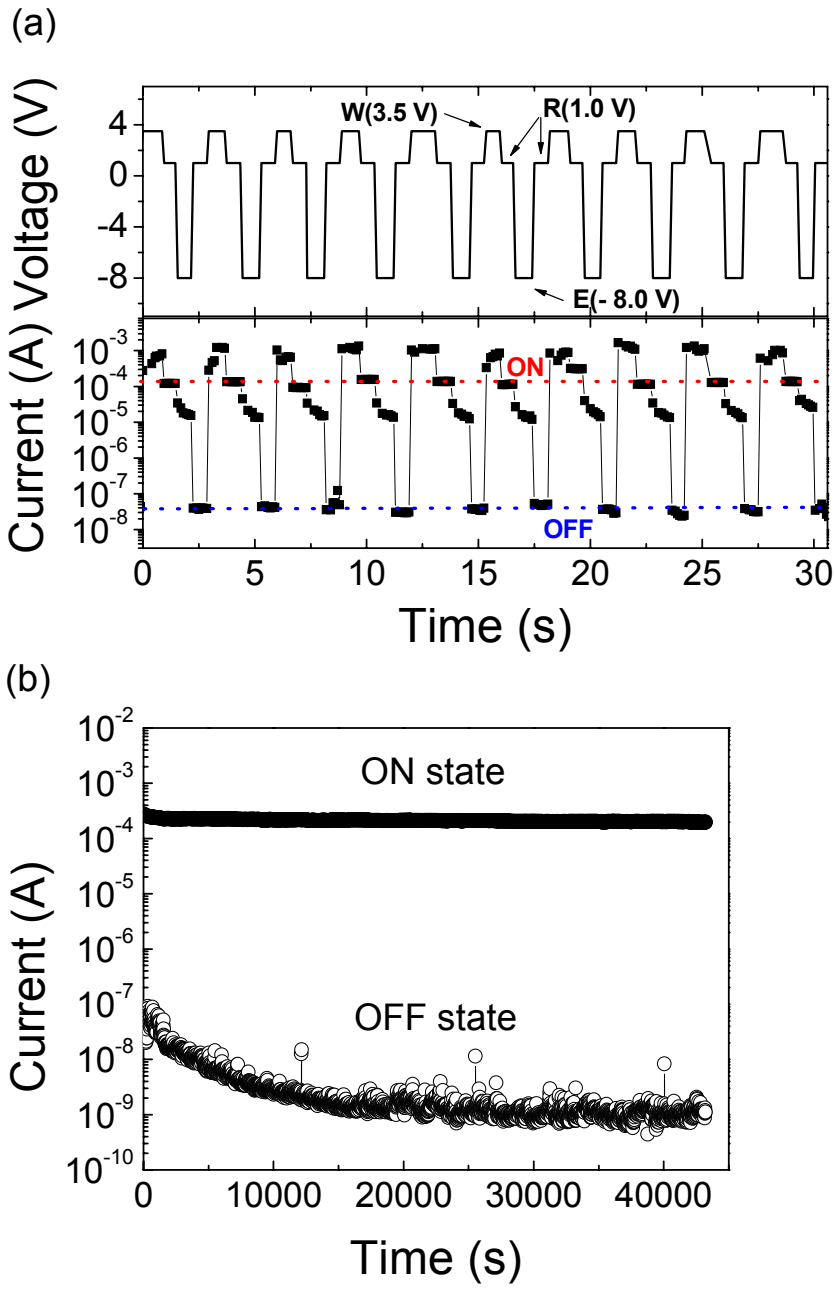

Figure 4.13 (a) Typical current responses to the write-read-erase-reread cycles of device **II** with the structure ITO(+)/Ag-NDs/PVK (150 nm)/Al(–). The write (W), read/reread (R), and erase (E) voltages are 3.5 V, 1.0 V, and –8.0 V, respectively. The red and blue dotted lines represent the average ON and OFF current levels at 1.0 V, respectively. (b) The stress test under an applied 1.0 V bias for ON and OFF states of the same device as in (a). The ON and OFF states have been programmed by a voltage pulse (500 ms) of 3.5 V and –8.0 V, respectively.

The response times of device **II** were measured by using a function generator and an oscilloscope. Figure 4.14 show the transition responses for the device **II** with PVK thickness of 150 nm at writing (4 V) and erasing (9 V) modes. The switching times from the ON state to OFF state and that in opposite direction were at 5 ms and 30 ms, respectively. Similar switching responses were previously observed by Simmons and Verderber[32] for a MIM device comprised of SiO_x layer embedded between Al and Au electrodes.

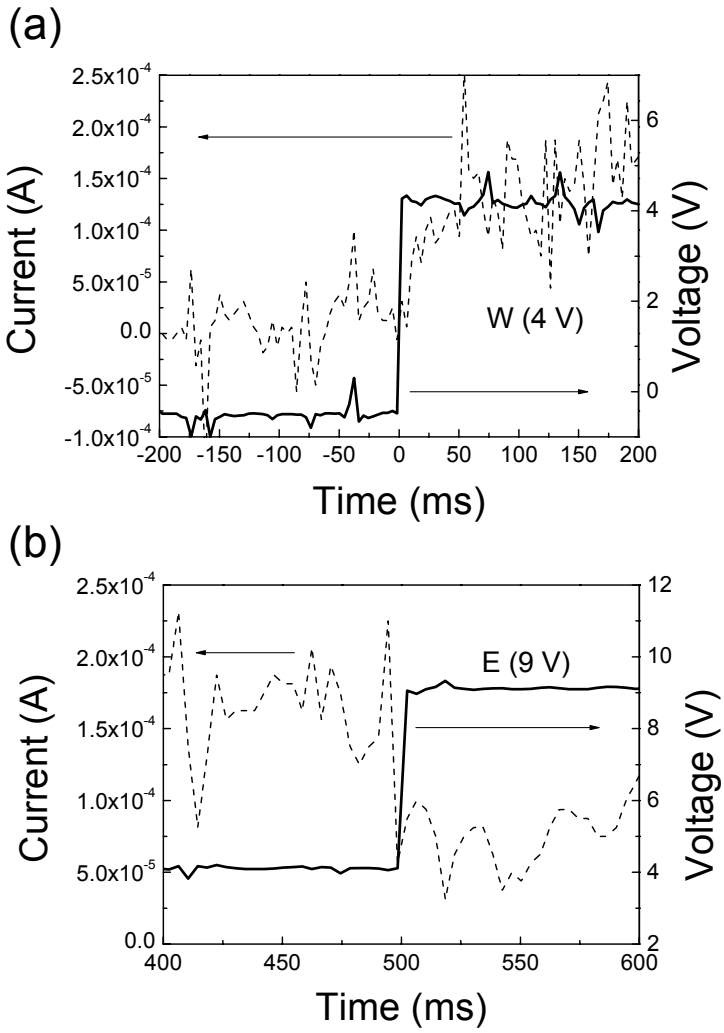

Figure 4.14 Transient responses for the device **II** with the structure ITO(+)/Ag-NDs/PVK (150 nm)/Al(–) at (a) writing (ca. 4 V) and (b)erasing (ca. 9 V) modes.

4.4 Studies of the switching mechanism

4.4.1 Proposed mechanism

Although NDR has been observed in the *J-V* characteristics of devices reported by other groups,[12,22,27-29] two distinctive features are observed in the devices studied in this work. A first observation is that both the current level at voltages between 0 V and V_{max}, and the threshold voltage V_{th}, are insensitive to the PVK thickness and/or how the Ag was incorporated (NPs or NDs). Second, the pristine devices start in the ON state. Such features, also including NDR, could not be explained by either models based on simple space-charge field inhibition of injection due to charge trapping[12,22,29,32] or on simple low-resistance pathways due to filaments formation.[26,30] In the simple charge trap model based on band theory proposed by Simons and Verderber,[32] the currents in both the ON and OFF states should depend on the thickness of the semiconductor layer. In the simple filament model, V_{th} should exhibit a linear-dependence on film thickness and NDR is not anticipated according to this model.[26,30]

The low-resistance states in our devices can be attributed to the inclusion of Al particles or their natural oxide particles[22,30] in the organic layer during the evaporation of the top electrode as many researchers have pointed out.[9,12,22,26-30] We propose the following operation mechanism for our devices. In a pristine state, Al-oxide particles may have a low-tunneling barrier and a small gap between adjacent particles. Thus, these particles will act as low-resistance pathways, when starting from zero bias. The current at low bias may be governed by these tunneling resistances and number of tunneling pathways. At a bias range of around V_{max}, tunneling electrons will start to be trapped in the oxide layer of particles and will be captured by trap sites in the organic layer. In the

NDR region, further trapping of electrons between tunneling sites will raise the interfacial barrier and reduce the current resulting in a switch to the OFF state. At the same time, if Ag-NDs or Ag-NPs are present in the organic layer, electron trapping will also occur at these sites and induce a large reduction of current. Consequently, the current flow should be dominated by a bulk limited transport in the organic layer. When a voltage-sweep starts from zero again, the OFF state will be kept until V_{th} is reached. V_{th} can be identified with the voltage required to detrap electrons from trap sites. This localized low-resistance area due to detrapping could accelerate a subsequently rapid escape of electrons from other sites and lead to an increasing current along that particular pathway. Therefore, the device **II** having trap sites at the interface of both electrodes should show a faster switching and better rewritability than trap sites dispersed homogenously through the organic layer.

This analysis is comparable to that discussed in the context of an electroformed MIM device with the Al/SiO_x/Au structure by Thurstans and Oxley.[43] They argued that the metal islands of the top electrode materials in the insulator are produced during the electroforming process, and that the electronic conduction process is trap-controlled thermally activated tunneling between metal islands. In this conduction process, the currents are governed by low-barrier tunneling through metal islands in the ON state, and by oxygen content and trapped charges in the OFF state. In our devices, the electroforming process is not necessary, and metal islands as activated tunneling sites may be already formed after evaporation of the top electrode (Al). Based on this scenario, the distinctive fact from previously reported organic memory devices that our pristine devices are in the ON state and the fact that the magnitude of the ON state current is

almost insensitive to the thickness of organic layer and the treatment of ITO surface can be explained. Another similarity with the memory effect observed by Thurstans and Oxley[43] is the pronounced noise near the region of NDR of the electrical characteristics.

4.4.2 Influence of light

In order to gain further information on the understanding of the conduction mechamism of our devices, the influence of light on switching properties was investigated. First, the device **II** with a 150 nm-thick PVK layer was operated in room light conditions. The same switching effect as the device in the dark was obtained in room light conditions. Next, the device was exposed to the UV light of a black lamp (λ_{max} = 365 nm), and we measured the change in currents for both the ON and OFF states. In the ON state, the current level was almost insensitive to the UV light. In contrast, the current of the OFF state was increased by a factor of two by the UV light (the distance from the lamp to sample was 10 cm) from ca. 5.0×10^{-5} mA/cm^2 to ca. 1.0×10^{-4} mA/cm^2 at 1.0 V. The increase in the OFF current by irradiation of the UV light may be caused by photo-generated carriers in the PVK layer, and the carriers should be holes in this case. This result supports the conduction mechamism of the OFF state governed by the bulk limited conduction with dominantly holes. It is worth mentioning that the reliability of the switching and stability of ON and OFF states under either of room light and the UV light conditions were confirmed by 100 WRER cycles and the stress test with the continuous biasing condition at 1.0 V for 1 hour. These results indicated that the device **II** with a 150 nm PVK film has a potential ability for operating in light conditions.

4.4.3 Influence of oxygen

Our proposed switching mechanism is similar to that proposed by Thurstans and Oxley.[43] They observed the deterioration of switching properties caused by exposing oxygen and pointed out that the switching properties of the device involving electron traps originating from oxygen or oxide layer of metal particles should depend on oxygen concentrations in operating environments. Therefore, the effect of oxygen on the switching properties of the device **II** with a 150 nm-thivk PVK film was investigated. The decrease in currents began immediately when air was in contact with the device. When the device was transferred into N_2 atmosphere again, the currents increased but generally V_{th}s increased to higher voltages to achieve complete switching from the OFF to the ON states. When the device was exposed to air for three days, conduction changes no longer occurred, and the device was locked into the OFF state. These results are consistent with the observations by Thurstans and Oxley and support our proposed switching mechanism.

4.4.4 Different top electrodes

In order to confirm the formation of diffusive metal particles originating from evaporated top metal electrodes, different top electrodes, Ag (with the same condition for evaporation as Al) and spin-coated poly(3,4-ethylenedioxythiophene) doped with polystyrenesulphonic acid (PEDOT:PSS), were investigated by using the devices **I** and **II** with a 150 nm-thick PVK film. Devices with an Ag top electrode showed the same switching phenomena as the devices with Al top electrodes. However, the devices with the PEDOT:PSS top electrode showed a quite different phenomenon. Typical *I-V*

characteristics of device **I** with ITO(–)/PVK(150 nm)/PEDOT:PSS(210 nm)(+) structure are shown in Figure 4.15. The pristine devices **I** and **II** with the PEDOT: PSS top electrodes showed a high current state when the voltage was swept from –8 V to 8 V. The currents increased and reached a local current maximum (V_{max} = 3 – 4 V) followed by NDR and a local current minimum (V_{min} = 4 – 8 V). After passing V_{min}, the devices were locked in a low current state and never returned in the high current state even though the voltage was swept in the backward direction. The electrical switching effect can occur only in pristine devices. Such a write-once-read many times (WORM) effect was previously observed by the Forrest *et al*.[44] in a device comprised of PEDOT:PSS film embedded between two electrodes. According to their studies, the WORM effect is caused by the change in injection barrier due to the reduction from $PEDOT^+$ to neutral PEDOT at high positive bias conditions. Although the PEDOT:PSS was used as the top electrode in our device, we suspect that the injection barrier change may occur at the interface of the organic layer and the PEDOT:PSS electrode. These results may confirm that diffusive metal particles contribute to the electrically repeatable switching effect.

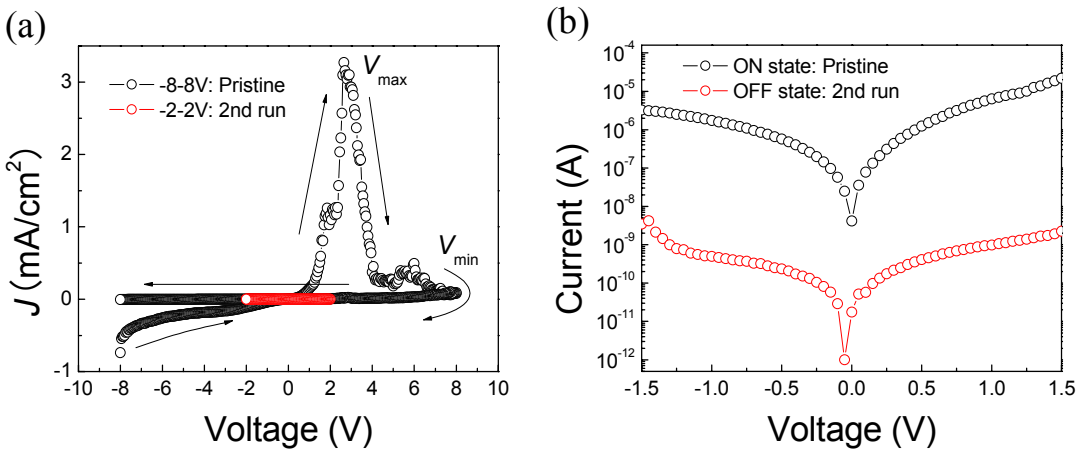

Figure 4.15 Typical *I-V* characteristics of the ITO(–)/PVK, 150 nm/PEDOT:PSS, 210 nm (+) device. (a) Hysteresis of ±8 V voltage window in pristine (black open-circles) and ±2 V voltage window in second run (red open-circles). (b) Semilogarithmic plot of (a) within ±1.5 V voltage window.

4.5 Examination of different organic materials

Other organic semiconducting materials, including compound **I** (Chapter 2), **3a/b** and **4a/b** (Chapter 3), and regioregular poly(3-hexylthiophene) (*rr*-P3HT), were investigated by using the structures of device **I** and **II**. The selection of these materials is based on two considerations. First, these materials are solution processable. Uniform thin films can be formed by spin coating as with PVK. Second, these materials have different energy band-gap compared to PVK (optical band gap ΔE_{op} = 3.5 eV) > **3a/b** or **4a/b** (ΔE_{op} = 2.8 eV) > compound **I** (ΔE_{op} = 2.3 eV) > *rr*-P3HT (ΔE_{op} = 1.7 eV[45]). These optical band-gaps are estimated from the onset of absorption for these materials in solution. Solutions of compound **I** (20 mg / 1mL toluene), **4a/b** or **3a/b**(20 mg / 1mL $CHCl_3$), and *rr*-P3HT (15 mg / 1mL chlorobenzene) were also spun on the cleaned ITO and the Ag-NDs modified ITO substrates to obtain a 200 nm, 120 nm, and 230 nm films,

respectively. The chemical structure of the materials used in this chapter as the organic layers are shown in Figure 4.16.

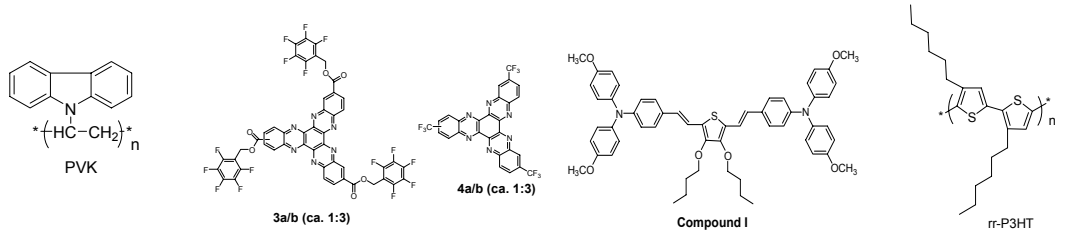

ΔE_{OP} = 3.5 eV > ΔE_{OP} = 2.9 eV > ΔE_{OP} = 2.3 eV > ΔE_{OP} = 1.7 eV[45]

Figure 4.16 Chemical structures of the materials used in this chapter as the organic layers.

Electrical switching phenomena with relatively small ON/OFF ratios compared to the PVK device were observed in devices **II** with the other three materials. The reliabilities of the rewritable switching in WERE cycles with the other three materials were inferior to those of the PVK devices (Table 4.3). Interestingly, devices **I** with films of compound **I**, compound **4a/b** or **3a/b**, and rr-P3HT showed no switching effect, while the significant switching effect was observed in device **I** with a PVK film. The stability of the programmed states in the device **II** with compound **I** film was examined by the stress test with the continuous biasing condition at 1.0 V. The currents of the ON state were stable for 6 hours while the currents of the OFF state increased suddenly to the same level of the ON state after applying 1.0 V for 50 min. Analogously, the currents of the OFF states in the devices **II** with films of **4a/b** (or **3a/b**) and *rr*-P3HT were unstable in the stress tests. Although the origin of the difference between PVK and the other three materials remains unclear, the comparison study of different materials as the organic layer indicates that larger band-gap materials may be favorable for active layers in organic memory devices attributed to charge trapping. One anticipates that trapped

charges in small band-gap materials may be unstable and detrapped easily. Table 4.3 summarized the switching properties of all devices studied in this chapter.

Table 4.3 Summary of the switching properties of the devices evaluated in this chapter.

Organic layer	Device Type	Switching properties	Operation voltages in WRER cycles and % of success in 100 cycles
PVK (150nm) ΔE_{OP} =3.5 eV	**I** Al top-electrode	Symmetrical *I-V* ON/OFF ratio: 10~20	W(3.5V)-R(1.0V)-E(-8.0V)-W(1.0V) 100%
	I Ag top-electrode	Symmetrical *I-V* ON/OFF ratio: 10~20	W(3.5V)-R(1.0V)-E(-8.0V)-W(1.0V) 90%
	I PEDOT:PSS Top-electrode	WORM effect ON/OFF ratio: 10^2~10^3	
	II Ag-NPs on ITO	Symmetrical *I-V* ON/OFF ratio: 10^2~10^3	W(3.5V)-R(1.0V)-E(-8.0V)-W(1.0V) 90%
	II Annealed Ag-NPs on ITO(Ag-NDs)	Symmetrical *I-V* ON/OFF ratio: 10^3~10^4	W(3.5V)-R(1.0V)-E(-8.0V)-W(1.0V) 100%
	III 1 wt.% dispersed Ag-NPs	Symmetrical *I-V* ON/OFF ratio: 10~20	W(3.5V)-R(1.0V)-E(-8.0V)-W(1.0V) 40%
	III 3 wt.% dispersed Ag-NPs	Symmetrical *I-V* ON/OFF ratio: 10^2	W(3.5V)-R(1.0V)-E(-8.0V)-W(1.0V) 40%
	III 10 wt.% dispersed Ag-NPs	Symmetrical *I-V* ON/OFF ratio: 10^2~10^3	W(3.5V)-R(1.0V)-E(-10.0V)-W(1.0V) 70%
4a/b (or **3a/b**) (120 nm) ΔE_{OP} =2.8 eV	**I** Al top electrode	No switching	
	II Annealed Ag-NPs on ITO (Ag-NDs)	Symmetrical *I-V* ON/OFF ratio: 10 Short retention OFF state: 30 min	W(3.5V)-R(1.0V)-E(-8.0V)-W(1.0V) 20%
Compound **I** (200 nm) ΔE_{OP} =2.3 eV	**I** Al top electrode	No switching	
	II Ag-NPs on ITO	Symmetrical *I-V* ON/OFF ratio: 10^2~10^3	W(3.0V)-R(1.0V)-E(8.0V)-W(1.0V) 70%
	II Annealed Ag-NPs on ITO (Ag-NDs)	Symmetrical *I-V* ON/OFF ratio: 10^2~10^3 Short retention OFF state: <1 hours	W(3.0V)-R(1.0V)-E(8.0V)-W(1.0V) 100%

Table 4.3 (CONT.)

rr-P3HT (230 nm) ΔE_{OP} =1.7 eV[45]	**I** Al top electrode	No switching	
	II Annealed Ag-NPs on ITO (Ag-NDs)	Switching occurred only negative bias ON/OFF ratio: 100 Short retention OFF state: 30 min	W(-3.0V)-R(-1.0V)-E(-8.0V)-W(-1.0V) 40%

4.6 Concluding remarks

The effects of the trapping sites utilizing Ag-NDs and Ag-NPs on the electrical memory properties in devices based on single-organic layer structures were studied. The electrical characteristics based on the comparison between three different device structures, thickness dependence, and temperature dependence indicated that the currents of the ON state may be attributed to low-resistance pathways through metal particles originating from the top metal electrode in the organic layer, and those of the OFF state may be controlled by electrons trapped to metal particles including Ag-NDs and Ag-NPs. And the comparison study between different materials for the organic layer indicated that a large band-gap material may be favorable as the active layer in the organic memory devices attributed to charge trapping. The device comprised of the Ag-NDs attached on the ITO electrode and PVK layer showed a drastic enhancement of the ON/OFF ratio up to 10^4. This level of performance could be achieved by modifying the ITO electrodes with some Ag-NDs that act as trapping sites, reducing the current in the OFF state. This device demonstrated the potential capability as a nonvolatile organic memory device, according to the results of the WRER cycle test, the stress tests, and the retention time measurements for the programmed states. The materials used in this device are readily available and relatively low-cost, and the active layer can be fabricated by solution

processes. We believe that this is the first demonstration of an organic memory device using Ag-NDs on an ITO electrode deposited by solution processing, and this approach to create NDs on the surface of substrates can easily control their physical properties, size, and density by using different kinds of NPs. Such material and process optimization will lead to further improved memory properties.

4.7 References

1. C. W. Tang and S. A. Van Slyke, Appl. Phys. Lett. **51**, 913 (1987).

2. J. H. Burroughs, D. D. C. Bradley, A. R. Brown, R. N. Marks, K. Mackay, R. H. Friend, P. L. Bums, and A. B. Holmes, Nature (London) **347**, 539 (1990).

3. F. Garnier, R. Hajlaoui, A. Yassar, and P. Srivastava, Science **265**, 1684 (1994).

4. N. S. Sariciftci, L. Smilowitz, A. J. Heeger, and F. Wudl, Science **258**, 1474 (1992).

5. A. Szymanski, D. C. Larson, and M. M. Labes, Appl. Phys. Lett. **14**, 88 (1969).

6. H. Carchano, R. Lacoste, and Y. Segui, Appl. Phys. Lett. **19**, 414 (1971).

7. L. Ma, J. Liu, S. Pyo, and Y. Yang, Appl. Phys. Lett. **80**, 362 (2002).

8. L. Ma, J. Liu, and Y. Yang, Appl. Phys. Lett. **80**, 2997 (2002).

9. L. Ma, S. Pyo, J. Ouyang, Q. Xu, and Y. Yang, Appl. Phys. Lett. **82**, 1419 (2003).

10. A. Bandyopadhyay and A. J. Pal, J. Phys. Chem. B **107**, 2531 (2003).

11. T. Oyamada, H. Tanaka, K. Matsushige, H. Sasabe, and C. Adachi, Appl. Phys. Lett. **83**, 1252 (2003).

12. L. D. Bozano, B. W. Kean, V. R. Deline, J. R. Salem, and J. C. Scott, Appl. Phys. Lett. **84**, 607 (2004).

13. L. Ma, Q. Xu, and Y. Yang, Appl. Phys. Lett. **84**, 4908 (2004).

14. T. Ouisse and O. Stéphan, Org. Electron. **5**, 251 (2004).

15. H. S. Majumdar, A. Bolognesi, and A. J. Pal, Synth. Met. **140**, 203 (2004).

16. S. H. Kang, T. Crisp, I. Kymissis, and V. Bulović, Appl. Phys. Lett. **85**, 4666 (2004).

17. J. H. A. Smits, S. C. J. Meskers, R. A. J. Janssen, A. W. Marsman, and D. M. de Leeuw, Adv. Mater. **17**, 1169 (2005).

18. R. J. Tseng, J. Huang, J. Ouyang, R. B. Kaner, and Y. Yang, Nano Lett. **5**, 1077 (2005).

19. Q. D. Ling, Y. Song, S. J. Ding, C. X. Zhu, D. S. H. Chan, D. L. Kwong, E. T. Kang, and K-G. Neoh, Adv. Mater.**17**, 455 (2005).

20. Q. D. Ling, S. L. Lim, Y. Song, C. X. Zhu, D. S. H. Chan, E. T. Kang, and K. G. Neoh, Langmuir **23**, 312 (2007).

21. J. Ouyang, C.-W. Chu, C. Szmanda, L. Ma, and Y. Yang, Nature Mater. **3**, 918 (2004).

22. L. D. Bozano, B. W. Kean, M. Beinhoff, K. R. Carter, P. M. Rice, and J. C. Scott, Adv. Funct. Mater.**15**, 1933 (2005).

23. S. Paul, A. Kanwal, and M. Chhowalla, Nanotechnology **17**, 145 (2005).

24. H. S. Majumdar, J. K. Baral, R. Osterbacka, O. Ikkala, and H. Stubb, Org. Electron. **6**, 188 (2005).

25. C.-W. Chu, J. Ouyang, J.-H. Tseng, and Y. Yang, Adv. Mater. **17**, 1440 (2005).

26. D. Tondelier, K. Lmimouni, D. Vuillaume, C. Fery, and G. Haas, Appl. Phys. Lett. **85**, 5763 (2004).

27. W. Tang, H. Shi, G. Xu, B. S. Ong, Z. D. Popovic, J. Deng, J. Zhao, and G. Rao, Adv. Mater. **17**, 2307 (2005).

28. J. Chen and D. Ma, Appl. Phys. Lett. **87**, 023505 (2005).

29. J. Chen and D. Ma, J. Apple. Phys. **100**, 034512 (2006).

30. M. Cölle, M. Büchel, and D. M. de Leeuw, Org. Electron. **7**, 305 (2006).

31. Q. Wang, Z. T. Song, W. L. Liu, C. L. Lin, and T. H. Wang, Apple. Surf. Sci. **230**, 8 (2004).

32. J. G. Simmons and R. R. Verderber, Proc. Roy. Soc. A. **301**, 77 (1967).

33. R. G. Freeman, K. C. Grabar, K. J. Allison, R. M. Bright, J. A. Davis, A. P. Guthrie, M. B. Hommer, M. A. Jackson, P. C. Smith, D. G. Walter, and M. J. Natan, Science **267**, 1629 (1995).

34. A. D. McFarland and R. P. Van Duyne, Nano Lett. **3**, 1057 (2003).

35. S. B. Rondinini, P. R. Mussini, F. Crippa, and G. Sello, Electrochem. Commun. **2**, 491 (2000).

36. G. Chumanov, K. Sokolov, B. W. Gregory, and T. M. Cotton, J. Phys. Chem. **99**, 9466 (1995).

37. W. Cheng, S. Dong, and E. Wang, Electrochem. Commun. **4**, 412 (2002).

38. H. Kajii, A. Sakakibara, H. Okuya, T. Morimune, and Y. Ohmori, Thin Solid Films **499**, 415 (2006).

39. S. Y. Kang and K. Kim, Langmuir **14**, 226 (1998).

40. P. M. Borsenberger, E. H. Magin, M. Van der Auweraer, and F. C. De Schryver, Phys. Stat. Sol. A **140**, 9 (1993).

41. N. F. Mott and D. Gurney, Electronic Processes in Ionic Crystals (Oxford University Press, New York, 1940), p.172.

42. M. B. Khalifa, D. Vaufrey, A. Bouazizi, J. Tardy, and H. Maaref, Materials Science and Engineering C **21**, 277 (2002).

43. R. E. Thurstans and D. P. Oxley, J. Phys. D: Appl. Phys. **35**, 802 (2002).

44. (a) S. Möller, C. Perlov, W. Jackson, C. Taussig, and S. R. Forrest, Nature **426**, 166 (2003). (b) S. Möller ans S. R. Forrest, J. Appl. Phys. **94**, 7811 (2003). (c) S. Smith and S. R. Forrest, Appl. Phys. Lett. **84**, 5019 (2004).

45. T.-A. Chen, X. Wu, and R. D. Rieke, J. Am. Chem. Soc. **117**, 233 (1995).

46. C. D. Bain, E. B. Troughton, Y.-T. Tao, J. Evall, G. M. Whitesides, and R. G. Nuzzo, J. Am. Chem. Soc. **111**, 321 (1989).

47. C. Donley, D. Dunphy, D. Paine, C. Carter, K. Nebesny, P. Lee, D. Alloway, and N. R. Armstrong, Langmuir **18**, 450 (2002).

48. W. Wang, T. Lee, and M. A. Reed, Phys. Rev. B **68**, 035416 (2003).

CHAPTER 5

ELECTRICAL SWITCHING EFFECTS IN AN AIR-STABLE SOLUTION-PROCESSED DEVICE CONTAINING SILVER ION AND A HEXAAZATRINAPHTHYLENE DERIVATIVE

5.1 Introduction

Organic memory devices using small molecules or polymeric materials have received considerable attention because of their potential for low-cost scalable fabrication, material variety, and mechanical flexibility. In addition, two-terminal organic memory devices offer the possibility for having several device layers stacked on top of one another to form a high-density array. In terms of low cost and ease of fabrication, solution processing, such as solution casting or direct printing, would be quite desirable. A number of two-terminal memory devices using thin films of small molecules as one of the active layers have been demonstrated;[1-5] however, in many cases using small organic molecules, the preparation of these films is currently restricted to a high vacuum thermal evaporation method due to their strong tendencies for crystallization or poor solubilities in common solvents. For example, switching phenomena in films containing charge-transfer complexes of metals and small organic molecules, such as Cu : 7,7,8,8-Tetracyanoquinodimethane (TCNQ) complex, have been reported.[6,7] However, Cu:TCNQ complex films prepared by a solution growth method showed a poly-crystalline morphology leading to problems associated with film-uniformity and device-reproducibility. To solve these problems, Okamoto *et al*.[8] fabricated a Cu:TCNQ based switching device by vacuum co-deposition allowing for control of Cu and TCNQ

concentrations and their film morphologies. Although polymeric materials have been selected as the active layers to be applicable to solution processing,[9-11] electrode materials have been restricted to metals or metal oxides prepared by dry processes. Conductive polymers, particularly poly(3,4-ethylenedioxythiophene) doped with polystyrenesulphonic acid (PEDOT:PSS),[12,13] have been widely explored as electrodes that are printable or patternable by solution processes. Although sheet resistances of PEDOT:PSS are higher than those of metals or metal oxides, it is possible to replace a metal electrode by PEDOT:PSS in a low-information memory application such as a replacement for magnetic strips of credit cards. Recently, organic memory devices based on ion-diffusion systems and using PEDOT:PSS layers doped with salts and plasticizers were demonstrated.[14,15] However, the programmed states of these devices showed relatively short retention times within one hour. Moreover, in these devices the PEDOT:PSS layers are supported by ITO electrodes. Organic memory devices using a stand-alone PEDOT:PSS film as one of the electrodes have not been reported.

The objective of this chapter is to design and characterize a (semi-)transparent organic memory device that can be fabricated by all-solution processing and operated in ambient conditions without any device encapsulation. This attempt is encouraged by a simple fabrication process utilizing the ability for solution processing of organic materials. In order to achieve the objective, we studied rewritable switching effects in thin solution processed films comprised of $AgNO_3$ and a small organic molecule anticipated to possess electron-transport properties, hexaazatrinaphthylene (HATNA) derivatives, compounds **3a/b** and **4a/b** (described in Chapter 3). A thin film of cross-linked poly-4-vinylphenol (PVP), which is a popular polymer dielectric material,[16,17] was

used as an ion-diffusion barrier layer. The PVP layer introduced between one of electrodes and the $AgNO_3$:**3a/b** or **4a/b** complex film plays an important role in generating rewritable electrical switching phenomena. Another interesting feature of these devices is that they are semi-transparent because PEDOT:PSS and ITO are used as the top and bottom electrodes, respectively. PEDOT:PSS electrodes were prepared by spin-coating and ink-jet printing. Such a (semi) transparent memory device may be useful for a current controlling element for display applications. Fabrication and characterization of the devices were performed in ambient conditions without any device encapsulation. *I-V* characteristics of these devices show a negative differential resistance regime. Switching from the low resistance to the high resistance state starts at 5.0 ± 3.0 V with PEDOT:PSS as the anode, and the reverse switch is observed at –7.0 ± 3.0 V. The electrical characteristics suggest that migrations of silver ions within the complex layer contribute to the reversible switching phenomena. The reliability and rewritability of devices have been confirmed by 200 write-read-erase-reread cycles, stress tests for 6 hours, and retention of programmed states for 3 days.

5.2 Operation hypothesis and device design

5.2.1 Operation hypothesis

In order to design an air-stable organic memory device, considerations of the origin of electrical switching are important. In the previous chapter, the switching properties of the organic memory devices were attributed to charge trapping deteriorated in ambient conditions. Thus, we considered an electrical switching effect originating from ion-diffusions in organic layers as a potential air-stable active component. Although these systems may be influenced by oxygen, we expect them to have a higher tolerance to oxygen concentrations than systems based on charge trapping.

$AgNO_3$ was selected as the active material potentially producing ion-diffusion of Ag^+ ions in an organic layer. The selection of Ag^+ ion is based on three considerations. First, amongst the known solid state ionic materials, Ag^+ ion conducting glasses have attracted considerable attention in recent years primarily due to their relatively higher values of ionic conductivity ($\sigma = 10^{-2} - 10^{-3}$ S/cm) at room temperature compared to other superionic solids.[18] A potential high ionic conduction may be important for inducing a high ON/OFF ratio in electronic memory application. Second, organic memory devices using ion-diffusion of Ag^+ ions or the redox reactions of Ag have not been reported. Third, unsubstituted 5,6,11,12,17,18-hexaazatrinaphthylene, HATNA, is known to be a ligand for transition metal ions, and a polymeric $AgNO_3$:HATNA complex has been reported by Bu *et al*.[19] According to their analyses based on single-crystal X-ray diffraction, each Ag^I center in the complex acts as a two-connecting node by connecting two ligands of HATNA, and the complex exhibits twofold interpenetrating networks with the two-connected (Ag^I) and three-connected (HATNA) nodes.

Thus, by analogy, we consider it is likely that the Ag cation complexes to the **3** or **4** in our materials as well, and these complexes with relative low $AgNO_3$ concentrations could be dissolved by a solvent such as chloroform, if isomer mixture **3a/b** or **4a/b**, which is a higher solubility and a lower melting point indicating a weaker molecular interaction compared to either of the pure isomers, are used.

Mixed solutions of $AgNO_3$:**3a/b** or **4a/b** with molar ratios exceeding 1:2 yielded an insoluble orange solid after mixing in the dark. This observation is consistent with the hypothesis that our HATNA derivatives, **3a/b** and **4a/b**, can act as a ligand for Ag^+ ion, and that the mixtures form partially "polymeric networks" at high $AgNO_3$ concentrations. However, we have not been able to obtain a single crystal suitable for definitive characterization; this is not unexpected since we used a mixture of isomers. For the sake of convenience in this chapter we will refer to the mixtures of $AgNO_3$:**3a/b** or **4a/b** as "complexes" with the understanding that they are not pure stoichiometric materials.

Next, we considered how to generate electronically switching effects by using the Ag^+ complex film. If the complex film is embedded between two electrodes as a single layer diode structure, currents will flow linearly as a function of applied voltage due to an ionic conduction in both positive and negative bias conditions. In this case, field-induced migrations of Ag^+ ions towards both electrodes depending on the direction of electric field will occur. Thus, it might be difficult to obtain a switching effect in this device. In order to generate a switching effect such as a large hysteresis or a change in the conductivity at a specific voltage, we considered an insulating layer introduced at the interface between the complex film and one of the electrodes. The insulating layer may act as an ion-diffusion barrier layer to block further ion-migration towards the electrode

covered with the insulating layer. The accumulation of Ag^+ ions at the interface of the complex layer and the electrode without insulating layer may reduce the barrier for charge injection resulting in a high conduction state, and the transport of Ag^+ ions from the electrode towards the insulating layer may reduce the conduction of the device. Therefore, if we set the electrode with the insulating layer as a cathode, the interlayer due to the accumulation of Ag^+ ions at the anode (without insulating layer) may be already created when the voltage is swept from a high negative bias, and the migration of Ag^+ ions towards the cathode will start at a specific positive bias resulting in decrease in current flow. After Ag^+ ions have migrated toward the cathode, the migration of Ag^+ ions toward the anode will be difficult unless a specific negative bias is applied to the device. In order to generate a repeatable electrical switching, the key point should be how to avoid the reduction from Ag^+ to Ag or the metallization at both the interfaces of electrodes. Because the reduced Ag may be difficult to transport in the complex film and to oxidize unless a large positive bias is applied. Therefore, the insulating layer may help to prohibit the reduction of Ag^+ ions at the cathode side. However, a small operational voltage is still required to prevent the reduction of Ag^+ ions at the anode side. The schematic illustrations of this hypothesis are shown in Figure 5.1.

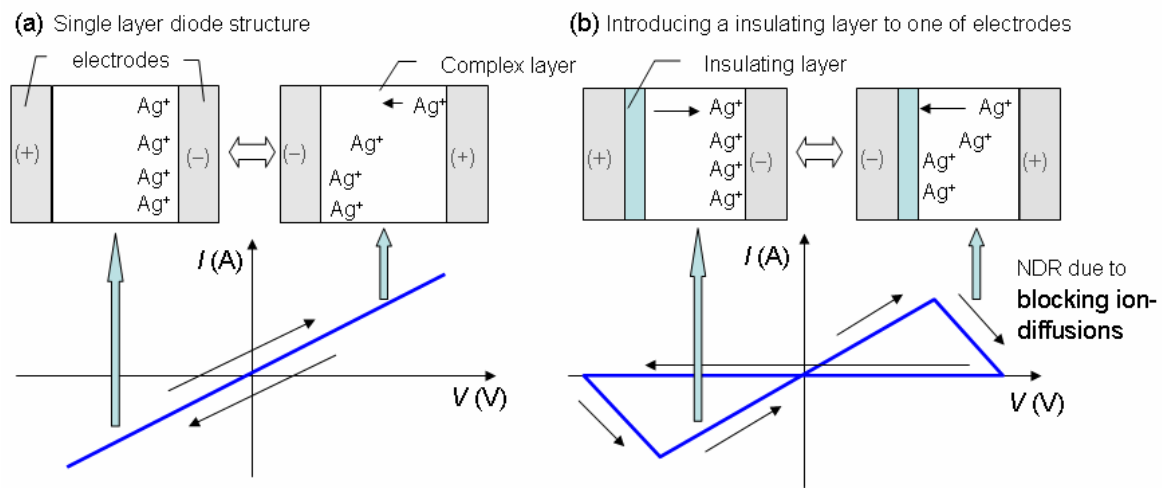

Figure 5.1 Schematic illustrations of (a) single layer diode structure and the predicted *I-V* curve, and of (b) the proposed device structure and the hypothetical electronic switching effect by using the Ag^+ ion complex film and the insulating layer.

5.2.2 Device design

Cross-linked PVP was used as the insulating layer introduced at the interface between the complex film and ITO bottom electrode. Spin-coated and ink-jet printed PEDOT:PSS were used as the top electrode for semi-transparent structure. The device using an ITO-coated glass substrate and a spun PEDOT:PSS electrode is denoted by G-ITO/PVP/$AgNO_3$:**3a/b** or **4a/b**/PEDOT:PSS-S (Figure 5.2a), and the device using an ITO-coated polyethylenenaphthalate (PEN) substrate and a PEDOT:PSS electrode prepared by ink-jet printing is denoted by PEN-ITO/PVP/$AgNO_3$:**3a/b** or **4a/b**/PEDOT:PSS-I (Figure 5.2b).

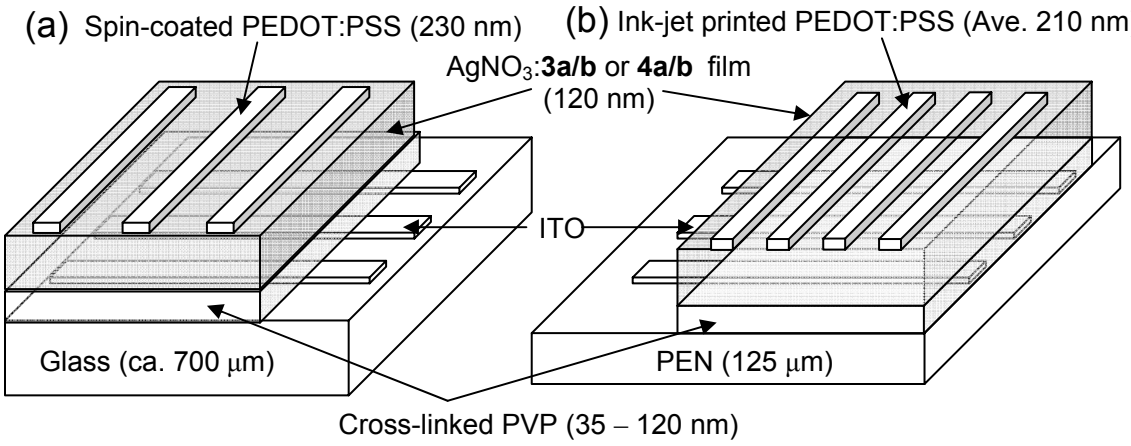

Figure 5.2 Schematic device structures of two different types. (a) Glass substrate G-ITO/PVP/$AgNO_3$:**3a/b** or **4a/b**/PEDOT:PSS-S (S) and (b) PEN-ITO/PVP/$AgNO_3$:**3a/b** or **4a/b**/PEDOT:PSS-I.

5.2.3 Experimental

The solutions containing mixtures of $AgNO_3$ and **3a/b** or **4a/b** (Chapter 3) were prepared by mixing a solution of $AgNO_3$ (Aldrich) in CH_3CN and a solution of **3a/b** or **4a/b** in $CHCl_3$ with specific molar ratios of $AgNO_3$: **3a/b** or **4a/b**, 0:1 (0 mol% $AgNO_3$), 1:10 (9.1 mol% $AgNO_3$), 3:10 (23 mol% $AgNO_3$), and 1:2 (33 mol% $AgNO_3$). The **3a/b** or **4a/b** solutions used had a concentration of 0.034 mol/L; different concentrations of $AgNO_3$ solutions were used to adjust the volume ratio of **3a/b** or **4a/b** solutions : $AgNO_3$ solution to a constant value of 10:1. Mixed solutions with ratios exceeding 1:2 yielded an insoluble solid after mixing under dark conditions. Pre-coated ITO-glass substrates (ca.150 nm thickness ITO, 60 Ω/□, Colorado Concept Coatings LLC) were used as the bottom electrodes for the devices, and spin coated PEDOT:PSS, as the top electrodes Also, pre-coated ITO-PEN substrates (125 μm PEN, ca.100 nm thickness ITO, 120 Ω/□, LINTEC Corp.) were used as the bottom electrodes for the devices using the top

electrodes of ink-jet printed PEDOT:PSS. In either case the ITO substrates were washed with detergent, de-ionized water, ethanol, and acetone, and then treated with air-plasma for 1 min. PVP films on ITO substrates were formed by spin coating. The PVP solution was formulated as the follows: 70 mg of PVP (MW = 20,000, Aldrich) , 25 mg of polymelamine-co-formaldehyde (CYMEL 300 RESIN, Cytec Industries Inc.) as a cross-linking agent, and 5 mg *p*-toluenesulfonic acid monohydrate (Aldrich) as a catalyst for the cross-linking reaction were dissolved in 1.9 g of *n*-butanol. After spin coating, the substrates were subsequently cross-linked by heating at 175 ºC for 1 h on a hot plate. The thicknesses of PVP films were controlled by varying spin speeds and the concentrations of the PVP solution. Films of 50 nm, 70 nm, and 120 nm thicknesses were obtained at 5000 r.p.m., 4000 r.p.m., and 3000 r.p.m., respectively. A solution of PVP solution diluted by an additional 2.0 g of *n*-butanol was used for the production of films thinner than 50 nm. We obtained a 35 nm film by using the diluted solution at the spin speed of 5000 r.p.m. After cooling substrates at room temperature, $AgNO_3$: **3a/b** or **4a/b** "complex" solutions were spun (1000 r.p.m for 90 s) on the cross-linked PVP layer and dried at 150 ºC for several minutes to yield the complex film with ca. 120 nm thickness. Finally, a high conductive grade of PEDOT:PSS solution (Baytron F-HC, H.C. Starck Inc.) was spun or printed on the $AgNO_3$: **3a/b** or **4a/b** complex films and dried at 150 ºC for 1 hour to form the top electrode. An average thickness of ca. 230 nm was obtained by spin coating at 1000 r.p.m. for 90 s using the original solution of Baytron F-HC, and an average thickness of ca. 210 nm was obtained by ink-jet printing using a diluted solution (1.5 mL DMSO was added into 10 mL Baytron F-HC). The ink-jet printing was carried out by using Dimatix Materials Printer DMP-2831 (Dimatix, Inc.). The sheet resistivities

of both PEDOT:PSS films were measured by a four point probe, and found to be in the range of 1.2 – 3.0 k Ω/□. Active areas of the devices using the spin coated PEDOT:PSS electrodes were isolated by a sharp blade, and each active area was around 0.05 cm^2. In the devices using the printed PEDOT:PSS electrodes, the active area of 0.03 cm^2 was defined by a cross-point of a ITO line (width of 2.5 mm) and a PEDOT:PSS line (width of 1.2 mm). A typical cross-section profile of the ink-jet printed PEDOT:PSS line was a mountain shape with a maximum thickness (ca. 300 nm) in the middle and minimum thicknesses (ca. 150 nm) at both edges. All processes involved in the device fabrication were performed in ambient conditions. POM images were obtained using an Olympus BX51 microscope equipped with an Olympus U-TU1 X digital camera and an Instec ST200 temperature controller. *I-V* characteristics and write-read-erase-reread cycles were carried out by using a computer-controlled Keithley 2400 source meter. The capacitances of devices were measured by used a Agilent 16048A test leads connected to a Agilent 4284A precision LCR meter. These electrical measurements were performed under ambient conditions.

5.3 Film morphologies of the $AgNO_3$:4a/b complex

The morphologies of $AgNO_3$:**4a/b** films in G-ITO/PVP/$AgNO_3$:**4a/b**/PEDOT:PSS-S structures were investigated with a polarized optical microscopy (POM) under crossed polarizers. The POM images of films with the $AgNO_3$:**4a/b** in molar ratios of 0:1 and 1:10 reveal crystalline textures (Figure 5.3a and b). For the pure **4a/b** film (i.e., 0:1), crystalline textures exhibiting grain boundaries and defects are observed over the whole active area. The crystalline textures in the 1:10 ratio film are isolated from each other and their shapes resemble the spherulite texture obtained in the slow cooled films of **3b** (Chapter 3). In contrast, the films with a higher fraction of $AgNO_3$ made from the $AgNO_3$:**4a/b** with molar ratios of 3:10 and 1:2 produce optical images that are isotropic. These results suggest that, at least within this concentration regime, $AgNO_3$ reduces the tendency of **4a/b** film to crystallize and allows formation of a uniform film by spin coating. An insoluble orange solid was precipitated at $AgNO_3$ concentration ratios of greater than 1:2, presumably due to formation of partially polymeric networks;[19] thus, the maximum ratio for solution processing is close to 1:2. Analogously, the film morphologies of the AgNO3:**3a/b** with the same range of molar ratio as the $AgNO_3$:**4a/b** were also investigated, and similar phenomena were obtained.

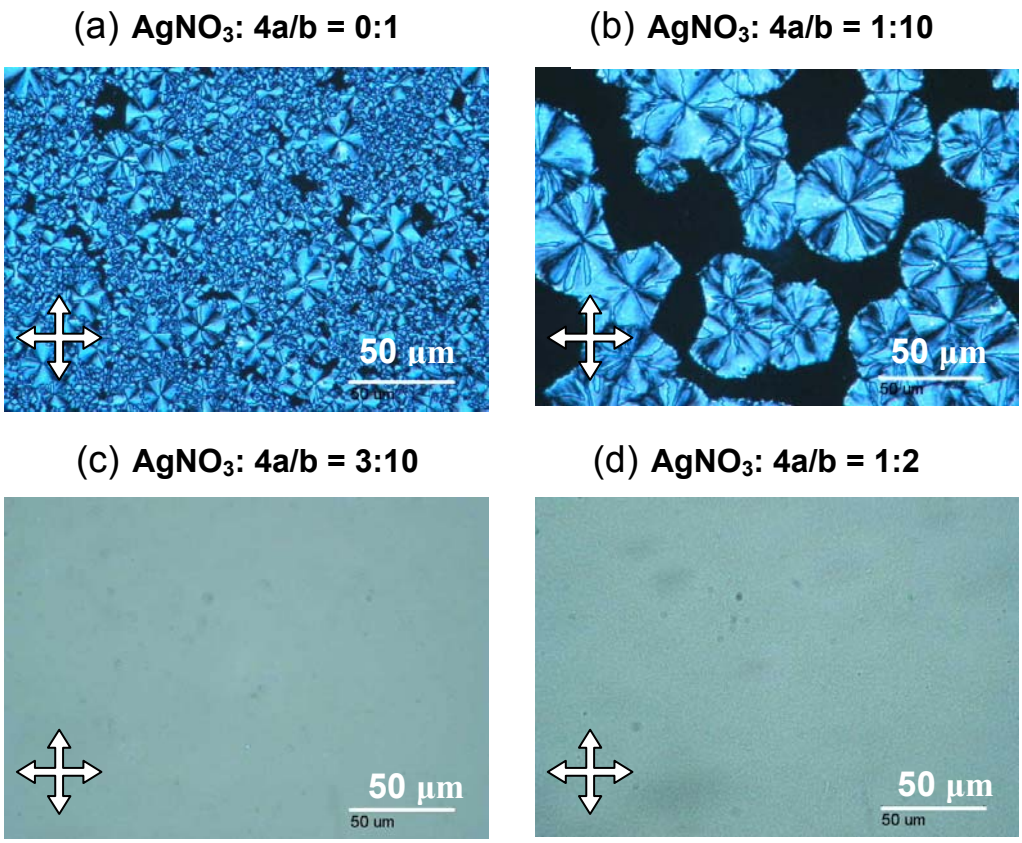

Figure 5.3 Polarized optical microscope images of $AgNO_3$:**4a/b** layers between ITO/PVP and PEDOT:PSS electrodes with $AgNO_3$:**4a/b** molar ratios of (a) 0:1, (b) 1:10, (c) 3:10, and (d) 1:2. The images of (c) and (d) are overexposed. The arrows represent the direction of the polarizer and analyzer.

5.4 Dependence of switching characteristics on Ag concentration

Typical *I-V* characteristics of G-ITO/PVP/$AgNO_3$:**4a/b**/PEDOT:PSS-S devices with films using different $AgNO_3$:**4a/b** molar ratios are shown in Figure 5.4. In this chapter, all *J-V* curves were plotted with the absolute value of current density and taken after several voltage-sweep cycles at a sweep-rate of 0.4 V/s. Usually, pristine devices showed higher current densities over the entire voltage range than did devices that had been cycled several times; however, the current levels were stabilized after several cycles.

Significant memory effects are observed in the devices with (b) 1:10, (c) 3:10, and (d) 1:2 molar ratios but importantly not in device (a) without $AgNO_3$. The current level in the device without $AgNO_3$ is much higher than that of other devices, and currents follow almost a linear relationship with applied voltage. This high conduction behavior may be caused by leakage currents due to the poor film quality containing pin-holes or defects as shown in Figure 5.3a.

When voltages are swept from –15 V towards 15 V with ITO as the cathode, the devices using the $AgNO_3$:**4a/b** "complex" films are in the low-resistance state (ON states) compared to when voltages are swept in the backward direction in the range from –7.0 ± 3.0 V to 10 ± 2.0 V. In the forward direction of the voltage-sweep, currents reach a local maximum current at 5.0 ± 2.0 V and then decrease to a local minimum current at 10 ± 2.0 V. The region between the local maximum and minimum in currents is defined as the negative differential resistance (NDR) regime. When the direction of the voltage-sweep is reversed after the voltage reaches 15 V, the devices remain in the high-resistance state (OFF states) until at a threshold voltage of –7.0 ± 3.0 V where the switching from the OFF state to the ON state occurs. The offset voltages at which there is zero current in the device decreases with increasing $AgNO_3$ concentration. It is possible that the offset voltages and residual currents at 0 V are probably caused by redox reactions of **4a/b** due to a small number of mobile ions originating from the PEDOT:PSS electrodes. The same phenomenon was observed previously in devices using PEDOT:PSS electrodes.[15,20] The ON/OFF ratios at 5 V are 500, 6000, and 800 with $AgNO_3$:**4a/b** concentrations of 1:10, 3:10, and 1:2, respectively. The device with the lowest $AgNO_3$ concentration (1:10 molar ratio) showed a relatively low current level in the ON state and a large threshold voltage

(–8.0 ± 2.0 V). In contrast, a high current level in the OFF state and a small threshold voltage (–6.0 ± 2.0 V) were observed in the device with the highest $AgNO_3$ concentration (1:2 molar ratio).

These results indicate that the origin of these hysteresis effects is probably field-induced migration of Ag^+ ions towards electrodes or redox reactions of Ag^+ at the interface electrodes, particularly the migration of Ag^+ ions towards electrodes may occur dominantly in this operational voltage window. The accumulation of Ag^+ ions at the interface of the complex layer and the PEDOT:PSS electrode may reduce the barrier of charge injection from PEDOT:PSS into the complex layer resulting in an ON state, and the migration of Ag^+ ions from the PEDOT:PSS electrode towards the PVP layer may increase the barrier height of charge injection because the PVP layer may act as a barrier layer for ion diffusion. The migration of Ag^+ ions towards the PVP layer will start at a specific positive voltage which is the starting point of the NDR regime. The accumulated Ag^+ ions near the PVP layer will be difficult to move unless a negative bias is applied, that is, at the threshold voltage. According to this scenario, the device with a low $AgNO_3$ concentration may have a small reduction of the barrier of charge injection due to a small amount of the accumulated Ag^+ ions at the interface of the complex film and the PEDOT:PSS electrode, and the device with a high $AgNO_3$ concentration may have a difficulty of removing Ag^+ ions from the interface of the complex film and PEDOT:PSS electrode completely, which would lead to a relatively large current density in the OFF state.

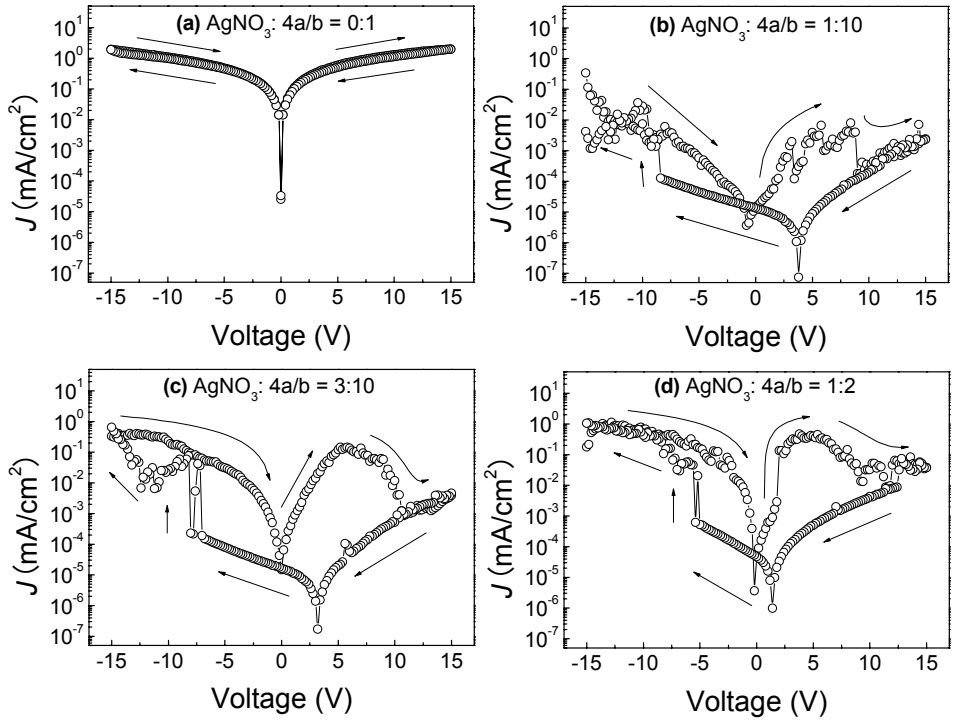

Figure 5.4 Typical *I-V* characteristics of G-ITO/PVP/$AgNO_3$:**4a/b**/PEDOT:PSS-S devices with $AgNO_3$:**4a/b** molar ratios of (a) 0:1, (b) 1:10, (c) 3:10, and (d) 1:2. The thicknesses of the PVP layers and the $AgNO_3$:**4a/b** complex layers are 50nm and 120nm, respectively.

To further understand the switching mechanism, capacitance-voltage (*C-V*) measurements were carried out for the G-ITO/PVP/$AgNO_3$:**4a/b**/PEDOT:PSS-S device with $AgNO_3$:**4a/b** in the molar ratio of 3:10 using the constant sweep-rate of 0.4 V/s. A progressively increasing DC bias with a test voltage of V_{rms} = 1.0V at 1 kHz was applied to the device as indicated by the numbers in Figure 5.6. The change in injection barriers due to the formation of an interface layer caused by the accumulated Ag^+ ions should be accompanied by a change in the device capacitance.[21] The hysteresis behaviors are observed in both (a) the capacitance and (b) in the conductance as shown in Figure 5.5.

The hysteresis shapes of the capacitance-voltage and the conductance-voltage are similar to that of the *I-V* curve, where the changes in capacitance and conductance occur dominantly in the forward direction of voltage-sweep, and the switching from the low/high to the high/low capacitance/conductance states and *vice versa* correspond with the NDR and V_{th} in the *I-V* curve. These results support our proposed switching mechanism.

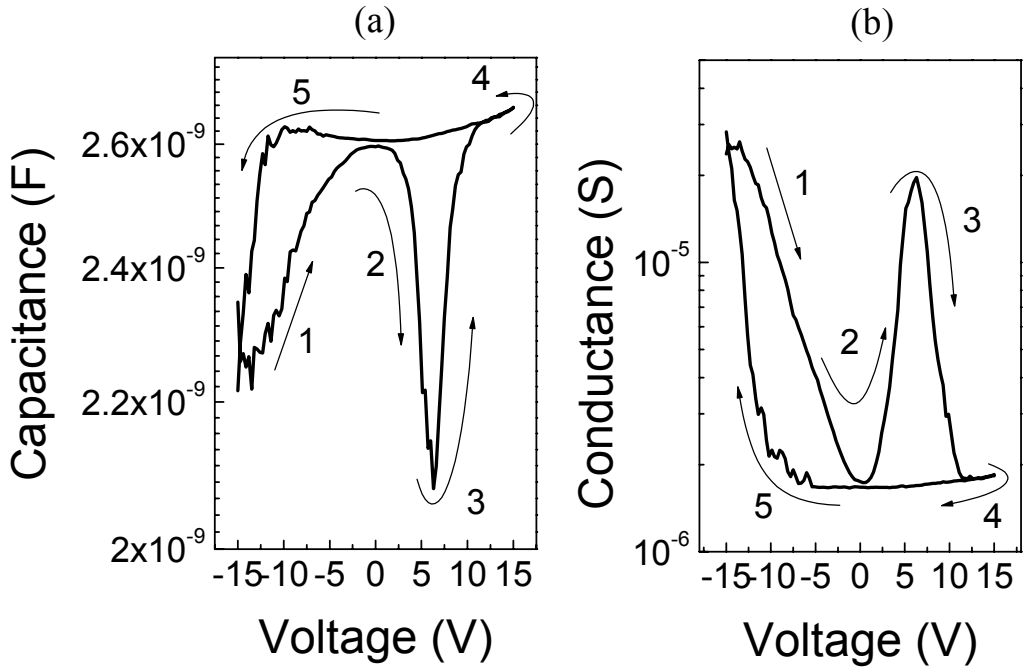

Figure 5.5 (a) Capacitance and (b) conductance as a function of DC voltages for a G-ITO/PVP/$AgNO_3$:**4a/b**/PEDOT:PSS-S device with $AgNO_3$:**4a/b** in a molar ratio of 3:10 and a PVP layer of 50 nm.

5.5 Dependence of switching characteristics on PVP thickness

To confirm the role of the PVP layer, we investigated how the switching characteristics depend on the thickness of the PVP layer in G-ITO/PVP/$AgNO_3$:**4a/b**/PEDOT:PSS-S devices with a $AgNO_3$:**4a/b** molar ratio of 3:10.

Figure 5.6 shows typical *I-V* characteristics of devices with PVP layers of (a) 0 nm, (b) 50 nm, (c) 70 nm, and (d) 120 nm, respectively. The device without a PVP layer shows a high current level and no switching effect. The devices with PVP layers clearly show a dependence of the switching characteristics on the PVP thickness, and, in particular, the device with a PVP layer of 50 nm displays a larger hysteresis and a lower threshold voltage. These results indicate that large ON/OFF ratios and facile migration of Ag^+ ions require a thin dielectric layer possessing the capability of being a barrier to the diffusion of ions.

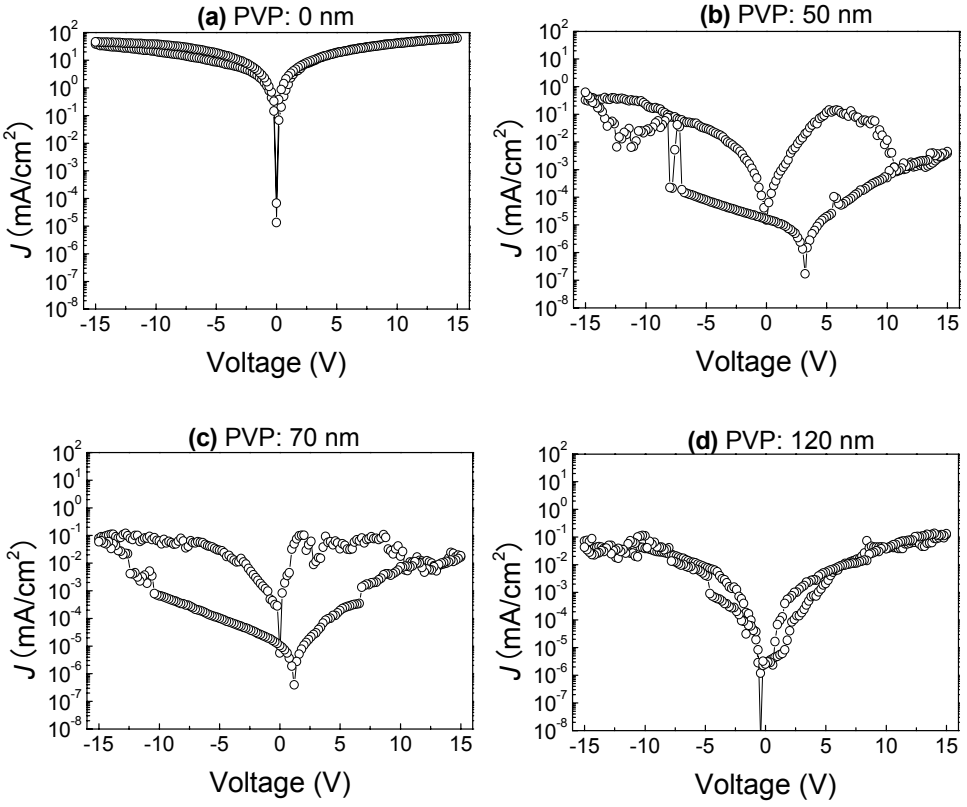

Figure 5.6 Typical *I-V* characteristics of G-ITO/PVP/$AgNO_3$:**4a/b**(120 nm)/PEDOT:PSS-S devices with a PVP thickness of (a) 0 nm, (b) 50 nm, (c) 70 nm, and (d)120 nm. Every device uses the complex layers of $AgNO_3$:**4a/b** in a molar ratio of 3:10.

5.6 Reliability of switching

Keeping in mind the observed dependence of the switching effect on the concentration of $AgNO_3$ and the thickness of the PVP layer, we fabricated PEN-ITO/PVP/$AgNO_3$:**4a/b** (120 nm)/PEDOT:PSS-I devices with $AgNO_3$:**4a/b** in a molar ratio of 3:10 and a PVP layer of 35 nm. The *I-V* characteristics of this device after the write-read-erase-reread (WRER) cycle experiment and after stress testing for 6 hours (× 4sets: the ON and OFF states with two different reading voltages) are shown in Figure 5.7. The device with a reduced PVP thickness operates over a lower voltage range (–10 V to 10 V) compared to the devices with thicker PVP films that were discussed previously. The NDR regime begins around 4 V, threshold voltages are about –4 V, and the ON/OFF ratios are 10^2 – 10^3 at ±2 V for this device. Figure 5.8a shows 10 typical WRER cycles for this device. The length of each voltage-pulse was about 1.2 s. The voltages for write, read, and erase were –10 V, –2 V, and 10 V, respectively. In the case, the erase voltage means a reset voltage required to switch from the ON state to the OFF state. The ON/OFF ratios of 10^2 – 10^3 in the WRER cycle experiment are consistent with those of the voltage-sweep experiments. WRER cycle tests with a read voltage of 2 V showed similar results to those with a read voltage of –2 V. The reliability and rewritability of this device was confirmed by 200 operating cycles. Figure 5.8b shows the change in the currents of both the ON and OFF states at –2 V as a function of the number of WRER cycles. Although the currents of both the ON and OFF states decrease slightly with increasing the number of cycles, ON/OFF of about 10^2 – 10^3 are maintained.

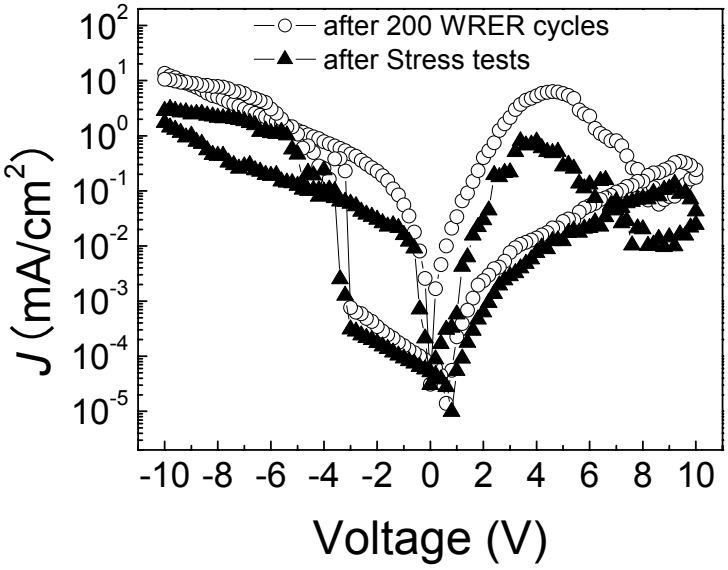

Figure 5.7 *I-V* characteristics of PEN-ITO/PVP/$AgNO_3$:**4a/b**(120 nm)/PEDOT:PSS-I device with a $AgNO_3$:**4a/b** molar ratio of 3:10 and a PVP layer of 35 nm after the 200 WRER cycles (open circles) and after the stress testing for 6 hours × 4 sets (closed circles).

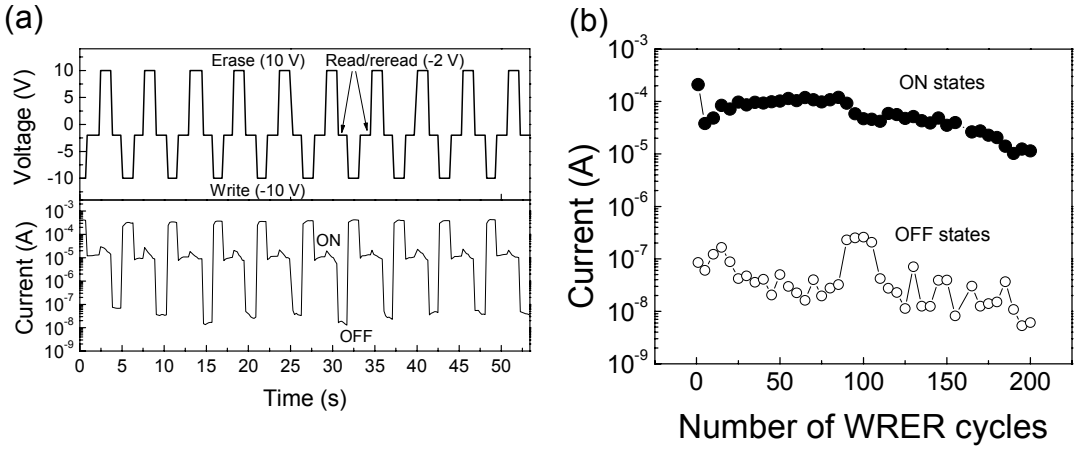

Figure 5.8 (a) Typical current responses to WRER cycles of the same device as in Figure 5.7. The write, read/reread, and erase voltages are –10 V, –2V, and 10 V, respectively. (b) Currents of the ON and OFF states as a function of the number of WRER cycle for the same device as in (a).

The stability of PEN-ITO/PVP/$AgNO_3$:**4a/b**/PEDOT:PSS-I devices was measured under continuous bias conditions; i.e., the device was subjected to a so-called stress test. The stress tests for both the ON and OFF states at two different read voltages are shown in Figure 5.9a. The ON and OFF states were programmed by applying –10 V and 10V, respectively, for a pulse duration of 1.0 s. The currents of the ON states being read with a voltage of 2 V decrease rapidly, and the ON state is only retained for about 30 min. The decay rate of the ON state is faster than that of the OFF state. In contrast, the currents of the ON state decrease more slowly when reading with a voltage of –2 V, and the decay rate is almost same as that of the OFF state. Consequently, the observed ON/OFF ratios can be retained for at least 6 hours. When the ON state were read with a small negative bias, Ag^+ ions would stay at the interface of the complex film and the PEDOT:PSS electrode, consequently a longer retention may be possible compared to the case of reading with a small positive bias. One of reasons for the decrease in currents of both the ON and OFF states during the WRER cycles and the stress tests is probably a degradation of the PEDOT:PSS electrode. Indeed, the current level of the device after the stress test decreases over the entire voltage range in the voltage-sweep experiment as shown in Figure 5.7. The retention abilities of both the ON and OFF states were tested by leaving the device without any applied voltage in ambient and dark conditions after programming. This experiment was carried out by using the device after the 200 WRER cycles and the stress tests for 6 hours (× 4 sets). The programming conditions were the same as those during the stress tests. Figure 5.9b shows *I-V* characteristics for voltages from –2 V to 2 V for the device with several different time periods between programming and reading. The ON state can be retained still after 3 days when read with a negative

bias, but the currents in the positive bias region for a device that was programmed to be in the ON state decrease to the same level as the OFF state after 1 day. The currents of the OFF state did not change significantly even after 3 days.

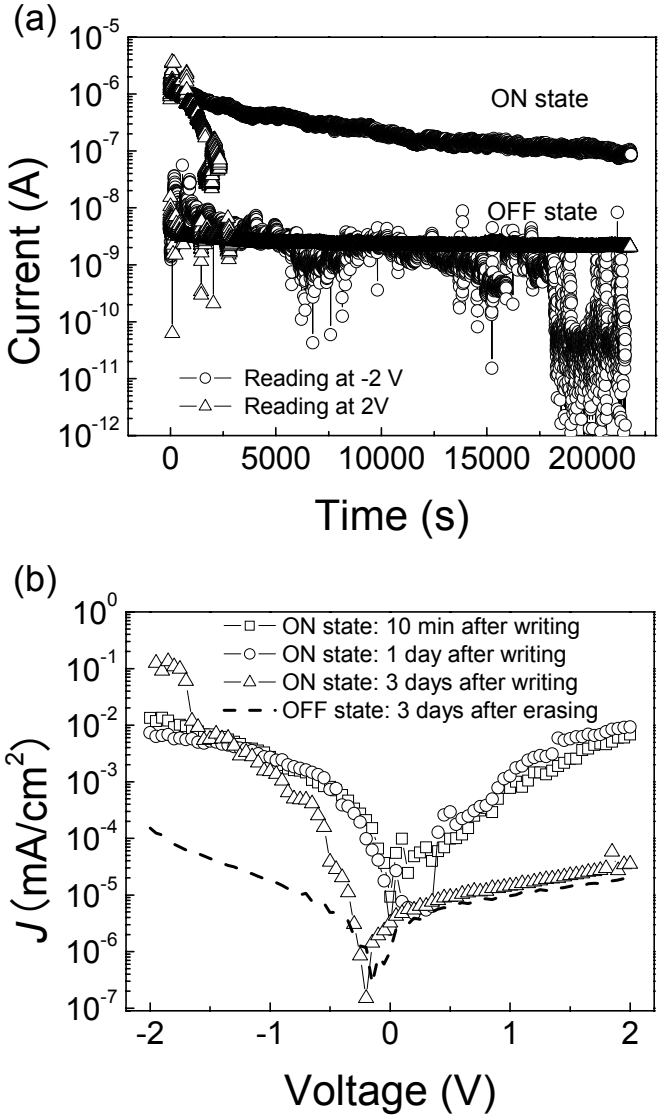

Figure 5.9 (a) Stress tests with applying –2 V and 2 V on the ON and OFF states of the same device as in Figure 5.7 and 5.8. (b) Comparison of *I-V* characteristics (from –2 V to 2 V) at different times after being programmed. The ON states measured 10 min, 1 day, and 3 days after programming are represented by the open square, the open circle, and the open triangle, respectively. A typical *I-V* characteristic of the OFF state is represented by the dash line. In these experiments, the ON and OFF states were programmed by voltage pulse of –10 V and 10 V for 1.0 s, respectively.

The response times of the PEN-ITO/PVP/$AgNO_3$:**4a/b** (120 nm)/PEDOT:PSS-I devices with $AgNO_3$:**4a/b** in a molar ratio of 3:10 and a PVP layer of 35 nm were measured by using a function generator and an oscilloscope. Figure 5.10 show the transition responses at writing (–10 V) and erasing (10 V) modes. The delay time from the OFF state to the ON state was approximately a few milliseconds. However, the switching from the ON state to the OFF state lasted ca. 300 ms.

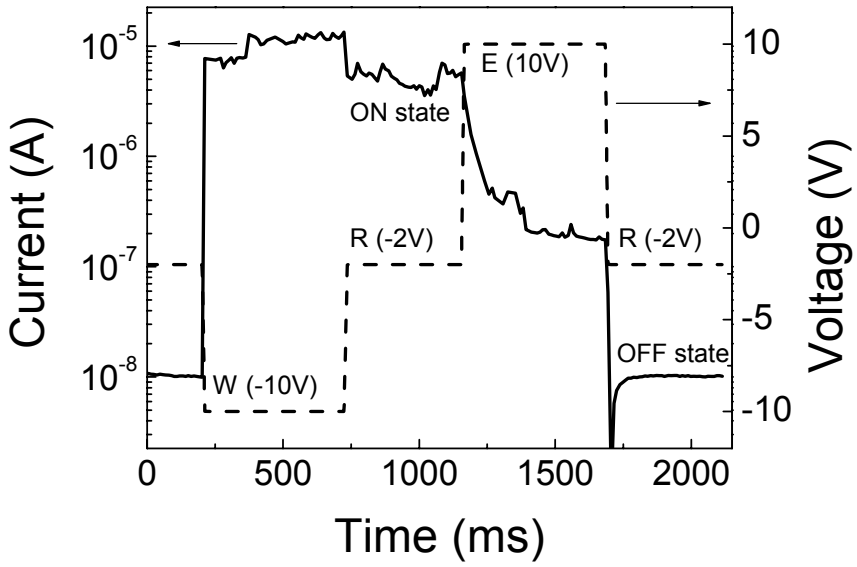

Figure 5.10 Transient responses for PEN-ITO/PVP/$AgNO_3$:**4a/b** (120 nm)/PEDOT:PSS-I device with $AgNO_3$:**4a/b** in a molar ratio of 3:10 and a PVP layer of 35 nm at writing (–10 V) and erasing (10 V) modes.

One important feature for a (semi)transparent device is the ability to operate under room-light or sun-light conditions. This property is effectively desirable for display or open-air applications. Thus, the influence of a room-light on the switching properties was investigated by using PEN-ITO/PVP/$AgNO_3$:**4a/b** (120 nm)/PEDOT:PSS-I device with $AgNO_3$:**4a/b** in a molar ratio of 3:10 and a PVP layer of 35 nm. Figure 5.11 shows the

comparisons of (a) *I-V* characteristics, (b) WRER cycles, (c) stress test for ON states, and (d) retention ability for both the ON and OFF states between dark and in room-light conditions. In the *I-V* characteristics and WERE cycle experiments, no significant differences were observed between the two different conditions. The stress test reading at –2V in room-light conditions shows a faster decay rate of the ON currents compared to those in dark conditions. In the case of operation under room-light conditions, the ON currents decreased by one order of magnitude (from 10^{-6} A to 10^{-7} A) after reading for 30 min. According to this result, the device should be kept in the dark when reading at continuous bias conditions for a long time is required. However, the retention abilities of both the ON and OFF states without a continuous bias are not influenced strongly by room-light. In room-light conditions, both the ON and OFF currents were maintained for 3 days as in the dark. According to these results, it is necessary to improve the reliability of this device in room-light conditions, particularly the stability of the ON currents with continuous bias conditions.

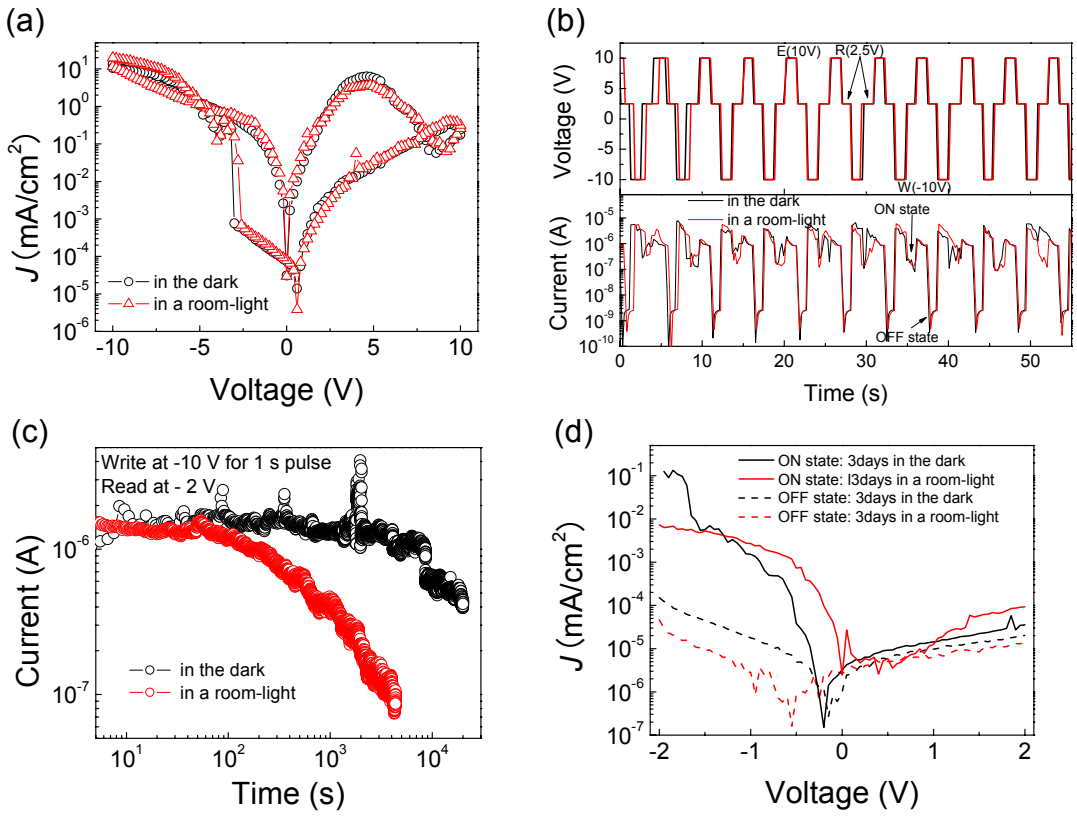

Figure 5.11 Comparison of the switching properties between in the dark and in a room-light condition: (a) typical *I-V* characteristics, (b) WERE cycles (the write, read/reread, and erase voltages are –10 V, 2.5V, and 10 V, respectively), (c) the stress test for the ON state, and (d) *I-V* characteristics (from –2 V to 2 V) at different times after being programmed. In these experiments, the ON and OFF states were programmed by voltage pulse of –10 V and 10 V for 1.0 s, respectively.

5.7 Concluding remarks

Rewritable organic devices utilizing films of $AgNO_3$: **3a/b** or **4a/b**, thin polymer dielectric layers, and conducting polymer electrodes were demonstrated. These devices were fabricated using only solution processing techniques (spin-coating and ink-jet printing) except for the ITO-coated electrode substrates. The morphologies of the complex film are influenced by the $AgNO_3$ concentration, and uniform thin films are obtained with $AgNO_3$:**4a/b** molar ratios of 3:10 and 1:2 by spin coating. The presence of a PVP film between the ITO electrode and the complex film plays an important role in generating a switching effect. The operation voltages were able to be lowered by reducing the PVP thickness, which act as a diffusion barrier to ions. The accumulation of Ag^+ ions mainly at the interface of the complex film and PEDOT:PSS anode may contribute to the switching effect. The device using pre-coated ITO on plastic substrate, 35 nm PVP, a $AgNO_3$:**4a/b** (3:10) thin film, and a PEDOT:PSS electrode prepared by ink-jet printing showed reproducible switching characteristics with ON/OFF ratios of 10^2–10^3 under ambient conditions without any device encapsulation. These device characteristics may be useful for a low-cost memory application.

5.8 References

1. L. Ma, J. Liu, S. Pyo, and Y. Yang, Appl. Phys. Lett. **80**, 362 (2002).

2. L. Ma, J. Liu, and Y. Yang, Appl. Phys. Lett. **80**, 2997 (2002).

3. L. D. Bozano, B. W. Kean, V. R. Deline, J. R. Salem, and J. C. Scott, Appl. Phys. Lett. **84**, 607 (2004).

4. D. Tondelier, K. Lmimouni, D. Vuillaume, C. Fery, and G. Haas, Appl. Phys. Lett. **85**, 5763 (2004).

5. J. Chen and D. Ma, Appl. Phys. Lett. **87**, 023505 (2005).

6. R. S. Potember, T. O. Poehler, and D. O. Cowan, Appl. Phys. Lett. **34**, 405 (1979).

7. R. S. Potember, T. O. Poehler, A. Rappa, D. O. Cowan, and A. N. Bloch, Synth. Met. **4**, 371(1982).

8. T. Oyamada, H. Tanaka, K. Matsushige, H. Sasabe, and C. Adachi, Appl. Phys. Lett. **83**, 1252 (2003).

9. J. Ouyang, C.-W. Chu, C. Szmanda, L. Ma, and Y. Yang, Nature Mater. **3**, 918 (2004).

10. Q. D. Ling, Y. Song, S. J. Ding, C. X. Zhu, D. S. H. Chan, D. L. Kwong, E. T. Kang, and K.-G. Neoh, Adv. Mater.**17**, 455 (2005).

11. J.-S. Choi, J.-H. Kim, S.-H. Kim, and D. H. Suh, Appl. Phys. Lett. **89**, 152111 (2006).

12. L. B. Groenendaal, F. Jonas, D. Freitag, H. Pielartzik, and J. R. Reynolds, Adv. Mater. **12**, 481 (2000).

13. S. Kirchmeyer and K. Reuter, J. Mater. Chem. **15**, 2077 (2005).

14. J. H. A. Smits, S. C. J. Meskers, R. A. J. Janssen, A. W. Marsman, and D. M. de Leeuw, Adv. Mater. **17**, 1169 (2005).

15. V. Frank, M. C. J. Stefan, and A. J. J. René, Chem. Mater. **18**, 2707 (2006).

16. H. Klauk, M. Halik, U. Zschieschang, G. Schmid, W. Radlik, and W. Weber, J. Appl. Phys. **92**, 5259 (2002).

17. H. Klauk, M. Halik, U. Zschieschang, G. Schmid, W. Radlik, and W. Weber, Adv. Mater. **14**, 1717 (2002).

18. R. C. Agrawal and R. Kumar, J. Phys. D: Appl. Phys. 29, 156 (1996).

19. X.-H. Bu, K. Biradha, T. Yamaguchi, M. Nishimura, T. Ito, K. Tanaka, and M. Shionoya, Chem. Commun., 1953 (2000).

20. S. Smith and S. R. Forrest, Appl. Phys. Lett. **84**, 5019 (2004).

21. M. Cölle, M. Büchel, and D. M. de Leeuw, Org. Electron. **7**, 305 (2006).

CHAPTER 6

CONCLUSIONS AND OUTLOOK

The research presented in this thesis focuses on *I-V* characteristics of organic films embedded between two electrodes. The objectives of the thesis were to find molecular glasses or solution processable materials possessing high charge carrier mobilities in the films by through analyzing *I-V* characteristics, and to design organic memory devices by using interfacial controlled organic/metal junctions. The research can be divided into two parts: (1) the study of charge transport properties in films of organic semiconductors based on molecular glasses by using theoretical *I-V* characteristics and (2) the study of anomalous *I-V* characteristics of solution processable material films introducing additional interlayer as organic memory devices.

First of all, we investigated the limiting factor of *I-V* characteristics as a mobility measurement technique. According to the comparison studies with TOF, FET, and SCLC, TOF led to the highest mobility values whereas FET and SCLC mobility values were limited by contact resistance and injection efficiency, respectively. The study using the HT material allowing the high injection efficiency (0.43) showed excellent agreement among three different techniques. It confirms the validity of using *I-V* characteristics in the SCLC regime to determine the mobility of organic semiconductors. The measured mobility depends on the injection efficiency, and a low injection efficiency may lead to an underestimation of the intrinsic mobility of the material. HATNA derivatives tri-substituted by electron withdrawing groups were synthesized and separated as the symmetrical isomer **a**, the less symmetrical isomer **b**, and their mixtures **a**/**b** as potential

ET molecular glasses. The presence of two isomers had important implications for film morphology and effective mobility. Using *I-V* characteristics based on SCLC regime, the effective mobilities of the HATNA derivatives **3** and **4** were determined. Amorphous films of the isomer mixture, **3a/b** (ca. 1:3), showed effective mobilities in the range of 10^{-2} cm^2/Vs, which are the same order as the highest reported value for molecular glasses. The films of **4a/b** (ca. 1:3) showed effective mobilities in the range of 10^{-3} cm^2/Vs. On the other hand, films of the pure isomers, **a** and **b**, showed strong tendencies to crystallize. Using the same condition of the film preparation, the pure isomer **b** of both **3** and **4** showed higher effective mobilities than those of the isomer mixtures. However, for the pure isomer **a** of both **3** and **4** we could not obtain films of sufficient quality allowing for determination of their effective mobilities. The preparation of **a** films may be restricted to a high-vacuum thermal evaporation method.

The effective mobility extracted by the SCLC method may be limited by the injection efficiency, which depends on the energy barrier between the conduction bands of the semiconductors and the work function of the electrode. Therefore, the estimation of the EAs and IPs of **3** and **4** was attempted by comparison to the solid state EA and IP values either of parent HATNA and Alq_3. EAs of **3** and **4** were estimated as –3.1 – –3.5 eV from the first reduction potentials in the CV measurements and the solid state EA values of the reference compounds. However, IPs of **3** and **4** were still unclear due to the lack of a first oxidation potential in the CV measurements. Thus, IPs of **3** and **4** were merely estimated as a larger than that of **1** (> 6.6 eV), according to the trend of the DFT calculations. In the device using ITO for the both anode and cathode, the injection barriers for both holes and electrons are relatively large values of > 1.8 eV and 1.3 – 1.7

eV, respectively, if the work function of ITO is set as 4.8 eV. Although the injection barrier for electrons is smaller than that for holes, it is difficult to obtain an intrinsic mobility or mono-carrier mobility due to the relatively large injection barrier for both holes and electrons. This is one of drawback of the SCLC method based on *I-V* characteristics. A comparison to other techniques for evaluating charge carrier mobilities is important for further understanding charge transport properties of these compounds. In addition, to gain an understanding of the relationship between film preparation methods (morphologies) or device structures and charge transport properties of HATNA derivatives, a comparison study between SCLC and FET measurements using thin films prepared by evaporation or co-evaporation varying isomer ratios should be interested due to the potential to control morphologies and mobilities.

Another interesting topic worthy of continued the study for this class of compounds is their capability of forming large, self-organized crystal domains with a specific molecular orientation of **3b** and **4b**. In a film of **3b** with the slow cooling rate of 1.0 °C / min, large spherulites having a diameter exceeding a few micrometers were obtained. The self-organization behavior of **3b**, consisting of nucleation and directional crystal growth, suggests that some alignment techniques may obtain macroscopically ordered structures. Such highly-ordered structures could be promising candidates as organic semiconductor materials for FET devices due to an anisotropic charge transporting property. It may be possible to control the direction of charge transport and the channel direction between source-drain electrodes.

In the study of anomalous *I-V* characteristics for organic memory devices, the influences of trapping sites utilizing Ag-NDs and Ag-NPs, and the accumulation of Ag^+

ions at the interface of electrodes on the *I-V* characteristics were investigated. In the devices using the Ag-NDs and Ag-NPs, electrical switching behavior was observed. Based upon the observed electrical characteristics, the currents of the ON state may be attributed to low-resistance pathways through included metal particles originating from the top metal electrode in the organic layer, and those of the OFF state may be dictated by electrons trapped to metal particles including the Ag-NDs and Ag-NPs. The comparison study between different materials for the organic layer indicated that a large band-gap material may be favorable as the active layer in the organic memory device attributed to charge trapping. The device comprised of the Ag-NDs attached on the ITO electrode and PVK layer showed the drastic enhancement of the ON/OFF ratio up to 10^4. This device demonstrated the potential to function as a nonvolatile organic memory device, based upon the large ON/OFF ratio, the 1000 write-read-erase-reread cycles, the stress tests for 12 hours, and the long retention times at least for 3 days in the programmed states. This level of performance could be achieved by modifying the ITO electrodes with some Ag-NDs that act as trapping sites, reducing the current in the OFF state.

The solution-based self-assembly approach to create NDs on the surface of substrates can be used to easily control their physical properties, size, and density by using different kinds of NPs. Also, the interfacial morphology of a top electrode and an organic layer can be controlled by changing the conditions for the evaporation of the top electrode, such as deposition rate and temperature of the substrate. Such material and process optimization will lead to further improved memory properties.

In the devices using ion diffusion of Ag^+ ions, rewritable memory effects in ambient conditions were demonstrated by using complex films of $AgNO_3$: **4a/b** (or **3a/b**),

thin polymer dielectric layers, and conducting polymer electrodes. These devices were fabricated using solution processing techniques (spin-coating and ink-jet printing) except for the ITO electrodes. The morphologies of the complex films were influenced by $AgNO_3$ concentration, and uniform thin films were obtained with $AgNO_3$:**4a/b** molar ratios of 3:10 and 1:2 by spin coating. We found that a PVP film between an ITO electrode and a complex film plays an important role in generating the switching effect, and the operation voltages could be lowered by reducing PVP thickness, which acts as a diffusion barrier to ions. The electric characterizations of the devices suggest that the accumulation of Ag^+ ions near the interface of the complex film and PEDOT:PSS electrode contribute to the rewritable switching effect. The device using pre-coated ITO on a plastic substrate, 35 nm of PVP, a $AgNO_3$:**4a/b**(3:10) thin film, and a PEDOT:PSS electrode prepared by ink-jet printing showed reproducible switching characteristics with ON/OFF ratios of $10^2 - 10^3$ under ambient conditions without any device encapsulations.

Future the work on the devices using the complex films of Ag^+/HATNA derivatives, may include use of different Ag salts and HATNA derivatives to improve switching properties. Silver salts having different dissociation constants such as $AgBF_4$ and $AgCF_3SO_3$ probably could change the operation voltage or response time of the switching.

With respect to device fabrication and practicality, both the top and bottom electrodes in devices should use the same preparation method and material. We fabricated devices using ink-jet printed PEDOT:PSS electrodes for both the top and bottom electrodes. However, no significant switching effect was observed. The reason for no electrical switching is probably large leakage currents due to poor film quality leading

to an edge effect. We confirmed that the cross-sections of PEDOT:PSS lines prepared by ink-jet printing have a mountain shape with a maximum thickness (ca. 300 nm) in the middle and a minimum thicknesses (ca. 150 nm) in the edge. Thus, the overlap areas with the complex film and the bottom PEDOT:PSS electrode may have a extremely thin area in comparison to the average thickness of the complex film. Therefore, the development of a printing technique allowing for the formation of uniform films or the optimization of the conditions for ink-jet printing are necessary to further develop practical organic memory devices. Another problem related with the PEDOT:PSS electrode is the higher resistance comparing to metals and metal oxides electrodes. Therefore, the memory devices using PEDOT:PSS electrodes will need to be restricted to low density arrays and operation at low frequencies. In order to reduce device resistances and the voltage drop within electrodes, we can try to use other solution processable or printable electrodes such as metal nanoparticle composites and carbon nanotube electrodes. Such materials have a lower resistance than PEDOT:PSS, and they would help to reduce the voltage drop effect.